Exploring Collective Radiative Phenomena with Ultracold Matter Waves

A Dissertation Presented

by

Youngshin Kim

to

The Graduate School

in Partial Fulfillment of the Requirements

for the Degree of

Doctor of Philosophy

in

Physics

Stony Brook University

May 2024

Stony Brook University

The Graduate School

Youngshin Kim

We, the dissertation committee for the above candidate for the Doctor of Philosophy degree, hereby recommend acceptance of this dissertation.

Dominik Schneble – Dissertation Advisor
Professor, Department of Physics and Astronomy

Tzu-Chieh Wei – Chairperson of Defense
Professor, Yang Institute of Theoretical Physics
Professor, Department of Physics and Astronomy

Eden Figueroa – Committee Member
Associate Professor, Department of Physics and Astronomy
Joint Appointment, Brookhaven National Laboratory

Chen-Lung Hung – Committee Member
Associate Professor, Department of Physics and Astronomy
Purdue University

This dissertation is accepted by the Graduate School.

Celia Marshik
Dean of the Graduate School

Abstract of the Dissertation

Exploring Collective Radiative Phenomena with Ultracold Matter Waves

by

Youngshin Kim

Doctor of Philosophy

in

Physics

Stony Brook University

2024

Ultracold atoms find applications in the simulation of diverse physical phenomena spanning from condensed matter physics to cosmology. They can also be used to simulate quantum optics, using atomic matter waves in lieu of photons. Such an approach allows for investigations of waveguide quantum electrodynamics (QED), which deals with quantum emitters coupled to a one-dimensional photonic environment. The geometric confinement and presence of bandgaps enable tunable long-range interactions and quantum information processing with photons, but also challenge Markovian theories of open quantum systems.

In this dissertation, we explore collective radiative effects in waveguide QED with ultracold atoms. As initial states, superfluid (SF) and Mott-insulating (MI) phases are prepared in an array of matter-wave emitters. When the vacuum coupling is adiabatically turned on in a bandgap, we observe the renormalization of transport properties and access the polaritonic energy branches with modulation spectroscopy. When the vacuum coupling is suddenly turned on

in the continuum, we observe super- and subradiant emission of matter waves from the SF phase as well as directional collective emission. The slow propagation of matter waves allows us to investigate non-Markovian collective dynamics, including the onset of superradiance and a beating of atom-photon bound states in and outside the continuum. In the MI phase, we directly probe the spontaneous formation of coherence first described by Dicke, and demonstrate the coherence induced in a non-decaying spectator state of the emitters.

The results presented in this dissertation establish ultracold atoms as a versatile simulator of many-body quantum optics, opening the door to future studies beyond canonical configurations.

To my parents

Contents

List of Figures **ix**

Acknowledgements **xi**

1 Introduction **1**

2 Waveguide Quantum Electrodynamics with Matter Waves **6**
2.1 Survey of experimental platforms 6
2.1.1 Photonic systems and Purcell factor 6
2.1.2 Matter-wave quantum emitters in an optical lattice . . 7
2.2 Effective descriptions 11
2.2.1 Weisskopf-Wigner model 11
2.2.2 Master equation for many-body dynamics 17
2.2.3 Conditions for Markovian behavior 19
2.2.4 Bound state in a bandgap ("atom-photon" bound state) 21
2.2.5 Exact numerical simulations 23
2.3 Collective radiative phenomena 25
2.3.1 Introductory remarks 25
2.3.2 Single-photon superradiance 27
2.3.3 Collective bound states in and outside the continuum . 32
2.3.4 Polaritonic excitations 35
2.3.5 Non-Markovian collective dynamics 37
2.3.6 Many-body superradiance 38

3 Experimental Techniques for Bose-Einstein Condensates **43**
3.1 Conceptual basics 43
3.1.1 Bose-Einstein condensation 43
3.1.2 Atom-light interactions 44
3.2 Trapping and cooling of atoms 46
3.2.1 Laser system for ^{87}Rb atoms 46
3.2.2 Laser cooling 49

3.2.3 Magnetic trapping 50
3.2.4 Evaporative cooling and optical trapping 52
3.3 Imaging of atoms 53
3.3.1 Absorption imaging 53
3.3.2 State-selective imaging with Stern-Gerlach separation . 55
3.3.3 Post-processing with principal component analysis . . . 56
3.4 Control of internal states 60
3.4.1 Breit-Rabi formula 60
3.4.2 Microwave and RF control 61
3.4.3 Magnetic-field tagging 64
3.5 Optical lattices 66
3.5.1 Kapitza-Dirac diffraction 66
3.5.2 State-dependent optical potentials 67
3.6 Autonomous machine operation 70
3.6.1 System design 70
3.6.2 Parameter drifts caused by the environment 73
3.6.3 Regulating the atom number and magnetic field 75
3.6.4 Future improvements 77

4 Super- and Subradiant Dynamics of Quantum Emitters Mediated by Atomic Matter Waves 78
4.1 Introduction 78
4.2 Experimental platform and scheme 80
4.3 Directional collective emission 82
4.4 Collective dynamics 84
4.5 Spontaneous coherence formation 87
4.6 Conclusion 89
4.7 Methods 90
4.7.1 System preparation 90
4.7.2 Imaging and post-processing 91
4.7.3 Decay rates 92
4.7.4 Numerical simulation of decay dynamics 93
4.7.5 Spectral structure and bound states in the continuum (BIC) 96
4.7.6 Auxiliary measurements 99

5 Theoretical Basics on Interacting Bose Gases 104
5.1 Weakly interacting bose gas 104
5.1.1 Quasiparticle excitations and superfluidity 105
5.1.2 Mean-field approximation 107
5.1.3 Bose gas in one dimension 108

5.2 Strongly interacting Bose gas 109
5.2.1 Band theory in an optical lattice 110
5.2.2 Tight-binding approximation 113
5.2.3 Bose-Hubbard model 114
5.2.4 Lieb-Liniger parameter in one dimension 120

6 Realization of a Polaritonic Bose-Hubbard Model 121
6.1 Introduction 121
6.2 Polaritonic Bose-Hubbard model 122
6.3 Probing transport properties 128
6.4 Probing the polariton energy branches 130
6.5 Concluding remarks 132

7 Conclusion and Future Directions 133

Bibliography 138

A Feshbach resonance in a state-dependent lattice 161

B Some details on autonomous operation 163

C Further discussion on coherence of interacting Bose gases 170

List of Figures

2.1 A matter-wave quantum emitter 9
2.2 Density of state, coupling, and time integral in Weisskopf-Wigner theory 19
2.3 Spatial amplitudes of the bound state 22
2.4 Exact diagonalization of the single-excitation Hamiltonian. . . 25
2.5 Collective spontaneous emission of two emitters. 28
2.6 Decay rates from Fermi's golden rule and exact simulations. . 31
2.7 Bound states in the continuum (BICs) for 3 emitters 33
2.8 Collective bound states in the gap (BIGs) for 3 emitters . . . 34
2.9 Polariton band structure 36
2.10 Superradiance beyond the standard rate for 3 emitters. 38
2.11 Superradiant burst from fully excited emitter arrays. 40
2.12 Spontaneous coherence formation in the quasimomentum distribution of an emitter array. 42

3.1 Picture of our ultracold-atom apparatus 47
3.2 The energy levels of the ^{87}Rb atom. 48
3.3 Beam paths in the x-y plane and the top-down view of our apparatus around the Science cell. 54
3.4 Absoprtion images with Stern-Gerlach separation 56
3.5 Two-variable example of principal component analysis 58
3.6 Sample PCA image and its amplitudes along the principal components 60
3.7 Energy shift of hyperfine ground states according to the Breit-Rabi formula 62
3.8 AC noise measurements with the field-tagging method 64
3.9 State-dependent energy shift of the hyperfine ground states . . 69
3.10 Schematics of the autonomous experimental control. 72
3.11 Measurement of atom number fluctuations. 74
3.12 Atom number vs. room temperature with the airflow control. . 74
3.13 Measurement of magnetic field drift 75

3.14 Regulation of the atom number and magnetic field with autonomous operation. 76

4.1 Schematics of the experiments. 81
4.2 Phase control of emission characteristics in the SF regime . . . 83
4.3 Super- and subradiant dynamics in the SF regime. 85
4.4 Spontaneous coherence formation in the MI regime. 88
4.5 Numerical simulations of an M-emitter array containing a single excitation. 94
4.6 Supplementary data and simulation for Fig. 4.4. 95
4.7 Spectral contributions to the simulated dynamics of 3 emitters. 98
4.8 Collective emission versus coherence. 100
4.9 Collective dynamics at the continuum edge in the SF regime. . 101
4.10 Radiative decay of thermal excitations. 103

5.1 Band structures in an optical lattice of various depths. 111
5.2 Bloch waves in an optical lattice 112
5.3 Wannier functions in an optical lattice. 113
5.4 Phase diagram of the Bose-Hubbard model 117
5.5 Single-particle density matrix (SPDM) of the Bose-Hubbard model. 118

6.1 Polariton and bare tunneling rates $\tilde{J}, J$. 124
6.2 Theoretical properties of the polariton system. 126
6.3 Experimental setup for matter-wave polaritons. 127
6.4 Renormalization of the tunneling rate extracted from the momentum distribution of the $|r\rangle$. 129
6.5 Modulation spectroscopy in the Mott regime. 131

7.1 Scattering of a matter wave from an emitter array. 135
7.2 Fano resonance and electromagnetically induced transparency of a matter wave scattering from an emitter array. 136

A.1 Feshbach resonance in a state-selective lattice and tubes. . . . 162

B.1 The Flowchart of our UiPath bot. 165
B.2 A snippet of the bot code for updating Cicero variables. 169

C.1 Superfluid potential with spontaneously broken symmetry . . 171

Acknowledgements

I started my PhD program at Stony Brook University in 2017. Almost seven years have passed, and I inevitably have many people who I am grateful for helping me to make this far.

First of all, I would like to thank my advisor, Prof. Dominik Schneble. He is not only a source of deep insights in ultracold atomic physics, but also the best mentor that you can wish for. Despite his various responsibilities, Dominik always makes time for long and deep discussions with his students. He took all the questions seriously, often with a sense of humor, and I knew that I could ask just about anything, from research to life. Dominik's leadership style is also exemplary and unique; he chose to become an integral part of the lab by stationing himself in his small lab office right near the apparatus. Here, he led us on the front line of research, often staying until the late hours to help resolve experimental or technical issues. These experiences gave me confidence that there is nothing that cannot be solved or understood if you are persistent. Dominik has such high standards for writing a paper, and I even heard his critical voice as I was writing this dissertation. However, I knew deep down that it is all about producing results that you can truly be proud of, and that he deeply cares about the growth and success of his students. Our intense meetings, some of them lasting for days on end were formative experiences for me to develop a critical thinking. Of all things, he constantly encouraged me to believe that I can achieve something great, whenever I encountered a serious setback or self-doubt. I am grateful to have spent the last four years (plus nine months!) as a part of the Schneble lab, in which I have grown as a scientist and also have become a better person.

I also thank my colleagues in our lab, and we have one of the best teams. First, I would like to thank Joonhyuk Kwon, who first introduced me to the lab and taught me essential experimental techniques. He is not only a great physicist, but also an effective leader with ability to see the core of problems and to quickly find a solution. His leadership was critical in solving various technical issues and carrying out our experiments on polaritons successfully. I really enjoyed working alongside him, and I will fondly remember the long,

nerve-wracking, but exciting measurements runs lasting through the nights. I also appreciate his friendship and support even after his graduation, remotely sharing knowhows, reading our manuscript, and inviting me to his beautiful house in the Land of Enchantment. Another important person I'd like to thank is Alfonso Lanuza, my long-time labmate and a talented theorist. I am always awed by his ability to tackle complicated analyses, and the deep insights that he magically brings out of pages of calculations. He also has been a great friend, always open to conversations and willing to help on anything. It was fun to have him as a company on the various conference trips, including the visits to the Alligator Capital of the World and the hometown of Archimedes. I would also like to mention the contributions from our theorist friends, Yabo Li, who introduced us to inspiring theoretical ideas in our joint meetings, and Gabriel Cardoso, for his profound analysis on the LZ transition. I also had a brief overlap with Michael Stewart, and learned a lot from his clear presentations and positive vibes. His early theoretical analyses have been invaluable for many parts of our later experiments.

More recently, our lab has been very fortunate to have Hongyi Huang as the leader of the new generation. He quickly revealed his talent as a great experimentalist, examining the ins and outs of our apparatus more carefully than anyone else. He is now the master of our machine, improving it in so many ways, and is making a spectacular progress on our new experiment on scattering. Combined with his ability to model physical problems, as demonstrated in his earlier theoretical papers, and with his persistence, I can already see a great success in the near future. I also extend my thanks to Muxi Liu and Loc Ngo, who, despite their brief stay, brought warmth to our cold lab with their lively contributions on STA and optical techniques. Our most recent member, Tanner O'Neal, is already demonstrating his talent in analyzing experimental data, and is ready to tackle new experiments with atomic mixtures. We also have very talented undergraduate members in our lab. Following Max Frankel, who pioneered new light-projection methods for our apparatus, Hyunjun Park and Kevin O'Shea are continuing the tradition of excellence, making important contributions to our imaging and optical systems. Last but not least, I have greatly benefited from the presence of Dr. Martin Cohen. His broad understanding of lasers and their companies has been invaluable, and he always brought fresh perspectives that sharpened our research direction. I especially thank him for the tireless readings of our manuscript and letters, independent of the number of revisions.

I also appreciate the committee members of my dissertation. Prof. Tzu-Chieh Wei has provided invaluable comments with his profound theoretical insights, and I have also greatly benefited from our joint journal club sessions.

His understanding in both theoretical and experimental research, along his passion for quantum information science, has been inspiring. I also thank Prof. Eden Figueora for for insightful comments and suggestions, and his guidance during my time in his lab. There, I learned how to think like an experimentalist for the first time, often valuing actions rather than abstract analysis, and also how to focus on the broader vision despite technical challenges. I also deeply thank Prof. Chen-Lung Hung from Purdue University, who graciously agreed to serve on my committee as an external member. It is not easy to find someone whose expertise spans both ultracold atomic physics and quantum optics, and my dissertation has benefited greatly from his critical insights and robust feedback rooted in his deep understanding of both fields.

One of the bright sides of being in the basement was belonging to the brotherly, warmhearted AMO community at Stony Brook. I would first like to thank the early members of the QIST lab, especially Mael Flament, Sonali Gera, Guodong Cui, and Steven Sagona-Stophel, who guided my first steps in becoming an experimentalist and showed me how to remain strong and positive. I also thank all the comrades of the basement in the past and present, including Brian Arnold, Bertus Jordaan, Mehdi Namazi, Spencer Horton, Ludwig Krinner, Alessia Schriminich, Leonardo Castillo-Veneros, Shane Andrewski, Yusong Liu, Samet Demircan, Dillion Cottrill, Andrea Londono, Brian Kaufman, Chuang Cheng, Yifan Fang, Xiaoyang Liu, Jay Rutledge, Eli Rafkin, Ian Schwartz, Myles Silfies, Sam McClung, Julia Codere, Log Ngo, Chase Wallace, Dounan Du, Gonenc Mogol, Edoardo Buonocore, Zachary Withers, Yuanchi Qing, and many new members, for being together at the DAMOP conferences, AMO lunches, Friday Socials, custom hat-making parties, soccer matches, and many casual encounters in the basement corridor. I also extend my gratitude to the leadership of the AMO community at Stony Brook, Profs. Hal Metcalf, Dominik Schneble, Thomas Weinacht, Thomas Allison, Eden Figueora, Ash Kumar, Jesús Pérez Ríos, Kunal Das, and Dr. Eric Jones, for cultivating an open and vibrant environment.

There are many people in the department from whom I received the support and guidance at various points. I thank Prof. Christopher Herzog (now at King's College London) for giving me the opportunity to work with him when I was a master's student, and for his patience despite my slow progress, which eventually led to a paper. I thank Prof. Derek Teaney for his great course in Classical Electrodynamics and for writing a recommendation letter for my PhD program application. I still remember his advice, "Think outside the box". Indeed, I could not have imagined that I would become an experimentalist, let alone fixing lasers and staying all night to take measurements. I thank Donald Sheehan, Susan Russo, Prof. Jacobus Verbaachot, and Prof. Matt Dawber, for

their help in navigating various graduation requirements and financial matters. I also thank Vladislav Zakharov and Ryan Richards for their kindness as my first housemates at Stony Brook.

I thank the Korean student group in the physics department, which used to be large once upon a time. I would like to especially thank the friends of the Foxhill house, Junsik Yoo, Joonhyuk Kwon, Jaehyeok Chang, Dongwon Han, and Kyle Lee. They are serious, hard-working people both in terms of conducting research and having fun. I thank their invitations on various occasions, especially on holidays, which made me feel closer to home. I also thank Gongjun Choi, Taeho Ryu, Saebyeok Jeong, Hyeyun Park, Nanoom Lee, Changha Choi, Changhyun Cho, Jaesung Lee, and Yichul Choi. Most of them have left already, but showed me that the life after the graduate school will be great. I am also grateful for the holiday dinners at The Pie hosted by Prof. Chang Kee Jung every year. Toward the end of my master's program, I was a bit lost, and I remember visiting him once for advice. He told me to ask myself who I am. I believe I understand that a little better now, and I hope to always stay true to myself. I also thank the fellows of the Korean Graduate Student Association, and also the members of the 3-generation tennis club. I should not forget my old friends back in Korea. Thank you for hanging out with me whenever I am back, as if I have never been away.

Most importantly, I would like to thank my family for being there through my PhD journey. My girlfriend, Daeun Noh, who also recently got her PhD, has been the one person with whom I can always share the ups and downs of the experimental research. Thanks to her, my time here at Stony Brook has been so much brighter than I originally imagined. Especially during the last two years, despite being two thousand miles away, she has sent me her love and encouragement with patience, through which I could finally catch up with her. I also thank Daeun's sister for tolerating my frequent visits to their house, sharing delicious food, and also taking us along on wonderful road trips. I also thank Daeun's brother for being my grocery buddy, during my last, lonely year. I myself have an older brother, who has always been my source of inspiration since I was a kid. He always pointed me toward the right direction when I had a hard time deciding what matters the most, and showed me what might be there if you follow an unknown path. When I have to make an important decision, his advice continues to be a guiding light. Finally, I thank my parents, who have supported me all the way and tried their best to help my long journey toward whatever I am trying to become. My father, who is a strong pillar of our family, showed me that there is nothing to worry about. My mother taught me how to stay positive and persistent, and always encouraged me to believe in myself. When I am exhausted, they have provided

a place to fall back on, and told me that it is okay to fail. I am grateful for their love, and this dissertation is dedicated to them.

I am grateful for the generous support from the National Science Foundation of the United States of America (NSF), and by Stony Brook University's Center for Distributed Quantum Processing.

Chapter 1

Introduction

Quantum many-body systems are intrinsically hard to simulate due to their large number of degrees of freedom. The quantum states of a collection of M two-level systems, for example, require 2^M-dimensional Hilbert space, as opposed to the classical counterpart described by M bits. This leads to the idea of using quantum systems themselves for the purpose of quantum simulations, as proposed by R. Feynman [1]. We can build a physical platform that is programmable at the quantum level, either in the digital or analog manner, such that important models can be simulated in a range of parameter space, deepening our understanding [2]. Since the first realization of Bose-Einstein condensates (BEC) [3, 4], ultracold atoms have been a major force driving this field, as the low temperatures and precision controls bring the macroscopic coherence and scalability. Indeed, quantum phase transitions were first observed with ultracold atoms in optical lattices [5], and there have been a large number of important works afterward [6–12].

While many experiments are being aimed at condensed matter systems, there are also emerging creative approaches to simulate diverse physical models, such as lattice gauge theories [13], quantum chemistry [14], or even cosmological models [15]. A proposal by de Vega et al. suggested that ultracold atoms in an optical lattice can be also used to simulate radiative phenomena [16, 17], where atomic matter waves replace photons, and the potential wells play the role of matter-wave emitters. Our lab has pioneered implementing this idea of simulating quantum optics and analyzing it in detail [18, 19]. The previous experiments from our lab have demonstrated spontaneous emission of matter waves [20], which is an emblematic process of Weisskopf-Wigner theory, as well as novel scenarios such as emission into a photonic crystal and formation of atom-photon bound states [20, 21].

The matter-wave platform turns out to be particularly suitable for waveguide quantum electrodynamics (QED) [19], a nascent field of quantum optics.

Waveguide QED has two important characteristics distinguishing it from conventional paradigms in quantum optics, such as cavity QED [22]. The first is that it deals with quantum emitters interacting with photons mainly in one-dimensional geometries, combining the features of an open quantum system with confinement effects. The confinement to one dimension can alter quantum optics in interesting ways, such as in the total reflection of a photon by a single emitter [23, 24], or in long-range interactions without diminishing strength [25], making collective effects much stronger than in free space. The second characteristic is that the photon dispersion can be modified to feature bandgaps, such as in a photonic crystal waveguide [26]. Because a photon cannot propagate in a bandgap, it instead forms an evanescent cloud surrounding an emitter, leading to an atom-photon bound state [27, 28]. In addition, the diverging density of states near a band edge can escape the conventional Markovian descriptions of quantum optics, posing interesting theoretical challenges [29, 30].

Collective dynamics in waveguide QED have gained interest in the context of quantum information processing, and have been explored with various types of emitters in the single-photon regime, including transmon qubits [31–34], atoms near nanophotonic structures [35–37] or nanofibers [38, 39], and quantum dots [40]. As the control over emitters improves, the effect of propagation delay becomes an important question [41, 42]. This leads to the idea of non-Markovian collective dynamics, whose theoretical studies have only recently become active [43–46] (including a recent work from our group [47]). As with any quantum system, understanding many-body dynamics of quantum emitters, especially in extended geometries, is a hard problem [48–52]. This regime is yet to be observed in a strongly coupled waveguide-QED setup, and there are only a few early explorations, such as multi-excitation subradiant states in two distant pairs of transmon qubits [33] or, more recently, a superradiant burst in a large ensemble chirally and weakly coupled to a nanofiber [53].

The matter-wave platform provides several advantages over canonical configurations of quantum optics in investigating waveguide-QED phenomena, and we highlight some of them.

- An important figure of merit in waveguide QED is the coupling efficiency β [25] between emitters and a waveguide. While photonic platforms cover a range of β for various purposes, an ideal scenario requires $\beta = 1$. This is naturally achieved with a one-dimensional optical lattice.

- As we will see, matter-wave emitters are fully and dynamically tunable, in terms of their vacuum coupling and energy levels [20].

- The platform is intrinsically scalable, as the optical lattice, playing the role of an emitter array, can be easily made large and homogeneous.

- The toolbox of ultracold atoms can be used, for example, in preparation of many-body states and imaging of momentum distributions. It also enables interesting additional features, such as a band structure for matter waves [21], or in principle, the implementation of fermionic quantum optics [54].

In this dissertation, we discuss two recent experiments conducted with our matter-wave platform [55, 56], each focusing on collective dissipative and coherent phenomena, respectively. We explore how the characteristics of photonic-crystal waveguide QED, photons being in one dimension and having a gapped nonlinear dispersion, shape the collective effects in an array of quantum emitters. We will first cover basic concepts and numerical studies regarding waveguide QED based on matter waves in Chapter 2, and technical details related to our apparatus in Chapter 3. We also address some elementary concepts on interacting Bose gas in Chapter 5.

In Chapter 4, we focus on collective dissipative phenomena, introducing an experiment on super- and subradiant dynamics of quantum emitters. There are two main mechanisms by which superradiance can be achieved. The first is by directly preparing a phase-coherent state of emitters, usually in the single-excitation regime, which are referred to as timed Dicke states (TDSs) [57, 58]. This is also closely related to subradiance in waveguide QED, as phase mismatches can prohibit the decay into certain modes. The second way of superradiance is to allow coherence to emerge spontaneously, e.g. through the decay process of fully excited emitters, resulting in a superradiant burst [59] in the many-body (many-excitation) regime.

In our experiment, we realize timed Dicke states via macroscopically occupied coherent states in a superfluid phase, and demonstrate collectively enhanced, suppressed, and directional spontaneous emission. We realize super- and subradiant dynamics in the non-Markovian regimes for the first time. In this regime, we observe the delayed onset of superradiance, and also an interesting interplay between the non-Markovianities originating from the continuum edge and the propagation delay, resulting in a beating of a bound state in the gap (BIG) and a bound state in the continuum (BIC). To explore many-body superradiance, we can prepare a fully excited state of the emitter array in a Mott-insulating phase, even though we do not yet reach the regime of a burst due to technical considerations. However, with the capability to observe the quasimomentum distribution of emitter excitations, we directly probe the early stage of the spontaneous coherence formation in the array, and reveal

the role of matter-wave emission in imprinting the phase. This is the first time, since the original discussion by Dicke 70 years ago, that such coherence buildup has been directly observed.

In Chapter 6, we turn to collective coherent phenomena, with dissipation largely suppressed in a bandgap. We introduce a new type of Bose-Hubbard model (BHM) that encompasses not only waveguide QED, but also the broad concept of polaritons [60–63]. The formation of bound states in a bandgap, whose photonic component is localized near each emitter, enables controllable long-range interactions, and has motivated many theoretical proposals [26, 64–70] for quantum many-body physics. Taking a thermodynamic limit, i.e. in a large array with negligible boundary effects, the bound states generalize to polariton eigenmodes of the system [71]. The dispersion of these quasiparticles forms a polariton band structure, and the ground band can serve as a new basis for a polaritonic BHM [68]. Our quasiparticles, which we named matter-wave polaritons, realize an analogue of exciton-polaritons [72, 73], and provide a first example of such particles in strongly interacting regimes. To probe the polaritonic character of our system, we use the modulation spectroscopy [74–76] that reveals the energy gaps in the Mott regime, and examine the system's transport properties through the momentum-distribution images. We demonstrate the control of transport via the vacuum coupling and emitter detuning, which provides an alternative way to drive the celebrated quantum phase transition [5, 74].

We end the dissertation in Chapter 7 with future perspectives, including some preliminary simulations on scattering experiments.

Publication of this PhD work described either in part or in full:

- In Chapter 5
  Super- and subradiant dynamics of quantum emitters mediated by atomic matter waves
  Y. Kim, A. Lanuza, and D. Schneble
  arXiv:2311.09474

- In Chapter 6
  Formation of matter-wave polaritons in an optical lattice
  J. Kwon, Y. Kim, A. Lanuza, and D. Schneble
  Nature Physics **18**, 657-661 (2022)

Publication co-authored during this PhD work (not included in this thesis):

- *Multiband and array effects in matter-wave-based waveguide QED*
  A. Lanuza, J. Kwon, Y. Kim, and D. Schneble
  Phys. Rev. A **105**, 023703 (2022)

Chapter 2

Waveguide Quantum Electrodynamics with Matter Waves

In this chapter, we discuss waveguide quantum electrodynamics (QED) realized with ultracold matter waves. After a brief introduction to waveguide QED, we will explain how the framework is implemented in our ultracold-atomic platform. We discuss some descriptions of waveguide QED systems in the Markovian and non-Markovian limits, and collective effects that can be observed in an array of quantum emitters.

2.1 Survey of experimental platforms

2.1.1 Photonic systems and Purcell factor

The coupling of light with an atom in free space is very inefficient [25, 26]. The cross section of an atom is given by $\sigma_0 = 3\lambda^2/2\pi$ with λ being the resonant wavelength, while the effective beam area is bounded from below by the diffraction limit $A_{\text{eff}} \gtrsim \lambda^2$, restricting the interaction probability σ_0/A_{eff}. This can be overcome by modifying the radiative environment in a cavity, whose effect was demonstrated by E. Purcell, where the decay rate in a strongly damped cavity is enhanced by the Purcell factor $(3/4\pi^2)\lambda^3 Q/V$ [77, 78].[1] For an atom placed near a waveguide, a similar enhancement factor can be defined

[1] According to Fermi's Golden rule, the transition rate is proportional to the spectral density of modes per unit volume ρ, and the Purcell factor can be understood from $\Gamma_{\text{cavity}}/\Gamma_{\text{free}} = \rho_{\text{cavity}}/\rho_{\text{free}}$, with $\rho_{\text{free}} \propto \nu^2/c^3$ in free space and $\rho_{\text{cavity}} = Q/\nu V$ in a cavity [79], where $Q = \nu/\Delta\nu$ and $\Delta\nu$ is the spectral bandwidth.

[26],

$$P_{1D} = \frac{\Gamma_{1D}}{\Gamma'} \tag{2.1}$$

where Γ_{1D} is the decay rate into the waveguide, and Γ' is the decay rate into other modes in free space. This provides a figure of merit for the system, and with a large $P_{1D} \gg 1$, one can treat the system as effectively one-dimensional. Furthermore, in this limit, purely coherent dynamics may be realized if the dissipation into the waveguide is suppressed, such as in a bandgap (Section 2.2.4). From P_{1D}, one can alternatively define the coupling efficiency [25]

$$\beta = \frac{P_{1D}}{P_{1D}+1} = \frac{\Gamma_{1D}}{\Gamma_{1D}+\Gamma'}, \tag{2.2}$$

which has a maximum value of 1. A wide range of β (or P_{1D}) is covered by different atomic and solid-state platforms.

In the optical range, quantum dots coupled to a photonic crystal waveguide [80, 81] can reach up to $P_{1D} \sim 5$ ($\beta = 0.99$ in a cryostat [82]), which however suffers from inhomogeneous broadening [25] and are not easy to scale up to many dots. Alternatively, solid-state defects like silicon vacancies [83] can reach $P_{1D} \sim 2$ to 3. Molecules also have been coupled to a waveguide by dopping in an organic crystal, with $\beta \sim 0.18$ [84]. Thousands of atoms can be trapped near an optical-nanofiber waveguide, with $\beta \sim 0.01$ [39, 53, 85], which can be good for specialized applications like quantum memory [38]. In the microwave regime, superconducting circuits provide a powerful platform, where a few transmon qubits can be coupled to a transmission line with $\beta = 0.999$ [32–34]. In general, it is hard to achieve both high β and high number of emitters M in photonic platforms [25].

2.1.2 Matter-wave quantum emitters in an optical lattice

Ultracold atoms in an optical lattice provide an interesting setup for studying waveguide QED phenomena. Treating the occupation number 0 and 1 of each lattice well as the two levels of a quantum emitter (also referred to as an impurity or an effective spin), one can realize an array of such quantum emitters coupled to the vacuum of matter waves.[2] Here, the idea is to use a state-selective lattice, and the trapped and untrapped states, which are Rabi

[2]With the reservoir being initially empty; when the impurities are embedded in a BEC, one realizes the spin-boson model with coupling to the sound modes [86].

coupled, to play the role of an excitation and a photon, respectively. Based on the initial proposal [17, 87], our lab has established matter-wave quantum emitters [18, 19] and observed various phenomena that are typically associated with quantum optics in a photonic crystal, such as non-Markovian decay and bound states near bandgaps [20, 21].

To obtain a quantum-optical model of matter-wave emitters, we start from the second-quantized picture of atoms in an optical lattice with internal hyperfine ground states r and b ("red" and "blue") coupled by a classical microwave field (we do not include collisional interactions here),

$$\hat{H} = \int d^3\boldsymbol{r}\hat{\psi}_r^\dagger(\boldsymbol{r})\left[\hat{H}_A + \frac{\hat{\boldsymbol{p}}^2}{2m} + V_r(\boldsymbol{r})\right]\hat{\psi}_r(\boldsymbol{r}) + \int d^3\boldsymbol{r}\hat{\psi}_b^\dagger(\boldsymbol{r})\left[\hat{H}_A + \frac{\hat{\boldsymbol{p}}^2}{2m} + V_b(\boldsymbol{r})\right]\hat{\psi}_b(\boldsymbol{r}) - \int d^3\boldsymbol{r}\left[\hat{\psi}_r(\boldsymbol{r})\hat{\psi}_b^\dagger(\boldsymbol{r})\boldsymbol{\mu}_{br} + \hat{\psi}_r^\dagger(\boldsymbol{r})\hat{\psi}_b(\boldsymbol{r})\boldsymbol{\mu}_{rb}\right]\cdot\boldsymbol{B}(\boldsymbol{r},t) \tag{2.3}$$

where $\hat{H}_A$ is the atomic Hamiltonian for the internal electronic configurations and $V_{r/b}(\boldsymbol{r})$ is the lattice potential experienced by each species. The magnetic dipole matrix elements $\boldsymbol{\mu}_{ij}$ are independent of the position $\boldsymbol{r}$, i.e. $\boldsymbol{\mu}_{ij}(\boldsymbol{r}) = \langle 0|\,\hat{\psi}_i(\boldsymbol{r})(-\mu_B)\hat{\boldsymbol{L}}(\boldsymbol{r})\hat{\psi}_j^\dagger(\boldsymbol{r})\,|0\rangle/\hbar = \langle 0|\,\hat{\psi}_i(0)(-\mu_B)\hat{\boldsymbol{L}}(0)\hat{\psi}_j^\dagger(0)\,|0\rangle/\hbar$ where $\hat{\boldsymbol{L}}(\boldsymbol{r}) = (\hat{\boldsymbol{r}}-\boldsymbol{r})\times\hat{\boldsymbol{p}}$ being the angular momentum operator and μ_B being the Bohr magneton. The Hamiltonian already assumes the dipole approximation[3], but the phase of the coupling can still depend on the position of an atom itself relative to the magnetic field $\boldsymbol{B}(\boldsymbol{r},t) = (B_0\hat{\boldsymbol{e}}e^{i\boldsymbol{k}_\nu\cdot\boldsymbol{r}-i\nu t} + B_0^*\hat{\boldsymbol{e}}^*e^{-i\boldsymbol{k}_\nu\cdot\boldsymbol{r}+i\nu t})/2$. In our experiments, our sample size ~ 10 μm is much smaller than the microwave wavelength ~ 1 cm, and the phase will be only relevant if two microwave fields with different phases are used.

The operators $\hat{\psi}_r^\dagger$, $\hat{\psi}_b^\dagger$ create the eigenstates of the internal states, but not the motional eigenstates. Our experiments are typically conducted in a one-dimensional state-selective lattice, $V_r(\boldsymbol{r}) = V_0\sin^2(k_{\mathrm{r}}z)$ and $V_b(\boldsymbol{r}) = 0$ (with the recoil momentum $k_{\mathrm{r}} = 2\pi/\lambda = \pi/d$ and lattice spacing $d = \lambda/2$), and thus the two species share the same motional eigenstate $\psi^\perp(x,y)$ in the transverse directions, x and y (if confined in a deep tube, this will be a harmonic ground state). We assume that the lattice is very deep, and each well can be approximated as a harmonic oscillator, with atoms occupying only the ground state. We can then expand the operators as

$$\hat{\psi}_r(\boldsymbol{r}) = \psi^\perp(x,y)\sum_j \phi_j(z)\hat{r}_j, \quad \hat{\psi}_b(\boldsymbol{r}) = \psi^\perp(x,y)\sum_k \psi_k(z)\hat{b}_k, \tag{2.4}$$

[3]Expansion near the atomic position $\boldsymbol{r}$, $e^{i\boldsymbol{k}\cdot\hat{\boldsymbol{r}}} \approx e^{i\boldsymbol{k}\cdot\boldsymbol{r}}(1 + i\boldsymbol{k}\cdot(\hat{\boldsymbol{r}}-\boldsymbol{r}) + \dots)$.

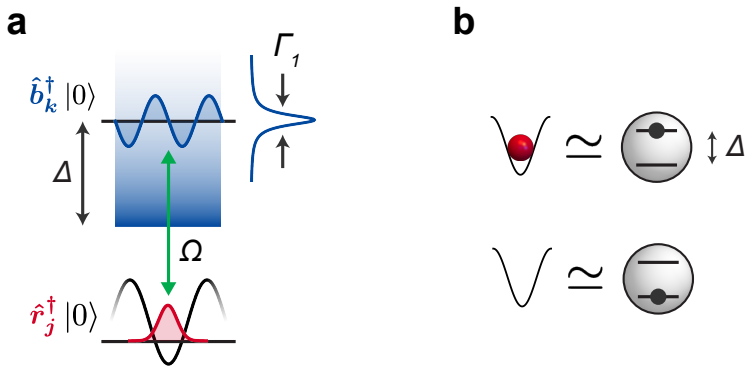

Figure 2.1: Matter-wave quantum emitter. **a,** The lattice trapped state $\hat{r}_j^\dagger|0\rangle$ and the free state $\hat{b}_k^\dagger|0\rangle$ are coupled with strength Ω and detuning Δ from the edge $k = 0$ of the mode continuum. **b,** The occupation number of the lattice well, 1 and 0, corresponds to the excited and ground state of the emitter, respectively, with the energy difference $\hbar\Delta$.

where $\psi_k(z) = L^{-1/2}e^{ikz}$ is the free-particle wavefunction, $\phi_j(z) = (\pi a_{\rm ho}^2)^{-1/4}e^{-(z-z_j)^2/2a_{\rm ho}^2}$ is the harmonic oscillator ground state at jth site with $z_j = dj$, and the new operators follow $[\hat{r}_i, \hat{r}_j^\dagger] = \delta_{i,j}$ and $[\hat{b}_i, \hat{b}_j^\dagger] = \delta_{i,j}$. We are assuming that the system is in a box of size L. In practice, there is a residual harmonic confinement holding atoms against gravity, which can be ignored for our experimental time scales. The Hamiltonian (Eq. 2.3) can be written as

$$\begin{aligned}\hat{H} =& \sum_j(\hbar\omega_{0,r} + \hbar\omega_{\rm ho}/2)\hat{r}_j^\dagger\hat{r}_j + \sum_k(\hbar\omega_{0,b} + \hbar\omega_k)\hat{b}_k^\dagger\hat{b}_k \\ &- \sum_{j,k}\left[\gamma_{k,j}\hat{r}_j\hat{b}_k^\dagger\boldsymbol{\mu}_{br} + \gamma_{j,k}\hat{r}_j^\dagger\hat{b}_k\boldsymbol{\mu}_{rb}\right]\cdot(B_0\hat{\boldsymbol{e}}e^{-i\nu t} + B_0^*\hat{\boldsymbol{e}}^*e^{i\nu t})/2, \qquad (2.5)\end{aligned}$$

where $\omega_{0,r} < \omega_{0,b}$ are the internal energies, $\omega_{\rm ho} = \hbar/ma_{\rm ho}^2$ is the harmonic oscillator frequency, and $\omega_k = \hbar k^2/2m$ is the free-particle dispersion. We also defined the wavefunction overlap

$$\begin{aligned}\gamma_{j,k} \equiv& \int dz\phi_j^*(z)\psi_k(z) \\ =& \sqrt{\frac{2}{L}}(\pi a_{\rm ho}^2)^{1/4}e^{-k^2a_{\rm ho}^2/2}e^{ikz_j} = \sqrt{\frac{2}{L}}\left(\frac{2\pi}{k_{\rm ho}^2}\right)^{1/4}e^{-(k/k_{\rm ho})^2}e^{ikz_j} \qquad (2.6)\end{aligned}$$

(also referred to as the Franck-Condon overlap), whose position dependence gives a phase factor, $\gamma_k \equiv |\gamma_{j,k}|e^{ikz_j}$. We have defined $k_{\rm ho} \equiv \sqrt{2m\omega_{\rm ho}/\hbar}$, and

also define $\gamma_{k,j} \equiv \gamma^*_{j,k}$ for later convenience. To get rid of the time dependence, we can change to the rotating-wave frame with the unitary transformation $\hat{U} = \exp[i(\omega_{0,b} - \nu)t \sum_j \hat{r}^\dagger_j \hat{r}_j + i\omega_{0,b} t \sum_k \hat{b}^\dagger_k \hat{b}_k]$. Also applying the rotating-wave approximation (dropping the counter-rotating terms), we obtain the time-independent Hamiltonian[4]

$$\hat{H}^{\mathrm{RWA}} = \sum_j \hbar\Delta \hat{r}^\dagger_j \hat{r}_j + \sum_k \hbar\omega_k \hat{b}^\dagger_k \hat{b}_k + \frac{\hbar}{2} \sum_{j,k} \left[\Omega \gamma_{k,j} \hat{r}_j \hat{b}^\dagger_k + \Omega^* \gamma_{j,k} \hat{r}^\dagger_j \hat{b}_k \right], \quad (2.7)$$

where $\Omega = \boldsymbol{\mu}_{br} \cdot B_0 \hat{\boldsymbol{e}}/\hbar$ is the standard Rabi frequency between the internal levels (the minus sign was absorbed, e.g. with an additional transformation). For the detuning of the microwave, we include the shift of the resonance due to the lattice confinement as $\Delta = \nu - [\omega_{0,b} - (\omega_{0,r} + \omega_{\mathrm{ho}}/2)]$. The most compact form of the Hamiltonian may be obtained in the interaction picture,

$$\hat{H}^I = \frac{\hbar\Omega}{2} \sum_{j,k} \gamma_k e^{-i(\Delta - \omega_k) - ikz_j} \hat{r}_j \hat{b}^\dagger_k + \mathrm{H.c.}, \quad (2.8)$$

where we also made the position dependence of a phase factor explicit. We will also use the notation $\Delta_k \equiv \omega_k - \Delta$ later on [18, 87].

In a deep lattice, we may assume the collisional blockade regime $\hat{r}^\dagger_j \hat{r}^\dagger_j |0\rangle = 0$, and the operators can be mapped to the occupational spin operators as $\hat{r}^\dagger_j = \hat{\sigma}^+_j = |1\rangle\langle 0|$ and $\hat{r}_j = \hat{\sigma}^-_j = |0\rangle\langle 1|$. We then recognize that the Hamiltonian (Eq. 2.7 or 2.8) is the standard Hamiltonian of the atom-photon interactions [18, 19, 87], with bosonic atoms $\hat{b}^\dagger_k |0\rangle$ replacing photons, and the lattice wells playing the role of quantum emitters. On the other hand, in a shallow lattice, if the collisional interactions between r atoms are negligible, the system realizes an array of harmonic oscillators [17, 88].

In our experiments, the lattice spacing $d \equiv \lambda/2$ defines the typical length scale, and we use the recoil wavevector (momentum) $k_{\mathsf{r}} \equiv \pi/d = 2\pi/\lambda$, recoil frequency $\omega_{\mathsf{r}} = \hbar k^2_{\mathsf{r}}/2m$, and recoil energy $E_{\mathsf{r}} = \hbar\omega_{\mathsf{r}}$ to express the magitudes of various parameters. The lattice depth is written as $V_0 = E_{\mathsf{r}} s$, and the harmonic frequency of each well is $\omega_{\mathrm{ho}} = (2/\hbar)\sqrt{V_0 E_{\mathsf{r}}} = 2\omega_{\mathsf{r}}\sqrt{s}$.

As depicted in Fig. 2.1, the parameters $\Omega\gamma_k/2$ and Δ define the vacuum coupling

$$g_{j,k} \equiv \Omega^* \gamma_{j,k}/2 \quad (2.9)$$

[4] $\hat{H}_U = \hat{U}\hat{H}\hat{U}^{-1} - i\hbar\hat{U}\partial_t\hat{U}^{-1}$. Also used the identity $\hat{b}_i e^{\alpha\sum_j \hat{b}^\dagger_j \hat{b}_j} = e^{\alpha\sum_j (\hat{b}^\dagger_j \hat{b}_j + \delta_{ij})}\hat{b}_i$ and $\hat{b}^\dagger_i e^{\alpha\sum_j \hat{b}^\dagger_j \hat{b}_j} = e^{\alpha(\sum_j \hat{b}^\dagger_j \hat{b}_j - \delta_{ij})}\hat{b}^\dagger_i$.

and the excitation energy $\hbar\Delta$ of these matter-wave quantum emitters, which are fully tunable (up to the k dependence). The dispersion ω_k can be tuned with the additional lattice potential that the b atoms are subject to, and for the free case $V_b(z) = 0$, it is quadratic $\omega_k = \hbar k^2/2m$, with a bandgap below $k = 0$. Importantly, there is no decay into free space ($\Gamma' = 0$) other than those into the one-dimensional modes ($\Gamma_{1\mathrm{D}}$), and thus the Purcell factor diverges, $P_{1\mathrm{D}} = \infty$ ($\beta = 1$), allowing us to realize ideal scenarios of waveguide QED.

2.2 Effective descriptions

2.2.1 Weisskopf-Wigner model

In the semi-classical treatment of atom-light interactions (cf. Eq. 3.4), the interactions vanish in the limit of zero electromagnetic fields, contrary to the observation that an atom can interact with the vacuum and emit a photon, the process known as the spontaneous emission. Only in the quantized form, the electromagnetic field has non-zero vacuum fluctuation $\langle 0| E^2 |0\rangle \neq 0$ [89, 90], and can induce the irreversible, exponential decay. It was first described by the Weisskopf-Wigner model of spontaneous emission [91, 92] that invokes the Markov approximation to compute the decay rate (and the Lamb shift), which is also obtained from Fermi's Golden Rule.

In this section, we introduce an array version of the Weisskopf-Wigner model in one dimension (see also [18, 19, 93]; for 3D, [17, 87]), and discuss the validity of the Markov approximation. We start with a general Hamiltonian of quantum emitters coupled to bosonic excitations (photons),

$$\hat{H} = \sum_j \hbar\Delta \hat{\sigma}_j^+ \hat{\sigma}_j^- + \sum_k \hbar\omega_k \hat{b}_k^\dagger \hat{b}_k + \sum_{j,k} \hbar g_{j,k} \hat{\sigma}_j^+ \hat{b}_k + \mathrm{H.c.} \tag{2.10}$$

For concreteness, we discretize the photon momenta $\delta k = 2\pi/L$ in a box of L, which can be taken to infinity later. We focus on the single-excitation manifold,

$$|\psi(t)\rangle = \sum_j A_j(t) |e_j\rangle e^{-i\Delta t} + \sum_k B_k(t) |1_k\rangle e^{-i\omega_k t}, \tag{2.11}$$

where A_j and B_k are the interaction-picture amplitudes, and $|e_j\rangle \equiv \hat{\sigma}_j^+ |0\rangle$, $|1_k\rangle \equiv \hat{b}_k^\dagger |0\rangle$. The equations of motion for the amplitudes are

$$i\dot{A}_j(t) = \sum_k B_k(t) g_{j,k} e^{-i\Delta_k t}, \quad i\dot{B}_k(t) = \sum_j A_j(t) g_{k,j} e^{i\Delta_k t} \tag{2.12}$$

where $\Delta_k \equiv \omega_k - \Delta$. The photon amplitudes B_k can be eliminated by integrating the second and inserting into the first, which gives the equation for the excitation amplitudes A_j:

$$\dot{A}_j(t) = -\sum_{j'} \int_0^t dt' \sum_k g_{j,k} g_{k,j'} e^{-i\Delta_k(t-t')} A_{j'}(t'), \tag{2.13}$$

where $g_{k,j} = g^*_{j,k}$.

The Markovian approximation in this context amounts to simply taking $A_{j'}(t')$ out of the integral, and sending the integral limit t to ∞. This means that we are focusing on the emitters, and are integrating out the photonic degrees of freedom (bath), reducing them to c-numbers. To understand when such an approximation is valid, we identify the integrand as the bath correlation function [89, 94, 95],

$$G_{j,j'}(t-t') = \langle 0 | \, \hat{B}_j(t) \hat{B}^\dagger_{j'}(t') \, | 0 \rangle = \sum_k g_{j,k} g_{k,j'} e^{-i\omega_k(t-t')}, \tag{2.14}$$

where the operator of the bath is defined as $\hat{B}_j = \sum_k g_{j,k} \hat{b}_k$ and in the interaction picture as $\hat{B}_j(t) = e^{iH_B t/\hbar} \hat{B}_j e^{-iH_B t/\hbar}$ with $H_B = \sum_k \hbar\omega_k \hat{b}^\dagger_k \hat{b}_k$. In terms of these,

$$\dot{A}_j(t) = -\sum_{j'} \int_0^t dt' G_{j,j'}(t-t') e^{i\Delta(t-t')} A_{j'}(t'). \tag{2.15}$$

The integral depends on all past values of $A_j(t)$, which we would like to take out of the integral. We use the idea of coarse-graining [89, 94], with the time interval τ much smaller than the typical time scale τ_A of the change of $A_j(t)$,

$$\dot{A}_j(t) = -\sum_{j'} \left[A_{j'}(t) \int_{t-\tau}^t dt' + A_{j'}(t-\tau) \int_{t-2\tau}^{t-\tau} dt' + \dots \right] G_{j,j'}(t-t') e^{i\Delta(t-t')}. \tag{2.16}$$

We focus on the first integral and make the change of variable $\tilde{t} = t - t'$,

$$\int_{t-\tau}^t dt' G_{j,j'}(t-t') e^{i\Delta(t-t')} = \int_0^\tau d\tilde{t} G_{j,j'}(\tilde{t}) e^{i\Delta\tilde{t}}. \tag{2.17}$$

The correlation function $G_{j,j'}(t)$ can be further specified by taking the continuum limit $(1/\delta k) \sum_k \delta k \to (L/2\pi) \int dk$ and changing the variable from k to

ω,

$$\int_0^\tau d\tilde{t} G_{j,j'}(\tilde{t}) e^{i\Delta\tilde{t}} = \int_0^\tau d\tilde{t} \sum_k |g_{0,k}|^2 e^{ik(z_j - z_{j'})} e^{-i\omega_k \tilde{t}} e^{i\Delta\tilde{t}}$$
$$= \int_0^\infty d\omega \mathcal{D}(\omega) |g_\omega|^2 \frac{1}{2} \sum_{k(\omega)=k_\pm(\omega)} e^{ik(\omega)(z_j - z_{j'})} \int_0^\tau d\tilde{t} e^{-i(\omega-\Delta)\tilde{t}}, \tag{2.18}$$

where $\mathcal{D}(\omega) = (L/\pi)dk/d\omega$ is the density of states, including the degeneracy factor of 2 for the left- and right-moving momenta, and the summation is over the two momenta $k_\pm(\omega) = \pm k(\omega)$ (the positive and negative solutions of $\omega = \omega_k$).[5] We have assumed symmetric coupling $g_{j,k} = g_{j,-k}$ and the phase dependence $g_{j,k} = g_{0,k} e^{ikz_j}$ with z_j being the position of the jth emitter, and defined $g_\omega = g_{0,k(\omega)}$.

Focusing on the case $\Delta > 0$, the time integral

$$I(\omega) = \int_0^\tau d\tilde{t} e^{-i(\omega-\Delta)\tilde{t}}, \tag{2.19}$$

as a function of ω, is peaked at $\omega = \Delta$ and falls off quickly outside its width $\sim 2\pi/\tau$ due to the fast oscillation of the integrand. The area π of $I(\omega)$ does not depend on τ, and $I(\omega)$ reduces to a delta function if the upper limit of the integral is sent to ∞. This would be allowed if the rest of the integrand in (2.18), which depends on the density of states $\mathcal{D}(\omega)$ and coupling $|g_\omega|^2$ in particular, does not change appreciably over some range $\omega \in (\Delta - 2\pi/\tau_c, \Delta + 2\pi/\tau_c)$ with $\tau_c \ll \tau$. The time scale τ_c is interpreted as the correlation time, beyond which the contribution of $G_{j,j'}(\tilde{t})$ to the integral is negligible. We want τ_c to be smaller than the coarse-grained interval τ, which is also restricted from above by τ_A, the time scale of $A_j(t)$. Hence, there are two time scales restricting τ [94],

$$\tau_c \ll \tau \ll \tau_A, \tag{2.20}$$

for the time integral to be fully eliminated and the dynamics to become fully Markovian. When such τ exists (the condition will be discussed further in Section 2.2.3), i.e. $\tau_c \ll \tau_A$, we can proceed to solve the integral by taking $\tau \to \infty$,

$$I_\infty(\omega) = \int_0^\infty d\tilde{t} e^{-i(\omega-\Delta)\tilde{t}} = \pi\delta(\omega - \Delta) - \mathcal{P}\left[\frac{i}{\omega - \Delta}\right]. \tag{2.21}$$

[5] Here we define $k(\omega) > 0$.

This also means that the subsequent terms in the coarse-grained integral in (2.16) are negligible, as they involve integrations further out in time $\tilde{t} > \tau$. By combining (2.21) and (2.18) and inserting into (2.16), we arrive at the effective equations of motion for the emitters in the Markovian limit,

$$\dot{A}_j(t) = -\sum_{j'} \left[\int_0^\infty d\tilde{t} G_{j,j'}(\tilde{t}) e^{i\Delta\tilde{t}} \right] A_{j'}(t) = -\sum_{j'} \left[\Gamma_{j,j'}/2 + iJ_{j,j'} \right] A_{j'}(t), \tag{2.22}$$

with the dissipative and coherent terms, $\Gamma_{j,j'}$ and $J_{j,j'}$, resulting from the delta function and the Cauchy principal value in (2.21). The dissipative part is responsible for the collective Markovian decay, while the imaginary part $J_{j,j'}$ induces the Lamb shift and coherent exchange of the excitation.

For $\Delta < 0$, i.e. the excitation energy inside the bandgap, the approximation is applicable provided that $|\Delta|$ is large. The density of states $\mathcal{D}(\omega)$ in 1D diverges at the edge $\Delta = 0$ in Eq. 2.18, and thus the time integral $I(\omega)$ (Eq. 2.19) is mostly relevant near $\omega = 0$. Furthermore, the integral $I(\omega)$ does not change appreciably for $\tau \gtrsim 2\pi/|\Delta|$, beyond which the exponential rapidly oscillates. Therefore, assuming $\tau_A \gg 2\pi/|\Delta|$, we can again evaluate the integral by taking $\tau \to \infty$ (Eq. 2.21). For $\Delta < 0$, the real part $\delta(\omega - \Delta)$ vanishes, leading to no decay in the bandgap in the Markovian limit. However, the imaginary part is finite, leading to purely coherent interactions between the emitters.

Calculations of $\Gamma_{j,j'}$ and $J_{j,j'}$

Some quantitative results can be obtained for matter-wave quantum emitters, whose vacuum coupling $g_{j,k} = \Omega\gamma_{j,k}/2$ (with $\gamma_{j,k}$ given in Eq. 2.6) depends on momentum k, due to the finite size a_{ho} of the excitation in each emitter well. The density of states is $\mathcal{D}(\omega) = (L/\pi)\sqrt{m/2\hbar\omega}$ for the free-particle dispersion. The dissipative term can be computed as

$$\begin{aligned}
\Gamma_{j,j'} &\equiv 2\,\mathrm{Re} \int_0^\infty d\tilde{t} G_{j,j'}(\tilde{t}) e^{i\Delta\tilde{t}} \\
&= 2\,\mathrm{Re} \int_0^\infty d\omega \mathcal{D}(\omega) |g_\omega|^2 \frac{1}{2} \sum_{k(\omega)=k_\pm(\omega)} e^{ik(\omega)(z_j - z_{j'})} \left[\pi\delta(\omega - \Delta) - \mathcal{P}\frac{i}{\omega - \Delta} \right] \\
&= 2\pi\mathcal{D}(\Delta)|g_\Delta|^2 \cos[k(\Delta)(z_j - z_{j'})]\Theta(\Delta) \\
&= \Gamma_1 \cos[k(\Delta)(z_j - z_{j'})]\Theta(\Delta)
\end{aligned} \tag{2.23}$$

where $\Theta(\Delta)$ is a unit step function. The single-emitter decay rate (cf. Section 2.3.2) is given by

$$\begin{aligned}\Gamma_1 = 2\pi\mathcal{D}(\Delta)|g_\Delta|^2 &= \frac{\Omega^2}{\Delta}\frac{\sqrt{\pi}}{2}a_{\rm ho}k(\Delta)e^{-k(\Delta)^2a_{\rm ho}^2} \\ &= \frac{\Omega^2}{\sqrt{\Delta}}\sqrt{\frac{\pi}{2\omega_{\rm ho}}}e^{-2\Delta/\omega_{\rm ho}},\end{aligned} \tag{2.24}$$

which depends on the microwave Rabi frequency Ω, and also moderately on the detuning Δ in a deep lattice $\omega_{\rm ho} \gg \Delta$.

To solve the coherent coupling, we make use of the tight-binding approximation [18, 19, 93]. We first write it as

$$\begin{aligned}J_{j,j'} &\equiv {\rm Im}\int_0^\infty d\tilde{t}G_{j,j'}(\tilde{t})e^{i\Delta\tilde{t}} \\ &= {\rm Im}\sum_k |g_k|^2 e^{ik(z_j-z_{j'})}\int_0^\infty d\tilde{t}e^{-i(\omega_k-\Delta)\tilde{t}} \\ &= \frac{\Omega^2 a_{\rm ho}}{4\sqrt{\pi}}\int_{-\infty}^\infty dk e^{-k^2a_{\rm ho}^2}e^{ik\bar{z}}\left[-\mathcal{P}\frac{1}{\omega_k \mp |\Delta|}\right],\end{aligned} \tag{2.25}$$

where the sign $\mp$ is for $\Delta > 0$ and $\Delta < 0$, respectively, and $\bar{z} \equiv z_j - z_{j'}$. In a very deep lattice, we may assume that $a_{\rm ho}$ is very small and the wavefunction in a well is almost point-like, such that $e^{-k^2a_{\rm ho}^2} \approx 1$ in the integral. For $\Delta > 0$, the quantity in the bracket is sharply peaked at $k = k(|\Delta|)$. For $\Delta < 0$, the quantity peaks at $k = 0$ and decreases sufficiently at k on the order of $\pm k(|\Delta|)$. Therefore, the approximation amounts to the condition $k(|\Delta|)^2a_{\rm ho}^2 \ll 1$, which is typically satisfied in our experiments except for large Δ. (The approximation can also be understood in the form $a_{\rm ho}^2/\lambda(|\Delta|)^2 \ll 1$, i.e. the size of emitters is not resolved by the resonant matter waves.) In this limit, we get

$$J_{j,j'} \approx -\frac{\Omega^2 a_{\rm ho}}{4\sqrt{\pi}}\frac{k(|\Delta|)}{|\Delta|}\mathcal{P}\int_{-\infty}^\infty d\tilde{k}e^{i\tilde{k}k(|\Delta|)\bar{z}}\frac{1}{\tilde{k}^2 \mp 1}, \tag{2.26}$$

with the change of variable $\tilde{k} = k/k(|\Delta|)$. The integral can be exactly solved,[6]

[6]Using the standard results (either using the residue theorem or computer algebra), $\int_{-\infty}^\infty dx\frac{e^{iax}}{x^2\mp 1} = \pi\sin|a|$ or $\pi e^{-|a|}$ for each sign, except for $a = 0$.

and we obtain [18][7]

$$J_{j,j'} \approx -\frac{\Omega^2}{|\Delta|}\frac{\sqrt{\pi}}{4}a_{\rm ho}k(|\Delta|) \times \begin{cases} \sin\left[k(\Delta)|z_j - z_{j'}|\right] & \text{for } \Delta > 0 \\ \exp\left[-k(|\Delta|)|z_j - z_{j'}|\right] & \text{for } \Delta < 0. \end{cases} \tag{2.27}$$

The result for $\Delta < 0$ gives rise to the effective spin-exchange interactions with tunable range [26, 64, 66, 96]. This is related to the atom-photon bound state [27], a partial excitation surrounded by a virtual photon (matter-wave) cloud mediating the interactions, which we discuss further in Section 2.2.4. The exponential dependence is not limited to the free-particle dispersion, as any photonic dispersion near a bandgap at $k = k_0$ may be approximated as quadratic $\omega(k) \approx \omega(k_0)+(1/2)(k-k_0)^2(d^2\omega/dk^2)|_{k_0}$. It can be also understood by noting that for $\Delta < 0$, the dispersion $\omega_k = \hbar k^2/2m$ yields an imaginary momentum, $k = \sqrt{-2m|\Delta|/\hbar} = ik(\Delta)$, such that the free-particle wavefunction becomes an evanescent wavefunction $\propto e^{-z/\xi(|\Delta|)}$ with the localization length $\xi(|\Delta|) = 1/k(|\Delta|)$.

We note that the self-energy $J_{j,j} = J_{0,0}$ vanishes for the tight-binding approximation for $\Delta > 0$. The exact integral instead can be written as

$$\begin{aligned} J_{0,0} &= -\frac{\Omega^2 a_{\rm ho}}{4\sqrt{\pi}}\frac{k(\Delta)}{\Delta}\mathcal{P}\int_{-\infty}^{\infty} d\tilde{k} e^{-\tilde{k}^2 k(\Delta)^2 a_{\rm ho}^2}\frac{1}{\tilde{k}^2 - 1}, \\ &= -\frac{\Omega^2 a_{\rm ho}}{4\sqrt{\pi}}\frac{k(\Delta)}{\Delta} \times \begin{cases} -2\sqrt{\pi}F(k(\Delta)a_{\rm ho}) & \text{for } \Delta > 0 \\ e^{-k(\Delta)^2 a_{\rm ho}^2}\pi\mathrm{Erfc}(k(\Delta)a_{\rm ho}) & \text{for } \Delta < 0. \end{cases} \end{aligned} \tag{2.28}$$

where $F(x)$ is called the Dawson function [97],[8] which can be expanded as $F(x) = e^{x^2}\int_0^x e^{t^2}dt = x - 2x^3/3 + \mathcal{O}(x^5)$, and $\mathrm{Erfc}(x)$ is the complementary error function, which is expanded to $1 - 2x/\sqrt{\pi} + \mathcal{O}(x^3)$. The leading order term provides the Lamb shift $(\Omega^2/2\Delta)a_{\rm ho}^2 k(\Delta)^2 = \Omega^2/\omega_{\rm ho}$ (subleading order for $\Delta < 0$) [18, 20].

[7] In (6.34) of [93], the same equation for $\Delta < 0$ is expressed using $a_{\rm ho} = \sqrt{\hbar/m\omega_{\rm ho}}$ as $J_{j,j'} = -\frac{\Omega^2}{2\omega_{\rm ho}}\sqrt{\frac{\pi\omega_{\rm ho}}{2|\Delta|}}e^{-\sqrt{2|\Delta|/\omega_{\rm ho}}|z_j - z_{j'}|/a_{\rm ho}}$.

[8] The integral of the form $H(y) \equiv \pi^{-1}\mathcal{P}\int_{-\infty}^{\infty} e^{-x^2}/(y-x)$ is called the Hilbert transformation, and $H(y) = 2\pi^{-1/2}F(y)$ [98].

2.2.2 Master equation for many-body dynamics

The Markovian equations of motion (2.22) for a single excitation suggest an effective Hamiltonian for the emitter degrees of freedom [25, 26],

$$H_{\text{eff}} = \sum_j \hbar\Delta\hat{\sigma}_j^+\hat{\sigma}_j^- + \sum_{j,j'}(-i\hbar\Gamma_{j,j'}/2 + \hbar J_{j,j'})\hat{\sigma}_j^+\hat{\sigma}_{j'}^-. \tag{2.29}$$

This Hamiltonian, which is also referred to as the "spin model" [26], is non-Hermitian due to the dissipative term.[9] It can also be expressed as the master equation [94, 95] for the reduced density matrix, given in the Lindblad form [99],

$$\dot{\rho}_A(t) = \frac{1}{i\hbar}[H_0 + H_J, \rho_A] + \sum_{j,j'}\frac{\Gamma_{j,j'}}{2}\Big[2\hat{\sigma}_j^-\rho_A\hat{\sigma}_{j'}^+ - \{\hat{\sigma}_j^+\hat{\sigma}_{j'}^-, \rho_A\}\Big], \tag{2.30}$$

where $H_0 = \sum_j \hbar\Delta\sigma_j^\dagger\sigma_j$ and $H_J = \sum_{jj'}\hbar J_{jj'}\sigma_j^\dagger\sigma_j$. The second term can be partially absorbed into the first term, $\dot{\rho}_A(t) = (H_{\text{eff}}\rho_A - \rho_A H_{\text{eff}}^\dagger)/i\hbar + \sum_{jj'}\Gamma_{jj'}\sigma_j\rho_A\sigma_{j'}^\dagger$, where H_{eff} is identical to Eq. 2.29. The leftover term ensures the conservation of the overall population.

The master equation is the standard technique to study open quantum systems [89, 94, 95]). We outline a derivation for quantum emitters, closely following [94]. The Hamiltonian can be written as $H = H_0 + V$, where

$$H_0 = \sum_j \hbar\Delta\hat{r}_j^\dagger\hat{r}_j + \sum_k \hbar\omega_k\hat{b}_k^\dagger\hat{b}_k, \quad V = \sum_{j,k}(\hbar g_{j,k}\hat{r}_j^\dagger\hat{b}_k + \text{H.c}). \tag{2.31}$$

For generality, we used the bosonic impurity operators $\hat{r}_j^\dagger, \hat{r}_j$, which behave as spin operators in the collisional blockade regime. The reduced density matrix $\tilde{\rho}_A = \text{Tr}_B\tilde{\rho}(t)$ is obtained by tracing over the bath degrees of freedom, where the tilde indicates the interaction picture $\tilde{\rho} = e^{iH_0t/\hbar}\rho e^{-iH_0t/\hbar}$. The equation of motion under the Born-Markov approximation is given by [94]

$$\frac{\delta\tilde{\rho}_A}{\delta t} = -\frac{1}{\hbar^2\delta t}\int_0^\infty d\tau\int_t^{t+\delta t} dt'\text{Tr}_B[\tilde{V}(t'), [\tilde{V}(t'-\tau), \tilde{\rho}_A(t)\otimes\rho_B]], \tag{2.32}$$

where δt is some coarse-grained interval. The bath is assumed to be initially empty and remain unperturbed, i.e. $\tilde{\rho}_B(t) \approx \rho_B(0) = |0\rangle\langle 0|$ (Born approxi-

[9] Note since $G_{j,j'}(t)^* = G_{j',j}(-t)$, $\Gamma_{j,j'}^* = \Gamma_{j',j}$ and $J_{j,j'}^* = J_{j',j}$.

mation). The coupling $\tilde{V}(t) = \sum_{j,k} \hbar g_{j,k} \tilde{r}_j^\dagger(t) \tilde{b}_k(t)$ can be inserted to yield

$$\begin{aligned}\frac{\delta\tilde{\rho}_A}{\delta t} = &-\frac{1}{\delta t}\int_0^\infty d\tau \int_t^{t+\delta t} dt' \sum_{j,j'} \mathrm{Tr}_B \big[\tilde{r}_j^\dagger(t')\tilde{r}_{j'}(t'-\tau)\tilde{\rho}_A(t)G_{j,j'}(\tau) \\ &- \tilde{r}_j(t')\tilde{\rho}_A(t)\tilde{r}_{j'}^\dagger(t'-\tau)G_{j',j}(-\tau) - \tilde{r}_{j'}(t'-\tau)\tilde{\rho}_A(t)\tilde{r}_j^\dagger(t')G_{j,j'}(\tau) \\ &+ \tilde{\rho}_A(t)\tilde{r}_{j'}^\dagger(t'-\tau)\tilde{r}_j(t')G_{j',j}(-\tau)\big],\end{aligned} \tag{2.33}$$

where the bath correlation function $G_{j,j'}(t-t') = \mathrm{Tr}_B[\rho_B \hat{B}_j(t)\hat{B}_j^\dagger(t')]$ has already been defined in Eq. 2.14. Noting that $\tilde{r}_j(t) = \hat{r}_j e^{-i\Delta t}$ and $G_{j,j'}(t-t') = G_{j',j}^*(t'-t)$, this equation can be simplified to

$$\frac{\delta\tilde{\rho}_A}{\delta t} = -\sum_{j,j'}\Big\{\overline{G}_{jj'}[\hat{r}_j^\dagger\hat{r}_{j'}\tilde{\rho}_A(t) - \hat{r}_{j'}\tilde{\rho}_A(t)\hat{r}_j^\dagger] + \overline{G}_{jj'}^*[\tilde{\rho}_A(t)\hat{r}_{j'}^\dagger\hat{r}_j - \hat{r}_j\tilde{\rho}_A(t)\hat{r}_{j'}^\dagger]\Big\} \tag{2.34}$$

where $\overline{G}_{j,j'} \equiv \int_0^\infty d\tau G_{j,j'}(\tau)e^{i\Delta\tau}$. The right-hand side is no longer dependent on δt, and thus we replace $\delta\tilde{\rho}_A/\delta t$ by $\dot{\tilde{\rho}}_A$. As in Eq. 2.22, we may define $\overline{G}_{j,j'} \equiv \Gamma_{j,j'}/2 + iJ_{j,j'}$ with $\Gamma_{j,j'}/2$ and $J_{j,j'}$ as the real and imaginary part. Using $\overline{G}_{j,j'} = \overline{G}_{j',j}$ (valid if $\omega_{-k} = \omega_k$), the equation simplifies further as

$$\begin{aligned}\dot{\tilde{\rho}}_A(t) = &-i\sum_{j,j'} J_{j,j'}(\hat{r}_j^\dagger\hat{r}_{j'}\tilde{\rho}_A(t) - \tilde{\rho}_A(t)\hat{r}_j^\dagger\hat{r}_{j'}) \\ &+ \sum_{j,j'}\frac{\Gamma_{j,j'}}{2}(2\hat{r}_j\tilde{\rho}_A(t)\hat{r}_{j'}^\dagger - \hat{r}_j^\dagger\hat{r}_{j'}\tilde{\rho}_A(t) - \tilde{\rho}_A(t)\hat{r}_j^\dagger\hat{r}_{j'}).\end{aligned} \tag{2.35}$$

Going back to the Schrödinger picture, we arrive at the master equation

$$\dot{\rho}_A = \frac{1}{i\hbar}[H_0 + H_J, \rho_A] + \sum_{j,j'}\frac{\Gamma_{j,j'}}{2}\Big[2\hat{r}_j\rho_A\hat{r}_{j'}^\dagger - \{\hat{r}_j^\dagger\hat{r}_{j'}, \rho_A\}\Big], \tag{2.36}$$

where $H_J = \sum_{j,j'}\hbar J_{j,j'}\hat{r}_j^\dagger\hat{r}_{j'}$ is the Lamb-shift term. The dissipative coupling (Eq. 2.23) has contributions from left-moving and right-moving photons, $\Gamma_{j,j'} = (\Gamma_1/2)\sum_{k=\pm k(\Delta)} e^{ik(z_j - z_{j'})}$ with $\pm k(\Delta) \equiv \pm k(\Delta)$, and it may be useful to define the collective jump operators [48, 52, 100] for each direction,

$$\hat{\mathcal{O}}_k = \sum_j e^{-ikz_j}\hat{r}_j, \tag{2.37}$$

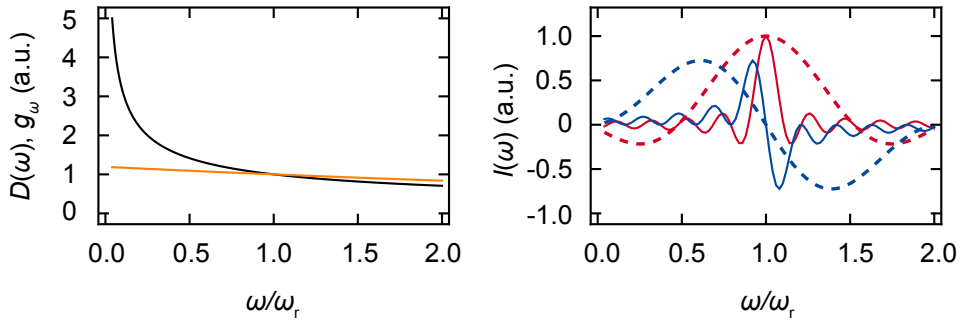

Figure 2.2: Left: Density of state $\mathcal{D}(\omega)$ (black solid) and coupling g_ω (orange) for our system featuring a quadratic dispersion. Right: The real and imaginary parts (red and blue) of the time integral $I(\omega) = \int_0^\tau d\tilde{t} e^{-i(\omega-\Delta)\tilde{t}}$ (Eq. 2.18) for $\tau = 1/\Gamma_1$. All values were computed for $\Omega = 0.3\omega_\mathsf{r}$ (solid) and $\Omega = 1.5\omega_\mathsf{r}$ (dashed), with other parameters at $\Delta = \omega_\mathsf{r}$, and $s = 8$.

in terms of which the master equation is written as

$$\dot{\rho}_A = \frac{1}{i\hbar}[H_0 + H_J, \rho_A] + \frac{\Gamma_1}{4} \sum_{k=\pm k(\Delta)} \left[\hat{\mathcal{O}}_k \rho_A \hat{\mathcal{O}}_k^\dagger - \{\hat{\mathcal{O}}_k^\dagger \hat{\mathcal{O}}_k, \rho_A\}\right]. \tag{2.38}$$

These jump operators can be thought of as collective dipole operators, and the collective decay can be represented as its action on a state (cf. Section 2.3.2).

2.2.3 Conditions for Markovian behavior

In this section, we outline order-of-magnitude estimations for parameter regimes in which the Markovian approximation is applicable. We first ignore the collective enhancement effects, which we discuss in Section 2.3.

Coupling strength

As discussed in the context of Weisskopf-Wigner theory, the coarse-grained integral (2.16) is valid if $A_j(t)$ changes slowly for the interval, $\tau \ll \tau_A$. For the continuum case $\Delta > 0$, we may estimate $\tau_A^{-1} \sim \Gamma_1/2 = \pi\mathcal{D}(\Delta)|g_\Delta|^2$. We also want the time scale bounded below by $\tau_c \ll \tau$. The bath correlation time τ_c has been translated to the frequency interval $\omega \in (\Delta - \delta\omega_c, \Delta + \delta\omega_c)$ for which the integrand of Eq. 2.18 does not change appreciably, where we identify $\tau_c = 2\pi/\delta\omega_c$. Since g_Δ is mostly flat, ignoring the phase factor $e^{ik(z_j - z_{j'})}$ for the moment, we estimate $\delta\omega_c$ from

$$\delta\omega_c \mathcal{D}'(\Delta) \lesssim 2\pi\mathcal{D}(\Delta), \tag{2.39}$$

where $\mathcal{D}'(\Delta) = d\mathcal{D}(\omega)/d\omega|_{\omega=\Delta}$. The condition $\tau_c \ll \tau_A$ (Eq. 2.20) is then written as

$$2\pi\mathcal{D}'(\Delta) \ll \pi^{-1}|g_\Delta|^{-2}. \tag{2.40}$$

We show the typical parameter dependencies in Fig. 2.2 for matter-wave emitters coupled to a bath with a quadratic dispersion. Using $\mathcal{D}'(\omega) = (L/\pi)\sqrt{m/2\hbar}\omega^{-3/2}$ and $|g_\omega|^2 \approx (\sqrt{\pi}/L)(\Omega^2/2)a_{\rm ho}$ (in the tight-binding limit $e^{-k^2a_{\rm ho}^2} \approx 1$), the Markovian regime is obtained as

$$\frac{\Omega^2}{\Delta^2} \ll \frac{1}{2}\left(\frac{2}{\pi}\right)^{3/2}\sqrt{\frac{\omega_{\rm ho}}{\Delta}} \sim 1. \tag{2.41}$$

This result implies that strong non-Markovian behaviors are expected when the decay timescale, which depends on $1/\Omega$, exceeds the optical period, as defined by $2\pi/\Delta$. In our experiments, we generally have $\Delta < \omega_{\rm ho}$, and thus use $\Omega \ll \Delta$ as a general condition to remain in the Markovian regime [20, 21].

In the bandgap $\Delta < 0$, the relevant time scale is $\tau \gtrsim 2\pi/|\Delta|$, beyond which $I(\omega) = \int_0^\tau d\tilde{t}e^{-i(\omega-\Delta)\tilde{t}}$ (Eq. 2.19) does not change much, such that we can take $\tau \to \infty$. For the Markovian calculation to be valid, we want $2\pi/|\Delta| \ll \tau_A$. As a simple estimate, we take $\tau_A \sim 1/|J_{0,0}|$ and use Eq. 2.73 from the tight-binding limit, $J_{0,0} \approx (\Omega^2/\sqrt{\Delta\omega_{\rm ho}})\sqrt{\pi/8}$. We then obtain the same estimate for the Markovian regime,

$$\frac{\Omega^2}{|\Delta|^2} \ll \frac{1}{2}\left(\frac{2}{\pi}\right)^{3/2}\sqrt{\frac{\omega_{\rm ho}}{|\Delta|}} \sim 1. \tag{2.42}$$

Distance between emitters

There is another important consideration regarding the radiative retardation. When the distance between the emitters is large, the phase delay $e^{ik(\omega)(z_j-z_{j'})}$ of $G_{j,j'}(t)$ can become significant. We may expand $k(\omega)$ as $k(\omega) \approx k(\Delta) + (\omega-\Delta)dk/d\omega|_\Delta$, and we can write the total phase factor of $G_{j,j'}(t)e^{i\Delta t}$ (Eq. 2.18) as

$$e^{ik\bar{z}}e^{-i(\omega-\Delta)t} = e^{ik(\Delta)\bar{z}}e^{-i(\omega-\Delta)(t-\bar{z}/v_g(\Delta))}, \tag{2.43}$$

where $\bar{z} \equiv z_j - z_{j'}$ and $v_g(\Delta) = d\omega/dk|_{k=k(\Delta)}$. This shows that the contribution of the bath correlation function is effectively delayed by $\bar{z}/v_g$. The typical frequency width of the variation of the phase delay may be obtained from

$\delta\omega_c|(de^{ik(\omega)\bar{z}}/d\omega)e^{-ik(\omega)\bar{z}}| \lesssim 1$, which near $\Delta = 0$ yields

$$\delta\omega_c \lesssim v_g(\Delta)/|\bar{z}|. \tag{2.44}$$

Comparing $\delta\omega_c$ to $\tau_A \sim 2/\Gamma_1$, we find the condition for the Markovian limit

$$\frac{|z_j - z_{j'}|}{v_g(\Delta)} \ll \frac{1}{\pi\Gamma_1}. \tag{2.45}$$

This means that we want the propagation time of the wave packets to be smaller than the decay time. The quantity v_g/Γ_1 is also referred to as the coherence length of photons [44], and in this language we want the size of an emitter ensemble to be smaller than the coherence length, and otherwise we have to consider the memory effect caused by the time delay.

2.2.4 Bound state in a bandgap ("atom-photon" bound state)

We have already seen that, in the bandgap $\Delta < 0$, the dissipative term in Eq. 2.22 vanishes, but there still is a coherent coupling between the emitters, with its strength exponentially decreasing over distance. This is related to the existence of the bound state in the bandgap (also termed the atom-photon bound state) [27, 28] with an evanescent photonic cloud. To see this, we focus on the single emitter Hamiltonian,

$$\hat{H}_1 = \hbar\Delta\hat{\sigma}^+\hat{\sigma}^- + \sum_k \hbar\omega_k\hat{b}_k^\dagger\hat{b}_k + \sum_k \left[\hbar g_k\hat{\sigma}^+\hat{b}_k + \text{H.c.}\right]. \tag{2.46}$$

The single-excitation state can be a superposition of an emitter excitation and matter-wave excitations,

$$|\psi_{\text{BS}}\rangle = A(t)\,|e\rangle + \sum_k B_k(t)\,|1_k\rangle\,. \tag{2.47}$$

The stationary Schrödinger equation $H_1\,|\psi_{\text{BS}}\rangle = \hbar\omega_{\text{bs}}\,|\psi_{\text{BS}}\rangle$ yields

$$(\omega_{\text{bs}} - \Delta)A = \sum_k g_k B_k, \quad (\omega_{\text{bs}} - \omega_k)B_k = g_k^* A. \tag{2.48}$$

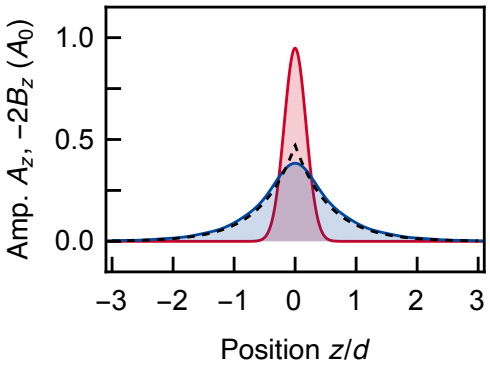

Figure 2.3: Spatial amplitudes of the bound state from the numerical solution, with $\Omega = 0.4\omega_r$, $\Delta = -0.25\omega_r$, and $s = 10$ ($\omega_{ho} \approx 6.3\omega_r$, $a_{ho} \approx 0.18d$). The dashed line is from the tight-binding approximation. The matter-wave part is scaled by a factor of -2.

Solving for B_k, we obtain the equation for the bound-state energy ω_{bs},

$$\omega_{bs} = \Delta + \sum_k |g_k|^2 \frac{1}{\omega_{bs} - \omega_k}, \tag{2.49}$$

where $\omega_B < 0$ is assumed.

The exact solution can be obtained analytically [18, 19] or numerically (Section 2.2.5), but the integral also becomes simpler by assuming coupling g_k being independent of k, $g_k \equiv g$, e.g. by taking the tight-binding limit for matter-wave emitters ($e^{-k^2 a_{ho}^2/2} \approx 1$ in Eq. 2.9; cf. Eq. 2.26). For a quadratic dispersion, ω_B is given as a solution to an algebraic equation [18, 64]

$$(|\omega_{bs}| + \Delta) = \beta^{3/2} |\omega_{bs}|^{-1/2} \tag{2.50}$$

where $\beta = (g^2(L/2)\sqrt{2m\hbar})^{2/3}$. In our experiments with matter-wave emitters, $\beta = [(\Omega^2/\sqrt{\omega_{ho}})\sqrt{\pi/8}]^{2/3}$ is typically small ($\beta \lesssim 1/3$), and deep in the gap $\Delta^2 \gg \Omega^2$ ($\Delta < 0$), the energy is simply $\omega_{bs} \approx \Delta$ to the leading order, i.e. that of the emitter. The next-leading-order correction leads to $\omega_{bs} \approx \Delta[1 + (\beta/\Delta)^{3/2}]$, from which we can see that the coupling lowers the energy of the bound state. We may recognize the similarity of this to the dressed-state energy of an emitter and a photon off-resonant by Δ, consistent with the diverging density of states near $k = 0$. Deep in the continuum $\Delta^2 \gg \Omega^2$ ($\Delta > 0$), the bound-state energy converges to $\omega_{bs} \lesssim 0$.

The second of Eq. 2.48 provides the spatial distribution of the photonic

part as

$$\begin{aligned}\langle 0|\,\hat{\psi}_b(z)\,|\psi_{\rm BS}\rangle &= g\sum_k \frac{A}{\omega_{\rm bs}-\omega_k}\,\langle 0|\,\hat{\psi}_b(z)\,|k\rangle \\ &= A\frac{g\sqrt{L}}{2\pi}\int_{-\infty}^{\infty} dk \frac{e^{ikz}}{\omega_{\rm bs}-\omega_k} = -A\frac{g\sqrt{L}}{2\pi}\int_{-\infty}^{\infty} dk \frac{e^{ikz}/|\omega_{\rm bs}|}{1+k^2/k_{\rm bs}^2} \\ &= -A\frac{g\sqrt{L}}{2}\frac{k_{\rm bs}}{|\omega_{\rm bs}|}e^{-k_{\rm bs}|z|} = -A\frac{\Omega}{2\sqrt{|\omega_{\rm bs}|\omega_{\rm ho}}}\left(\frac{\pi}{a_{\rm ho}^2}\right)^{1/4} e^{-k_{\rm bs}|z|}\end{aligned} \tag{2.51}$$

where $k_{\rm bs} = \sqrt{2m|\omega_{\rm bs}|/\hbar} = \sqrt{2|\omega_{\rm bs}|/\omega_{\rm ho}}/a_{\rm ho}$. We show the distribution in Fig. 2.3 obtained from the numerical and tight-binding solutions. The (radiative) matter-wave part is exponentially localized, and the discontinuous derivative at $z = 0$ reflects that by taking g_k to be constant, we are assuming that the emitter is point-like (tight-binding approximation). Bound states in a photonic crystal have been theoretically studied earlier [27, 28], and have been experimentally probed relatively recently with atoms near an alligator photonic crystal waveguide [101] and with a superconducting circuit [102] (also with a classical dipole [103]). The radiative part (Eq. 2.51) in momentum space has so far only been measured with matter-wave emitters [20, 21].

The excited-state fraction $|A|^2$ can be obtained from the normalization $|A|^2 + \sum_k |B_k|^2 = 1$, yielding

$$|A|^2 = \left[1 + \frac{L|g|^2 k_B}{4|\omega_{\rm bs}|^2}\right]^{-1} = \left[1 + \frac{1}{4}\sqrt{\frac{\pi}{2}}\left(\frac{\Omega}{\omega_{\rm bs}}\right)^{3/2}\left(\frac{\Omega}{\omega_{\rm ho}}\right)^{1/2}\right]^{-1}. \tag{2.52}$$

For $\Delta^2 \gg \Omega^2$ ($\Delta < 0$), the amplitude is mostly in the excited state, providing further support for treating quantum emitters in a bandgap effectively as a collection of spins with coherent coupling (Eq. 2.29). The bound-state induced, tunable long-range interactions can be used to realize interesting many-body models [64, 66, 68, 96], and we will discuss how this can change the transport properties of a Bose-Hubbard model in Chapter 6.

2.2.5 Exact numerical simulations

In the single-excitation regime, we can simulate the Hamiltonian of matter-wave emitters numerically with good accuracy. The system is defined by a box of length L, which discretizes the free-particle states as $L^{-1/2}e^{ik_l z}$ with

the momentum modes $k_l = \delta k l$ for $\delta k = 2\pi/L$ and integer l.[10] This makes the boundary periodic, but we make the box large such that the boundary condition is irrelevant. We obtain the matrix elements of the time-independent Hamiltonian (Eq. 2.7) in the basis that consists of the emitter excitations $\hat{r}_j^\dagger |0\rangle$ and the photon excitations $\hat{b}_{k_l}^\dagger |0\rangle$, with the free part

$$\langle 0| \hat{r}_j \hat{H} \hat{r}_{j'}^\dagger |0\rangle = \hbar \Delta_j \delta_{j,j'}, \quad \langle 0| \hat{b}_{k_l} \hat{H} \hat{b}_{k_{l'}}^\dagger |0\rangle = \hbar \omega_{k_l} \delta_{l,l'} \tag{2.53}$$

and the coupling part

$$\langle 0| \hat{r}_j \hat{H} \hat{b}_{k_l}^\dagger |0\rangle = (\hbar\Omega/2)\gamma_{j,k_l}, \quad \text{H.c.}, \tag{2.54}$$

where we labeled the emitter energy $\hbar\Delta_j$ for the possible inclusion of local shifts or disorder. As an example, we display the $\hat{H}$ matrix for a system of three emitters labeled by $j = -1, 0, 1$,

$$\hat{H} = \frac{\hbar}{2} \begin{pmatrix} 2\Delta_{-1} & & & \dots & \Omega\gamma_{-1,k_{-1}} & \Omega\gamma_{-1,k_0} & \Omega\gamma_{-1,k_1} & \dots \\ & 2\Delta_0 & & \dots & \Omega\gamma_{0,k_{-1}} & \Omega\gamma_{0,k_0} & \Omega\gamma_{0,k_1} & \dots \\ & & 2\Delta_1 & \dots & \Omega\gamma_{1,k_{-1}} & \Omega\gamma_{1,k_0} & \Omega\gamma_{1,k_1} & \dots \\ \vdots & \vdots & \vdots & \ddots & & & & \ddots \\ \Omega\gamma_{-1,k_{-1}}^* & \Omega\gamma_{0,k_{-1}}^* & \Omega\gamma_{1,k_{-1}}^* & & 2\omega_{k_{-1}} & & & \\ \Omega\gamma_{-1,k_0}^* & \Omega\gamma_{0,k_0}^* & \Omega\gamma_{1,k_0}^* & & & 2\omega_{k_0} & & \\ \Omega\gamma_{-1,k_1}^* & \Omega\gamma_{0,k_1}^* & \Omega\gamma_{1,k_1}^* & & & & 2\omega_{k_1} & \\ \vdots & \vdots & \vdots & & & & & \ddots \end{pmatrix}. \tag{2.55}$$

(Ω is assumed real.) To obtain the time evolution of states or stationary solutions, we apply the matrix to a state vector whose elements are the amplitudes of a single-excitation state $|\Psi(t)\rangle = \sum_j A_j(t)\hat{r}_j^\dagger |0\rangle + \sum_l B_{k_l}(t)\hat{b}_{k_l}^\dagger |0\rangle$.

The matrix is made finite by some cutoff $|k_l| \le k_\Lambda$ that is sufficiently high, i.e. $(k_\Lambda/k_\mathrm{r})^2 \gg \Omega/\omega_\mathrm{r}, \Delta/\omega_\mathrm{r}$, at the same time maintaining the system size larger than the propagation distance, e.g.

$$L \gg v_g(\Delta)/\Gamma \tag{2.56}$$

for some typical decay rate Γ, where $v_g(\Delta) = d\omega/dk|_\Delta$ is the group velocity of emitted waves. For the discrete radiative modes to behave like a continuum,

[10] Alternatively, one can use the discrete levels of the residual harmonic confinement [20]. The trap frequency is ~ 100 Hz, and our experiments are typically done in much shorter time scales. The box approach has an advantage as the wavefunction overlap γ_{j,k_l} has a simple analytic form.

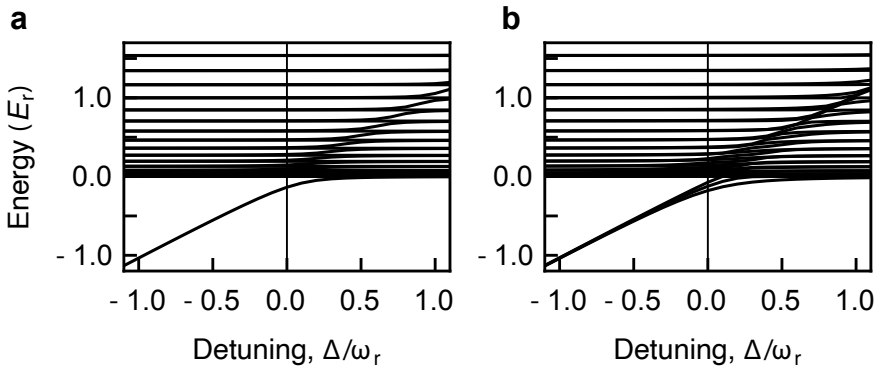

Figure 2.4: Exact diagonalization of the single-emitter Hamiltonian. The energy spectrum is shown as a function of emitter energy Δ for $\Omega = 0.5\omega_r$ and $s = 10$, with the system size $L = 25d$ and the momentum cutoff at $|k_{l=50}| = (2\pi/L)50 = 4k_r$. **a,** For 1 emitter. **b,** For 3 emitters.

we can also require that the energy uncertainty associated with the typical time $1/\Gamma$ is much larger than the energy spacing of the quasi-continuum, i.e. $\hbar\Gamma \gg \delta k(d\hbar\omega/dk)_\Delta$, which yields the same condition up to a constant.

We show the eigenvalue spectrum for 1 and 3 emitters in Fig. 2.4 obtained by diagonalizing the discrete Hamiltonian, as a function of emitter energy Δ. For large negative Δ, the continuum and the emitters are essentially independent. Near the continuum edge $\Delta = 0$, the emitters start to mix with the continuum. For 3 emitters, there are 3 eigenstates whose degeneracy is lifted near the edge, which we will discuss later.

2.3 Collective radiative phenomena

In this section, we discuss collective effects on spontaneous emission processes and bound states in waveguide QED, with special emphasis on matter-wave emitters.

2.3.1 Introductory remarks

Dicke first termed "superradiance" in [59], a phenomenon that refers to a burst of radiation emitted from a collection of emitters, which is compressed in time compared to a simple sum of individual emissions. The light is most intense in the middle of the Dicke ladder, and the intensity scales as $\propto (M/2)(M/2+1)$, where M is the number of emitters. The burst is associated with many-body effects, i.e. of many excitations. We can also consider a single excitation, for

example, the state at the last rung of the Dicke ladder (above the ground state), and while the intensity scales as $\propto M$ in this case, the intensity per excitation is in fact the strongest. This effect was pointed out as the greatest radiation intensity anomaly by Dicke himself [58, 104], and is often referred to as "single-photon superradiance", to distinguish it from many-body superradiance. In free space, superradiance of a fully excited state is only reached for closely spaced emitters [48, 59, 100][11], and special considerations are required for extended samples [105].

The distances become less of restriction in waveguide QED, where all emitters commonly interact via the guided modes in one dimension, with infinite-range coupling in the dissipative regime (cf. Eqs. 2.23 and 2.73). However, the positioning of emitters relative to the wavelength becomes rather important, and various new phenomena are expected in spatially extended systems [25, 26].

There are also subradiant states in the Dicke ladder, whose emission rate can be suppressed. The effect is called subradiance, and is generally weak in free space due to the large number of available modes [106, 107]. Again, waveguide QED allows strong subradiance, as the decay channels are restricted to one dimension in an ideal realization ($\beta = 1$). The subradiant states are related to polaritonic states [25] and also the bound states in the continuum (BIC) [108, 109], which we discuss further below.

Our platform of an array of matter-wave emitters can be an ideal testbed to study collective effects in waveguide QED, as the wavelength of the radiation is fully tunable, the emitters are homogeneous, and the system is fully one-dimensional. With ultracold atoms loaded into an optical lattice, we can achieve either a fully excited state in a Mott-insulating phase, or a macroscopically occupied single-excitation state in a superfluid phase. These many-body phases are discussed more in Chapter 5. We assume that these states are already prepared, and explore collective effects realized in these two regimes (cf. [17, 87] in higher dimensions). We note that collective effect can also generally refer to dynamics of multiple emitters, but not necessarily collective enhancement or suppression of decay rates, which might be specifically referred to as cooperative effects.

[11] The emitters should not be too close due to the energy shifts induced by dipole-dipole interactions [100].

2.3.2 Single-photon superradiance

Two emitters

We start with a simplified discussion, considering a system of two emitters containing a single excitation. The state of the system can be generally written as

$$|\psi_\phi\rangle = \frac{1}{\sqrt{2}}(|e_0\rangle + e^{i\phi}|e_1\rangle). \tag{2.57}$$

As we explain further below, Markovian decay via emitting a photon at a resonant momentum k can be described by the action of the operator $\hat{\mathcal{O}}_k = \sum_j e^{-ikz_j}\hat{r}_j$ (cf. Eq. 2.37). For two emitters with distance d, $\hat{\mathcal{O}}_k = \hat{r}_0 + \hat{r}_1 e^{-ikd}$, where the phase factor reflects the phase retardation of a photon emitted from the second emitter (Fig. 2.5a). Letting $\hat{\mathcal{O}}_k$ act on the state, we obtain

$$\hat{\mathcal{O}}_k|\psi_\phi\rangle = \frac{1}{\sqrt{2}}(1 + e^{i(\phi - kd)})|G\rangle\,, \tag{2.58}$$

where $|G\rangle = |g_0 g_1\rangle$ is the ground state of the array. The decay rate is obtained from $\langle\hat{\mathcal{O}}_k^\dagger\hat{\mathcal{O}}_k\rangle$, yielding

$$\Gamma_k = (\Gamma_1/2)[1 + \cos(\phi - kd)]. \tag{2.59}$$

Therefore, when the phase-matching condition $\phi - kd = \pi m$ is satisfied for integer m, the decay is enhanced by a factor of 2 for even m, and suppressed to zero for odd m, with respect to the direction k. Given an emitter energy Δ, there will be two resonant momenta $k = \pm k(\Delta)$. Only in the symmetric configuration, $k(\Delta)d = n\pi$ for integer n, we can achieve super- or subradiance in both directions simultaneously (Fig. 2.5b). For odd n, the symmetric state with $\phi = 0$, an example of the Dicke states, will be subradiant. The phase-matching condition can also be visualized in terms of the wavelength, $\lambda(\Delta) = 2\pi/k(\Delta)$. For example, if $k(\Delta) = 2k_\mathsf{r} = 2\pi/d$, the distance between the emitters is commensurate with the wavelength, resulting in constructive interference (and superradiance).

Additionally, one can realize directional spontaneous emission, by choosing one direction to be enhanced and the other to be suppressed. This is achieved, for instance, at $k(\Delta) = 1.5k_\mathsf{r} = 1.5\pi/d$ and $\phi = -0.5\pi$. The condition yields $\phi - k(\Delta)d = -2\pi$ for the positive direction and $\phi + k(\Delta)d = \pi$ for the negative direction. The photon will be emitted only into the positive direction.

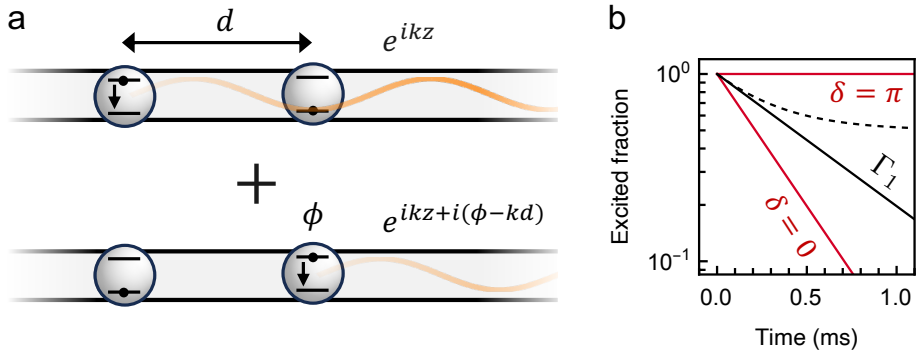

Figure 2.5: Collective spontaneous emission of two emitters. **a,** Illustration of a TDS of two emitters with a relative phase ϕ, emitting a photon (or a matter wave) at momentum k. The photon from the second emitter has a phase lag $\delta = \phi - kd$. **b,** Time evolution of the excited fraction for a TDS (red lines) at $\Delta = 4\omega_\mathrm{r}$ (corresponding to $k(\Delta)d = 2\pi$). Parameters at $\Omega = \omega_\mathrm{r}$, $\Delta = 4\omega_\mathrm{r}$, $s = 10$. The black line is the single-emitter decay, and the dashed line is for only one of two emitters excited.

M-emitter array

We now consider an array of M emitters, and define the single-excitation states in the form of the Bloch waves,

$$|\psi_q\rangle \equiv \hat{r}_q^\dagger |0\rangle \equiv \frac{1}{\sqrt{M}} \sum_j e^{iqz_j} \hat{r}_j^\dagger |0\rangle \,, \tag{2.60}$$

where the emitter positions $z_j = dj$ are periodic in d, and the quasimomentum q is defined in the first Brillouin zone $q \in (-k_\mathrm{r}, k_\mathrm{r}]$. We may also use the symbol ϕ for the phase gradient, in terms of which $e^{iqz_j} = e^{i\phi j}$. The phase gradient can be realized experimentally by subjecting the emitter array to a linear potential. Applying the jump operator $\hat{\mathcal{O}}_k$, we get

$$\hat{\mathcal{O}}_k |\psi_q\rangle = \frac{1}{\sqrt{M}} \sum_j e^{i(q-k)z_j} |G\rangle \,. \tag{2.61}$$

The decay rate for emission into each direction is

$$\Gamma_k = \frac{\Gamma_1}{2} \langle \hat{\mathcal{O}}_k^\dagger \hat{\mathcal{O}}_k \rangle = \frac{\Gamma_1}{2} \left| \frac{1}{\sqrt{M}} \sum_j e^{i(q-k)z_j} \right|^2 , \tag{2.62}$$

where the resonant momentum can be $k = \pm k(\Delta)$. The maximum enhancement occurs for the phase-matching condition at

$$q = q_\pm = \pm k(\Delta) + 2k_\mathsf{r} n, \quad \text{with some integer } n. \tag{2.63}$$

In particular, when the conditions for the two directions are the same $q_+ = q_-$, such as at $k(\Delta) = 0, k_\mathsf{r}, 2k_\mathsf{r}, ...$, we get the maximum total decay rate $\Gamma = \Gamma_{k(\Delta)} + \Gamma_{-k(\Delta)} = M\Gamma_1$, the situation that is also referred to as the "mirror configuration" [52].

Alternatively, we can examine the dissipative behavior through the Markovian equations of motion (Eq. 2.22),

$$|\dot{\psi_q}\rangle = \sum_j \dot{A}_j(t)\,|j\rangle \approx -\sum_{j,j'} [\Gamma_{j,j'}/2]\, A_{j'}(t)\,|j'\rangle\,. \tag{2.64}$$

The coupling $\Gamma_{j,j'}$ is the sum of left and right coupling (Eq. 2.23), $\Gamma_{j,j'} = \Gamma^{(-)}_{j,j'} + \Gamma^{(+)}_{j,j'}$ with $\Gamma^{(\pm)}_{j,j'} \equiv (\Gamma_1/2)e^{\pm ik(\Delta)(z_j - z_{j'})}$. Considering these as matrix elements and the amplitudes $A^{(q)}_j = M^{-1/2}e^{iqz_j}$ of $|\psi_q\rangle$ as vector elements, $A^{(q)}_j$ represent an eigenvector of $\Gamma^{(\pm)}_{j,j'}$ with an eigenvalue $M(\Gamma_1/2)$ if the phase-matching condition $q = q_\pm$ (Eq. 2.63) is satisfied. Therefore, with respect to each direction, $|\psi_{\pm q}\rangle$ are the superradiant states with the emission rate $M(\Gamma_1/2)$. There are additional $M-1$ eigenvectors with $q^{(l)}_\pm = q_\pm + (l/M)2k_\mathsf{r}$ with integer $l \neq 0$, whose eigenvalues are zero. In other words, these eigenvectors satisfy the subradiance condition $\Gamma^{(\pm)}_{j,j'} A^{(q^{(l)}_\pm)}_{j'} = 0$, i.e.

$$\sum_{j'} e^{\mp ik(\Delta)z_{j'}} A^{(q^{(l)}_\pm)}_{j'} = 0. \tag{2.65}$$

To summarize, there are one superradiant state and $M-1$ subradiant states for an array of M emitters, with respect to each direction, in this Markovian limit. For continuous values of q, the Bloch state will be in a superposition of these eigenstates, and there will be transitions between super- and subradiance as q is varied.

In free space, the single-excitation states with a phase gradient are also referred to as timed Dicke states (TDSs) [58]. The name is related to the timed arrival of a photon on each emitter that imprints the phase gradient, when such a state is prepared with a weak laser pulse. While the direction of spontaneous emission is arbitrary, if a macroscopic number of emitters are in phase, the emission into one specific direction becomes very strong, leading to directional spontaneous emission [57]. The waveguide QED version of TDSs

(Eq. 2.60) inherits this directionality, as one can choose q to match only one of q_+ or q_- (except when $q_+ \sim q_-$). The new feature is subradiance, which is achieved if both q_+ and q_- are avoided.

Fermi's golden rule

Fermi's golden rule (FGR) provides a simple prescription to obtain the decay rates in the Markovian limit. In particular, our single-excitation states are realized as a macroscopically occupied state of bosonic atoms in a superfluid phase in an optical lattice, e.g. $(\hat{r}_q^\dagger)^{N_{\rm SF}} |0\rangle$. We will see how the bosonic statistics affects the decay rate. The transition rate of an initial discrete state $|i\rangle$ into a final state $|f\rangle$ in a continuum by a weak coupling $\hat{H}'$ can be obtained [94]

$$\Gamma_{i\to f} = (2\pi/\hbar)|H'_{fi}|^2 \rho(E_f = E_i), \tag{2.66}$$

which depends on the transition matrix elements $H'_{fi} \equiv \langle f| \hat{H}' |i\rangle$ and the density of states $\rho(E) = (\delta k)^{-1} dk/dE = \hbar^{-1}\mathcal{D}(E/\hbar)$. The coupling part of the Hamiltonian for matter-wave emitters (Eq. 2.7) is

$$\hat{H}' = \frac{\hbar\Omega}{2} \sum_{j,k} \gamma_{j,k} \hat{r}_j^\dagger \hat{b}_k + \text{H.c.} \tag{2.67}$$

We calculate the transition rate from an initial state of $N_{\rm SF}$ emitter excitations populating a TDS over an array of M emitters, $|i_\phi\rangle = N_{\rm SF}!^{-1/2} \big(\hat{r}_\phi^\dagger\big)^{N_{\rm SF}} |0\rangle$, to a state $|f_{\phi,k}\rangle = (N_{\rm SF}-1)!^{-1/2} \hat{b}_k^\dagger (\hat{r}_\phi^\dagger)^{N_{\rm SF}-1} |0\rangle$ after losing an excitation. Here we use the symbol $\phi = qd$ for later connection to our experiments. We assume that the bath of radiation modes is always empty, in accordance with the Markovian approximation. With the density of states of the matter waves $\rho_{\rm dB}(E) = (L/2\pi\hbar)\sqrt{2m/E}$ (which includes a factor of 2 for the left-right degeneracy; dB indicating that the bath modes are the de Broglie waves), the transition rate normalized by $N_{\rm SF}$ follows as

$$\begin{aligned}
\Gamma_{\phi,M} &= N_{\rm SF}^{-1} \frac{2\pi}{\hbar} \sum_{k=k_\pm(\Delta)} |\langle f_{\phi,k}| \hat{H}' |i_\phi\rangle|^2 \rho_{\rm dB}(\hbar\Delta) \times \frac{1}{2} \\
&= M\Gamma_1 \frac{1}{2} \sum_{k=k_\pm(\Delta)} \left| \frac{1}{M} \sum_{j=\lfloor 1-M/2 \rfloor}^{\lfloor M/2 \rfloor} e^{i(\phi - kd)j} \right|^2 ,
\end{aligned} \tag{2.68}$$

where $\Gamma_1 \equiv \Gamma_{M=1}$ is the single-emitter decay rate (cf. Eq. 2.24) [18, 19], and the sum over $k_\pm(\Delta) = \pm k_{\rm r}\sqrt{\Delta/\omega_{\rm r}}$ accounts for the two directions of emission.

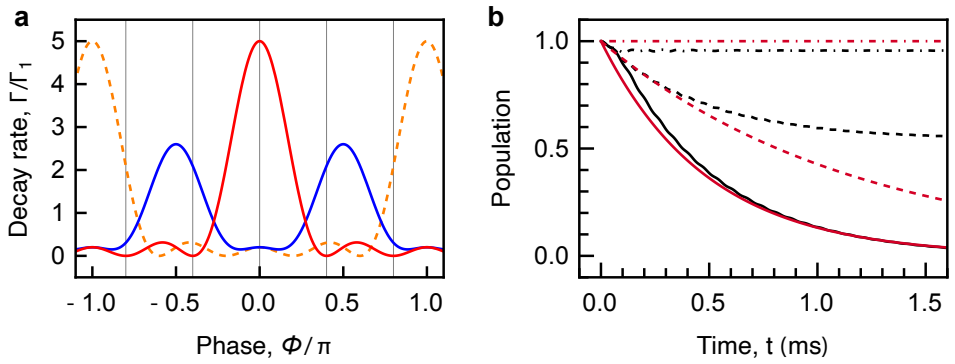

Figure 2.6: Decay rates from Fermi's golden rule (FGR) and exact simulations for 5 emitters. **a,** Decay rates as a function of emitter phase ϕ, for $\Delta = \omega_r$ ($k(\Delta) = k_r$; orange dashed), $\Delta = 2.25\omega_r$ ($k(\Delta) = 1.5k_r$; blue), and $\Delta = 4\omega_r$ ($k(\Delta) = 2k_r$; red). The vertical lines represent the eigenstates of the Markovian Hamiltonian (Eq. 2.64). **b,** Time evolution for $\Delta = 4\omega_r$ with $\Omega = 0.5\omega_r$ and $s = 10$ calculated from FGR (red) and exact simulations (black). The solid, dashed, and dot-dashed lines represent the emitter phase of $\phi = 0$, $\phi = 0.2\pi$, and $\phi = 0.4\pi$.

The last term leads to the modulation of the decay rate as a function of the initial phase ϕ. The rate peaks at $\phi \equiv k_\pm d \pmod{2\pi}$, and reduces to the Kronecker delta $\delta_{\phi \equiv k_\pm d \pmod{2\pi}}$ in the limit $M \to L/d$. This result also indicates that the macroscopic occupation of a TDS by N_{SF} bosonic excitations simply enhances the emission rate by N_{SF}.

We note that the result can also be expressed using the collective jump operator $\hat{\mathcal{O}}_k = \sum_j e^{-ikdj}\hat{r}_j$ [48, 100] (cf. Eq. 2.37) as

$$\Gamma_{\phi,M} = N_{\mathrm{SF}}^{-1}\frac{\Gamma_1}{2}\sum_{k=k_+,k_-}\langle\hat{\mathcal{O}}_k^\dagger\hat{\mathcal{O}}_k\rangle. \tag{2.69}$$

In this formalism of the FGR, the coupling Hamiltonian is $\sim \hat{\mathcal{O}}_k$, and the final state after a jump is $\hat{\mathcal{O}}_k\,|i\rangle$.

FGR vs. numerical simulations

We show the FGR decay rates and corresponding time evolutions for TDSs of various phases ϕ for an array of length $M = 5$ in Fig. 2.6, and their comparison to numerical simulations. Depending on the resonant momentum $k(\Delta)$, superradiance occurs at different phases. When $q_+ \neq q_-$ (e.g. for $k(\Delta) = 1.5k_r$), we observe two peaks corresponding to directional emission each at

half the rate of the maximum, $5\Gamma_1/2$. The FGR only predicts exponential decays, and deviates from numerical simulations in certain cases. There are very early deviations due to non-Markovianity from the propagation delay. Also, for $\phi = 0.2\pi$, the numerical simulation shows that the decay curve flattens out, deviating from a simple exponential. This is attributed to that the initial state of this phase is not an exact eigenstate of the effective Markovian Hamiltonian (Eq. 2.64). To obtain a more accurate result, we should reexpress the initial state as the eigenstates and count the populations in each eigenstate separately, one superradiant state and $M-1$ subradiant states. This is more obvious if we consider two emitters at the same position, with only one of them excited, e.g. $|e_0\rangle$. The state can be expressed as $2^{-1/2}(|+\rangle + |-\rangle)$ where $|\pm\rangle = 2^{-1/2}(|e_0\rangle \pm |e_1\rangle)$, and we can see that only the superradiant state $|+\rangle$ will decay, leaving the system in the subradiant state $|-\rangle$ [59].

2.3.3 Collective bound states in and outside the continuum

As we have seen in the time evolution, the subradiant states identified in the Markovian limit are not exactly non-radiant. This is apparent if one considers emitters that are infinitely far apart, in which case the decay of emitters will be independent of each other no matter how they are prepared. The exact stationary states are the bound states in the continuum (BIC), and a BIC is a superposition of an emitter-array excitation and a matter-wave excitation, with the latter being trapped in between the emitters [108]. This is in contrast to bound states in a bandgap (which we may abbreviate as BIG), whose photonic part is localized at the emitters.

To identify the bound states, we start from the single-excitation state $\psi_{\mathrm{BS}} = \sum_j A_j |j\rangle + \sum_k B_k |k\rangle$, and seek the solutions of $\hat{H}|\psi\rangle = \hbar\omega_{\mathrm{bs}}|\psi\rangle$. The amplitudes and energy should satisfy

$$(\omega_{\mathrm{bs}} - \Delta)A_j = \sum_k g_{j,k}B_k, \quad (\omega_{\mathrm{bs}} - \omega_k)B_k = \sum_j g_{k,j}A_j. \tag{2.70}$$

For $\omega_{\mathrm{bs}} < 0$, the second equation can be solved for B_k. However, for $\omega_{\mathrm{bs}} \geq 0$, the second equation is singular at $\omega_k = \omega_{\mathrm{bs}}$, which forces

$$\sum_j e^{\mp i k_{\mathrm{bs}} z_j} A_j = 0, \tag{2.71}$$

where $k_{\mathrm{bs}} = \sqrt{2m|\omega_{\mathrm{bs}}|/\hbar} = \sqrt{2|\omega_{\mathrm{bs}}|/\omega_{\mathrm{ho}}}/a_{\mathrm{ho}}$. We notice that this is the subradiant condition with respect to ω_{bs}, cf. Eq. 2.65. We may solve the

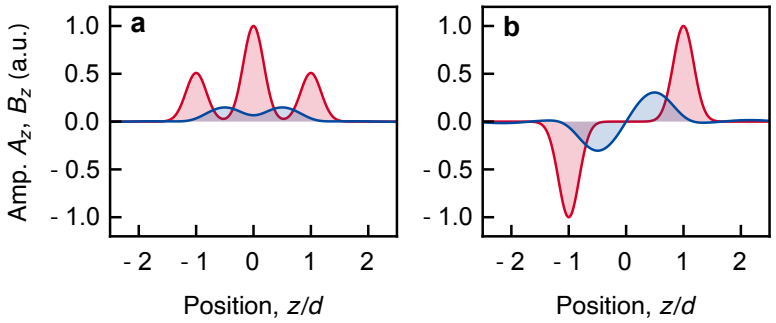

Figure 2.7: Bound states in the continuum (BICs) for 3 emitters, with $\Omega = 0.5\omega_\mathrm{r}$, $\Delta = \omega_\mathrm{r}$, and $s = 10$. There are 2 bound states obtained numerically, whose energies are at **a,** $\omega_\mathrm{bs} = 1.031\omega_\mathrm{r}$, **b,** $\omega_\mathrm{bs} = 1.028\omega_\mathrm{r}$.

second equation for B_k, and insert it into the first, with the understanding that $B_k = 0$ for $\omega_k = \omega_\mathrm{bs}$, and obtain

$$(\omega_\mathrm{bs} - \Delta)A_j = \sum_{j'} \left[-\sum_k \frac{g_{j,k}g_{k,j'}}{\omega_k - \omega_\mathrm{bs}} \right] A_{j'}. \tag{2.72}$$

The quantity in the bracket is identical to the coherent interaction $J_{j,j'}$ (Eq. 2.25) in the Weisskopf-Wigner model, with Δ replaced by ω_bs. To simplify the integral, we again use the tight-binding limit $e^{-k^2 a_\mathrm{ho}^2} \approx 1$, and obtain the coherent interactions

$$J_{j,j'}(\omega_\mathrm{bs}) \approx -\frac{\Omega^2}{|\omega_\mathrm{bs}|}\frac{\sqrt{\pi}}{4} a_\mathrm{ho} k(|\omega_\mathrm{bs}|) \times \begin{cases} \sin\left[k(\omega_\mathrm{bs})|z_j - z_{j'}|\right] & \text{for } \omega_\mathrm{bs} > 0 \\ \exp\left[-k(|\omega_\mathrm{bs}|)|z_j - z_{j'}|\right] & \text{for } \omega_\mathrm{bs} < 0. \end{cases} \tag{2.73}$$

(the approximation cannot be applied for $\omega_\mathrm{bs} = 0$ as the integral becomes divergent).

We first consider the bound states with positive energies $\omega_\mathrm{bs} > 0$. We examine the particular values of $\Delta = n^2\omega_\mathrm{r}$ with some positive integer n, corresponding to $k(\Delta) = nk_\mathrm{r}$. There is then a special solution $\omega_\mathrm{bs} = n\Delta$, with which the LHS of Eq. 2.72 vanishes, and also the RHS because $J_{j,j'} = 0$. The latter is due to the periodicity of the emitter positions $z_j = dj$, such that $\sin(nk_\mathrm{r}|z_j - z_{j'}|) = \sin(n\pi|j - j'|) = 0$. This leads to the bound states in the continuum (BIC), which only exist at the special values of Δ (corresponding to where the gaps open in a lattice). We note that the values also satisfy the mirror condition, $e^{-ik(\Delta)z_j} = e^{ik(\Delta)z_j}$, and therefore the subradiant condition (Eq. 2.71) is satisfied with respect to both emission directions. Beyond the

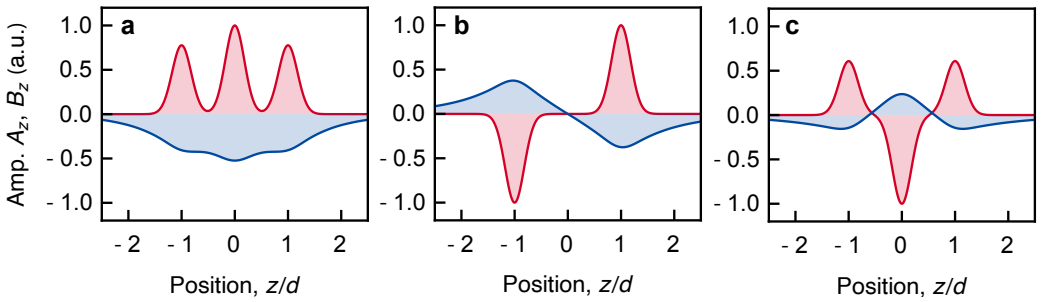

Figure 2.8: Collective bound states in the gap (BIG) for 3 emitters, with $\Omega = 0.5\omega_r$, $\Delta = 0$, and $s = 10$. There are 3 bound states obtained numerically, with energies at **a,** $\omega_{bs} = -0.179\omega_r$, **b,** $\omega_{bs} = -0.123\omega_r$, **c,** $\omega_{bs} = -0.073\omega_r$.

tight-binding limit, the finite size of the emitters in fact shifts the BIC energies slightly, as discussed in Section 4.7.5 of an exact spectral analysis.

For the bound states with negative energies $\omega_{bs} < 0$, i.e. the bound states in the gap (BIG),[12], we may first note that for small coupling $g_{j,k}$ and detuning deep in the gap $\Delta^2 \gg \Omega^2$ ($\Delta < 0$), the bound-state energy converges to $\omega_{bs} \approx \Delta$. The off-diagonal elements of $J_{j,j'}$ are exponentially suppressed, and Eq. 2.72 reduces to that of the single-emitter bound state for each isolated emitter. There will be M collective bound states that are different superpositions of the single-emitter bound states, with the same energy $\omega_{bs} \approx \Delta$. The degeneracy of the energies is lifted close to the edge $\Delta \sim 0$. To find the energies, we require that the eigenvalue equation, Eq. 2.72, has a non-trivial solution,

$$\det\left[(\Delta - \omega_{bs}) + \sum_{j'} J_{j,j'}(\omega_{bs}) A_{j'}\right] = 0. \tag{2.74}$$

There are typically M solutions, but as the excitation energy enters the deep continuum $\Delta^2 \gg \Omega^2$ ($\Delta > 0$), the number of solutions reduces to one, as the other bound states merge into the continuum.

To compute the emitter amplitudes A_j, the subradiance condition (Eq. 2.71) can be used for BICs, while the eigenvectors of Eq. 2.72 give those of BIGs. Once the values of ω_{bs} are obtained, we can use the secular equations (Eq. 2.70) to obtain the photonic amplitudes in momentum space.[13] While above analysis provides valuable insight, one can also obtain the bound-state energies and their wavefunctions by directly diagonalizing the Hamiltonian (cf.

[12]We use the language of a photonic band structure. The "gap" in our case is the energetically inaccessible region below the continuum edge, cf. Fig. 2.1a.

[13]For position space, $B_z = \sum_k B_k L^{-1/2} e^{ikz}$.

Section 2.2.5). In Fig. 2.8, we show the BIGs for 3 emitters, with the emitter energy at the continuum edge $\Delta = 0$. There are 3 bound states with energies in the gap, but the energies are slightly different from each other depending on the configurations. We also show BICs for 3 emitters in Fig. 2.7 for $\Delta = \omega_{\mathsf{r}}$. The radiative (matter-wave) excitations are trapped between the cavity-like geometries formed by the emitters in the waveguide [108, 110].

2.3.4 Polaritonic excitations

When the emitter array is large such that the emitter excitations and photons are confined in the bulk, it may be more useful to describe the system in the quasiparticle basis, instead of the individual constituents. Such a case is found, for example, in describing the excitons coupled to light in solid-state physics, where if the coupling strength exceeds the dissipation rates, the system admits exciton-polaritons as new eigenmodes [111]. The light-matter hybrid particles are generally called polaritons, and might also be found in waveguide QED [68].

For an array of emitters, if the periodic boundary condition is assumed, the system has a discrete symmetry and can be described via Bloch waves. In the quasimomentum basis, we can write the operators for the emitter excitations as

$$\hat{r}_j^\dagger = \frac{1}{\sqrt{M}} \sum_q e^{-iqz_j} \hat{r}_q^\dagger, \quad \hat{r}_q^\dagger \equiv \frac{1}{\sqrt{M}} \sum_j e^{iqz_j} \hat{r}_j^\dagger, \tag{2.75}$$

where M is the number of emitters in the array. In this finite system, the quasimomentum q is discrete with spacing $\delta q = (1/M)2k_{\mathsf{r}}$. By expressing the momentum k in terms of the quasimomentum q, the matter-wave excitations also can be written as

$$\hat{b}_{n,q}^\dagger \equiv \hat{b}_{k_{n,q}}^\dagger, \quad \text{with} \quad k_{n,q} = q - \mathrm{sgn}(q)(-1)^n \lfloor n/2 \rfloor (2k_{\mathsf{r}}), \tag{2.76}$$

and we may choose $\mathrm{sgn}(0) = -1$.[14] These operators generate quasimomentum eigenstates, e.g. $\hat{T}_d \langle 0| \hat{\psi}(z) \hat{b}_{n,q}^\dagger |0\rangle = e^{ik_{n,q}(z+d)} = e^{iqd} \langle 0| \hat{\psi}(z) \hat{b}_{n,q}^\dagger |0\rangle$, where $\hat{T}_d$ is the translation operator. With this choice, the Hamiltonian (Eq. 2.7) can be written as

$$\hat{H} = \sum_q \hbar\Delta \hat{r}_q^\dagger \hat{r}_q + \sum_{n,q} \hbar\omega_{n,q} \hat{b}_{n,q}^\dagger \hat{b}_{n,q} + \sum_{n,q} \left(\hbar g_{n,q} \hat{r}_q^\dagger \hat{b}_{n,q} + \mathrm{H.c.} \right), \tag{2.77}$$

[14] This enforces the top edge of each band always mapped to $k > 0$ (e.g. $k_{n,q=0} > 0$ for even n), but the other choice is also fine.

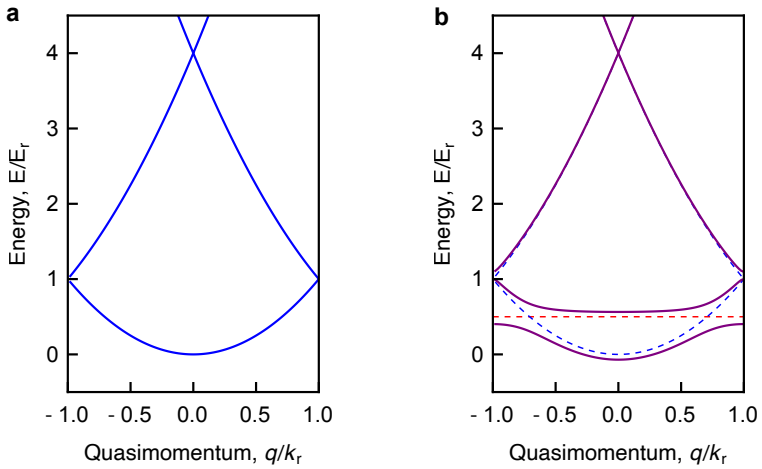

Figure 2.9: Polariton band structure obtained numerically for $\Omega = 0.5\omega_{\mathrm{r}}$, $\Delta = 0.5\omega_{\mathrm{r}}$, and $s = 10$. **a,** Band structure of free matter waves (bath modes). **b,** Band structure of polaritons. The dashed lines are the band structures for the bath modes (blue) and emitter excitations (red) without coupling.

where we defined $g_{q,n} \equiv \sqrt{M} g_k = \sqrt{M}|g_{j,k}|$ and $\omega_{n,q} \equiv \omega_{k_{n,q}}$, and the phase factor $e^{ik_{n,q}z_j} = e^{iqz_j}$ of $g_{j,k}$ has been absorbed into $\hat{r}_q$. It becomes apparent that the Hamiltonian decouples the subspaces of quasimomentum eigenstates,

$$\hat{H} = \sum_q \hat{H}_q \tag{2.78}$$

where $\hat{H}_q = \hat{\Delta}\hat{r}_q^\dagger \hat{r}_q + \sum_n \hbar\omega_{n,q}\hat{b}_{n,q}^\dagger \hat{b}_{n,q} + \sum_n (\hbar g_{n,q}\hat{r}_q^\dagger \hat{b}_{n,q} + \text{H.c.})$. If we cut off the band index of the bath modes at some value $n_{\max}$, $\hat{H}_q$ will be a square matrix of dimension $n_{\max} + 1$.

We can look for the single-excitation quasimomentum eigenstates labeled by the new band index $\tilde{n}$,

$$|\psi_{\tilde{n},q}\rangle = A_{\tilde{n},q}\hat{r}_q^\dagger |0\rangle + \sum_n B_{\tilde{n},n,q}\hat{b}_{n,q}^\dagger |0\rangle \tag{2.79}$$

The amplitudes and the energies can be obtained from $\hat{H}_q |\psi_{\tilde{n},q}\rangle = \tilde{\omega}_{\tilde{n},q} |\psi_{\tilde{n},q}\rangle$, leading to the secular equations [19, 56, 68]

$$(\tilde{\omega}_{\tilde{n},q} - \Delta)A_{\tilde{n},q} = \sum_n g_{n,q}B_{\tilde{n},n,q}, \quad (\tilde{\omega}_{\tilde{n},q} - \omega_{n,q})B_{\tilde{n},n,q} = g_{n,q}A_{\tilde{n},q}. \tag{2.80}$$

Solving the second for $B_{\tilde{n},n,q}$, we obtain the equation for the polariton disper-

sion $\tilde{\omega}_{\tilde{n},q}$,

$$\tilde{\omega}_{\tilde{n},q} - \Delta = \sum_n \frac{g_{n,q}^2}{\tilde{\omega}_{\tilde{n},q} - \omega_{n,q}}. \tag{2.81}$$

Alternatively, the Hamiltonian $\hat{H}_q$ can also be directly diagonalized with some cutoff $n_{\max}$ to obtain the energies and amplitudes. We show the dispersion of polariton eigenmodes in Fig. 2.9 obtained numerically.

We can define the operators $\hat{c}^\dagger_{\tilde{n},q} = A_{\tilde{n},q}\hat{r}^\dagger_q + \sum_n B_{\tilde{n},n,q}\hat{b}^\dagger_{n,q}$ for the polariton quasiparticles, and in the position space $\hat{c}^\dagger_{\tilde{n},j} = M^{-1/2}\sum_q e^{-iqz_j}\hat{c}^\dagger_{\tilde{n},q}$, they can form the basis for the effective many-body system with on-site interactions. Typical waveguide QED setups with two-level emitters are described by adding the interaction term $(U_r/2)\hat{r}^\dagger_j\hat{r}^\dagger_j\hat{r}_j\hat{r}_j$ and taking the hardcore boson limit $U_r \to \infty$ [68], but more general scenarios can also be considered with finite U, which can be realized, e.g. by adding nonlinearity to harmonic oscillator emitters. Such scenarios are naturally realized in our optical lattice, and we discuss the polaritonic many-body model in Chapter 6.

2.3.5 Non-Markovian collective dynamics

As discussed earlier (Section 2.2.3), the Weisskopf-Wigner model starts to break down in two different scenarios, when the emitter energy is close to the band edge, $|\Delta|/\Omega \lesssim 1$, and also when the propagation delay is large, $|z_j - z_{j'}|/v_g \gtrsim 1/\Gamma$. The non-Markovianity of the first kind can occur for single emitters, leading to oscillatory dynamics with fractional decay [18, 103]. Collective effects can enhance these non-Markovian dynamics [19], as has been observed in [20, 21] and is discussed further in Section 4.7.6.

The non-Markovianity of the second kind only occurs for multiple emitters, and can modify super- and subradiant dynamics. As has already been noticed (Fig. 2.6), the onset of superradiance can be delayed by the propagation effect, and the subradiant states only become truly non-radiant in the form of BICs. While emitters will behave independently in the limit of infinitely large distances between them, there can be an interesting regime when the distances are neither too close nor too far. This can be illustrated by "superradiance paradox" [44, 45] as follows. We consider a superradiant state (TDS) in an array of emitters with spacing d, such that the array size is Md. We adjust the size Md in between the two length scales

$$v_g/(M\Gamma_1) < Md < v_g/\Gamma_1. \tag{2.82}$$

The quantity v_g/Γ is referred to as the photon coherence length [44], and if

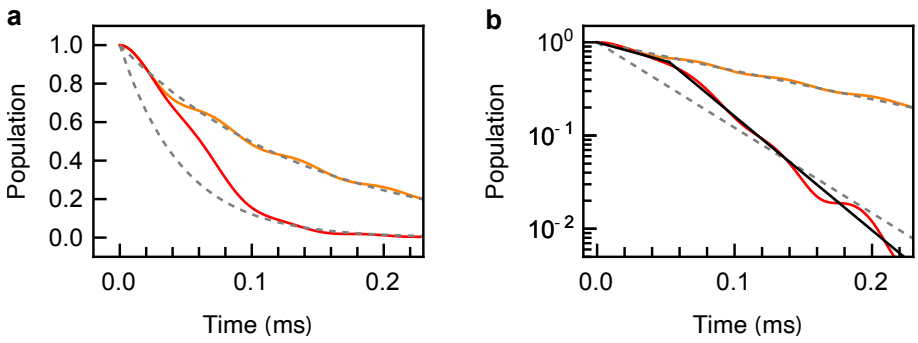

Figure 2.10: Superradiance beyond the standard rate for 3 emitters with $\Omega = 1.8\omega_r$, $\Delta = 4\omega_r$, and $s = 100$, shown in **a,** on a linear scale, and **b,** on a log scale. The solid red and orange lines are for 3 and 1 emitters. The dashed lines are the Markovian decay for 3 and 1 emitters. The solid black line is a double-linear fit, which yields an instantaneous decay rate $\Gamma/\Gamma_1 \approx 4.0$.

we use $v_g/(M\Gamma_1)$ as the length scale with the enhanced rate $M\Gamma_1$, the Markovian condition is violated. In other words, the coherence length is too short for emitters to interact via the common modes, and superradiance is compromised. On the other hand, if we now use v_g/Γ_1 instead as the coherence length, the condition is satisfied, and we should expect superradiance, seemingly contradicting the previous violation.

Exact treatments are required in this intermediate regime, leading to interesting effects, such as collective spontaneous emission rate beyond the standard Dicke superradiance [43, 44]. We can parameterize the effective separation as $\eta = d/(v_g/\Gamma_1)$. For two emitters with linear dispersion, the instantaneous decay rate can be as high as $\Gamma/\Gamma_1 = 4.59$ at $\eta = \eta_c = 0.56$, due to the delayed photon wavepackets [44]. For matter-wave emitters, η can be tuned by controlling $v_g = d\omega_k/dk|_{k=k(\Delta)} = (\hbar k_r/m)\sqrt{\Delta/\omega_r}$ or $\Gamma_1 \sim \Omega^2/\sqrt{\Delta}$ (in the tight-binding limit). While the non-Markovianity from the band edge as well as the non-linear dispersion make the system more complex, such enhancement might indeed be observed for potentially accessible experimental parameters, as shown for 3 emitters in Fig. 2.10.

2.3.6 Many-body superradiance

As Dicke showed [59], the two-level emitters can be mapped to effective spins, and the states can be labeled by the angular momentum J and the magnetic quantum number m, when all the emitters are at a single position. The spin operators can be defined as $\hat{J}_j^+ = \hat{\sigma}_j^+$, $\hat{J}_j^+ = \hat{\sigma}_j^-$, $\hat{J}_j^z = \hat{\sigma}_j^z/2$ (without $\hbar$), with the total angular momentum operator $\hat{\boldsymbol{J}} = \sum_j \hat{\boldsymbol{J}}_j$. The Hamiltonian is sym-

metric under the exchange of two emitters (permutation symmetry), and also preserves J, resulting in the decay along a single ladder. Recognizing that the total angular momentum ladder operator $\hat{J}^- = \sum_j \hat{J}_j^-$ is the collective jump operator (without the phase factor as the emitters are at the same position), we can obtain the emission rate (the number of photons emitted per unit time) of a state labeled by J and m as (cf. Eq. 2.69)

$$\langle J, m| \hat{J}^+ \hat{J}^- |J, m\rangle = \Gamma_1 (J + m)(J - m + 1). \tag{2.83}$$

The states in the ladder of highest angular momentum $J = M/2$ radiate most strongly, and Dicke called J the "cooperation number". Furthermore, the decay rate reaches the maximum in the middle of the ladder $m \sim 0$, with intensity $\propto \Gamma_1 (M/2)(M/2 + 1)$, predicting an initially growing intensity and a burst of radiation from fully excited emitters.

As Dicke noted, the mapping to spins also works for emitters not at the same position, if we restrict the decay to a single direction (mode) k. Noting that the coupling term $\hat{H}' = \sum_{j,k} \hbar g_{j,k} \hat{\sigma}_j^+ \hat{b}_k + \text{H.c.}$ (Eq. 2.7) has the position-dependent phase $g_{j,k} = g_k e^{ikz_j}$, we define collective operators as [59]

$$\hat{J}_k^\pm = \sum_j \hat{J}_j^\pm e^{\pm ikz_j}, \quad \hat{J}^z = \sum_j \hat{J}_j^z, \tag{2.84}$$

with which the Hamiltonian can be written as $\hat{H}' = \sum_k \hbar g_k \hat{b}_k \hat{J}_k^+ + \text{H.c.}$ We can also write

$$\begin{aligned} \hat{J}_k^x &= (\hat{J}_k^+ + \hat{J}_k^-)/2 = \sum_j \hat{J}_j^x \cos kz_j - \hat{J}_j^y \sin kz_j \\ \hat{J}_k^y &= (\hat{J}_k^+ - \hat{J}_k^-)/2i = \sum_j \hat{J}_j^x \sin kz_j + \hat{J}_j^y \cos kz_j. \end{aligned} \tag{2.85}$$

From the fundamental commutation relations $[\hat{J}_j^x, \hat{J}_j^y] = i\hat{J}_j^z$, $[\hat{J}_j^y, \hat{J}_j^z] = i\hat{J}_j^x$, $[\hat{J}_j^z, \hat{J}_j^x] = i\hat{J}_j^y$ for angular momentum, one can show that $\hat{J}_k^x$, $\hat{J}_k^y$, $\hat{J}^z$ follow the same commutation relation. It follows that the total angular momentum, defined as $\hat{J}_k^2 \equiv (\hat{J}_k^x)^2 + (\hat{J}_k^y)^2 + (\hat{J}^z)^2$, commutes with the k part of Hamiltonian $\hat{H}_k' = \hbar g_k \hat{b}_k \hat{J}_k^+ + \text{H.c.}$, $[\hat{J}_k^2, \hat{H}_k'] = 0$.

In the Markovian limit, we can again use the jump operator $\hat{\mathcal{O}}_k = \hat{J}_k^-$ to describe the decay processes. If there is a strongly preferred direction k, we still expect the superradiant cascade, with each emission of a photon imprinting a coherent phase upon the emitters. To illustrate this, we consider a fully excited state of 3 emitters. The decay process successively goes through the

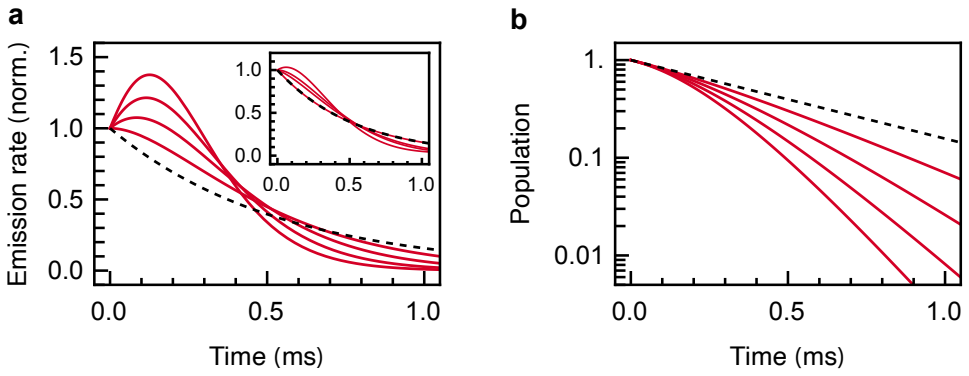

Figure 2.11: Superradiant burst from fully excited emitter arrays with $\Omega = \omega_r$, $\Delta = 4\omega_r$, $s = 15$. **a,** Normalized emission rate, $R = -(\Gamma_1 M)^{-1}(dN/dt)$. **b,** Population on a log scale. The solid red lines are for the array lengths $M = 2, 3, 4, 5$. The dashed line is for a single emitter. Inset: For $\Delta = 2.25\omega_r$, with $\Omega = 0.69\omega_r$ adjusted to yield the same single-emitter decay rate.

following states,

$$
\begin{aligned}
|J = 3/2, m = 3/2\rangle &= |e_{-1}e_0e_1\rangle \\
|J = 3/2, m = 1/2\rangle &= (1/\sqrt{3})(e^{-ikz_{-1}}\,|g_{-1}e_0e_1\rangle + e^{-ikz_0}\,|e_{-1}g_0e_1\rangle \\
&\quad + e^{-ikz_1}\,|e_{-1}e_0g_1\rangle) \\
|J = 3/2, m = -1/2\rangle &= (1/\sqrt{3})(e^{-ik(z_0+z_1)}\,|e_{-1}g_0g_1\rangle + e^{-ik(z_{-1}+z_1)}\,|g_{-1}e_0g_1\rangle \\
&\quad + e^{-ik(z_{-1}+z_0)}\,|g_{-1}g_0e_1\rangle) \\
|J = 3/2, m = -3/2\rangle &= e^{-ik(z_{-1}+z_0+z_1)}\,|g_{-1}g_0g_1\rangle\,. \qquad (2.86)
\end{aligned}
$$

These are the superradiant states with respect to k, with their decay rates into the mode k coherently enhanced. We recognize that the single-excitation state $|J = 3/2, m = -1/2\rangle$ is a TDS by factoring out $e^{-ik(z_{-1}+z_0+z_1)}$, i.e. $|\psi_k\rangle = \sum_j e^{ikz_j}\,|e_j\rangle$. In free space, if the emitter sample is elongated, the superradiant emission can be directional [100, 112], but the enhancement will become weaker as the emitters become more spread out.

In waveguides, there are only two resonant modes $k = \pm k(\Delta)$, and a superradiant burst can always occur above a certain threshold number of emitters [52]. In Fig. 2.11, we show the emission rate of fully excited emitter arrays of various lengths, calculated from the master equation (Eq. 2.36). We use the

normalized photon emission rate,

$$R = -\frac{1}{M\Gamma_1}\frac{dN}{dt}, \tag{2.87}$$

which is the negative of the number of excitations lost per unit time, normalized to that of M independent emitters at $t = 0$, where N is the number of excitations in the array. In this example, the choice of the emitter energy $\Delta = 4\omega_\mathrm{r}$ satisfies the mirror condition, $e^{ik(\Delta)z_j} = e^{-ik(\Delta)z_j}$. Therefore, the superradiant states with respect to $\pm k(\Delta)$ are identical, and an array can exhibit the full burst as if the emitters are at the same position. However, for $\Delta = 2.25\omega_\mathrm{r}$, $k(\Delta) = 1.5\pi/d$, the superradiant states are different with respect to different directions. In this case, a higher number of emitters $M \geq 5$ is required to see the burst. In particular, the normalized rate R is identical for $M = 2$ and $M = 1$, which can be attributed to the fact that the TDS of 2 emitters is superradiant with respect to one direction but subradiant with respect to the other. We note that the calculation assumes the lack of knowledge regarding the bath degrees of freedom. If the photons can be directly detected, one may observe large shot-to-shot fluctuations in which direction they are emitted as the small asymmetry of the initial photon emission can be amplified in the avalanche-like decay [52]. Our calculation also ignores any non-Markovian effects on this many-body collective dynamics, such as the propagation delay, which is still a largely unexplored subject [22].

1234

Spontaneous coherence formation

In our experiments with matter-wave emitters, the emergence of coherent phases, like those shown in Eq. 2.86, are directly probed in the quasimomentum distribution, which can be obtained in an optical lattice through the bandmapping technique (cf. Section 4.7.2). From the reduced density matrix $\rho_A(t)$ calculated with the master equation (Eq. 2.36), we can obtain the quasimomentum density as

$$n(q) = \mathrm{Tr}[\rho_A(t)\hat{n}(q)], \tag{2.88}$$

where $\hat{n}(q) = \hat{r}_q^\dagger \hat{r}_q$ and $\hat{r}_q^\dagger = M^{-1}\sum_j e^{iqz_j}\hat{r}_j^\dagger$ (as defined in Eq. 2.75). The number M of emitters might be finite, but we can imagine that the emitter array is part of a larger array of length $M' \gg M$ (with the periodic boundary condition), with only the original M emitters being populated. We can use the normalization M'^{-1} in the operators $\hat{r}_q^\dagger$ and $\hat{r}_q$ instead, and the distribution $n(q)$ becomes a continuous function in the limit $M' \to \infty$. In Fig. 2.12, we

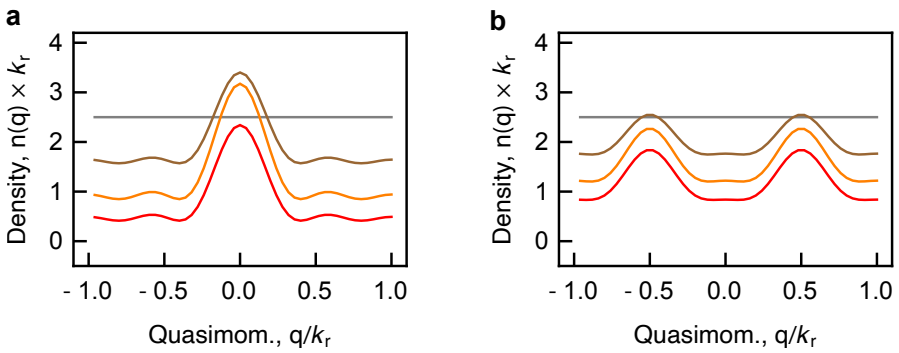

Figure 2.12: Spontaneous coherence formation in the quasimomentum distribution of an initially fully excited 5-emitter array ($s = 15$). **a,** For $\Delta = 4\omega_r$ (corresponding to $k(\Delta) = 0$) and $\Omega = \omega_r$. **b,** For $\Delta = 2.25\omega_r$ (corresponding to $k(\Delta) = 1.5k_r$) and $\Omega = 0.69\omega_r$ (adjusted to yield the same Γ_1). The colors represent the different times $t = 0.0, 0.1, 0.2, 0.3$ ms (gray, brown, orange, red).

show the quasimomentum distribution of an initially fully excited 5-emitter array undergoing spontaneous decay, for $\Delta = 4\omega_r$ and $2.25\omega_r$. The emission of a photon at $k = \pm k(\Delta)$ results in the imprinting of the coherent phase around $q = \phi/d$, with $\phi = \pm k(\Delta)d \pmod{2\pi}$. This can be also understood from the action of the jump operator $\hat{\mathcal{O}}_k = \sum_j e^{-ikdj}\hat{r}_j$, where the phase factor can be written as $e^{-i\phi j}$. With the the mirror condition $\Delta = \omega_r$, a single peak appears, and otherwise there will be two peaks, corresponding to the two emission directions (Fig. 2.12). In Section. 4.5, we discuss the first experimental observation of these coherence peaks.

Chapter 3

Experimental Techniques for Bose-Einstein Condensates

3.1 Conceptual basics

3.1.1 Bose-Einstein condensation

An ideal bosonic gas, in the absence of interactions, condenses into a single-particle ground state when cooled below the transition temperature T_c. We briefly discuss its derivation and the concept of phase-space density, closely following [113]. The value of T_c is inferred from the distribution function in a grand canonical ensemble, i.e. the Bose-Einstein distribution

$$f_{\mathrm{BE}}(\epsilon) = \frac{1}{e^{(\epsilon-\mu)/k_B T} - 1} \tag{3.1}$$

with μ being the chemical potential. In a closed system with a fixed atom number N, the chemical potential $\mu(T)$ depends on the temperature through $\int_{\epsilon_{\min}}^{\infty} d\epsilon g(\epsilon) f_{\mathrm{BE}}(\epsilon) = N$.[1]

The density of states is generally written in the form $g(\epsilon) = C_\alpha \epsilon^{\alpha-1}$. In 3D free space ($\alpha = 3/2$), $g(\epsilon) = C_{3/2}\epsilon^{1/2}$ where $C_{3/2} = (L^3 m^{3/2}/\sqrt{2}\pi^2\hbar^3)$, and in a 3D harmonic trap ($\alpha = 3$), $g(\epsilon) = C_3\epsilon^2$ where $C_3 = (2\hbar^3\bar{\omega}^3)^{-1}$ and $\bar{\omega} = (\omega_x\omega_y\omega_z)^{1/3}$.[2] Below the transition temperature T_c, the ground-state fraction N_0 becomes non-negligible, i.e. $N = N_0 + \int_{\epsilon_{\min}^+}^{\infty} d\epsilon g(\epsilon) f_{\mathrm{BE}}(\epsilon)$. The

[1] The condition $\mu \leq \epsilon_{\min}$ is required for f_{BE} to be physical.

[2] In d dimensions, $\alpha = d/2$ in free space and $\alpha = d, C_\alpha = ((d-1)!\prod_i \hbar\omega_i)^{-1}$ in a harmonic trap.

critical temperature is given by

$$k_B T_c = \left[\frac{N}{C_\alpha \Gamma(\alpha)\zeta(\alpha)}\right]^{1/\alpha}. \tag{3.2}$$

where $\Gamma(\alpha)$ is the Euler gamma function and $\zeta(\alpha)$ is the Riemann zeta function.

One way of quantifying the degeneracy of a gas is through the phase-space density. The typical momentum of a gas at T gives the thermal de Broglie wavelength $\lambda_T = (2\pi\hbar^2/mk_BT)^{1/2}$, and the phase-space density is defined as

$$\text{PSD} = n\lambda_T^3 = n\left(\frac{2\pi\hbar^2}{mk_BT}\right)^{3/2}, \tag{3.3}$$

which is the number of particles concentrated within λ_T. In free space, the critical temperature is reached at PSD $= \zeta(3/2) \approx 2.612$.

Our BECs are made in a harmonic trap, where $k_BT_c = \hbar\bar{\omega}N^{1/3}/[\zeta(3)]^{1/3} \approx 0.94\hbar\bar{\omega}N^{1/3}$. We can write the critical temperature as $T_c \approx 4.52(\bar{\omega}/\omega_{\text{typ}})N^{1/3}$ nK, with $\omega_{\text{typ}} = 2\pi \times 100$ Hz being the typical trap frequency of our apparatus. For a million atoms ($N = 10^6$), $T_c \approx 452$ nK, while for ten thousands atoms ($N = 10^4$), $T_c \approx 97$ nK. To compute the PSD at the center of a harmonic trap, one may choose the maximum density $n(0)$ of a thermal ensemble, $n(0) = (m/2\pi k_BT)^{3/2}\bar{\omega}^3 N$. At $T = T_c$, we find PSD $= \zeta(3)^3 \approx 1.74$.

3.1.2 Atom-light interactions

The manipulation of atoms, such as cooling, trapping, and state controls, fundamentally depends on the atom-light interactions, especially the force exerted on the atoms [114]. We briefly review some basics, including the Hamiltonian of an atom interacting with a single-frequency light field.

An electron bound to an atom in the presence of an external field is described by $\hat{H} = (1/2m)[\hat{\boldsymbol{p}} + e\boldsymbol{A}(\boldsymbol{r},t)]^2 - e\Phi(\boldsymbol{r},t) + V(r)$. In the Coulomb gauge and the dipole approximation $\boldsymbol{A}(\boldsymbol{r},t) \approx \boldsymbol{A}(t)$, the Hamiltonian becomes [90, 94, 115]

$$\hat{H} = \hat{H}_A - \hat{\boldsymbol{d}} \cdot \boldsymbol{E}(\boldsymbol{r}=0,t), \tag{3.4}$$

where $\hat{H}_A$ is the atomic part without the field and the electric field is $\boldsymbol{E}(\boldsymbol{r},t) = (E_0\hat{\boldsymbol{e}}e^{i\boldsymbol{k}\cdot\boldsymbol{r}-i\nu t} + E_0^*\hat{\boldsymbol{e}}^*e^{-i\boldsymbol{k}\cdot\boldsymbol{r}+i\nu t})/2$ with E_0 being a slowly-varying envelope and $\hat{\boldsymbol{e}}$ being a unit polarization vector. We consider a ground and an excited states $|g\rangle, |e\rangle$ with the energy $\hat{H}_A = \hbar\omega_0 |e\rangle\langle e|$ and electric dipole moment $\hat{\boldsymbol{d}} = |g\rangle\langle e|\boldsymbol{d}_{ge} + |e\rangle\langle g|\boldsymbol{d}_{eg}$ where $\boldsymbol{d}_{ij} = \langle i|(-e)\hat{\boldsymbol{r}}|j\rangle$. We can write the Hamiltonian

and a state in a matrix form,

$$\hat{H} = \begin{pmatrix} 0 & -\boldsymbol{d}_{ge} \cdot \boldsymbol{E} \\ -\boldsymbol{d}_{eg} \cdot \boldsymbol{E} & \hbar\omega_0 \end{pmatrix}, \quad |\psi\rangle = \begin{pmatrix} c_g \\ c_e \end{pmatrix}. \tag{3.5}$$

To deal with the rapid time dependence of the field, we change to a rotating frame in which the relative phase between the states is slowly varying, via a unitary transformation $|\tilde{\psi}\rangle = \hat{U}_\phi |\psi\rangle$ where

$$\hat{U}_\phi = \begin{pmatrix} 1 & 0 \\ 0 & e^{i\phi} \end{pmatrix}, \tag{3.6}$$

with $\phi = \omega_0 t$. The new state $|\tilde{\psi}\rangle$ follows the transformed Hamiltonian, $\hat{H}_\phi = \hat{U}_\phi \hat{H} \hat{U}_\phi^{-1} - i\hbar \hat{U}_\phi \partial_t \hat{U}_\phi^{-1}$, which is written as

$$\hat{H}_\phi = \begin{pmatrix} 0 & -\boldsymbol{d}_{ge} e^{-i\omega_0 t} \cdot (E_0 \hat{\boldsymbol{e}} e^{-i\nu t} + E_0^* \hat{\boldsymbol{e}}^* e^{i\nu t})/2 \\ -\boldsymbol{d}_{eg} e^{i\omega_0 t} \cdot (E_0 \hat{\boldsymbol{e}} e^{-i\nu t} + E_0^* \hat{\boldsymbol{e}}^* e^{i\nu t})/2 & 0 \end{pmatrix}. \tag{3.7}$$

In this frame, we can see that there are rapidly oscillating terms $e^{\pm 2i(\nu+\omega_0)t}$ (counter-rotating terms) relative to the others $e^{\pm 2i(\nu-\omega_0)t}$. We then make the standard assumption that the dynamics are much slower than this, and drop the oscillating terms, which is referred to as the rotating-wave approximation (RWA). Going back to the original frame and transforming to the rotating-wave frame with $\phi = \nu t$, we obtain the time-independent Hamiltonian

$$\hat{H}_{\text{RWA}} = -\frac{\hbar}{2} \begin{pmatrix} 0 & \Omega^* \\ \Omega & 2\Delta \end{pmatrix}, \tag{3.8}$$

where we defined the detuning $\Delta \equiv \nu - \omega_0$ and the Rabi frequency $\Omega \equiv \boldsymbol{d}_{eg} \cdot (E_0 \hat{\boldsymbol{e}})/\hbar$. We also added $-2\Delta \hat{I}$ to put it into standard form. The dynamics of interests evolve at rates $\sim \Omega, \Delta$, and thus the validity of the RWA can be expressed as $\Omega, \Delta \ll \nu, \omega_0$. We note that if the phase of the field is fixed, we can absorb the phase of Ω to make it real and positive by conducting an additional transformation $\hat{U}_{\phi'}$ with some ϕ'. We assume that this has been done in the following.

For off-resonant light $|\Delta| \gg \Omega$, the ground state will not be excited appreciably. In this limit, one can diagonalize Eq. 3.8 to obtain the energy shift

$$\Delta E_g = \frac{\hbar\Omega^2}{4\Delta} = \frac{3\pi c^2}{2\omega_0^3} \frac{\Gamma}{\Delta} I, \tag{3.9}$$

where $I = c\epsilon_0|E_0|^2/2$ is the intensity and Γ is the decay rate of the excited state. This energy shift is generally called AC Stark shift or light shift. For the second equality [116], we use the expression for the decay rate in terms of the dipole matrix element as [89]

$$\Gamma = \frac{\omega_0^3|\wp|^2}{3\pi\epsilon_0\hbar c^3} \tag{3.10}$$

where $\wp \equiv \boldsymbol{d}_{eg} \cdot \hat{\boldsymbol{e}}$ with the polarization vector $\hat{\boldsymbol{e}}$ being parallel to the dipole in this expression, i.e. $|\wp|^2 = |\boldsymbol{d}_{eg}|^2$. For red-detuned light $\Delta < 0$, the energy decreases, and ground-state atoms will be attracted toward higher intensity, and for the blue-detuned light $\Delta > 0$, the atoms will be repelled.

Atoms can also scatter off the light, with the scattering rate in the off-resonant limit being given by [76, 116]

$$\Gamma_{\rm sc} = \left(\frac{\hbar\Omega^2}{4\Delta}\right)\frac{\Gamma}{\hbar\Delta} = \frac{3\pi c^2}{2\hbar\omega_0^3}\left(\frac{\Gamma}{\Delta}\right)^2 I = \frac{\Gamma}{\hbar\Delta}(\Delta E_g). \tag{3.11}$$

It can also be obtained from the imaginary part of $\Delta E_g = \hbar\Omega^2/4(\Delta + i\Gamma/2)$ as $\Gamma_{\rm sc}/2$.

3.2 Trapping and cooling of atoms

In this section, we briefly summarize the steps for preparing Bose-Einstein condensates with our apparatus. Since many details can be found in the previous theses of our group, e.g. [117–119], and our machine paper [120], we only highlight some basics that are important in daily operations and troubleshooting. As seen in Fig. 3.1, our apparatus is divided into two parts, the 'MOT cell' (at the pressure $\sim 10^{-9}$ mbar) and the 'Science cell' (at $\sim 10^{-12}$ mbar; $2 \times 1 \times 5$ cm)[3], in which the lifetimes of mangetically trapped atoms are about ~ 1 s and ~ 100 s, respectively. Our quadrupole coil, mounted on a mechanical transporter (Parker Motion 6K2 Controller, GV-L3R Drive 1 and 2), traps and delivers atoms from the MOT cell to the Science cell.

3.2.1 Laser system for ^{87}Rb atoms

We use ^{87}Rb atoms, which belong to alkali metals (atomic number 37) and comprise 28% of the natural rubidium on Earth [121]. A ^{87}Rb atom has one valence electron (with electronic configuration $1s^2 2s^2 p^6 3s^2 p^6 d^{10} 4s^2 p^6 5s^1$), and

[3]See, for example, Fig. 2.4 in [118] for the drawing of our BEC apparatus.

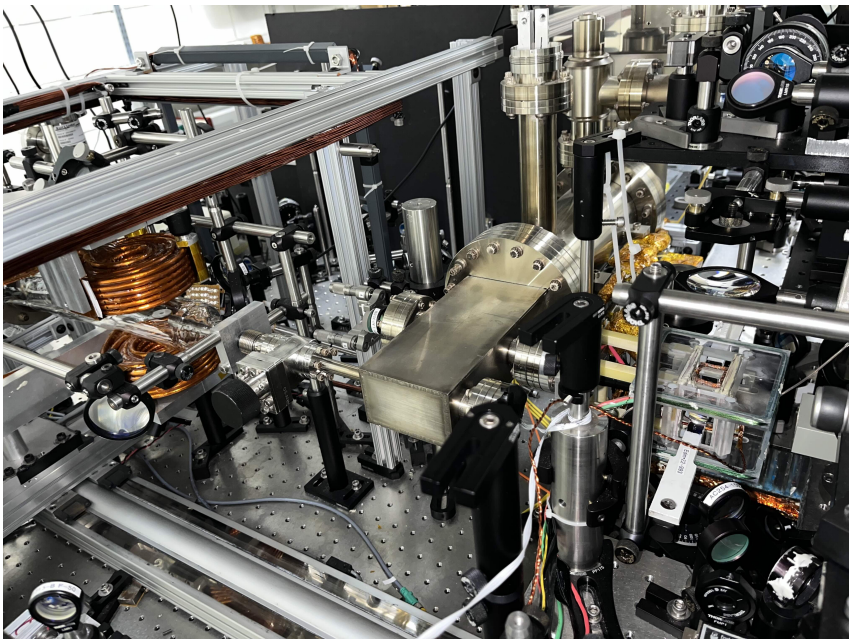

Figure 3.1: Picture of our ultracold-atom apparatus circa Feb. 2024, showing the MOT cell (left; sandwiched between the copper quadrupole coil) and the Science cell (right; sandwiched between the green-colored bias coils).

has a nuclear spin of $I = 3/2$. Compared to hydrogen, the energy levels of alkali atoms are largely modified by the quantum defect [115], induced by the non-negligible wavefunction of the valence electron inside the ion core. It depends on the orbital angular momentum L with largest correction at $L = 0$, leading to the 795 nm D_1 ($5^2S_{1/2} \rightarrow 5^2P_{1/2}$) line and 780 nm D_2 ($5^2S_{1/2} \rightarrow 5^2P_{3/2}$) line for ^{87}Rb, the latter of which has a cycling transition relevant for cooling and trapping. The spin-orbit coupling $\boldsymbol{L}\cdot\boldsymbol{S}$ and relativistic corrections are responsible for the fine-structure splitting between the excited $J = 1/2$ and $J = 3/2$ states where J is the angular momentum quantum number for $\boldsymbol{J} = \boldsymbol{L} + \boldsymbol{S}$, and the interaction $\boldsymbol{I}\cdot\boldsymbol{J}$ between the nuclear spin and the electron angular momentum leads to the hyperfine-structure levels labeled by F for the combined angular momentum $\boldsymbol{F} = \boldsymbol{I} + \boldsymbol{J}$ (Fig. 3.2).

For laser cooling, we address the D_2 line with our "cycling" and "repump" laser systems, respectively[4]. The cycling laser system consists of an external cavity diode laser (Toptica DLPro780) and a tapered amplifier chip (Toptica BoosTA),[5] while the repump laser system consists of another external cavity

[4]For a schematic of the laser setup, see Fig. 4.4 in [122].

[5]We replaced the diode (LD-0780-0200-1) on 2021.04.16, and also performed maintenance on the broken back panel of the supply rack (DC100) and the scan controller (SC110).

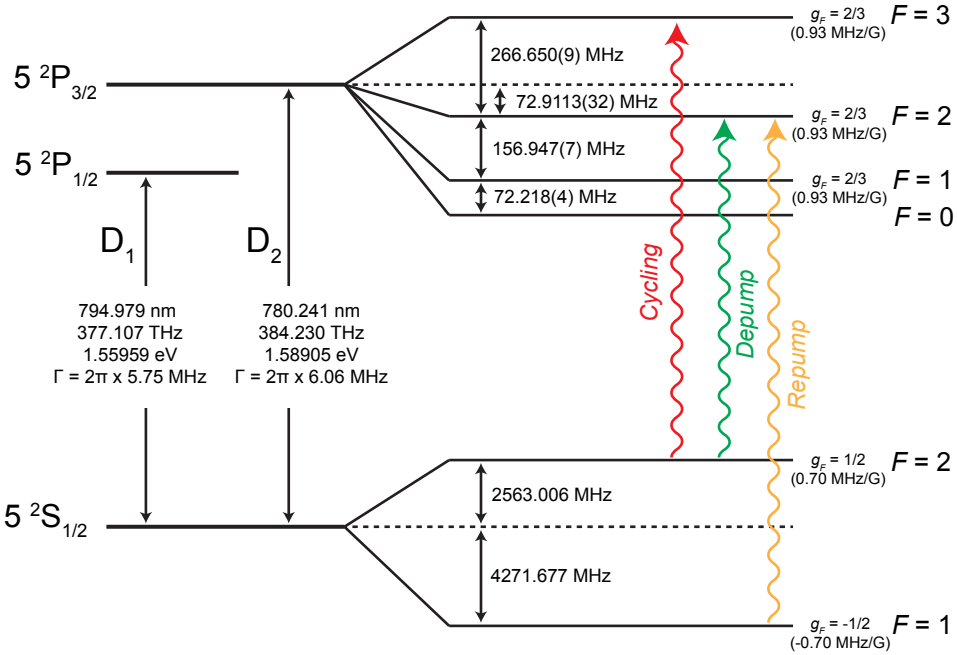

Figure 3.2: Energy levels of the ^{87}Rb atom. Data taken from [124].

diode laser (Toptica DL100)[6]. The frequency of the former is controlled by the piezo voltage of a diffraction grating, and is stabilized by a PID control with Doppler-free polarization spectroscopy (which uses the change of the refractive index near the resonance) to stabilize the frequency within $\lesssim 1$ MHz. Such a locking scheme provides a clean spectroscopy signal, which makes it easier to find a desired hyperfine peak to lock upon, but the offset of this peak can fluctuate due to a residual birefringence of the windows of the rubidium cell that varies with room temperature. For this reason, the frequency of the repump laser is stabilized using saturated absorption spectroscopy and a lock-in amplifier, avoiding the offset issue for a day-long operation [123].

The "cycling" system provides light for the cycling transition on $F = 2 \to F' = 3$ and the depump transition on $F = 2 \to F' = 2$ (Fig. 3.2). The cycling light is red-detuned by $\sim 3.5\Gamma = 18.7$ MHz [118, 123] for laser cooling. Due to a large separation between the ground states $F = 1$ and $F = 2$, the repump transition $F = 1 \to F' = 2$ is independently addressed by the "repump" system. The frequency (over about ~ 100 MHz range) and intensity are controlled by acousto-optic modulators in a double-pass (cat-eye) configuration to allow stable coupling into single-mode fibers (cf. Fig. 3.2 in [119]).

[6]The piezoelectric transducer for the diffraction grating was replaced on 2021.05.28.

3.2.2 Laser cooling

Creation of a BEC typically starts with a magneto-optical trap (MOT) [125]. Our MOT chamber is connected to an "oven" containing 1 g of a natural isotope mixture of rubidium metal. The metal is maintained at 15 °C via a Peltier cooler attached to a water-cooled heat reservoir [123]. The rubidium vapor pressure is $P_{\mathrm{v}} = 1 \times 10^{-7}$ torr at 15 °C (compared to $P_{\mathrm{v}} = 3 \times 10^{-7}$ torr at 25 °C; using the equation (1) in [124]), which keeps the MOT cell at an ideal pressure [123].

Our MOT is made of three orthogonal pairs of circularly-polarized counter-propagating beams (details in [117]), combined with the magnetic field created by quadrupole coils (attached to the transporter) in anti-Helmholtz configuration. Without the coils, the beam configuration cools the atoms via a process called optical molasses [114]. Intuitively, the cooling process can be understood as the absorption of directional photons and subsequent isotropic emission, resulting in a net change of momentum and a loss of kinetic energy. To see how this leads to damping, consider a particle moving at velocity v in one dimension. The Doppler effect changes the perceived frequency of light to $\omega \simeq \omega_0(1 \pm v/c)$ (positive for light moving in the opposite direction) and thus the detuning $\delta \simeq \delta_0 - kv$ of a laser beam, where k is the photon wavevector. For red-detuned light ($\delta_0 < 0$), the photons that are moving in the opposite direction of the atoms $kv < 0$ become more resonant. In a pair of counter-propagating beams $k_\pm = \pm k$, the scattering force is $\langle F \rangle = \Gamma_{\mathrm{sc}}(\delta_0 - k_+ v)\hbar k_+ + \Gamma_{\mathrm{sc}}(\delta_0 - k_- v)\hbar k_-$ where the scattering rate is $\Gamma_{\mathrm{sc}}(\delta) = \Omega^2[(\Gamma/4)/(\delta^2 + \Gamma^2/4)]$ [114]. At the leading order in kv, we find the damping force

$$\langle F \rangle \simeq -\beta v \tag{3.12}$$

with the damping coefficient $\beta = (-\delta_0)\Omega^2\Gamma\hbar k^2/(\delta_0^2 + \Gamma^2/4)^2$.

In addition, spatial confinement of atoms can be achieved by the addition of the quadrupole magnetic field, in which the magnetic substates of atoms experience position-dependent shifts of energy levels. When the laser beams are circularly polarized, they address specific transitions, and thus the resonances become position-dependent, leading to a spatially varying force. The combined effect of momentum- and position-dependent resonances can be summarized as the average force $\langle F \rangle \simeq -\beta v - \kappa z$ (near $v \simeq 0$ and $z \simeq 0$), which simultaneously traps and cools the atoms.

The cooling rate by optical molasses is given by $\langle F \cdot v \rangle = -\beta v^2$, but the final temperature achievable is, in principle, limited by the random scattering of photons with a discrete energy. For a heuristic derivation of such limit,

we assume that each of the absorption and emission of a photon imparts the recoil energy $E_r = \hbar\omega_r = \hbar^2k^2/2m$ to an atom. From the two beams, the overall heating rate is $4\hbar\omega_r\Gamma_{\rm sc}$ [114]. At the equilibrium $4\hbar\omega_r - \beta v^2 = 0$ where the heating and cooling rates become equal, the kinetic energy is given by $mv^2/2 = (\hbar/4)(\delta_0^2 + \Gamma^2/4)/(-\delta_0)$, which is lowest at $\delta_0 = -\Gamma/2$. Using the expression for the average kinetic energy $(1/2)k_BT$ of a gas at a temperature T, the lowest Doppler temperature (or the Doppler cooling limit) is deduced as

$$T_D = \hbar\Gamma/2k_B \tag{3.13}$$

(See [115] for 3D configuration). For $\Gamma = 2\pi \times 6.06$ MHz of the D2 line of ^{87}Rb atoms, $T_D = 145$ μK. In our machine, we achieve a temperature of several hundred micro Kelvin for about 9×10^9 atoms in the MOT, determined from time-of-flight measurements [117]. This temperature is well above the Doppler limit, and is influenced by the re-scattering of photons in the optically dense cloud.

Due to the Zeeman substates of the ground state and the presence of spatially periodic polarization gradients in the light field of 3D MOT configuration, additional cooling mechanisms are present [126, 127]. This leads to the so-called Sisyphus effect, in which an atom climbs up a potential gradient (AC stark shift for a given Zeenman level) and then loses its energy as its internal state falls to a lower one through optical pumping, from which the process repeats (like the boulder in the Greek mythos of Sisyphus). The atoms can be cooled to a temperature roughly equal to the depth of the standing wave formed by the beams, $k_BT \simeq U_0 \propto I/|\delta|$ [115], but is limited to well above the recoil limit $k_BT_r = \hbar^2(2\pi/\lambda)^2/2m = k_B180$ nK at which the atom's de Broglie wavelength is comparable to the periodicity of the potential gradient and the semiclassical picture becomes no longer valid.

In our BEC sequence, the intensity (detuning) is gradually reduced (increased) during sub-Doppler cooling, as the cooling only works over a narrow range of velocities. The step lasts about 7 ms, during which the magnetic coil is off, and the Earth's magnetic field is compensated to guarantee the degeneracy of Zeeman levels. Our atomic cloud thus achieves a temperature less than 50 μK with atom number $\sim 10^9$ [117, 123].

3.2.3 Magnetic trapping

After the MOT and sub-Doppler cooling steps, the atoms are in the $F = 2$ states (the buildup of population in $F = 1$, which can happen in < 1 ms [123], is prevented by the repump light). We transfer them to a magnetic trap [128]

produced by our quadrupole coil in an anti-Helmholtz configuration with a gradient of 480 G/cm along the axial direction [123, 129], and at a current of 500 A maximum (supplied by our Lambda ESS-500-20 power supply). A magnetic dipole in a magnetic field experiences a potential

$$V = -\boldsymbol{\mu} \cdot \boldsymbol{B} = g_F \mu_B m_F B \tag{3.14}$$

where g_F is the Landé g factor [115], μ_F is the Bohr magneton, and m_F is the magnetic quantum number. The quadrupole magnetic field is given by

$$\boldsymbol{B} = b \begin{pmatrix} x \\ y \\ -2z \end{pmatrix} \tag{3.15}$$

where b is the field gradient. As the dipoles follow the field direction (adiabatically, i.e. with the Larmor frequency satisfying $\omega_L \ll B^{-1}dB/dt$ [118]), the potential only depends on the absolute magnitude $B \equiv |\boldsymbol{B}|$. Due to the sign of g_F, the states that can be trapped near the potential minimum are $|F = 1, m_F = -1\rangle$, $|2, 1\rangle$, and $|2, 2\rangle$ (low-field seekers). Right before the transfer, the depump light is applied shortly[7] to change the internal state to $F = 1$ (Fig. 3.2). However, if the depump light is linearly polarized, about 2/3 of atoms are lost after the catch by the magnetic trap. This is partially overcome by σ^- polarization, which reduces the lost-atom fraction to about 1/3 [123]. After the catch by the magnetic trap, the atoms heat up to ~ 0.5 mK during adiabatic compression to the full field gradient [117, 123], and are then transported to the Science cell for evaporative cooling.

An issue with the quadrupole trap, especially at the low temperature after evaporative cooling, is the loss due to nonadiabatic spin flips (Majorana spin flips) from a trapped to an untrapped state at the center of the trap, where the Larmor frequency can be too low compared to the change of the field direction. To overcome this limitation, we realize a TOP trap (time-averaged, orbiting potential trap) by adding an orbiting field of $\boldsymbol{B}_o = B_o(\cos\omega_{\text{top}}t, \sin\omega_{\text{top}}t, 0)$ supplied by two orthogonal pairs of Helmholtz coils around the Science cell. When time-averaged, such addition makes our magnetic trap effectively quadratic, with an offset B_o at the center. For adiabatic following, the rotating frequency needs to satisfy $\omega_{\text{trap}} < \omega_{\text{top}} < \omega_L$. The Larmor frequency $\omega_L = -\gamma B_o$ is proportional to the gyromagnetic ratio $\gamma = |\boldsymbol{\mu}|/|\boldsymbol{F}| \sim -g_F\mu_B/\hbar$ where $\boldsymbol{F}$ is the total angular momentum. For $B_o = 18G$ used in our apparatus [122], ω_L is on the order of 10 MHz, while the

[7]The duration of the depump pulse has been reduced from ~ 7 ms to ~ 2 ms to improve the catch efficiency by the magnetic trap on 2022.07.30.

trap frequencies are $\omega_{\rm trap} = 2\pi \times 70$ Hz in the axial (along z) and $2\pi \times 25$ Hz in the radial directions (along x and y) [122]. The rotation frequency of our bias field is in between, $\omega_{\rm top} = 2\pi \times 10$ kHz [118].

3.2.4 Evaporative cooling and optical trapping

Evaporative-cooling scheme is a standard step to achieve Bose-Einstein condensation [130]. It works by letting the most energetic atoms escape and the rest of atoms rethermalize to a lower temperature (according to the Boltzmann distribution) via collisional interactions. This can be precisely done in a magnetic trap by the "RF knife", which uses the oscillating magnetic field at the radio-frequency to flip the spin of atoms at the desired energy difference, $\hbar\omega_{\rm RF} = g_F \mu_B (m_F - m'_F) B(\boldsymbol{r})$ [123]. In practice, the trap depth (the position of the RF knife) is continuously reduced. As the atoms cool down and collision rates go up, runaway evaporation can occur, in which the cooling become more and more efficient [115]. Our RF pulse is generated from an RF coil below the Science cell driven by a function generator (Agilent 33250A) and an amplifier (Delta RF LA-10-1-512-40) [118]. We sweep the RF from 75 MHz to 10 MHz for about 6s in the quadrupole trap, and from 24 MHz to 17 MHz in the TOP trap for another 6s.[8] Further evaporation can be done at lower frequencies and powers (to reduce the power broadening), to achieve a BEC in a magnetic trap.

For most of our experiments, we do not produce BECs in our TOP trap, but load clouds close to degeneracy into our crossed optical dipole trap (XODT), where we conduct the final evaporation. The XODT is formed by crossing two laser beams (far-off resonant at $\lambda_\perp = 1064$ nm) in the x-y plane. The beams are provided by our ytterbium fiber laser (YLR-20-1064-LP-SF/PL series) running at 16 W output. They are controlled by AOMs ($\gtrsim 80$ % efficiency), and are delivered to the Science cell table via optical fibers ($\gtrsim 70$ % coupling efficiency). A pair of logarithmic photo didoes [123] typically monitor their power via the pick-off paths (cf. Fig. 3.3). The light potential experienced by the atoms will be proportional to the beam intensity (cf. Eq. 3.9), whose distribution is usually described by a Gaussian profile [131] (with z and ρ as the propagation and radial directions, respectively), $I(z,\rho) = I_0 \left(w_0/w(z)\right)^2 e^{-2\rho^2/w(z)^2}$, where the beam waist $w(z) = \sqrt{1 + (z/z_R)^2}$ is given in terms of the Rayleigh range $z_R = \pi w_0^2 n/\lambda$. Our beams have a waist $w_0 = 140$ μm [119, 122], but the actual trap position and frequency (in the harmonic approximation) will depend on the gravitational sag [119]. A recent measurement yielded the trap frequency

[8] These evaporation times can be adjusted to achieve higher atom numbers in BECs. Note that 1 kHz corresponds to ~ 50 nK.

$\omega_z = 2\pi \times 73$ Hz in the z direction.[9] We evaporate atoms by lowering the laser power, allowing the escape of the atoms due to gravity. The optical setup, which we have used for many years (e.g. see [76, 119]), is shown in Fig. 3.3. We typically arrive at BECs with atom numbers between 10^4 and 10^5.

3.3 Imaging of atoms

We use the time-of-flight method to access the momentum distribution of an atomic cloud. We suddenly turn off the trapping potential and let the could to freely expand for ~ 15 ms. The position-space distribution of the atoms will then reflect their initial momentum distribution right before the expansion (ignoring mean-field interactions). We use absorption imaging to obtain the 2D number density of the expanded cloud, with our CCD camera (Princeton PIXIS 1024B 16-bit resolution; 1024×1024 pixels with the pixel area 13 μm $\times$ 13 μm). The imaging beam is magnified by a factor of 10/3 ($f = 500$ and $f = 150$ lenses), and each pixel corresponds to 3.9 μm at the Science cell. Our imaging beam can be directed along the ODT1 or ODT2 beams to look at the cloud from two different sides (Fig. 3.3).

In the following, we briefly review the absoprtion imaging. We then explain our state-selctive detection method with kinetic imaging and Stern-Gerlach, and also additional image-correction techniques.

3.3.1 Absorption imaging

The light intensity $I(\boldsymbol{r})$ passing through an atomic medium of density $n(\boldsymbol{r})$ is attenuated according to the (modified) Beer-Lambert law

$$dI(\boldsymbol{r})/dz = -n(\boldsymbol{r})\sigma I(\boldsymbol{r})/(1 + I(\boldsymbol{r})/I_{\rm sat}) \tag{3.16}$$

with the cross section $\sigma = \sigma_0/\alpha$ and saturation intensity $I_{\rm sat} = \alpha I^0_{\rm sat}$ with some correction $\alpha > 1$ due to polarization effects (the bare values are $\sigma_0 = 3\lambda^2/2\pi$ and $I^0_{\rm sat} = \pi hc\Gamma/3\lambda^3$) [132]. In the low intensity regime $I \ll I_{\rm sat}$, the intensity attenuation across a sample is given by $I(x, y, z_1)/I(x, y, z_0) = \exp[-\sigma \int_{z_0}^{z_1} dz' n(x, y, z')]$. The quantity in the exponent is the optical (column) density (OD) in the limit $-z_0, z_1 \to \infty$. In both the low and high-intensity

[9] The measurement was done using the oscillation of a BEC after kicking by the ODT beams. To confine the motion in the z direction, we added vertical tubes during the measurement, and obtained the value with the tubes from extrapolation.

[10] We acknowledge H. Huang for the initial drawing of the beam paths.

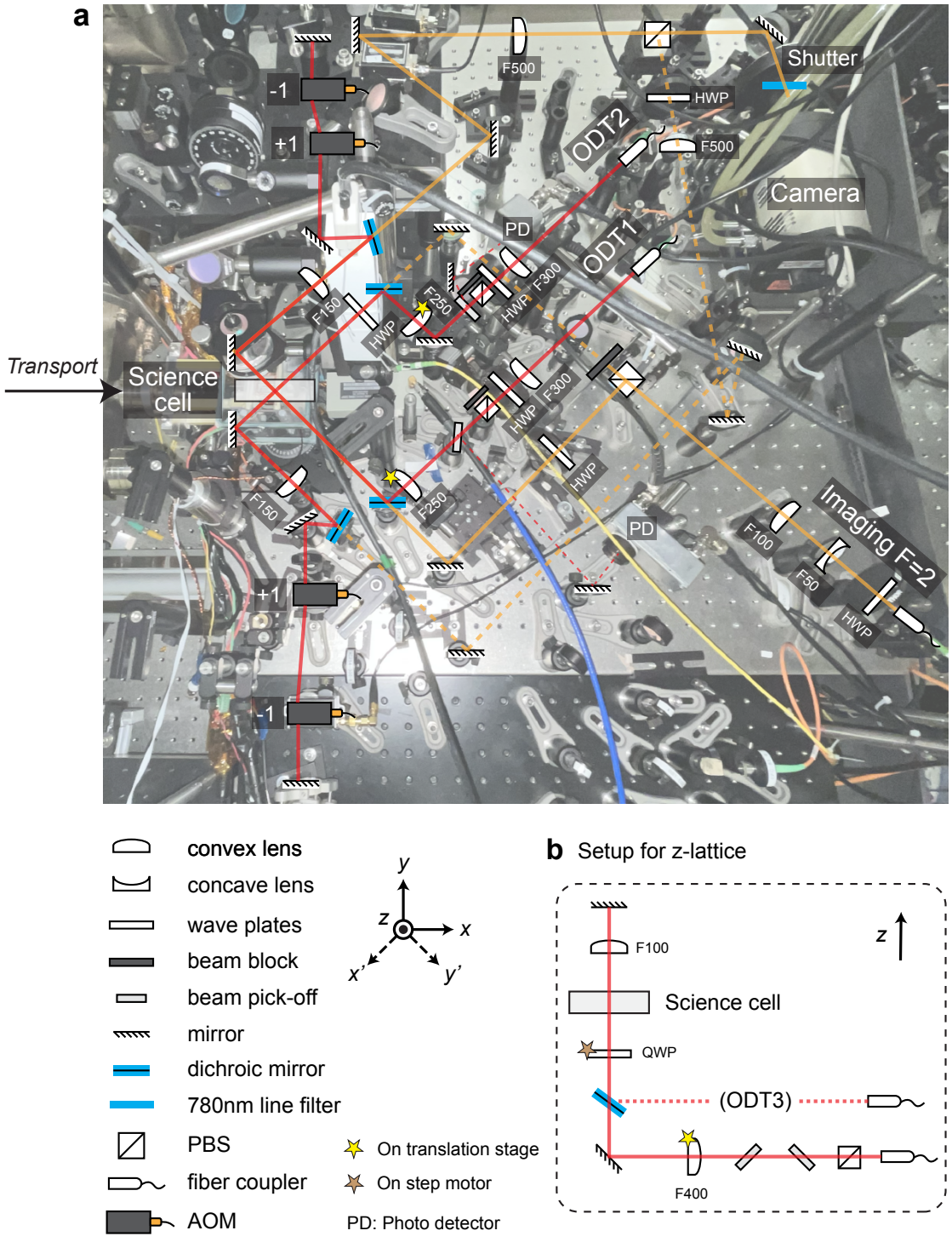

Figure 3.3: Beam paths in the x-y plane and the top-down view of our apparatus around the Science cell [10]. (In the picture, some optical elements are hidden below an optical breadboard.) The imaging path can be switched by moving the beam block near the PBS.

regimes [132],

$$OD(x,y) = \sigma \int_{-\infty}^{\infty} dz' n(x,y,z') = -\ln \frac{I_{\text{out}}(x,y)}{I_{\text{in}}(x,y)} + \frac{I_{\text{in}}(x,y) - I_{\text{out}}(x,y)}{I_{\text{sat}}}. \tag{3.17}$$

The intensity is estimated from the counts $C_{i,j}$ in each pixel (i,j) of the CCD camera, i.e. $\int_{A_{i,j}} dxdyI(x,y) \propto C_{i,j}$ where $A_{i,j}$ is the area of the object plane that is projected onto the pixel (i,j). There are 3 images needed to determine the OD: an image with atoms, $C_{i,j}^{\text{atoms}}$, an image without atoms, $C_{i,j}^{\text{empty}}$, and a dark image without the illumination, $C_{i,j}^{\text{dark}}$. The high-intensity regime is avoided in our experiment by keeping $C_{i,j} \lesssim 40000$ ($I_{\text{sat}} \sim 4$ mW/cm^2 for the cycling transition [118]). The optical density for each pixel is obtained as

$$OD_{i,j} = \frac{\sigma}{A_{i,j}} \int_{A_{i,j}} dxdy \int_{-\infty}^{\infty} dz' n(x,y,z') \approx -\ln \frac{C_{i,j}^{\text{atoms}} - C_{i,j}^{\text{dark}}}{C_{i,j}^{\text{empty}} - C_{i,j}^{\text{dark}}}. \tag{3.18}$$

Relating this to the atom number $N_{i,j}$ detected in each pixel requires the knowledge of the area $A_{i,j}$ and the cross section σ (dependent on polarization and bias field). The former is already known, and also can be calibrated from the time of flight, but the latter can be complicated. Alternatively, the proportionality factor between the $OD_{i,j}$ and $N_{i,j}$ can be calibrated using the fluorescence imaging in the MOT cell before and after the transport to the science cell [118]. In our experiments, we use the calibration factor of 125 such that $N_{i,j} \approx 125 OD_{i,j}$ and the total atom number is $N \approx 125 \sum_{i,j} OD_{i,j}$ [123].

3.3.2 State-selective imaging with Stern-Gerlach separation

In the optical trap, ^{87}Rb atoms can be in the various Zeeman sublevels of the hyperfine ground-state manifold $F = 1$ and $F = 2$. We use a 780 nm imaging beam (cycling transition $F = 2 \rightarrow F = 3$) for imaging, which first images the $F = 2$ atoms (for 200 μs duration). We wait for the $F = 2$ atoms to be scattered away, repump $F = 1$ atoms to $F = 2$, and then illuminate them with the imaging light. The process requires taking three images ($F = 2$, $F = 1$, and empty images) with short intervals in between (2.7 ms). To facilitate this, we use the Kinetics mode of our camera, which works by exposing only part of the CCD array (bottom rows). Once an image is taken, the charges of the exposed rows are quickly shifted up, and the area is ready for a new image (shifting a row takes less than a few microseconds).

To image the Zeeman sublevels separately, we use a Stern-Gerlach pulse,

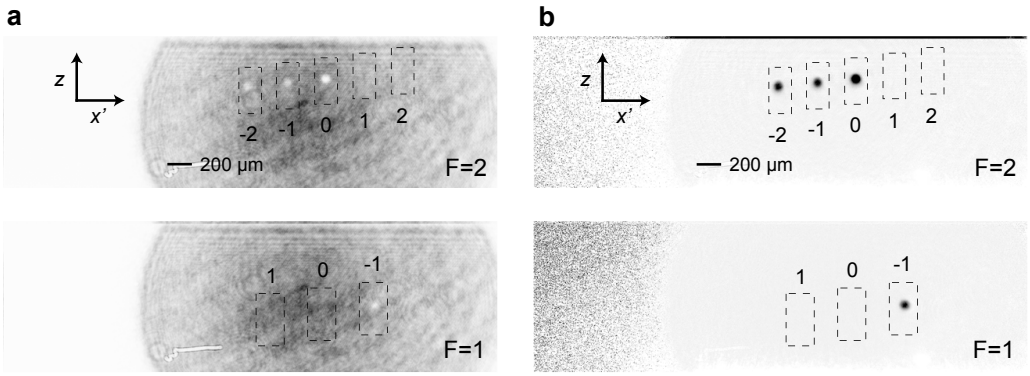

Figure 3.4: **a,** The two successive images taken for the $F = 2$ and $F = 2$ states with our CCD camera. The atoms are distributed among $|1, -1\rangle$, $|2, 0\rangle$, $|2, -1\rangle$, and $|2, -2\rangle$. **b,** The optical-depth (OD) images obtained using the CCD images of **a**, an empty CCD image (with illumination), and dark CCD images (without illumination). The square dashed boxes represent the regions where each Zeeman sublevel m_F is expected to appear.

generated by slightly shifting our quadrupole coil backward (in the negative x direction in Fig. 3.3) and turning it on shortly (2.5 ms). The falling atoms experience the radial field of the coil roughly in the x direction $\boldsymbol{B} \approx bx\boldsymbol{e}_x$, with a gradient $b \sim 100$ G (on average; the field will gradually rise). This is enough to separate out atoms in the different Zeeman states (Fig. 3.4).

3.3.3 Post-processing with principal component analysis

Our OD images can suffer from fringe noises, which can change the perceived atom numbers on the order of a few hundred, and are important when one is to obtain a clean 2D or 1D atomic density. The fringes can appear due to dust particles (circular fringes) or etaloning effects between planar surfaces (linear fringes) [123]. In principle, these fringes should be removed in the absorption imaging technique as we subtract empty, illuminated CCD images. However, if there is a time-dependence of fringes on the time scale between taking of an real image and an empty image (due to vibrations, air currents, moving dusts, laser intensity fluctuations, ...), the changes will appear in the final OD images. We use principal component analysis (PCA) [133, 134] to remove the fringes in the images. The technique is well known [135–137] and also described in previous theses from our group [123, 138]. We discuss the basic idea, which is to reduce the dimensionality of the data of correlated variables. As a simple example, we

can consider two variables, $\boldsymbol{x}^{(1)}$ and $\boldsymbol{x}^{(2)}$, with a set of n measurements on these variables, $\boldsymbol{d}^{(1)} = \{x_1^{(1)}, x_1^{(2)}\}, \boldsymbol{d}^{(2)} = \{x_2^{(1)}, x_2^{(2)}\}, ..., \boldsymbol{d}^{(n)} = \{x_n^{(1)}, x_n^{(2)}\}$, as shown in Fig. 3.5. Since we are typically interested in the variation, the variables are made to have zero mean $x_j^{(i)} \to x_j^{(i)} - \langle \boldsymbol{x}^{(i)} \rangle$, where $\langle \boldsymbol{x}^{(i)} \rangle = (1/n) \sum_{j=1}^{n} x_j^{(i)}$. The measurements and variables can be thought of as vectors, and we represent the entire data as a $2 \times n$ matrix

$$\boldsymbol{D} = \begin{bmatrix} \boldsymbol{d}^{(1)} & \boldsymbol{d}^{(2)} & ... & \boldsymbol{d}^{(n)} \end{bmatrix} = \begin{bmatrix} \boldsymbol{x}^{(1)} & \boldsymbol{x}^{(2)} \end{bmatrix}^T. \tag{3.19}$$

The 2×2 covariance matrix can be written as

$$\boldsymbol{C} = \boldsymbol{D}\boldsymbol{D}^T = \begin{bmatrix} \boldsymbol{x}^{(1)} \cdot \boldsymbol{x}^{(1)} & \boldsymbol{x}^{(1)} \cdot \boldsymbol{x}^{(2)} \\ \boldsymbol{x}^{(2)} \cdot \boldsymbol{x}^{(1)} & \boldsymbol{x}^{(2)} \cdot \boldsymbol{x}^{(2)} \end{bmatrix} \tag{3.20}$$

which includes information about the correlations between the variables. If the two variables are correlated, as shown in Fig. 3.5, this matrix will have off-diagonal components. We consider a transformation to a new basis,

$$\boldsymbol{D}' = \boldsymbol{P}\boldsymbol{D}, \tag{3.21}$$

where

$$\boldsymbol{P} = \begin{bmatrix} \boldsymbol{p}^{(1)} & \boldsymbol{p}^{(2)} \end{bmatrix}^T, \quad \text{and} \quad \boldsymbol{D}' = \begin{bmatrix} \boldsymbol{p}^{(1)} \cdot \boldsymbol{d}^{(1)} & \boldsymbol{p}^{(1)} \cdot \boldsymbol{d}^{(2)} & ... \\ \boldsymbol{p}^{(2)} \cdot \boldsymbol{d}^{(1)} & \boldsymbol{p}^{(2)} \cdot \boldsymbol{d}^{(2)} & ... \end{bmatrix} = \begin{bmatrix} \boldsymbol{x}'^{(1)} & \boldsymbol{x}'^{(2)} \end{bmatrix}^T \tag{3.22}$$

In this basis, we want the new variables to be uncorrelated, i.e. $\boldsymbol{C}' = \boldsymbol{D}'\boldsymbol{D}'^T$ to be diagonal, with the diagonal components being ordered. Each component also represents a projection, e.g. $C'_{11} = \sum_j (\boldsymbol{p}^{(1)} \cdot \boldsymbol{d}^{(j)})^2$ of the data onto the new basis. Our goal is to find $\boldsymbol{p}^{(1)}$ that yields the maximum variance, $\boldsymbol{p}^{(2)}$ with the next largest variance, and so on. Such vectors $\boldsymbol{p}^{(i)}$ are called the principal components (PC), and can be found as the eigenvectors of the covariance matrix $\boldsymbol{C}$ [133, 134],

$$\boldsymbol{D}\boldsymbol{D}^T \boldsymbol{p}^{(i)} = \lambda^{(i)} \boldsymbol{p}^{(i)}, \tag{3.23}$$

where $\lambda^{(i)}$ gives the corresponding variances. In Fig. 3.5, we show an example data with two variables, the principal components, and the data in the new basis $\boldsymbol{D}'$.[11] We note that the PCs also can be found via the singular value

[11] Note that the principal components can also refer to the transformed (derived) variables, and $\boldsymbol{p}_i$ can be called the vector of coefficients or loadings for ith PC [133]. Here we call $\boldsymbol{p}_i$ themselves the principal components.

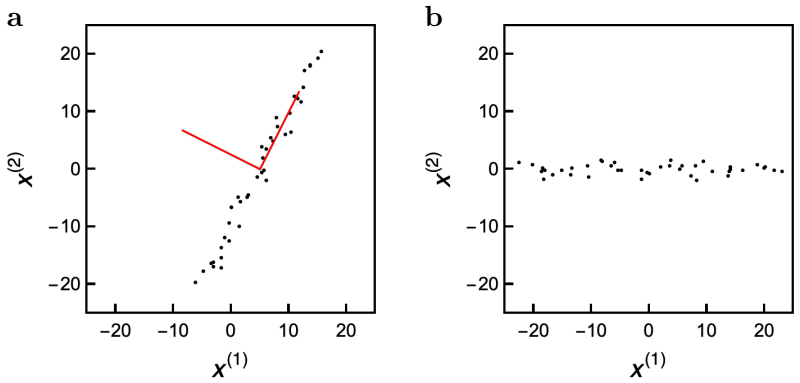

Figure 3.5: Example of the principal component analysis with two variables. **a,** The data $\boldsymbol{D}$ and the principal component vectors (scaled). **b,** The data in the new basis $\boldsymbol{D}'$.

decomposition of the matrix [133, 134] $\boldsymbol{D}^T = \boldsymbol{U}\boldsymbol{\Sigma}\boldsymbol{V}^T$, where $\boldsymbol{U}$ and $\boldsymbol{V}$ are orthogonal matrices and $\boldsymbol{\Sigma}$ is a rectangular diagonal matrix, where the columns of $\boldsymbol{V}$ gives the PCs.

The above discussion applies to a data set with p variables, $\{\boldsymbol{x}^{(1)}, ..., \boldsymbol{x}^{(p)}\}$. PCA can be used to extract common features appearing in the data, such as a set of facial images [139], with most of the features being captured by a handful of PCs. In our experiments, we take a set of n training images (experimental runs without atoms) interleaved between the real experimental runs, and extract the prevalent fridge patterns via PCA. The pixels in the images are considered as variables $\boldsymbol{x}^{(i)}$. An image is a measurement of these variables (pixels), and is represented as a vector $\boldsymbol{d}^{(j)} = \{ x_j^{(1)}, x_j^{(2)}, ..., x_j^{(p)}\}$. The set of the training images is then written as a single matrix $\boldsymbol{D} = [\boldsymbol{d}^{(1)}\boldsymbol{d}^{(2)}...\boldsymbol{d}^{(n)}]$. If there is a repeated fringe pattern, some of the variables will be highly correlated. By applying the PCA, we can represent a fringe pattern in a reduced number of variables in the new basis. Practically, the number of pixels, as high as $p = 1024 \times 1024$ (for our camera), is much larger than the number of training images, typically $n \sim 30$. It is not efficient to find the eigenvectors of the $p \times p$ covariance matrix $\boldsymbol{D}\boldsymbol{D}^T$ (with $\sim 10^{12}$ elements), as the rank of the matrix will be much smaller than p. Instead, one computes the eigenvectors $\boldsymbol{u}^{(i)}$ of $\boldsymbol{D}^T\boldsymbol{D}$ as

$$\boldsymbol{D}^T\boldsymbol{D}\boldsymbol{u}^{(i)} = \lambda^{(i)}\boldsymbol{u}^{(i)}, \quad \boldsymbol{D}\boldsymbol{D}^T(\boldsymbol{D}\boldsymbol{u}^{(i)}) = \lambda^{(i)}(\boldsymbol{D}\boldsymbol{u}^{(i)}) \tag{3.24}$$

from which we can identify $\boldsymbol{p}^{(i)} \propto \boldsymbol{D}\boldsymbol{u}^{(i)}$, and the problem reduces to solving the $n \times n$ matrix.

Typically, we are interested in the variations in images, so the mean of each image is made to be zero [139], in addition to making the mean of each pixel to be zero. These amount to defining new image vectors $\tilde{\boldsymbol{d}}^{(i)}$ with elements $\tilde{d}_l^{(i)} = d_l^{(i)} - \langle \boldsymbol{d}^{(i)} \rangle - \bar{d}_l$, where $\bar{d}_l$ is the element of $\bar{\boldsymbol{d}} = (1/n)\sum_{j=1}^{n} \boldsymbol{d}^{(j)}$. Once (normalized) PCs are obtained, the training images can be reconstructed as

$$\tilde{\boldsymbol{d}}^{(i)} = \sum_{j=1}^{n} (\boldsymbol{p}^{(j)} \cdot \tilde{\boldsymbol{d}}^{(i)}) \boldsymbol{p}^{(j)}, \tag{3.25}$$

and we can get $\boldsymbol{d}^{(i)}$ by adding back the subtracted means. To remove the fringe patterns from a real image $\boldsymbol{r}$ (in the presence of atoms), we subtract its projection as

$$\tilde{\boldsymbol{r}}^{\mathrm{PCA}} = \tilde{\boldsymbol{r}} - \sum_{j=1}^{n} (\boldsymbol{p}^{(j)} \cdot \tilde{\boldsymbol{r}}^{(i)}) \boldsymbol{p}^{(j)}, \tag{3.26}$$

where $\tilde{\boldsymbol{r}} = \boldsymbol{r} - \bar{\boldsymbol{d}}$ is a shifted image. In principle, the mean $\langle \boldsymbol{r} \rangle$ of the image should also be subtracted, but the atoms can shift mean and complicate the procedure. The region with atoms can also overlap with the PCs, leading to residual subtractions even without fringes. These effects are small for the typical atom number of our experiments, $\sim 10^4$, on the order of 0.1 atoms per pixel or less [123]. However, for large atom numbers, one may consider masking the region where the atoms appear.

In our lab, we use the Mathematica function called PrincipalComponents to compute PCs. It is designed to take an input in the form of $\boldsymbol{D}^T$ (each row is a measurement or a trial), and yields an output in the form of $\boldsymbol{D}^T\boldsymbol{P}^T$, that is, the transformed data in the PC basis. Considering Eq. 3.24, we use $\boldsymbol{D}$ as an input (i.e. PrincipalComponents[$\boldsymbol{D}$]) instead of $\boldsymbol{D}^T$, and obtain the output $\boldsymbol{D} \times [\boldsymbol{u}^{(1)}\boldsymbol{u}^{(2)}...\boldsymbol{u}^{(n)}]$, which is identified as $\boldsymbol{P}^T$ (of n PCs instead of p PCs as columns) up to normalization. We caution that PrincipalComponents automatically subtracts the mean from each variable, i.e. each column of $\boldsymbol{M}$ in PrincipalComponents[$\boldsymbol{M}$], which is equivalent to subtracting the mean from each image in our usage. In Fig. 3.6, we show a sample OD image, its shifted version, and its PCAed version. We see that simply subtracting the mean of the training images might create additional fringes.

In practice, we use the PCA only when taking important data, due to additional overheads such as collecting empty images in between runs and applying the PCA computation to images (which can take tens of seconds for a few hundred images). Normally, we only apply some simple adjustment to our 1D density, to correct the intensity fluctuation and gradient of the

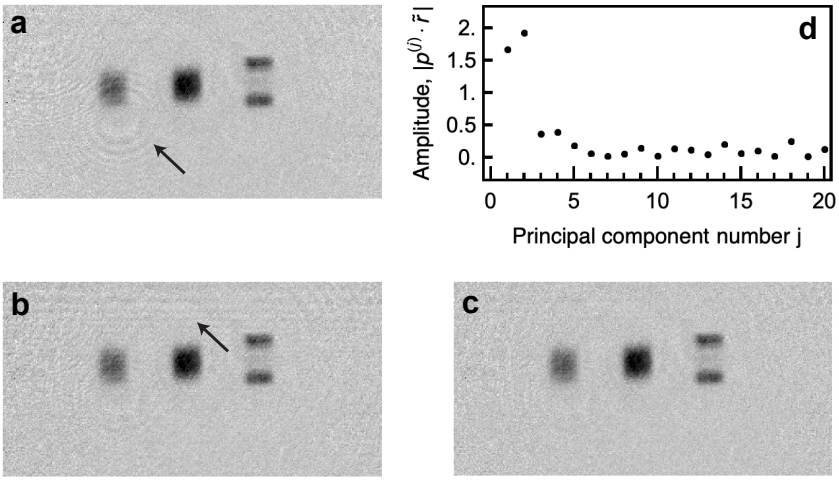

Figure 3.6: Sample PCA image and its amplitudes along the principal components. **a,** Sample OD image, with the arrow pointing to a circular fringe. **b,** Shifted image generated by subtracting the mean of training images. The arrow points to an additional linear fringe. **c,** PCAed image with all fringes being removed. **d,** Projections of the sample image along each principal component.

imaging light. For a given integrated 1D density n_i from a selected region (ROI) of a length L in an image, we take the first and last few pixels to estimate the background and the gradient, e.g. $n_{\rm bg} = (\sum_{i=1}^{10} n_i + \sum_{i=L-9}^{L} n_i)/20$ and $n_{\rm lin} = (\sum_{i=L-9}^{L} n_i - \sum_{i=1}^{10} n_i)/(L-10)$, which are subtracted as $n_j \to n_j - n_{\rm bg} - (j - L/2)n_{\rm lin}$.

3.4 Control of internal states

Interesting scenarios with atomic mixtures can be realized by utilizing multiple internal degrees of freedom (effective spins). We discuss the hyperfine ground states of ^{87}Rb in $^2S_{1/2}$ and their manipulation.

3.4.1 Breit-Rabi formula

The ground states have a spin angular momentum $S = 1/2$ and an orbital angular momentum $L = 0$, whose coupling leads to the fine-structure splitting labeled by the total electron angular momentum $J = 1/2$. This further couples with the nuclear spin $I = 3/2$, and the ground-state manifold splits into the hyperfine manifolds $F = I \pm 1/2 = 1, 2$ with energy difference

$\Delta_{\mathrm{HFS}} \approx 2\pi \times 6.834682610904290(90)$ GHz [124]. The degeneracy of levels in each manifold is lifted by a magnetic field $\boldsymbol{B}$, called the Zeeman effect. For $J = 1/2$, when the energy shift due to $\boldsymbol{B}$ is weaker than the fine-structure splitting, the Hamiltonian can be written as $\hat{H} = \hat{H}_{\mathrm{hfs}} + \hat{H}_B$ where

$$\hat{H}_{\mathrm{hfs}} = hA_{\mathrm{hfs}}\hat{\boldsymbol{I}} \cdot \hat{\boldsymbol{J}}, \quad \hat{H}_B = \mu_B(g_J\hat{\boldsymbol{J}} + g_I\hat{\boldsymbol{I}}) \cdot \boldsymbol{B}, \tag{3.27}$$

where the fine structure and nuclear Landé g-factors are $g_J \approx 2.002$ and $g_I \approx -0.001$. If the energy shift due to $\boldsymbol{B}$ is even weaker than the hyperfine splittings, we can further reduce the interaction Hamiltonian to $\hat{H}_B \approx \mu_B g_F \hat{\boldsymbol{F}} \cdot \boldsymbol{B}$, where the hyperfine Landé g-factor is $g_F \approx g_J[F(F+1) - I(I+1) + J(J+1)]/2F(F+1)$ (ignoring g_I). In this limit, the Zeeman shift is simply determined by m_F with the quantization axis along the direction of $\boldsymbol{B}$. On the other hand, if the field is sufficiently strong (but not too strong to break the spin-orbit coupling leading to Paschen-Back effect), the energy shift will dominated by $\hat{H} \approx \mu_B g_J \hat{\boldsymbol{J}} \cdot \boldsymbol{B}$ and can be determined by $m_J = \pm 1/2$. Between these two limits, one has to diagonalize the Hamiltonian (Eq. 3.27). It can be done exactly for $J = 1/2$, resulting in the Breit-Rabi formula for the hyperfine states in $F = I \pm 1/2$,

$$E_{F=I\pm1/2,m_F}(B) = -\frac{\Delta E_{\mathrm{hfs}}}{2(2I+1)} + \mu_N g_I m_F B \pm \frac{\Delta E_{\mathrm{hfs}}}{2}\sqrt{1 + \frac{2m_F x}{I+1/2} + x^2} \tag{3.28}$$

where $x \equiv (\mu_B g_J - \mu_N g_I)B/\Delta E_{\mathrm{hfs}}$ and $\Delta E_{\mathrm{hfs}} = hA_{\mathrm{hfs}}(I+1/2)$ is the energy splitting between the two hyperfine levels (for $m_F = -(1+1/2)$, the square root should be replaced by $1-x$ to avoid sign ambiguity). As shown in Fig. 3.7, the energy shift is $\propto \mu_B g_J m_J B z$ in the strong-field regime, and $\propto \mu_B g_F m_F B_z$ in the weak field regime, later of which are relevant to our experiments in a few Gauss range.

3.4.2 Microwave and RF control

In our experiments, we apply a $B \sim 5$ G bias field in the z direction to separate energies of the Zeeman sublevels of the hyperfine ground-state manifolds. Coherent transitions between these states, within the selection rules $\Delta L = 0$, $\Delta F = 0, \pm 1$ and $\Delta m_F = 0, \pm 1$ for the magnetic dipole transition, are achieved by our radio-frequency field systems. The transitions between the $F = 1$ and $F = 2$ manifolds (~ 6.8 GHz) can be addressed with our "microwave" pulses, and those within a manifold (a few MHz range) can be addressed with our "RF" pulses (the same ones used for evaporative coolings in our magnetic

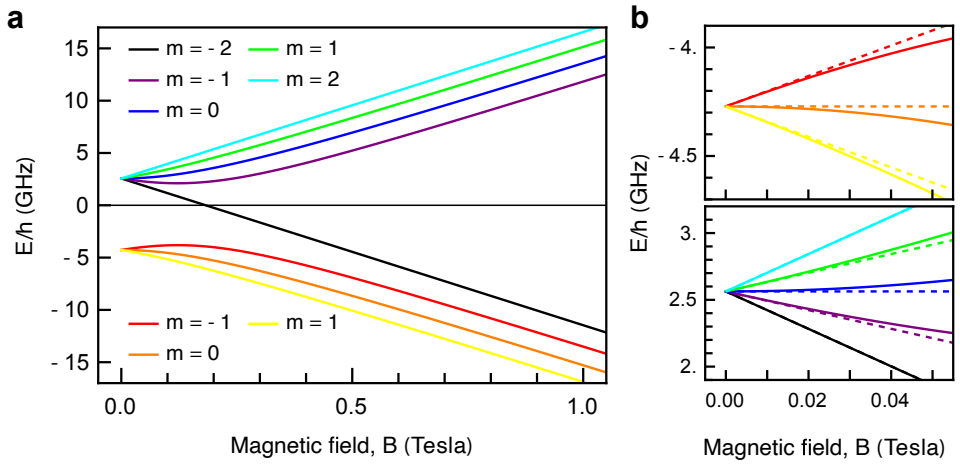

Figure 3.7: Energy shift of hyperfine ground states according to the Breit-Rabi formula. **a,** Energy shift vs. B field. **b,** Same in the weak coupling regime.

traps [118]).

As detailed in [122], the carrier frequency 6.807 GHz of our microwave signal is generated by our frequency source locked to 10MHz rubidium frequency standard (Microsource SNP-0608-520-02 and SRS SIM 940; the source can be programmed between 6 and 8 GHz with a 1 Hz resolution via a RS232 cable). The source is combined with the output of a function generator through an IQ mixer, which is then amplified and delivered to our microwave antenna. A recent upgrade of the amplifier (Triad RF Systems TA1029; [138]) and repositioning of the antenna closer to the Science cell improved the field amplitude (Rabi frequency) by a factor of ~ 3.

With the energy levels well separated, one can apply the oscillating field to address two specific states, which behave like a two-level system. The RWA Hamiltonian (Eq. 3.8) can be used to describe the dynamics, which can be written in terms of the Pauli matrices [78]

$$\hat{H} = \frac{\hbar}{2}\boldsymbol{\omega}\cdot\boldsymbol{\sigma} = \frac{\hbar}{2}\tilde{\Omega}\hat{\boldsymbol{n}}\cdot\boldsymbol{\sigma} = -\frac{\hbar}{2}\begin{pmatrix} -\Delta & \Omega^* \\ \Omega & \Delta \end{pmatrix} \tag{3.29}$$

where $\omega_x \equiv \mathrm{Re}(-\Omega)$, $\omega_y \equiv \mathrm{Im}(-\Omega)$, and $\omega_z \equiv \Delta$. We also defined a unit vector $\hat{\boldsymbol{n}} \equiv \boldsymbol{\omega}/\tilde{\Omega}$, where the magnitude $\tilde{\Omega} \equiv |\boldsymbol{\omega}| = \sqrt{|\Omega|^2 + \Delta^2}$ is the generalized Rabi frequency. The time evolution is described by $U(t) = e^{-i(\tilde{\Omega}t/2)\boldsymbol{n}\cdot\boldsymbol{\sigma}} = \cos(\tilde{\Omega}t/2)\mathbf{1} - i\sin(\tilde{\Omega}t/2)\boldsymbol{n}\cdot\boldsymbol{\sigma}$. Applying to a ground state $U(t)\,|g\rangle$, we find that the excited-state amplitude is given by $-i\Omega/\tilde{\Omega}\sin(\tilde{\Omega}t/2)$, which gives the

probability

$$P_e(t) = \frac{|\Omega|^2}{\tilde{\Omega}^2} \sin^2\left(\tilde{\Omega}t/2\right) = \frac{|\Omega|^2}{|\Omega|^2 + \Delta^2} \sin^2\left(\sqrt{|\Omega|^2 + \Delta^2}t/2\right), \tag{3.30}$$

which describes the Rabi oscillations. For Ω real and $\Delta = 0$, the state evolves as $|\psi\rangle = \cos(\Omega t/2)\,|g\rangle - i\sin(\Omega t/2)\,|e\rangle$, providing a method to coherently prepare a superposition state. The state will be flipped with a π pulse, $\Omega t = \pi$. The Rabi frequency Ω between the two states depends on the power and geometry of our microwave radiated from the antenna, which is hard to characterize. Instead, we calibrate Ω from the frequency of the resonant Rabi oscillations, and demonstrating examples can be found in the previous thesis, e.g. [76, 138]. The phase of the microwave field can be adjusted to implement the imaginary Rabi frequency, which could be useful to manipulate the state in the Bloch sphere for shortcut to adiabaticity [140–142]. In this work, we restrict Ω to be real.

To find the resonant frequency $\nu = \nu_0$ of the microwave with which $\Delta = \nu - \omega_0 = 0$, we scan ν over a certain range with a fixed Ω and t (but $\Omega t \sim \pi$). While the width of the Rabi spectrum (Eq. 3.30) will be narrower with smaller Ω leading to higher accuracy, we also want the spectral width to be large enough to cover the typical magnetic field fluctuations, a few mG throughout the day (between the $|1, -1\rangle$ and $|2, 0\rangle$ states, the resonant frequency depends on the magnetic field as ≈ 0.70kHz/1mG). Because of the experimental cycle time $\sim$ 30s, it takes a long time to scan over a large frequency range. To scan over tens of kHz or more, we may instead use the Landau-Zener sweep [143], by adiabatically varying $\nu = at$ over a certain range. If the transition is observed, we iteratively lower the range (e.g. to a half) to locate the resonance. The energy uncertainty associated with the crossing time $\tau \sim \Omega/a$ should be smaller than the energy gap at the resonance, $\hbar/\tau \ll \hbar\Omega \to \Omega^2/a \ll 1$. The jump probability can also be given in a closed form as $P = e^{-(\pi/2)\Omega^2/a}$ [144].

To drive the transition between the states with $\Delta m_F > 1$, we can use our microwave and RF pulses simultaneously to induce a two-photon transition. For example, we can drive the transition from $|g\rangle = |1, -1\rangle$ to $|e\rangle = |2, 1\rangle$ using $|i\rangle = |2, 0\rangle$ as the intermediate state, which has an advantage that the transition frequency is stable against the B field fluctuation as their linear Zeeman shift is the same. The effective Rabi frequency of a two-photon transition driven by two fields with strengths Ω_a and Ω_b, valid for $\Delta_i \ll \Omega_a, \Omega_b$, is given by [145]

$$\Omega_{ab}^{(2)} = \frac{\Omega_a \Omega_b}{2\Delta_i}, \tag{3.31}$$

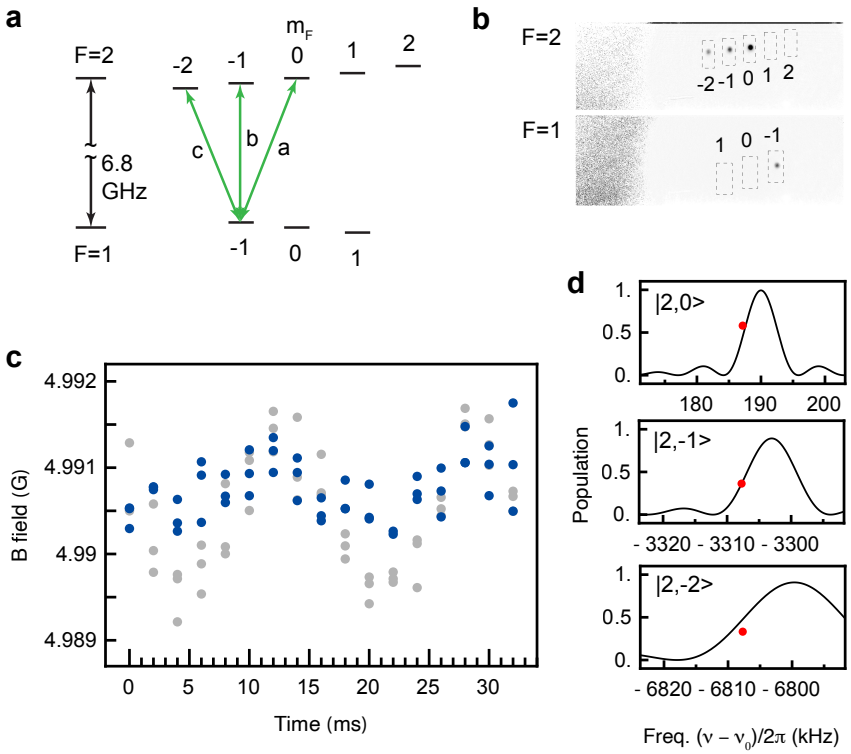

Figure 3.8: AC noise measurements with the field-tagging method. The parameters of each microwave field are $\nu_j = 6831000 + (187.15, -3307.74, -6807.71)$ kHz, $\Omega_j = (3.16, 3.94, 8.05)$ kHz, and $t_j = (150, 100, 50)$ μs. **a,** 3 transitions used for the field tagging. **b,** Sample image of atoms distributed among the hyperfine Zeeman sublevels. **c,** B field versus time (after the AC line trigger) with and without the AC noise compensation (blue and gray). **d,** Rabi formula fitted to the transferred populations (red circles) for each transition, with B as the fitting parameter. The x-axis shows the relative frequency $\nu - \nu_0$ where $\nu_0 = 2\pi \times 6831.000$ GHz.

where $\Delta_i = \nu_a - \omega_{ig}$ is the detuning of the Ω_a field from the transition $|g\rangle \to |i\rangle$. While the bare detuning of the two-photon field is $\Delta_e = \nu_a + \nu_b - \omega_{eg}$, the effective detuning should incorporate the AC start shift caused by each field as $\Delta_{\text{eff}} = \Delta_e - (\Omega_b^2 - \Omega_a^2)/4\Delta_i$.

3.4.3 Magnetic-field tagging

For our experiments in a state-selective optical lattice, it is critical to accurately know the detuning of our microwave field within about 10 % of the typical energy scale $\omega_r = 2\pi \times 3.67$ Hz, corresponding to the B fluctuation of

~ 0.5 mG. Measuring the field at this level right near the atom, for example using a magnetometer, is very hard, as the atoms are in a vacuum cell and are surrounded by other objects like the TOP coils.[12] Our lab has developed a method to measure the magnetic field with atoms themselves in a single cycle as detailed in [123, 146]. This method can be applied during the real experimental cycles to monitor the magnetic field in situ, such that each cycle has a tag attached indicating the B value. While an experiment is running, one can monitor the B field experienced by atoms and actively compensate for the drift by changing the bias field via the coil current. Additionally, the final data can be post-selected based on the tagged B values within a certain range. We have applied a simplified version of it in the experiment of Chapter 4.

The idea is to drive transitions to multiple hyperfine ground states, and infer the magnetic field from the transferred fractions. We consider atoms initially in the $|1,-1\rangle$ state, and the transitions a, b, and c to $|2,0\rangle$, $|2,-1\rangle$, and $|2,-2\rangle$, respectively (Fig. 3.8). Driving these transitions with 3 successive microwave pulses each with frequency, strength, and duration (ν_j, Ω_j, and t_j), the atoms are distributed among the hyperfine states, $N = N_{1,-1} + N_{2,0} + N_{2,-1} + N_{2,-2}$. The transferred fraction for each transition can be written as

$$P_a = \frac{N_{2,0}}{N_{1,-1} + N_{2,-1} + N_{2,-2}}, \quad P_b = \frac{N_{2,-1}}{N_{1,-1} + N_{2,-2}}, \quad P_c = \frac{N_{2,-2}}{N_{1,-1}}. \tag{3.32}$$

Each of these fractions should follow the Rabi formula

$$P_j(B) = \frac{\Omega_j^2}{\Omega_j^2 + \Delta_j(B)^2} \sin^2\left(\sqrt{\Omega_j^2 + \Delta_j(B)^2} t_j/2\right), \tag{3.33}$$

where $j = a, b, c$ and $\Delta_j(B) = \nu_j - \omega_{0,j}(B)$ with $\omega_{0,j}$ being the transition frequency computed from the Breit-Rabi formula. With all the microwave parameters are known (e.g. from separate calibrations), the transferred fractions are solely determined by B, and thus we can estimate the value of B from the fitting. As an example, we show a measurement of the field noise over 30 ms after the AC line trigger in Fig. 3.8, showing the periodic noise at 60 Hz felt by atoms. This noise originates from various equipment connected to the AC power line. Our apparatus has an extra coil that produces an additional bias field to compensate for this periodic noise. We note that one of the Rabi frequencies Ω_j was chosen larger than others, such that the tagging can cover a

[12] From about 30 cm away from the atoms, we measure ~ 0.02 mG shift with our magnetometer (Bartington Instruments Mag-03 Three-axis) when the atoms experience ~ 1 mG shift.

wide frequency range and thus robust against occasional large fluctuations.

3.5 Optical lattices

Optical lattices are generated by interfering two or several (counter-propagating) beams coherently. These potentials localize atoms and arrange them in regular configurations. In particular, we can selectively trap atoms of different internal states with our state-selective optical lattice, which is integral to our experiments with matter waves. In the x-y plane, we prepare the (state-independent) optical lattices by the retro-reflections of the ODT1 and ODT2 beams, each of which is controlled by a mirror and two AOMs (Fig. 3.3a). This produces the transverse lattices, forming a bundle of vertical tubes spaced by $\lambda_\perp/2 = 532$ nm. The state-selective optical lattice is generated by an additional laser beam in the z direction. The forward beam is controlled by an AOM, which is always retro-reflected by a mirror (Fig. 3.3b). The beam has a relatively large waist 230 mW to ensure homogeneity across the tubes, and a power ~ 100 mW. In the following, we discuss how we characterize our optical lattices, and how we realize the state-dependent optical lattices (SDOL).

3.5.1 Kapitza-Dirac diffraction

A BEC can be thought of as a single-particle matter wave up to the mean-field interactions. When an optical lattice is pulsed onto this wave at zero momentum, it undergoes the Kapitza-Dirac diffraction [147] at the integer multiples of $2\hbar k_\mathsf{r}$ in the momentum space, i.e. in unit of the lattice photon momentum $k_\mathsf{r} = 2\pi/\lambda$. To quantitatively obtain the populations in each diffraction order, we need to solve the equations of motion with the Hamiltonian $\hat{H} = -(\hbar^2/2m)\partial^2 + V_0 \sin^2 k_\mathsf{r} z$. As discussed in the section 5.2.1, the state in the presence of the lattice can be expanded in the Bloch waves, and the initial state with $k = 0$ will be a sum of the Bloch waves with $q = 0$, $\psi(t) = \sum_l c_l(t) e^{i2lk_\mathsf{r}z}$. The time-dependent amplitudes follow

$$i\hbar\dot{c}_l = (2l)^2 E_\mathsf{r}^2 c_l + \frac{V_0}{4}(c_{l-1} + c_{l+1} + 2c_l), \tag{3.34}$$

where $E_\mathsf{r} = \hbar^2 k_\mathsf{r}^2/2m$. In the limit of small kinetic energy, called the Raman-Nath approximation, one can ignore the kinetic term and the solution after a time t is given in terms of the Bessel functions, with the populations given by $P_l = |c_l|^2 = J_l^2(V_0 t/2\hbar)$ [89, 148, 149]. It will be valid if the kinetic term is smaller than the potential term, $(2l_{\max}E_\mathsf{r})^2 \ll V_0/4$. The maximum diffraction order $l_{\max}$ is estimated $l_{\max} \approx V_0 t/\hbar$ [89] by inspecting the Bessel functions, and

the condition becomes $t \ll 1/(4\sqrt{V_0\omega_r})$. This is 5equivalent to requiring the time to be much less than the harmonic oscillator period, $\omega_{ho} = 2\sqrt{V_0\omega_r}$. For $V_0 = 20E_r$ and $\lambda = 790$ nm, this period is about 30 μs. In our experiments, we calibrate the lattice depth with a 10 μs pulse, and the exact numerical solution of Eq. 3.34 is used to accurately determine the lattice depth.

For a small depth $V_0 \lesssim 0.1E_r$, the relative populations in the nonzero orders are too small to detect with our apparatus [123]. In this case, one can obtain an amplified signal using the Talbot-resonant kicking method [150]. While the population in the first diffracted order oscillates with small amplitude, using a series of short pulses (kicks) separated by $t = 2\pi/\omega_r$, we can make the amplitude grow monotonically as a function of the number of kicks [123]. We typically use a set of 10 kicks with a pulse length 10 μs separated by 68 μs to verify that a certain hyperfine state is tuned out from our state-selective optical lattice.

3.5.2 State-dependent optical potentials

The capability to generate state-dependent optical potentials has been a key to our experiments, and the technique is described in many previous theses of our group, e.g. [76, 122]. We briefly discuss the main idea, especially from the perspective of polarizability. For a static field, the polarizability α is defined as the induced dipole moment $\boldsymbol{d} = \alpha\boldsymbol{E}$, where α can be a scalar or more generally a tensor (3× 3 matrix) [151]. If a time-dependent field $\boldsymbol{E} = (E_0\hat{\boldsymbol{e}}e^{-i\nu t} + E_0^*\hat{\boldsymbol{e}}^*e^{i\nu t})/2$ induces an oscillating dipole $\boldsymbol{d} = (d_0\hat{\boldsymbol{e}}e^{-i\nu t} + d_0^*\hat{\boldsymbol{e}}^*e^{i\nu t})/2$, the polarizability can be complex, relating the amplitudes as $d_0 = \alpha E_0$. In terms of α, the interaction energy can be written as [113, 116]

$$\Delta E = -\frac{1}{2}\langle \boldsymbol{d}\cdot\boldsymbol{E}\rangle_t = -\frac{1}{4}\,\mathrm{Re}(\alpha)|E_0|^2 = -\frac{1}{2\epsilon_0 c}\,\mathrm{Re}(\alpha)I, \tag{3.35}$$

where $\langle ...\rangle_t$ is a time average and we used $I = \epsilon_0 c|E_0|^2/2$. The scattering rate (power absorbed per $\hbar\nu$) is related to the imaginary part as

$$\Gamma_{sc} = \frac{1}{\hbar\nu}\langle \dot{\boldsymbol{d}}\cdot\boldsymbol{E}\rangle_t = \frac{1}{2\hbar}\,\mathrm{Im}(\alpha)|E_0|^2 = \frac{1}{\hbar\epsilon_0 c}\,\mathrm{Im}(\alpha)I. \tag{3.36}$$

For multi-level atoms with excited states $|j\rangle$ (in hyperfine manifolds), the energy shift of the ground state $|g\rangle = |i\rangle$ induced by a light field can be obtained from the second-order time-dependent perturbation theory [94, 113,

116]

$$\Delta E_i = \sum_{j \neq i} \frac{|\langle j| \hat{H}' |i\rangle|^2}{\tilde{E}_i - \tilde{E}_j}, \tag{3.37}$$

where $\hat{H}' = -\hat{\boldsymbol{d}} \cdot \boldsymbol{E}$. The energies can be considered as those of the dressed states of the atom and the light field of n photons, i.e. $\tilde{E}_i = \hbar\omega_i + \hbar\nu n$ and $\tilde{E}_j = \hbar\omega_j + \hbar\nu(n \mp 1)$. Then the energy shift becomes

$$\Delta E_i = \sum_{j \neq i} \left[\frac{1}{\nu - \omega_{ji}} - \frac{1}{\nu + \omega_{ji}} \right] \frac{|\langle j| \hat{\boldsymbol{d}} \cdot \hat{\boldsymbol{e}} |i\rangle|^2}{4\hbar} |E_0|^2, \tag{3.38}$$

where $\omega_{ji} = \omega_j - \omega_i$. We may ignore the second, counter-rotating term, which is relatively small compared to the first term, which diverges closer to the zero of the detuning $\Delta_{ij} = \nu - \omega_{ji}$. Computing the light shift requires the knowledge of the transition matrix elements $\langle j| \hat{\boldsymbol{d}} \cdot \hat{\boldsymbol{e}} |i\rangle$ between the states labeled by L, J, F, and m_F, beside the selection rules $\Delta L = \pm 1$, $\Delta J = 0, \pm 1$, $\Delta F = 0, \pm 1$, and $\Delta m_F = 0, \pm 1$ (except for $J = 0 \to J' = 0$ and $F' = 0 \to F' = 0$, which necessarily violates $\Delta L = \pm 1$) [114]. One approach to compute them is defining the polarizability tensor operator [152, 153], $\hat{\boldsymbol{\alpha}} = -\sum_{j \neq i} \hat{\boldsymbol{d}}^\dagger |j\rangle \langle j| \hat{\boldsymbol{d}} / \hbar\Delta_{ij}$. The energy shift can be written as

$$\Delta E_i = -\frac{1}{4} (\hat{\boldsymbol{e}} E_0)^* \cdot \langle i| \hat{\boldsymbol{\alpha}} |i\rangle \cdot \hat{\boldsymbol{e}} E_0, \tag{3.39}$$

which is in a similar form to the c-number version (Eq. 3.35). One can then systematically expand $\hat{\boldsymbol{\alpha}}$ by inserting the projection operators $\hat{P}_F = \sum_m |F, m\rangle \langle F, m|$ and $\hat{P}_{F'} = \sum_{m'} |F', m'\rangle \langle F', m'|$ for the ground and excited states, respectively, such that $\hat{\boldsymbol{\alpha}} = -\sum_{F'} \hat{P}_F \hat{\boldsymbol{d}} \hat{P}_{F'} \hat{\boldsymbol{d}} \hat{P}_F / \hbar\Delta_{F,F'}$.

The picture gets simpler if one considers the specific level structure of the alkali atoms such as ^{87}Rb. There are typically three energy scales ordered as $\Delta_{FS} \gg \Delta_{HFS} \gg \Delta'_{HFS}$ [116], for the fine structure of the excited states ($J' = 1/2, J' = 3/2$), hyperfine structure of the ground state (F), and of the excited states (F'), respectively. We can take the limit of unresolved hyperfine structure with large detuning, i.e. $\Delta_{FS} \gg \Delta_{F,F'} \gg \Delta_{HFS}, \Delta'_{HFS}$, and compute instead $\hat{\boldsymbol{\alpha}}' = -\sum_{J'} \hat{P}_J \hat{\boldsymbol{d}} \hat{P}_{J'} \hat{\boldsymbol{d}} \hat{P}_J / \hbar\Delta_{J,J'}$. The polarizability for the hyperfine ground states can be approximated as $\hat{\boldsymbol{\alpha}} \approx P_F \hat{\boldsymbol{\alpha}}' P_F$ [152]. Furthermore, $\hat{\alpha}'_{ij} = \hat{D}_i^\dagger \hat{D}_j$ is a dyadic tensor, where $\hat{D}_j \propto P_{J'} \hat{\boldsymbol{d}}_j P_J$, and can be decomposed into spherical tensors of rank 0,1, and 2.[13] The rank-2 part should vanish as the

[13] $a_i b_j = \frac{1}{3} \boldsymbol{a} \cdot \boldsymbol{b} \delta_{ij} + \frac{1}{2}(a_i b_j - a_j b_i) + \left[\frac{1}{2}(a_i b_j + a_j b_i) - \frac{1}{3} \boldsymbol{a} \cdot \boldsymbol{b} \delta_{ij} \right]$. The first and second

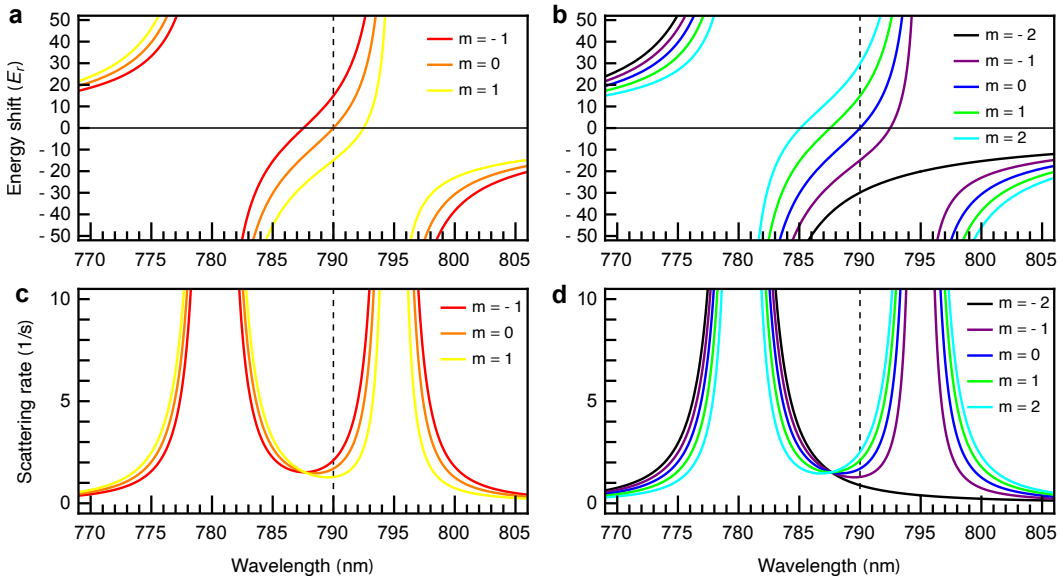

Figure 3.9: State-dependent energy shifts and scattering rates of the hyperfine ground states for a light intensity 100 mW/230 μm^2 = 1.89 W/mm^2. **a, b,** Energy shifts for $F = 1$ (left) and $F = 2$ (right) states. **c, d,** Corresponding scattering rates.

operator is in 2-dimensional Hilbert space ($m_J = 1/2, -1/2$), which can be written in a sum of the scalar and vector operators $\{\hat{I}, \hat{\sigma}_i\}$. The scalar part $\propto |E_0|^2 \hat{I}$ is independent of the field direction, but the vector part $\propto |E_0|^2 (\hat{\boldsymbol{e}}^* \times \hat{\boldsymbol{e}}) \cdot \hat{\sigma}$ gives a fictitious magnetic field [116, 152, 153], which depends on the polarization of light. Combining the contributions from the D_1 ($J' = 1/2$) and D_2 ($J' = 3/2$) transitions, one obtains a simple formula for the light shift of the hyperfine ground state [76, 116, 122, 154],

$$\Delta E_{F,m_F} = \frac{\pi c^2 \Gamma}{2\omega_0^3} \left(\frac{2 + g_F m_F q}{\Delta_{D_2}} + \frac{1 - g_F m_F q}{\Delta_{D_1}} \right) I, \tag{3.40}$$

where $\Gamma = \Gamma_{D_2} \approx \Gamma_{D_1}$ and $\omega_0 = \omega_{D_2} \approx \omega_{D_1}$ are the decay rates and transition frequencies from $^2P_{1/2}$ and $^2P_{3/2}$ to $^2S_{1/2}$, $\Delta_{D_2} = \nu - \omega_{D_2}$ and $\Delta_{D_1} = \nu - \omega_{D_1}$ are the detunings, and $q = 0, \pm 1$ is for the π and $\sigma^\pm$ polarizations. The scattering rates can be related to this using Eq. 3.11, $\Gamma_{\rm sc} = \Gamma(\Delta E_g)/\hbar\Delta$. In our lab, we use a $\lambda = 790.0$ nm laser beam with σ^- polarization relative to the quantization axis defined by the 5 G bias magnetic field. At this tune-out wavelength, the energy shift is zero for $|2, 0\rangle$ and $|1, 0\rangle$ states, and the

terms can be also written as $\frac{1}{3}\,\mathrm{Tr}(\boldsymbol{a}\boldsymbol{b}^T)\delta_{ij} + \frac{1}{2}\varepsilon_{ijk}(\boldsymbol{a} \times \boldsymbol{b})$.

scattering rates remain low $\sim 1/\mathrm{s}$ for all ground states, as shown in Fig. 3.9.

3.6 Autonomous machine operation

One of the major difficulties of operating an ultracold atom apparatus is the drifts of experimental parameters, such as the magnetic field or BEC atom number. These are typically caused by environmental changes, for example in temperature, humidity, airflow, stray magnetic fields (e.g. from neighboring labs or building elevators), or vibrations (e.g. from constructions or skateboarding overground). They not only lower the quality of data (large uncertainties in parameters), but also require constant human intervention during a long-term operation, like adjusting MOT loading time or current through the field coils. The difficulty is aggravated by various exceptional situations, some common ones including loss of laser locking, laser power loss, transporter drive failure, software error ("red screen") potentially caused by an electronic glitch. Our lab has been using a control program called Cicero Word Generator (Version 1.64rev7; along with the server utility Atticus) [155], which is widely used in the ultracold atom community. The program is very strong in its graphical user interface (GUI) for experimental sequence design, but it only runs a set of experimental cycles (iterations) with preset input parameters,[14] and cannot actively interact with the apparatus. We have implemented a software bot to address the above issues, which were deployed in some preliminary measurements. We discuss its implementation, use cases, and potential improvements for the future.

3.6.1 System design

We want our software bot to have the following list of desired functionalities/properties:

- *Active monitoring and parameter updates.* After every iteration, it can check various experimental parameters (atom number, B field, etc) and modify the input parameters for the upcoming iterations.

- *Integration of the various programs.* Our apparatus is controlled and monitored by various programs (Cicero/Atticus for digital and analog

[14] We will distinguish "experimental" and "input" parameters, where the former is for values to be measured, while the latter are input values of various pieces of equipment. The latter are called variables in Cicero. By an experimental "cycle", we mean a period from the preparation of an atomic sample to its destructive imaging, and in Cicero an execution of a sequence for one period with a specific parameter set is called an "iteration".

outputs, WinView for CCD image readout, Mathematica for data analysis, Motion Planner for transporter control, Matlab for digital multimeter reading, HOBOware for temperature logging, etc). The bot can control each of these programs and mediate the interactions between them. For example, the bot asks Mathematica to analyze an image to detect drifts of certain variables, and update the parameters in Cicero to compensate for the drifts.

- *Handling of exceptional situations.* Experimental cycles are sometimes interrupted by various errors, such as the red screens of Cicero or equipment failures. There are also unnoticed exceptional situations, such as unlocked lasers (resulting in empty pictures). The bot can detect various exceptional scenarios, and determine the proper response (e.g. make a beeping sound or send an email to the user).

- *Ease of implementation and extension.* A sophisticated program, like Cicero built with C# and .NET framework, may require a dedicated programmer and many development hours. On the other hand, our apparatus is typically maintained by a small number of people ($1 \sim 2$), and thus the bot should be relatively easy to implement. Furthermore, its code should be easily understood and well documented, such that people can extend it for additional functionalities even after the original developer leaves.

With these considerations, we decided to use an RPA[15] software called UiPath,[16] which has powerful capabilities to manipulate Microsoft Windows-based programs. For example, it can recognize certain UI elements in a program (such as texts and input boxes), and simulate the keyboard and the mouse to control them.

The overall architecture of the autonomous experimental control is shown in Fig. 3.10. Roughly, we can divide it into a machine layer, a software layer, and a data layer, as well as interfaces between them. The main difference from the normal operation is that the UiPath bot manipulates Cicero, such as changing variables, initiating/halting iterations, etc. The bot also controls the Motion Planner program to check the transporter status (e.g. positions), and in principle can manipulate any other programs if necessary.[17] The instructions for the next experimental cycle, mainly the names and values of the variables to

[15]RPA stands for Robotic Process Automation.

[16]UiPath Inc. 2024. *UiPath Studio* (Version 2024.2.1. Community Edition). Available at `https://cloud.uipath.com/`.

[17]Multiple bots can also be implemented on different computers and can be coordinated.

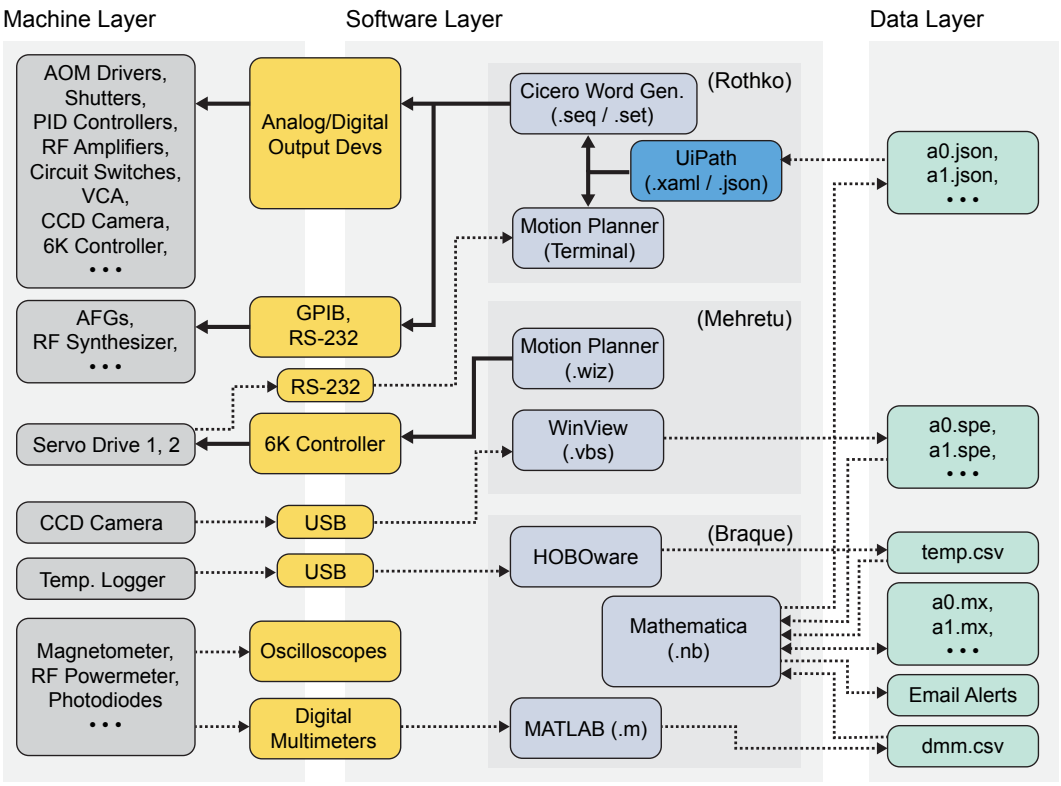

Figure 3.10: **Schematics of the autonomous experimental control.** The solid arrows represent the directions of control, while the dashed arrows indicate the directions of data flow. The equipment in the machine layer is programmed and controlled through various interfacing devices, including analog and digital output devices (NI PCI-6713, two of NI PCI-6733, and two of NI PCI-DIO-32HS), motion controller (6K Controller), and various communication ports (GPIB, RS-232, USB). The AFGs (arbitrary function generators) and DMMs (digital multimeters), connected to computers via GPIB cables, can be programmed and read out using the SCPI language (Standard Commands for Programmable Instruments). The collected data, such as images (.spe files from WinView), DMM readings (saved as .csv files by Matlab), and temperatures (from a temperature logger), are analyzed in a Mathematica notebook, which then can generate an instruction for the next run (as a .json file). The UiPath bot reads the .json file and update the parameters of the sequence in Cicero, while monitoring the stage position through Motion Planner to handle the transporter error. The control programs run on three different computers, named Rothko, Mehretu, and Braque, while all the data are stored in Braque and accessed through shared drive features of the Windows operating system.

be updated, are generated by Mathematica in the JSON format (See Appendix B). After each cycle, a Mathematica notebook analyzes the CCD image and various other data to determine the parameter adjustment necessary for the next iteration.

Analyzing the data, generating an instruction, and updating the Cicero variables can take up to a few seconds[18], which can add significantly to the cycle time $\gtrsim 25$ s. We have implemented two different versions, in which these tasks are carried out either in between the iterations or during each iteration (via the Variable Preview panel of Cicero). While the latter version is faster, a downside is that the implementation becomes more complicated, with each instruction being applied to the next next iteration, not the next one. For the latter version, a typical operation will look like the following.

0. The Mathematica notebook generates the first and second instructions (a0.json and a1.json). The UiPath bot reads the first instruction, opens the Cicero sequence (if necessary), changes the variables, and starts the first iteration.

1. While the current iteration is running, the bot update the variables for the next iteration (through the Variable Preview window).

2. After the current iteration is finished, an experimental picture is generated, and the next iteration starts automatically.

3. When the new picture arrives, the Mathematica notebook analyzes the picture, and generates a new instruction.

4. (Go to 1 and repeat).

3.6.2 Parameter drifts caused by the environment

Before we discuss the use of the autonomous operation for parameter stabilization, we first characterize the drifts of two important parameters that we aim to stabilize, the BEC atom number and the magnetic field.

A particular measurement of the atom number is shown in Fig. 3.11. In this measurement, the atom number periodically oscillates with an amplitude of almost 50% of the average. Given that such a large fluctuation is not observed for the thermal cloud before the evaporative cooling in our ODT (optical diopoe trap), we suspect that the instability is caused by the fluctuation of the final evaporation depth of the ODT. While the ODT beam powers are

[18]Since the bot interacts with other programs like a human using the keyboard and the mouse, the speed can be limited depending on the user interface of the program.

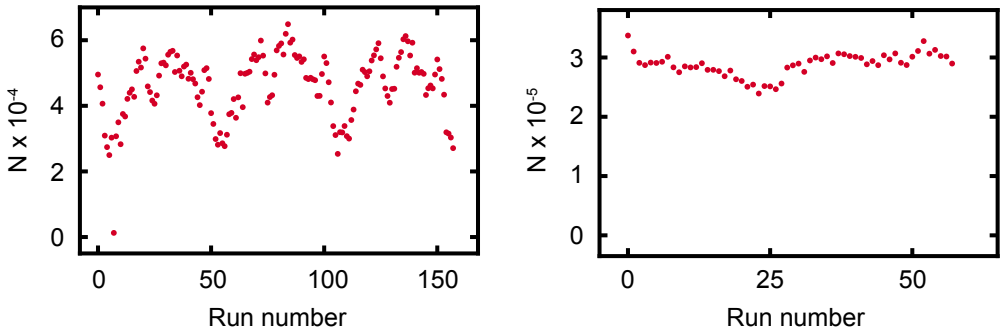

Figure 3.11: Measurement of atom number fluctuations. The left plot is for BECs, while the right plot is for thermal clouds right before the final evaporation step. Both are in the optical dipole trap. The data from 2021.02.16 and 2021.02.17, respectively. We note that this is not the typical performance of our apparatus. Normally, the fluctuation is on the 10% level (see text).

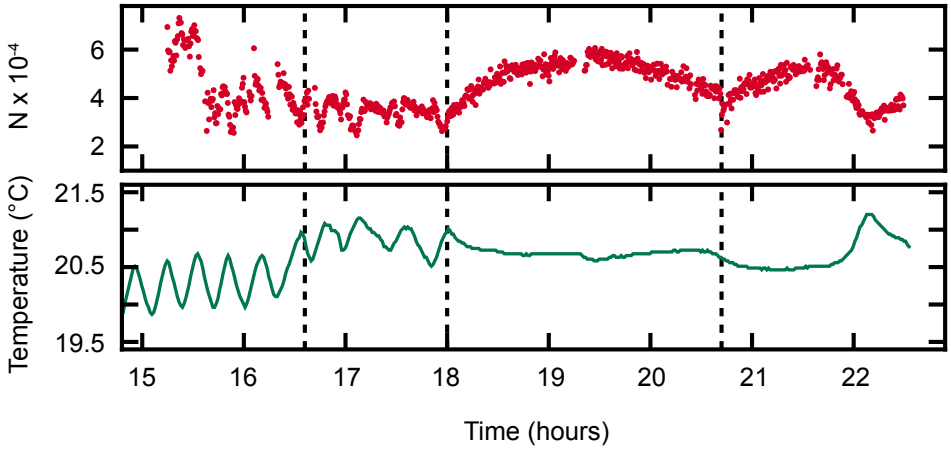

Figure 3.12: Atom number (top) and temperature of the machine room (bottom) measured by our thermometer near the Science cell. At 16.6 hours, we controlled the airflow by blocking 1/3 of the AC vent with cardboard. At 18.0 hours, we instead used the louvers on the vent to reduce the airflow. The kink at 20.7 hours is related to the relocking of the laser.

regulated via a PID controller, there seem to be other varying factors, such as the photo-diode sensitivity or beam alignments causing the fluctuation.

In this measurement, we notice that the atom number shows oscillations with a period of about ~ 20 minutes (~ 50 cycles), which corresponds to the cooling cycle of our air-conditioning (AC) unit. The airflow out of the AC vent on the wall, which never stops, turns out to be binary, i.e. either cold ~ 10°C or lukewarm ~ 20°C (measured with our infrared thermometer). This

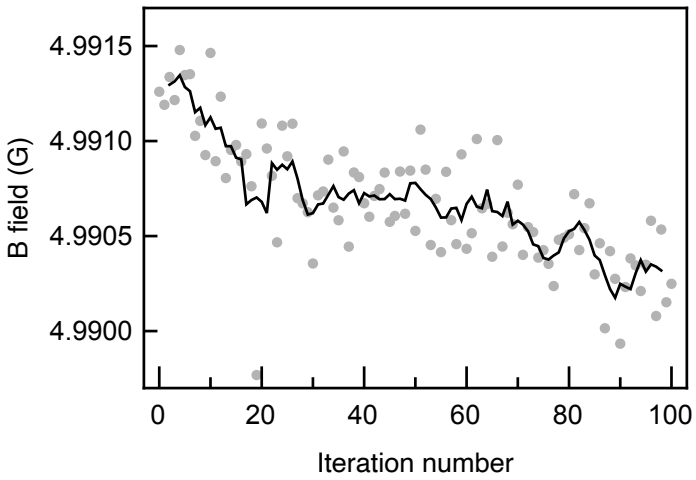

Figure 3.13: Magnetic field (B) drift over about an hour (100 cycles) measured through the B-tagging method. The line represents a moving average of 5 consecutive points.

is related to the behavior of our AC unit, which simply turn on its cooling when the temperature is above a certain threshold. We were able to avoid this binary behavior by diverting the airflow (by closing the louvers on the vent, while opening those of another vent somewhere), such that the temperature of our machine room stays at some equilibrium point (when the inflow of the cool air and the heat generated by the machine are balanced), and never reaches below the set point. This trick still leaves a long-term drift over a day (Fig. 3.12), likely due to the change in the building temperature.

Our experiments also require precise control of the ambient magnetic field B (after actively compensating the AC field noise [146]), due to the shift of Zeeman levels (fluctuation of 0.5 mG or less is desired). As discussed in Section 3.4.3, the B field can be monitored using the atoms themselves (B tagging). In Fig. 3.13, we show a measurement of the B field over 100 cycles ($\sim$ 1 hour), during which the moving average drifts $\sim$ 1 mG. If one post-selects real data using the B-field tagging method within a range 1.0 mG peak-to-peak, about 15 % of the data will have to be discarded.

3.6.3 Regulating the atom number and magnetic field

With our bot's ability to update the parameters in the middle of autonomous operation, we can demonstrate regulation of important experimental parameters, the atom number N and magnetic field B, to counteract the drifts. The atom number can be manipulated via the final depth of the ODT during the

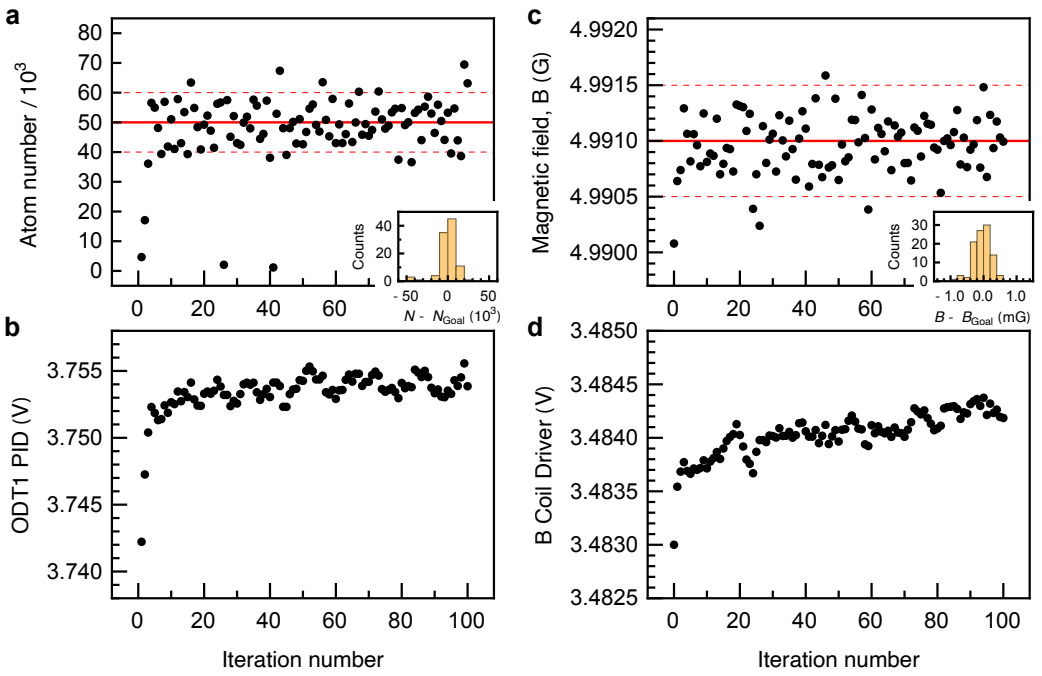

Figure 3.14: Regulation of the atom number and magnetic field with autonomous operation. **a,** Atom number, which is mostly within $\pm 10^4$ of the target value, $N_{\mathrm{goal}} = 50 \times 10^3$ (solid line). **b,** Input parameter $x^{(N)}$ controlling the final evaporation depth of the optical dipole trap. The algorithm uses a model $\Delta N = c^{(N)} \Delta x^{(N)}$ with $c^{(N)} = 3000/0.001$ V. **c,** Measured magnetic field B, which is mostly within ± 0.5 mG of the target value, $B_{\mathrm{goal}} = 4.991$ mG (solid line). The measurement was done using the tagging method. **d,** Input parameter $x^{(B)}$ controlling the bias coil current. The algorithm uses a model $\Delta B = c^{(B)} \Delta x^{(B)}$ with $c^{(B)} = 1.697$ mG/0.001 V. The insets show the histograms of the observed values.

evaporative cooling,[19] while the magnetic field can be controlled via the current through our bias coil. These values are controlled via our PID circuits taking inputs in the range $0 \sim 10$ V from our output cards. Denoting these inputs $x^{(N)}$ and $x^{(B)}$, the experimental parameters are modeled to be approximately proportional to the input values, $\Delta y^{(N)} = c^{(N)} \Delta x^{(N)}$ and $\Delta y^{(B)} = c^{(B)} \Delta x^{(B)}$, where $y^{(N)} \equiv N$ and $y^{(B)} \equiv B$. We use a simple algorithm to decide the input parameters for the $n+1$th iteration, based on the results of the previous n

[19] There are other options, like changing the MOT loading time.

iterations as

$$x_{n+1} = \sum_{j=1}^{n} w_j(x_j + \Delta x_j), \quad \Delta x_j = (y_{\text{goal}} - y_j)/c \tag{3.41}$$

with some weights w_j, where y_{goal} is a target value, and y_j is the observed value from the jth iteration. In Fig. 3.14, we find that the regulation works well for about an hour with a simple weight distribution $w_n = 4$, $w_{n-1} = 2$, $w_{n-2} = 1$, and $w_j = 0$ for all $j < n - 2$. Our algorithm finds the good input parameters within a few initial iterations, and is able to keep the experimental parameters near the target values. In particular, we see that the input for the bias coil current slowly changes over the course of this operation, indicating that the drift of the ambient magnetic field is compensated by the field from our bias coil.

3.6.4 Future improvements

We have shown that a simple bot can be implemented to automate the operation of our experimental apparatus. The bot can handle exceptional situations to enable uninterrupted operations, and a simple algorithm can be used to actively counter the drifts of various experimental parameters, improving the quality and also quantity of data by reducing the number of data points dropped by the post-selection. The algorithm part is implemented in a Mathematica notebook (see Appendix B), and more sophisticated algorithms can be easily implemented by users. For example, when there is a large parameter space to be explored, we might not know in advance which part of the space is worthwhile to scan. In such a case, one may define an objective function and implement a search algorithm that first explores a small region of the parameter space, and then decides which region to explore next based on, for example, the gradient-decent method.

Chapter 4

Super- and Subradiant Dynamics of Quantum Emitters Mediated by Atomic Matter Waves

This chapter is based on a substantially revised and extended version of the preprint, *Super-and subradiant dynamics of quantum emitters mediated by atomic matter waves*, arXiv:2311.09474 (2023) [55], with co-authors A. Lanuza and D. Schneble. The author of this dissertation gratefully acknowledge the contributions from the co-authors. Some texts on numerical methods have been moved to Chapter 2 and are explained in more details. The author, A. Lanuza, and D. Schneble conceived the experiments. The author took the measurements and analyzed the data. Numerical simulations and analytical descriptions were developed by the author and A. Lanuza, respectively. The results were discussed and interpreted by all co-authors. D. Schneble supervised the project. The manuscript was written by the author and D. Schneble with critical contributions from A. Lanuza.

4.1 Introduction

Dicke's theory of super- and subradiance [59], which describes how the spontaneous emission of photons can be enhanced or suppressed due to collective states of quantum emitters, introduced one of the earliest and central problems in quantum optics [100, 112, 156, 157]. In the standard description invoking the Born-Markov approximation [94, 100], the photonic degrees of freedom

are traced out, leaving only the system of quantum emitters with effective dissipative interactions between them. It is predicated on the assumption that the photons mediate such interactions instantaneously and that they are irreversibly lost to the vacuum. While this picture greatly reduces the complexity of problems and is broadly applicable in optical experiments with photons traveling through emitter ensembles within a fraction of the decay time [100, 158], it tends to obscure the role that the photons play as the mediators of interactions in collective dynamics. This aspect becomes especially important for ensembles of distant emitters, with separations on the order of the wavelength, a subject that has recently seen a surge of theoretical interest [25, 44, 50, 57, 159–163].

Photon-mediated interactions in free space are generally weak between distant emitters [106], and strong cooperative effects in extended ensembles can only be attained with special initial states or with a small number of available resonant modes per emitter [105]. While the spontaneous buildup of coherence across emitters leading to a burst of radiation [59, 112, 164] requires subwavelength separation [48], superradiant states in extended ensembles have been realized as so-called timed Dicke states [57], in which individual excitations are uniformly shared among emitters, and the phase lags of radiation from different emitter positions result in highly-directional emission due to constructive interference for a specific wavevector [165, 166]. Subradiant states, which are harder to access due to their decoupling from the environment, have only been indirectly observed in atomic clouds with high cooperativity [107, 167].

The free-space limitations can be overcome via coupling to guided modes that support long-range interactions [35, 36, 38, 39] in the paradigm of waveguide quantum electrodynamics [25, 26]. With emitters positioned at or in a one-dimensional waveguide, extended samples can undergo a buildup of coherence [53], and super- and subradiant states can exist even in a small number of distant emitters [31–34, 40]. In this setting, the dynamics of photons can play an important role, as propagation delays or trapping of radiation between cavity-like geometries of emitters in waveguides can exert coherent backaction, defying a Markovian picture [41, 42, 44, 45, 108–110]. Nonlinear dispersions near bandgaps can further modify the behavior of guided photons [26, 27, 160, 168, 169] by slowing down or binding them to form evanescent fields around emitters near photonic crystals [26, 35]. While modifications of decay dynamics due to these non-Markovian properties were observed for single emitters [80, 170], their effects on cooperative many-emitter dynamics remain largely unexplored.

In this paper, we investigate the role of radiation in the cooperative dynamics of an array of matter-wave emitters, using atoms in lieu of photons

to mediate interactions between them. Our emitters, which are coupled to a one-dimensional vacuum featuring a band edge [17, 20, 21, 87], are realized in a tunable optical lattice that allows us to initialize them in well-controlled many-body states, including single-excitation timed Dicke states in a superfluid, and incoherent, fully inverted states in a Mott phase. For systematic studies of collective radiative behavior, the vacuum coupling and excitation energy of the emitters can be independently controlled.

We demonstrate directional collective emission at variable normalized spacings d/λ_{dB} and phases ϕ between emitters, where λ_{dB} is the de Broglie wavelength of the emitted matter waves. Their slow propagation, on the time scale of the decay, makes it possible to observe radiative dynamics before the radiation spreads through the array [19], giving access to a nascent phase of super- and subradiance. Going beyond radiative retardation effects [44, 158], we uncover the role of collective emitter-photon bound states near the edge [27, 168, 169] and within [108–110] the continuum in a non-Markovian regime. While the limited coherence length of matter waves in our system prevents a direct observation of a superradiant burst from a Mott phase [17, 87], we probe the radiation-induced buildup of coherence [59, 112] across the array by accessing its phase distribution, which has not been achieved in other platforms. Finally, we explore a novel mechanism toward dissipative state engineering, in which a buildup of coherence is induced in a non-decaying atomic state acting as a spectator.

4.2 Experimental platform and scheme

Our experiments are performed with ultracold atoms in a state-selective optical lattice, as shown in Fig. 4.1a. We implement a Bose-Hubbard model of ^{87}Rb atoms in a hyperfine ground state $|r\rangle = |F = 1, m_F = -1\rangle$ ("red") in an optical lattice with variable depths s_z ($s_\perp$) in the longitudinal (transverse) directions, measured in units of the respective recoil energy $E_{\mathrm{r},i} = \hbar^2/2m\lambda_i^2$ where λ_z ($\lambda_\perp$) = 790 (1064)nm and m is the atomic mass. A near-resonant microwave field at 6.8 GHz couples the trapped $|r\rangle$ atoms to a second, hyperfine state $|b\rangle = |2, 0\rangle$ ("blue"), which is made insensitive to the z lattice by an appropriate choice of its wavelength and polarization, and is thus free to move longitudinally along tubes defined by $s_\perp$ (on time scales shorter than the residual confinement $2\pi\omega_z^{-1} \sim 10$ ms; Methods). The z lattice spacing $d = \lambda_z/2$ along the tube direction provides a natural length scale for our experiments, with a corresponding recoil momentum and recoil frequency, $k_{\mathrm{r}} = \pi/d$ and

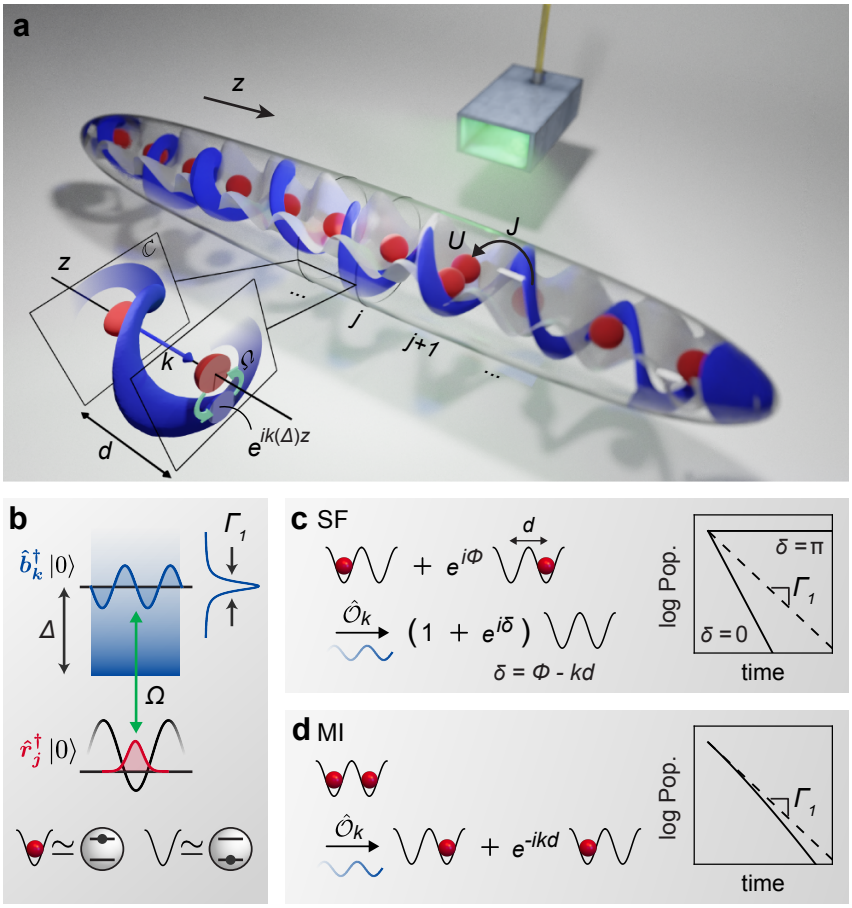

Figure 4.1: **Schematics of the experiments. a,** A state-selective optical lattice (along z, in gray) traps atoms in state $|r\rangle$ (red) and emits matter-wave radiation in state $|b\rangle$ (blue) upon application of microwave coupling (light green) between both states; atoms are transversely confined in lattice tubes of variable depth $s_\perp$, with only one shown. The initial $|r\rangle$ state is controlled via a Bose-Hubbard model with tunneling J and on-site interactions U, between superfluid (SF) and Mott insulating (MI). The example shows the complex amplitude of the radiation for directional emission in the SF regime with $\phi = -\pi/2$ at $\Delta = 2.25\omega_r$. [Figure credit: A. Lanuza] **b,** Each lattice site j acts as a matter-wave emitter, with excitation energy and vacuum coupling set by the microwave field (detuning Δ, coupling Ω). The excited emitter, $\hat{r}_j^\dagger|0\rangle$, is coupled to a continuum of momentum states, $\hat{b}_k^\dagger|0\rangle$, with a resonance of width Γ_1 centered around $\hbar k(\Delta)^2/2m = \Delta$. **c,d,** Illustrations of Markovian decay processes with a 2-emitter toy model. In the SF regime, the excitations occupy a phase coherent state ('timed Dicke state'), whose transition rate is determined by the initial array phase ϕ and the matter-wave phase lag $kd = 2\pi d/\lambda_{\mathrm{dB}}$. In the MI regime, each excitation is localized in a different emitter, and phase coherence builds up through the emission. A schematic of the Markovian decay prediction is shown in the two plots, with the dashed line denoting single-emitter decay.

$\omega_\mathsf{r} = \hbar k_\mathsf{r}^2/2m = 2\pi \times 3.7$ kHz.

Platform of matter-wave emitters. Applying the external microwave field converts each site j of the z lattice into a matter-wave emitter [20] described by the Hamiltonian, $\hat{H}_j = \hbar\Delta\hat{r}_j^\dagger\hat{r}_j + \sum_k \hbar\omega_k\hat{b}_k^\dagger\hat{b}_k + \sum_k(\hbar g_{k,j}\hat{b}_k^\dagger\hat{r}_j + \text{H.c.})$ of the Weisskopf-Wigner model in quantum optics [18, 87]. For each such matter-wave emitter, cf. Fig 1b, a de-excitation $\hat{r}_j$ (loss of an $|r\rangle$ atom from the site j) results in the emission of a matter wave (in $|b\rangle$) in a superposition of states $\hat{b}_k^\dagger|0\rangle$ with momentum k and frequency $\omega_k = \hbar k^2/2m$. The excitation energy of the emitter is defined by the detuning Δ of the microwave (Fig. 4.1b), and the effective vacuum coupling $g_{k,j} = \gamma_{k,j}\Omega/2$ is set by its strength Ω along with the state overlap $\gamma_{k,j} = \langle 0|\hat{b}_k\hat{r}_j^\dagger|0\rangle$. The Hamiltonian $\hat{H}_j$ thus provides a mechanism for spontaneous emission of matter waves [20] with de-Broglie wavelength $\lambda_\text{dB} = 2\pi/k$ around the resonant momenta $\pm k(\Delta) \coloneqq \pm k_\mathsf{r}\sqrt{\Delta/\omega_\mathsf{r}}$ with a decay rate $\Gamma_1 \sim \Omega^2/\sqrt{\Delta}$ in the Markovian limit $\Omega \ll \Delta$ [18, 20].

Preparation of initial states. The array of emitters spaced by d is described by the coupling Hamiltonian $\hat{H}' = \sum_{k,j}\hbar g_{k,j}\hat{b}_k^\dagger\hat{r}_j + \text{H.c.}$ in which the vacuum coupling $g_{k,j} = g_{k,0}e^{-ikdj}$ contains a position-dependent phase for the j-th emitter. We prepare collective initial states of the emitter array, such as collectively shared single excitations with variable phase between the emitters, or a fully inverted state (for $d = 0$ corresponding to the bottom and top rung of the Dicke ladder [59], respectively). In our system, these states appear and can be manipulated in the superfluid (SF) and Mott-insulating (MI) phases of the $|r\rangle$ atoms in the lattice [17, 87], as further explained below. We adiabatically realize these phases by controlling the ratio of the tunneling J between sites and the on-site interactions U during the state preparation (Methods). The tunneling $J \lesssim 2\pi \times 0.1$ kHz is negligible on the relevant time scale of our experiments, such that the picture of independent emitters only interacting via a common radiative environment is not compromised.

4.3 Directional collective emission

In the SF regime, each excitation of the emitter array (each $|r\rangle$ atom in the z lattice) is in a coherent superposition $\propto \sum_j \hat{r}_j^\dagger|0\rangle$ over the emitters (lattice sites j). This can be generalized to $\hat{r}_\phi^\dagger|0\rangle \propto \sum_j e^{i\phi j}\hat{r}_j^\dagger|0\rangle$ with a relative phase ϕ (or a Bloch quasimomentum ϕ/d), which behaves as a TDS [57] upon application of the vacumm coupling.

We prepare TDSs $\hat{r}_\phi^\dagger|0\rangle$ of variable ϕ by subjecting the $|r\rangle$ atoms in the

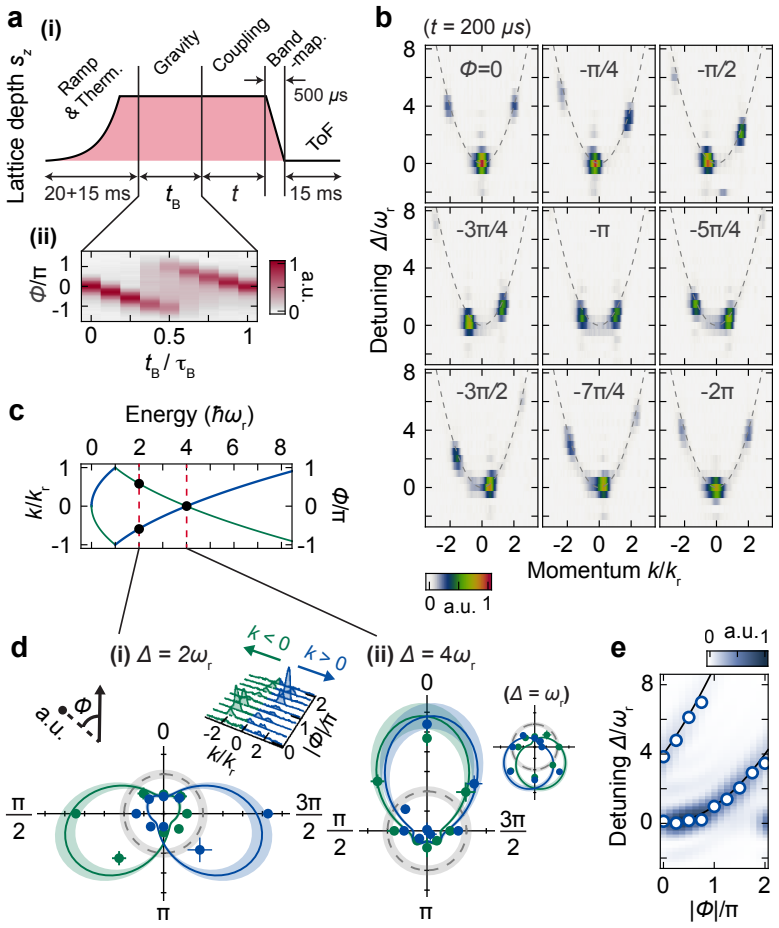

Figure 4.2: **Phase control of emission characteristics in the SF regime**. **a.** (i) Experimental sequence. After ramping up the optical lattice $(s_z, s_\perp) = (8, 0)$, a differential phase ϕ between emitters (lattice sites) is gravitationally imprinted for a duration t_B (in units of the Bloch period $\tau_B = 2\pi\hbar/(mgd) = 1.2$ ms). Subsequently a 200-μs-long coupling pulse with strength $\Omega/\omega_\mathrm{r} = 0.60(4)$ is applied to initiate the emission. (ii) Phase distribution in the array population ($|r\rangle$, obtained via lattice band-mapping) as a function of t_B. **b.** Momentum distributions of emitted matter waves ($|b\rangle$) versus Δ, plotted for various ϕ, each panel is normalized independently. The dashed lines are the dispersion $\omega_k = \omega_\mathrm{r}(k/k_\mathrm{r})^2$ of the matter waves. **c.** Matter-wave dispersion in the reduced zone scheme (blue and green lines for $k > 0$ and $k < 0$). **d.** Emitted population ($|b\rangle$) as a function of ϕ for (i) $\Delta = 2\omega_\mathrm{r}$ and (ii) $\Delta = 4\omega_\mathrm{r}$ (blue and green points for $k > 0$ and $k < 0$). The emission can be (i) directional (e.g. $\phi = -\pi/2$, the case also represented in Fig. 4.1a) or (ii) symmetric (e.g. $\phi = 0$). The solid lines represent finite-size simulations with 4 emitters, and the dashed line is the Markovian single-emitter prediction (shaded areas represent the uncertainty in Ω). The middle inset shows a 3D density plot of the momentum distributions for $\Delta = 2\omega_\mathrm{r}$. **e.** Simulated emitted population for $k < 0$ as a function of Δ and ϕ, overlaid with the fitted centers of the experimental emission peaks (circles); the black lines are the free dispersion. All data are averages of at least 3 measurements; the error bars show the standard error of the mean.

lattice to a potential gradient. For this purpose, we temporarily switch off the confining optical trap for a variable duration to induce a Bloch oscillation driven by gravity. After preparation of the TDS, we apply the microwave coupling for a fixed time and then record the momentum distribution of the emitted matter waves, as a function of the excitation energy $\hbar\Delta$ (or equivalently of the effective array spacing $d/\lambda_{\mathrm{dB}}(\Delta)$, varied up to $\sqrt{2}$). Data for emission from the TDSs are shown in Fig. 4.2b. In stark contrast to emission from a single emitter, in which the entire parabolic dispersion relation is visible and there is no energetic selectivity [20], the momentum distributions are strongly peaked, depending on the value of the relative phase ϕ.

Under the Markovian approximation, the collective effects on the spontaneous emission are fixed by the transition matrix element $\langle\hat{\mathcal{O}}_k^\dagger\hat{\mathcal{O}}_k\rangle$ at $k = \pm k(\Delta)$ (Methods), where the collective operator $\hat{\mathcal{O}}_k = \sum_j e^{-ikdj}\hat{r}_j$ [48, 100] acts on the initial state $\hat{r}_\phi^\dagger|0\rangle$ as depicted in Fig. 4.1c. This matrix element involves a coherent sum over amplitudes with a phase factor $\exp[i(\phi\mp k(\Delta)d)j]$ on each emitter j, and thus the matter waves can interfere constructively (or destructively) when $\phi \mp k(\Delta)d = 2\pi n$ with an integer n (or a half-integer). When this condition is met, the decay rate per excitation is expected to be proportional to the number of coherently contributing emitters; in our system, this number is effectively controlled by the superfluid coherence length of the $|r\rangle$ atoms in the lattice (Fig. 4.8 and Methods).

The phases ϕ giving constructive interference at a given Δ, cf. Fig. 4.2d, can be obtained by plotting the free dispersion of matter waves ω_k in a reduced zone scheme as in Fig. 4.2c. The emission can be strongly enhanced or suppressed (such as for $\phi = 0$ or $-\pi$ at $\Delta = 4\omega_{\mathsf{r}}$, cf. Fig. 4.2d (ii)), or be enhanced in one direction and suppressed in the other [57] (such as for $\phi = -\pi/2$ at $\Delta = 2.25\omega_{\mathsf{r}}$, cf. Fig. 4.2d (i)). For a choice of $\phi = 0$, the smallest non-zero excitation energies at which the spontaneously emitted matter waves can interfere constructively (destructively) are $\hbar\Delta = 4\hbar\omega_{\mathsf{r}}$ ($\hbar\omega_{\mathsf{r}}$), corresponding to $\lambda_{\mathrm{dB}}(\Delta) = d$ ($2d$), which is the situation that we consider in the following.

4.4 Collective dynamics

We probe super- and subradiant TDS dynamics at $\phi = 0$ for moderately weak couplings $(\Omega/\Delta)^2 \ll 1$. Fig. 4.3a shows the corresponding time evolutions, with Ω adjusted to give the same single-emitter decay rate $\Gamma_1 = 2\pi \times 0.24$ kHz (Methods). For $\Delta = 4\omega_{\mathsf{r}}$ we observe a clear enhancement of the decay rate over Γ_1, which however does not appear immediately. The idea of strict Markovianity, which assumes that the radiation instantaneously establishes

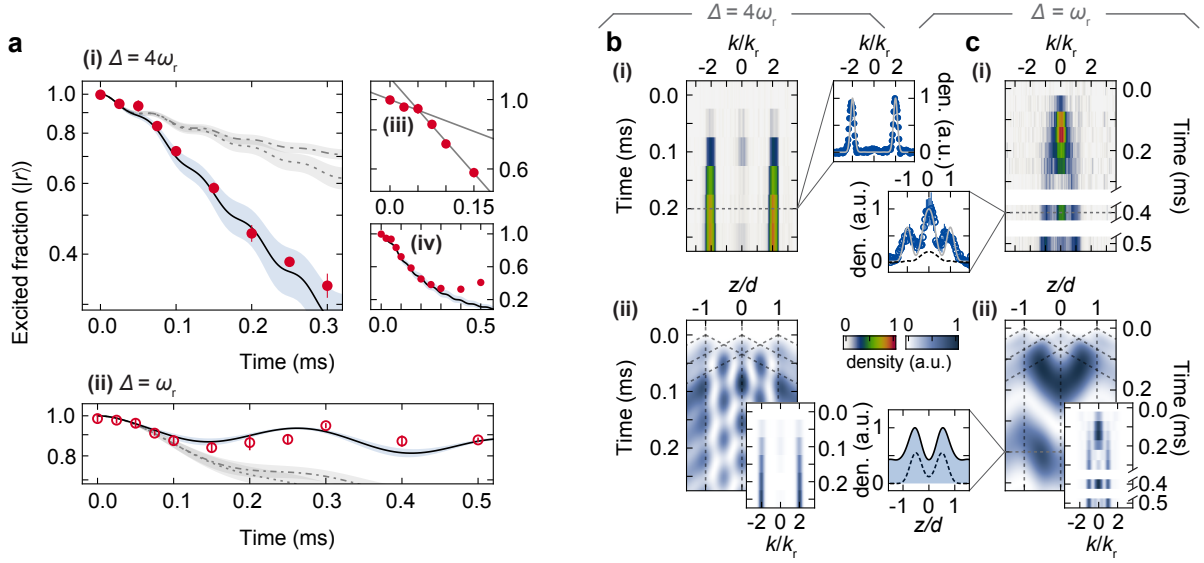

Figure 4.3: **Super- and subradiant dynamics in the SF regime.** **a**, Excited fraction as a function of time for $(s_z, s_\perp) = (8, 10)$, $\phi = 0$ at super- and subradiant excitation energies (i) $\Delta = 4\omega_r$ and (ii) $\Delta = \omega_r$ (red points and circles) with coupling strength adjusted to $\Omega/\omega_r = 1.00(7)$ and $\Omega/\omega_r = 0.42(3)$, respectively. The black solid lines are our simulations of a single excitation coherently spread over an array of three emitters (as opposed to an excitation localized in the middle emitter [20], dot-dashed lines; or for an isolated emitter, dotted line); shaded areas represent the uncertainty in Ω. Also shown are excited fractions at (iii) early times and (iv) late times for $\Delta = 4\omega_r$. The gray solid lines in (iii) are a piecewise linear fit, yielding the decay rates $\Gamma_{t<t_c}/\Gamma_1 = 1.1(2)$ and $\Gamma_{t>t_c}/\Gamma_1 = 3.2(2)$ with $t_c = 52(1)$ μs. **b**, (i) Momentum distribution of matter waves versus time for $\Delta = 4\omega_r$. The lineout plot shows the data at 0.2 ms (blue points) along with our simulation (gray solid line). (ii) Simulated position and momentum distributions of matter waves versus time. The dashed diagonal and vertical lines are the 'light-cones' $z(t) = dj \pm v_g t$ and the positions of the emitters. **c**, Same as **b**, but for $\Delta = \omega_r$. The lineouts are shown at 0.4 ms (with data in circles and simulations in solid lines); also shown are the BIC contributions from our analytic theory as black dashed lines. All data are averages of at least 3 measurements; the error bars show the standard error of the mean.

the dissipative interactions between emitters, would require the coherence length of the radiation to exceed the spatial extent of coherence in the emitter array [44, 158], where the latter in our system is determined by the superfluid coherence length ξ [171]. With an enhanced Markovian decay rate Γ_ξ, this translates to $v_g/\Gamma_\xi \gg \xi$, a condition that for our small group velocities $v_g = \hbar|k(\Delta)|/m \sim 1\mu$m/ms is not strictly fulfilled. It is thus necessary to consider the full non-Markovian dynamics, for which collective effects are expected to set in only once the emitted radiation reaches a neighboring emitter [44]. From a piecewise exponential fit, we find that the decay rate changes from $1.1(2) \times \Gamma_1$ (indeed close to the single-emitter rate) to an enhanced rate $3.2(2) \times \Gamma_1$ after a time comparable to the propagation time $d/v_g = 34$ μs (Fig. 4.3a (iii)); this double-exponential behavior is consistent with the predictions of a finite-size simulation and an exact non-Markovian analysis with an effective number of emitters (3) as the only fitting parameter (Methods). The fact that the effective array size is small compared to the size of our superfluid is consistent with phase fluctuations induced by collisional interactions in the confining optical lattice [171]. At late times we observe partial reabsorption (Fig. 4.3a (iv)), likely due to coupling to empty emitters beyond ξ [19].

The momentum space distribution of the emitted radiation, shown in Fig. 4.3b (i), provides a complementary picture of the dynamics. While the emission is peaked at $k = \pm 2k_\mathsf{r}$, there is a small off-resonant contribution at zero momentum due to coupling to the continuum edge, which causes residual non-Markovian oscillations in the time evolution [19]. The quantitative consistency of our model with the data motivates us to extrapolate to position space, cf. Fig. 4.3b (ii). We see that the time scale for the observed onset of superradiance is consistent with the overlap of 'light-cones' of matter waves emanating from neighboring emitters [44], which subsequently form standing waves.

For $\Delta = \omega_\mathsf{r}$, the TDS exhibits subradiant decay of the excited population (Fig. 4.3a (ii)) that deviates from single-emitter behavior after the propagation time $d/v_g = 68$ μs. The momentum-space distribution, cf. Fig. 4.3c (i), is dominated by an oscillation at zero momentum and smaller contributions at $\pm k_\mathsf{r}$. Translated to position space, the population is mostly concentrated between the emitters, a behavior reminiscent of a bound state in the continuum (BIC) [109, 110] as a polaritonic state [19, 56] with radiation partially trapped in the cavity-like geometry formed by the emitters [110]. A detailed analysis reveals that the non-Markovian dynamics has a residual superradiant component but is dominated by a persistent beating between a BIC with energy $1.02\hbar\omega_\mathsf{r}$ and a bound state slightly below the continuum edge, with the population average approaching ≈ 0.83 at long times (Methods).

Close to the continuum edge $\Delta \sim 0$, the radiative dynamics generally

becomes strongly coupled. In this regime, array effects have been found to enhance non-Markovian oscillations of a single excited emitter surrounded by empty neighbors [20, 21]. For an initial TDS at $\Delta = 0$, we observe an amplification of such array effects with an almost full amplitude and weak damping (Fig. 4.9). The observed TDS dynamics converges toward a beat between polaritonic bands [19, 172] in the limit of diverging coherence length.

4.5 Spontaneous coherence formation

In the previous sections we studied how a fixed relative phase between matter-wave emitters induces collective spontaneous decay; we now explore the reciprocal phenomenon of how collective decay can modify a broad distribution of relative phases between emitters by inducing coherence. In the MI regime, the initial state $\sim \prod_j \hat{r}_j^\dagger |0\rangle$ is expected to cascade down superradiantly via the spontaneous development of coherence [52, 87]. The first step of this process is illustrated in Fig. 4.4d(i) for a two-emitter model. Spontaneous emission of a matter wave around momenta $\pm k(\Delta)$ projects the initial state $\hat{r}_0^\dagger \hat{r}_1^\dagger |0\rangle$ into $\frac{1}{\sqrt{2}}(\hat{r}_1^\dagger + e^{\mp ik(\Delta)d}\hat{r}_0^\dagger)|0\rangle$. In the phase distribution of an emitter array, this produces a modification $\sim |\sum_j e^{i(\phi \mp k(\Delta)d)j}|^2$ (Methods), which again is centered at $\phi \equiv \pm k(\Delta)d \pmod{2\pi}$.

In the experiment, we set the emitters' excitation energy to $\Delta = 4\omega_\mathsf{r}$ and ω_r as before, again with Ω adjusted to give the same Markovian decay rate $\Gamma_1 = 2\pi \times 0.31$ kHz. As shown in Fig. 4.4a, and in contrast to the behavior of a TDS discussed in the previous sections, we find that the decay for both values of Δ follows that of an isolated emitter beyond the propagation time (34 and 68 μs, respectively). We also find a small excess near $\phi = 0$ in the shape of the phase distributions of the emitters when comparing $\Delta = 4\omega_\mathsf{r}$ to $\Delta = \omega_\mathsf{r}$ (see Fig. 4.4a insets).

To verify that this effect is indeed caused by the expected coherence formation (rather than reabsorption or ϕ-dependent losses; Methods), we consider a second, modified scenario. This time, we prepare every quantum emitter in a superposition $(|r\rangle + |g\rangle)/\sqrt{2}$ of the $|r\rangle$ state and a second state $|g\rangle$ ("green", $|g\rangle = |F = 2, m = 1\rangle$) that experiences the same confinement and on-site interactions as $|r\rangle$ but is decoupled from the matter-wave continuum. As illustrated in Fig. 4.4d(ii), the decay of the $|r\rangle$ state is now expected to imprint a phase onto the $|g\rangle$ state. Indeed, after turning on the vacuum coupling with the same parameters as before, we observe similar modifications to the phase distribution of the emitter array, this time for the decoupled $|g\rangle$ state. Because this state does not decay, it is possible to directly extract changes in the distribu-

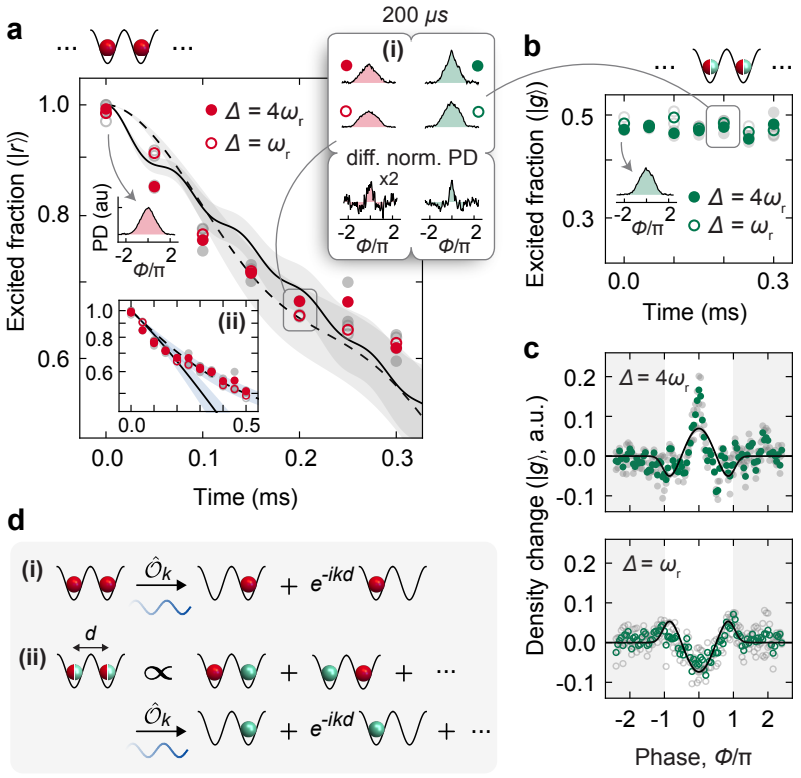

Figure 4.4: **Spontaneous coherence formation in the MI regime. a,** Decay dynamics for $(s_z, s_\perp) = (15, 40)$ at $\Delta = 4\omega_r$ and $\Delta = \omega_r$ (red points and circles) with coupling strengths adjusted to $\Omega/\omega_r = 1.00(7)$ and $\Omega/\omega_r = 0.50(4)$, respectively. The solid and dashed lines simulate an isolated emitter for corresponding parameters. Insets: (i) Phase distributions (PD) of the excited emitters ($|r\rangle$ atoms) at $t = 200$ μs, along with their difference after normalization. (ii) Decay dynamics including late times. The solid and dashed lines are our two-emitter model with and without an additional empty emitter. **b,** Time evolution of the decoupled $|g\rangle$ (green) population when starting in a superposition state $(|r\rangle + |g\rangle)/\sqrt{2}$, with all parameters as in **a**. **c,** Change of the normalized PD of the $|g\rangle$ state after 200 μs. The solid lines are computed using our two-emitter model. **d,** Mechanism for coherence formation in the two-emitter model. (i) Starting with the $|r\rangle$ state in each emitter, emitting into a shared mode k generates a relative phase factor e^{-ikd} (cf. Fig. 4.1c). (ii) Starting with a superposition of $|r\rangle$ and $|g\rangle$ in each emitter, the $|g\rangle$ population acquires coherence as the $|r\rangle$ population decays. The shaded areas around the curves in **a** and **c** indicate the uncertainty in Ω. All data are averages of two measurements; raw data are shown in gray circles and points.

tion of phases for a given excitation energy. For the two different excitation energies, we observe excess population at the expected phases, cf. Fig 4.4c, i.e. around $\phi = \pm\pi$ for $\Delta = \omega_r$ (with $k(\Delta)d = \pi$) and around $\phi = 0$ for $\Delta = 4\omega_r$ (with $k(\Delta)d = 2\pi$). The magnitude and functional dependence of the differential features on ϕ are close to the predictions of our simple model. We note that resonant collisional momentum exchange between $|g\rangle$ and the emitted $|b\rangle$ atoms is strongly suppressed for the chosen lattice parameters [171] and thus does not contribute to the observed effect.

In a superradiant cascade, the decay accelerates with time as the coherence builds up. However for the chosen lattice parameters, the coherence length of matter waves, which mediate such a coherence buildup, is limited to $\sim d$ [171] due to the strong transverse confinement in the tubes, so that we expect only small enhancements of the decay rate of order unity. In the experiment, we do not observe any enhancement but instead the decay soon slows down to rates below the single-emitter value (cf. Fig. 4.4a (ii)). As already discussed for the TDS, this slowdown effect is likely due to reabsorption of radiation by "empty" emitters [19, 20] outside the coherence length. In our simple model, such reabsorption processes can be included by adding an empty site; solving the time dynamics qualitatively reproduces the observed behavior.

Remarkably, for uncorrelated excitations (thermal $|r\rangle$ atoms), we observe losses rather than gains at the relevant phases (Fig. 4.10 and Methods). Such an ensemble can be viewed as a statistical mixture of timed Dicke states, of which a subset is lost through superradiant decay. This contrasting behavior highlights the idea that the coherence formation in the MI phase, as the precursor of a superradiant burst [59], is fundamentally a quantum many-body effect.

4.6 Conclusion

In this work, we have realized an array of quantum emitters interacting via atomic matter-wave radiation, which we found to play an integral role in determining collective sub- and superradiant emitter dynamics. The radiative retardation, responsible for some of the novel effects reported here, depends on the effective separation $\eta = d/(v_g/\Gamma_1)$ [44] and may be made stronger by exploiting the scaling behaviors $v_g \propto \sqrt{\Delta}$ and $\Gamma_1 \propto \Omega^2/\sqrt{\Delta}$ in sufficiently deep lattices while maintaining weak coupling $(\Omega/\Delta)^2 \ll 1$. Several exotic phenomena, attributed to time-delayed quantum feedback, have been predicted beyond the regime $\eta \sim 0.1$ of this work, including enhancement or suppression exceeding standard Dicke super- and subradiance [43, 44], Fano-like resonances

in the radiation spectrum [45], and entanglement generation processes that are of interest for quantum networks [41, 42]. Extensions to higher-dimensional geometries or more complex vacuum structures [19, 21] may give access to collective anisotropic emission [160] subradiant self-guided modes [161, 162]. Finally, our platform offers several unique opportunities at the intersection of quantum optics and condensed matter physics. Auxiliary atomic states, for example, may create novel possibilities for the dissipative engineering of quantum states [96], while adding on-site optical disorder can allow access to localized phases [173] and their interplay with subradiant dynamics. By making the transverse confinement of the tubes state-dependent, the coherence length of the emitted matter waves can be independently controlled in the MI regime. For weak confinement, this should give access to a larger part of the superradiant cascade [50, 87]. In strongly confining tubes, it should be possible to study the effects of fermionization of the radiation field, pointing towards fermionic quantum optics with matter waves [54].

4.7 Methods

4.7.1 System preparation

Each measurement begins with a Bose-Einstein condensate of around 2×10^4 ^{87}Rb atoms in the $S_{1/2}$ hyperfine state $|r\rangle \equiv |F = 1, m_F = -1\rangle$ (the "red" state) that is initially prepared in a nearly isotropic crossed optical-dipole trap (XODT) made of horizontal beams at a wavelength $\lambda_\perp = 1064$ nm. The transverse lattices of variable depth $s_\perp$ are implemented by partially retro-reflecting the XODT beams. The combined potential results in the residual harmonic confinement in the vertical z direction with the trap frequency $\omega_z \in 2\pi \times [73, 90]$ Hz for the range $s_\perp \in [0, 60]$. The state-selective z lattice of depth s_z is made of σ^--polarized vertical beams at a wavelength $\lambda_z = 790.0$ nm, which is tuned-out for the second hyperfine state $|b\rangle \equiv |F = 2, m_F = 0\rangle$ (the "blue" state) [20]. All the measurements are conducted in a constant bias field of $B_z = 5$ G in the z direction to provide the quantization axis and the Zeeman splitting.

The initial states of the $|r\rangle$ atoms in the optical lattices are prepared with an adiabatic exponential ramp of $s_\perp$ and s_z over ~ 200 ms, and their many-body phases are determined by the tunneling rate J (along z) and on-site interactions U. From our measurements of momentum peak width versus $s_\perp$ at a fixed $s_z = 15$, we estimate that the superfluid to Mott insulator transition occurs around $s_\perp = 12$, at which the ratio U/J is ~ 40 (cf. [5]). For the final

depths $(s_z, s_\perp) = (8, 10)$ and $(s_z, s_\perp) = (15, 40)$ used to prepare a superfluid and a Mott insulator, our calculations yield $U/J = 6.5$ and $U/J = 84.5$, respectively. For these calculations, we use the band structures $\varepsilon_q(s_z)$ to obtain the (nearest-neighbor) tunneling rate along z, $J = -1/(2k_\mathrm{r}) \int_{-k_\mathrm{r}}^{k_\mathrm{r}} dq e^{iqd} \varepsilon_q$, while Gaussian approximations of the Wannier functions $w(\boldsymbol{r})$ are used to compute the on-site interactions, $U = (4\pi\hbar^2 a/m) \int d\boldsymbol{r} |w(\boldsymbol{r})|^4$, where $a \approx 100 a_0$ is the scattering length in terms of the Bohr radius a_0. For the preparation of superfluids with a nonzero phase ($q \neq 0$) in Fig. 4.2, we momentarily turn off the XODT for a duration t_B, which induces a Bloch oscillation with period $\tau_B = 2\pi\hbar/(mgd) = 1.2$ ms due to gravity.

An externally applied microwave field of 6.8 GHz provides the coupling between the $|r\rangle$ atoms in the z lattice and the $|b\rangle$ atoms in one-dimensional free space. The coupling strength Ω is pre-calibrated via Rabi oscillation measurements; we use the peak-to-peak fluctuation of 7 % independently estimated from Rabi spectra taken over one month for the quoted uncertainty. The excitation energy of quantum emitters is given by the detuning $\Delta = \omega_\mu - \omega_\mathrm{res}$ of the microwave field from the resonance frequency $\omega_\mathrm{res} = \omega_{br} - \omega_0$ that includes the bare resonance $\omega_{br} (> 0)$ between the two hyperfine states, $|b\rangle$ and $|r\rangle$, and the zero-point energy ω_0 of the $|r\rangle$ state in the z lattice. We calibrate ω_res between each set of measurements (with the data for each figure divided into several such sets) via lattice transfer spectroscopy starting from a condensate in the $|b\rangle$ state [20]. For each figure, the measured values of ω_res fluctuated by 0.3 kHz r.m.s. (root mean squared), which is the dominant uncertainty in Δ.

In Fig. 4.4, for the purpose of characterizing the coherence formation, we introduce another hyperfine ground state $|g\rangle = |2, 1\rangle$ (the "green" state) without resonant coupling to the matter waves. This state experiences the same lattice potential as the $|r\rangle = |1, -1\rangle$ state, as its Landé factor g_F only differs by a sign [116]. To generate the local superposition of the $|g\rangle = |2, 1\rangle$ and $|r\rangle = |1, -1\rangle$ states, we prepare a Mott insulator of $|r\rangle$ atoms and apply a 1.3-ms-long two-photon $\pi/2$ Rabi pulse made of a 6.8-GHz microwave field and a 3.3-MHz radio-frequency field to create an equal superposition of the two states in each site, $\propto \prod_j (\hat{r}_j^\dagger + \hat{g}_j^\dagger) |0\rangle$.

4.7.2 Imaging and post-processing

The detection sequence starts with a 500-μs-long bandmapping step [21], during which all lattices are ramped down to convert the quasimomenta $q = \phi/d$ into momenta. The XODT is then completely turned off to let the atoms expand freely in time of flight (ToF) lasting 12 ms (15 ms) for the $|F = 2\rangle$ ($|F = 1\rangle$) state. During ToF, a magnetic field gradient is briefly applied to

spatially separate the atoms in different Zeeman sublevels (Stern-Gerlach separation). For absorption imaging, light on the D_2 cycling transition $F = 2 \rightarrow F' = 3$ is first applied for 200 μs to detect the $|F = 2\rangle$ atoms, and after an additional ToF of 2.7 ms, repump light on the D_2 transition $F = 1 \rightarrow F' = 2$ for 100 μs and a second 200-μs-long imaging pulse are applied to detect the $|F = 1\rangle$ atoms. Additional empty pictures without atoms are collected to eliminate fringes in the images via principal component analysis. During ToF expansion, the $|1, -1\rangle$ atoms are partially redistributed to the $|2, 1\rangle$ and $|2, 2\rangle$ states with Rabi pulses to infer the magnetic field *in situ* [146]. These separate images of $|r\rangle$ atoms transferred to different Zeeman states are later recombined to recover the original distributions of $|r\rangle$ atoms, which involves interpolating each image and rescaling the coordinates to compensate for different ToF times.

Various considerations are taken into account in analyzing the images. Due to residual heating during the ramping of lattices, a small fraction of $|r\rangle$ atoms are excited to higher bands that are decoupled from the matter waves. When counting the excited population, we only include the atoms in the ground band, $q \in [-k_\mathrm{r}, k_\mathrm{r}]$ (with an additional tolerance of $\sigma_k \approx 0.15 k_\mathrm{r}$ accounting for the measurement resolution). In Fig. 4.4a, the fraction of $|r\rangle$ atoms outside the first Brillouin zone is on average 13% at early times $t \leq 0.05$ ms but increases to 17% at later times $t \geq 0.2$ ms, effectively broadening the quasimomentum (or phase) distribution over the decay time. To accurately determine the populations in each state in Fig. 4.3 and 4.4, we subtract small background contributions contained in the $t = 0$ images and additional empty images. The momentum coordinates in the images are calibrated via Kapitza-Dirac diffraction of the $|1, -1\rangle$ and $|2, 1\rangle$ atoms [149]. During the $t_\mathrm{bm} = 500$ μs of bandmapping, the atoms are already moving, which contributes to the final distances traveled. For the $|b\rangle$ atoms, this time is added to the effective ToF time for the calibration. For the $|g\rangle$ and $|r\rangle$ atoms, the group velocity changes during the ramp down of the z lattice. We estimate an effective correction to the TOF time by $1/(2k_\mathrm{r}) \int_{-k_\mathrm{r}}^{k_\mathrm{r}} dq \int_0^{t_\mathrm{bm}} dt v_g(t)/v_g(t_\mathrm{bm})$, where the instantaneous group velocity $v_g(t) = |d\omega_q/dq|$ depends on the value of s_z at each time, yielding $0.3 t_\mathrm{bm}$ ($0.5 t_\mathrm{bm}$) for $s_z = 15$ ($s_z = 8$).

4.7.3 Decay rates

Fermi's golden rule. The emission peaks in Fig. 4.2b is consistent with the modulation of the decay rate obtained from Fermi's golden rule. The details

of the derivation is found in Section 2.3.2, whose result is

$$\Gamma_{\phi,M} = (2\pi/\hbar N) \sum_{k=k_+,k_-} |\langle f_{\phi,k}| \hat{H}' |i_\phi\rangle|^2 \rho_{\mathrm{dB}}(\hbar\Delta) \times \frac{1}{2} \tag{4.1}$$

$$= M\Gamma_1 \frac{1}{2} \sum_{k=k_+,k_-} \left| \frac{1}{M} \sum_{j=\lfloor 1-M/2 \rfloor}^{\lfloor M/2 \rfloor} e^{i(\phi - kd)j} \right|^2 .$$

Determination of the single-emitter decay rate. We extract the single-emitter decay rate from the experimental data using two different methods, and compare them to the prediction of our model.

(a) The initial decay up to the propagation delay time is expected to follow that of a single emitter. We fit the time evolution of the population in the SF regime to a double exponential (double linear on the log scale, cf. Fig. 4.2a (iii)), which yields the decay rates $\Gamma_{t<t_c} = 2\pi \times 0.25(6)$ kHz and $\Gamma_{t>t_c} = 2\pi \times 0.74(5)$ kHz before and after the critical time $t_c = 52(1)$ μs. The value for $\Gamma_{t<t_c}$ is consistent with the prediction $\Gamma_1 = 2\pi \times 0.24$ kHz for Markovian single-emitter decay obtained from Fermi's Golden rule (FGR, Eq. (4.1)) for the chosen parameters, $s_z = 8$, $\Delta = 4\omega_\mathsf{r}$ and $\Omega = \omega_\mathsf{r}$.

(b) A fully inverted state decays at the single-emitter rate when normalized by the number of excitations, before it evolves into superradiant states going down the Dicke ladder. The decay in the MI regime in Fig. 4a, which realizes such an inverted state of emitters, shows very good agreement with the single-emitter simulations, well beyond the propagation time $d/v_g \sim 34$ μs (68 μs) for excitation energy $\hbar\Delta = 4\hbar\omega_\mathsf{r}$ ($\hbar\omega_\mathsf{r}$). Two sets of coupling parameters $(\Delta,\Omega)_\mathrm{I} = (4,1)\omega_\mathsf{r}$ and $(\Delta,\Omega)_\mathrm{II} = (1,0.5)\omega_\mathsf{r}$ were chosen to yield similar Γ_1 according to the FGR. From an exponential fit to the combined decay data of Fig. 4a up to 200 μs (before reabsorption kicks in), we find $\Gamma_{1,\mathrm{Exp}} = 2\pi \times 0.36(1)$ kHz, which is comparable to the value extracted from a corresponding fit of the single-emitter simulations, $\Gamma_{1,\mathrm{Sim}} = 2\pi \times 0.33$ kHz. Both of these values are close to the FGR value $\Gamma_1 = 2\pi \times 0.31$ kHz, with some deviations due to residual non-Markovianities.

4.7.4 Numerical simulation of decay dynamics

Dynamics in the SF regime. As described in the main text, we use a single excitation in a finite-size array model to describe the radiative dynamics at early times in the superfluid regime. For details about the simulation, see Section 2.2.5. Starting from an initial timed Dicke state (TDS) coher-

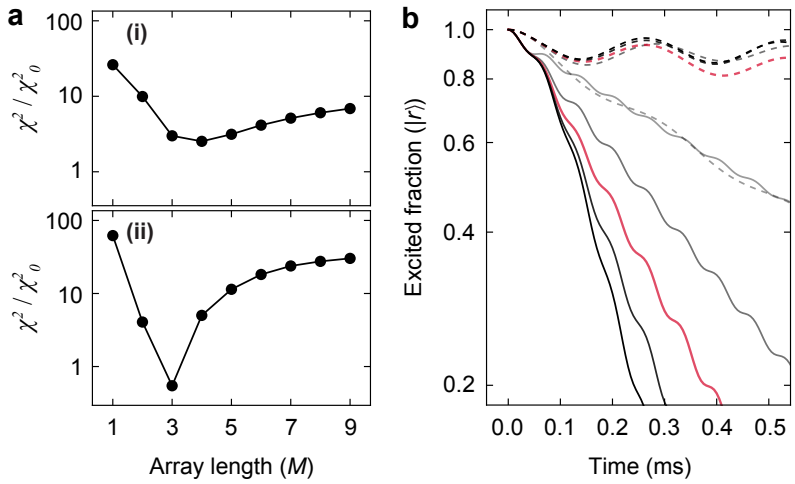

Figure 4.5: **Numerical simulations of an M-emitter array containing a single excitation. a,** χ^2 vs. M evaluated with respect to the data shown in Fig. 4.2d and Fig. 4.3a. In (i), the data at the phases $\phi \in (0, 2\pi]$ and the coupling parameters $\Delta/\omega_\mathrm{r} \in \{2, 4\}$ are used (with $\Omega/\omega_\mathrm{r} = 0.6$ and $t = 200$ μs). In (ii), the data at the coupling times $t \in [0, 0.25]$ ms for $(\Delta, \Omega)/\omega_\mathrm{r} = (4, 1)$ and at $t \in [0, 0.5]$ ms for $(\Delta, \Omega)/\omega_\mathrm{r} = (1, 0.42)$ are used. The normalization χ_0^2 is the value at which the cumulative χ^2 distribution reaches 95%. The lines are guides to the eyes. **b,** Simulated population versus time for $(\Delta, \Omega)/\omega_\mathrm{r} = (4, 1)$ and $(1, 0.42)$ (with $s_z = 8$, $\phi = 0$) shown as solid and dashed lines, with M varying from one to five (lightest to darkest colors; red for $M = 3$, the case also shown in Fig. 4.3a).

ently populating an array of M emitters with phase ϕ, the excitation and matter-wave amplitudes can be obtained as a function of time as $|\Psi(t)\rangle = \sum_j A_j(t)\hat{r}_j^\dagger |0\rangle + \sum_m B_{k_m}(t)\hat{b}_{k_m}^\dagger |0\rangle$. We use M as the only free parameter of the model reflecting the initial coherence length of the system, and determine M from the best fit to the data. The χ^2 values of the models with different M are obtained by computing the differences between the observed (P_i) and calculated ($\tilde{P}_i$) excited fractions, i.e. $\chi^2 = \sum_i (P_i - \tilde{P}_i)^2/\sigma_i^2$, where σ_i is the experimental uncertainty (see Fig. 4.5a). The analysis yields the best-fit values of $M = 4$ and 3 for data in Fig. 4.2d and 4.3a, respectively. We use the amplitudes B_{k_m} to generate the momentum distributions in Fig. 4.2e and Fig. 4.3b and c ($B_z = \sum_{k_m} L^{-1/2} e^{ik_m z} B_{k_m}$ for position space), with a Gaussian convolution of width $0.15k_\mathrm{r}$ to reflect the measurement resolution [21].

Dynamics in the MI regime. To simulate the decay dynamics in the Mott-insulating regime in Fig. 4.4, in which many-body effects are important,

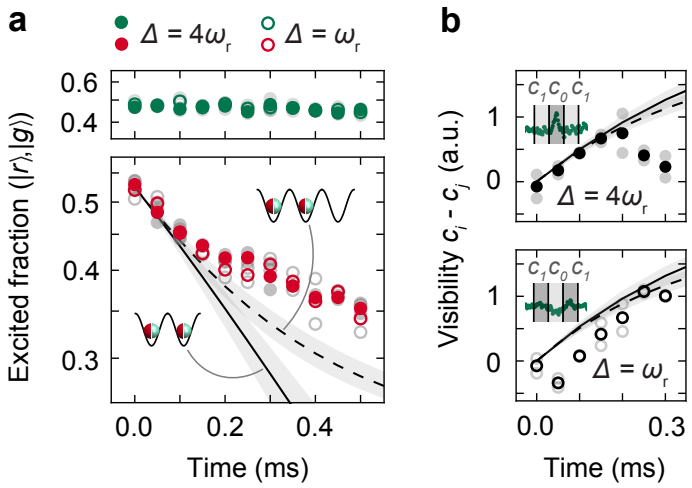

Figure 4.6: **Supplementary data and simulation for Fig. 4.4. a,** Time evolution of the array populations $(|r\rangle, |g\rangle)$ initially prepared in a superposition $(|r\rangle + |g\rangle)/\sqrt{2}$ corresponding to the measurements shown in Fig. 4.4b and c. The solid and dashed lines are our two-emitter model without and with an additional empty emitter (scaled by 1.05). **b,** Time evolution of the visibility defined as $c_0 - c_1$ $(c_1 - c_0)$ for $\Delta = 4\omega_r(\omega_r)$, where c_0 and c_1 are the integration of the change of the phase distributions (PD) over $|q| \in [0, 0.5k_r]$ and $|q| \in (0.5k_r, 1.5k_r]$ (cf. Fig. 4.4c). The solid and dashed lines are calculated from our model as in **a**.

we use a master equation for the reduced density matrix [94], $\bar{\rho} = \mathrm{Tr}_b \rho$, where the partial tracing is over the matter-wave modes, $\hat{b}_k^\dagger |0\rangle$. The master equation is given by the Lindblad form

$$\dot{\bar{\rho}} = [\tilde{H}, \bar{\rho}]/i\hbar + \sum_{jj'} (\Gamma_{jj'}/2) \left(2\hat{r}_{j'} \bar{\rho} \hat{r}_j^\dagger - \{\hat{r}_j^\dagger \hat{r}_{j'}, \bar{\rho}\} \right), \tag{4.2}$$

where $\tilde{H}/\hbar = \sum_j \Delta \hat{r}_j^\dagger \hat{r}_j + \sum_{jj'} J_{jj'} \hat{r}_j^\dagger \hat{r}_{j'}$ (we omit the contribution of $|g\rangle$ atoms, a constant energy offset). Each site can be modeled as a two-level emitter (or three-level if the auxiliary $|g\rangle$ state is included) as long as the on-site interaction U is much larger than the line width Γ_1, allowing no more than a single excitation per site, e.g. $\hat{r}_j^\dagger \hat{r}_j^\dagger |0\rangle = 0$ (hardcore-boson limit). Such a condition is fulfilled for our parameters, as $U \approx 0.46\omega_r \gg \Gamma_1 \approx 0.08\omega_r$. For the detailed derivation of the master equation (also calculations of $\Gamma_{jj'}$ and $J_{jj'}$), see Section 2.2.2.

The collective decay processes are also described by the collective oper-

ators $\hat{\mathcal{O}}_k = \sum_j e^{-ikdj}\hat{r}_j$ [48, 100], with which the master equation can be simplified to $\dot{\bar{\rho}} = [\tilde{H}, \bar{\rho}]/i\hbar + (\Gamma_1/2)\sum_{k=\{k_+,k_-\}}\left(2\hat{\mathcal{O}}_k\bar{\rho}\hat{\mathcal{O}}_k^\dagger - \{\hat{\mathcal{O}}_k^\dagger\hat{\mathcal{O}}_k, \bar{\rho}\}\right)$. The density matrix $\bar{\rho}(t)$ is obtained with the initial state $\bar{\rho}(0) = |M\rangle\langle M|$ where $|M\rangle = \prod_{j=\lfloor 1-M/2\rfloor}^{\lfloor M/2\rfloor}\hat{r}_j^\dagger|0\rangle$ (or $\prod_j 2^{-1/2}(\hat{r}_j^\dagger+\hat{g}_j^\dagger)|0\rangle$ for the superposition scenario) represents M excited emitters, and the excited population can be computed as $N_c = \mathrm{Tr}[\bar{\rho}\sum_j \hat{c}_j^\dagger\hat{c}_j]$ where $c \in \{r, g\}$ (Fig. 4.4a and Fig. 4.6a). The phase distribution is computed from $n_c(\phi) = \mathrm{Tr}[\bar{\rho}\hat{c}_\phi^\dagger\hat{c}_\phi]$, where $\hat{c}_\phi^\dagger = M^{-1/2}\sum_j e^{i\phi j}\hat{c}_j^\dagger$ (for the $|r\rangle$ and $|g\rangle$ states), again with an additional Gaussian convolution of width $0.15k_\mathsf{r}$ (cf. Fig. 4.4c and Fig. 4.6b). For a fully excited state of two emitters, spontaneous emission of a matter wave at a mode k leads to a relative phase kd between the emitters, as illustrated in Fig. 4.4d. More generally the emission results in the state $M^{-1/2}\hat{\mathcal{O}}_k|M\rangle$, whose phase distribution is given by $\langle\hat{r}_\phi^\dagger\hat{r}_\phi\rangle \propto M^{-2}\sum_{j\neq j'}(1+e^{i(\phi-kd)(j'-j)}) = 1-2/M+|M^{-1}\sum_j e^{i(\phi-kd)j}|^2$ and is peaked at $\phi \equiv kd \pmod{2\pi}$.

As discussed in the main text, we describe the collective dynamics in the MI regime with a two-emitter model, given the matter-wave coherence length $\sim d$, with an additional empty emitter to take into account reabsorption (Fig. 4.4a). In addition to the shape of the phase distribution $n_g(\phi)$ in the second scenario with the auxiliary state ($|g\rangle$), the model also captures its initial growth (Fig. 4.6b). However, the coherence feature fades away after ~ 0.2 ms and at the same time the decay of the $|r\rangle$ population slows down significantly (Fig. 4.6a). While our model is not able to capture this behavior, we note the possible role of interactions (between lattice-trapped, $|r\rangle, |g\rangle$ and free states, $|b\rangle$) in inducing dephasing on time scales $\gtrsim \hbar/U \sim 0.1$ ms.

4.7.5 Spectral structure and bound states in the continuum (BIC)

We use the analytic formalism developed in [19] to identify the spectral contributions including those of bound states for the initial $q = 0$ timed Dicke state in an array of 3 sites. The excitation amplitudes of each site can be broken down as $(A_1, A_2, A_3)^\intercal = I_1(t)/\sqrt{3}(1,1,1)^\intercal + I_2(t)/\sqrt{3}(0,1,0)^\intercal$ since the even parity of the initial state ($I_1(0) = 1, I_2(0) = 0$) is preserved throughout the decay. The exact time evolution is given by the integrals

$$I_j(t) = \frac{(-1)^j}{2\pi i}\int_{-\infty+i0^+}^{+\infty+i0^+} e^{-i\omega t}\mathcal{G}_{2,3-j}\det{}^{-1}\mathcal{G}\,\mathrm{d}\omega, \tag{4.3}$$

$\Delta = 4\omega_{\mathsf{r}}$

p	BS	sR	SR
ω_p	$-0.019(4)$	$4.07(1) - 7(3) \times 10^{-6} i$	$4.09(1) - 0.10(1)i$
$\boldsymbol{A}_{p,0}$	$\begin{pmatrix} 0.0038(7) \\ 0.0043(8) \\ 0.0038(7) \end{pmatrix}$	$\begin{pmatrix} -0.000034(9) - 0.0036(5)i \\ -0.00020(5) + 0.0071(9)i \\ -0.000034(9) - 0.0036(5)i \end{pmatrix}$	$\begin{pmatrix} 0.611(4) + 0.042(8)i \\ 0.597(2) + 0.027(5)i \\ 0.611(4) + 0.042(8)i \end{pmatrix}$

$\Delta = \omega_{\mathsf{r}}$

p	BS	sR	SR
ω_p	$-0.010(2)$	$1.023(3) - 3(1) \times 10^{-6} i$	$1.041(9) - 0.11(2)i$
$\boldsymbol{A}_{p,0}$	$\begin{pmatrix} 0.009(1) \\ 0.010(2) \\ 0.009(1) \end{pmatrix}$	$\begin{pmatrix} 0.371(2) - 0.0039(5)i \\ 0.742(4) + 0.0013(2)i \\ 0.371(2) - 0.0039(5)i \end{pmatrix}$	$\begin{pmatrix} 0.237(5) + 0.044(2)i \\ -0.225(3) - 0.036(9)i \\ 0.237(5) + 0.044(2)i \end{pmatrix}$

$\Delta = 0$

p	BS_1	BS_2	SR
ω_p	$-0.22(2)$	$-0.10(1)$	$0.28(2) - 0.033(1)i$
$\boldsymbol{A}_{p,0}$	$\begin{pmatrix} 0.281(1) \\ 0.36749(1) \\ 0.281(1) \end{pmatrix}$	$\begin{pmatrix} 0.042(1) \\ -0.067(1) \\ 0.042(1) \end{pmatrix}$	$\begin{pmatrix} 0.214(4) + 0.100(4)i \\ 0.3460(7) + 0.0137(6)i \\ 0.214(4) + 0.100(4)i \end{pmatrix}$

Table 4.1: Complex frequencies ω_p (in units of ω_{r}) and initial amplitudes $\boldsymbol{A}_{p,0}$ of the bound (BS), subradiant (sR), and superradiant (SR) states impacting the dynamics of 3 quantum emitters, for the parameters tested in the experiment (see Figs. 4.3 and 4.9).

where

$$\mathcal{G} = (\omega - \Delta)\mathbf{Id}_2 + i \begin{pmatrix} \tilde{G}_0(\omega) + \tilde{G}_1(\omega) + \tilde{G}_2(\omega) & \tilde{G}_1(\omega) \\ \tilde{G}_1(\omega) - \tilde{G}_2(\omega) & \tilde{G}_0(\omega) - \tilde{G}_1(\omega) \end{pmatrix} \tag{4.4}$$

and

$$\begin{aligned} \tilde{G}_n(\omega) = & \frac{\Omega^2 \pi^{1/2}}{8\sqrt{\omega \omega_{\mathsf{r}} \sqrt{s_z}}} e^{-\omega/(\omega_{\mathsf{r}}\sqrt{s_z})} \times \\ & \left[e^{in\pi\sqrt{\omega/\omega_{\mathsf{r}}}} \operatorname{erfc}\left(-i\sqrt{\frac{\omega}{\omega_{\mathsf{r}}\sqrt{s_z}}} - \frac{n\pi\sqrt[4]{s_z}}{2} \right) + n \leftrightarrow -n \right] \end{aligned} \tag{4.5}$$

is the Fourier transform of the bath correlation function $G_{j,j+n}(\tau)$.

These integrals (Eq. (4.3)) can be decomposed using the residue theorem into a non-Markovian decay branch-cut at the continuum edge (at $\omega = 0$) and a set of infinite simple poles satisfying $\det \mathcal{G}(\omega_p) = 0$ most of which have small contributions and decay extremely fast (well beyond superradiant rates). However, they provide a mechanism to avoid the "superradiant paradox" [44], as they help the initial decay to match the dynamics of a single emitter (cf. Fig. 4.3a).

Additionally, we identify three poles representing a bound state, a subra-

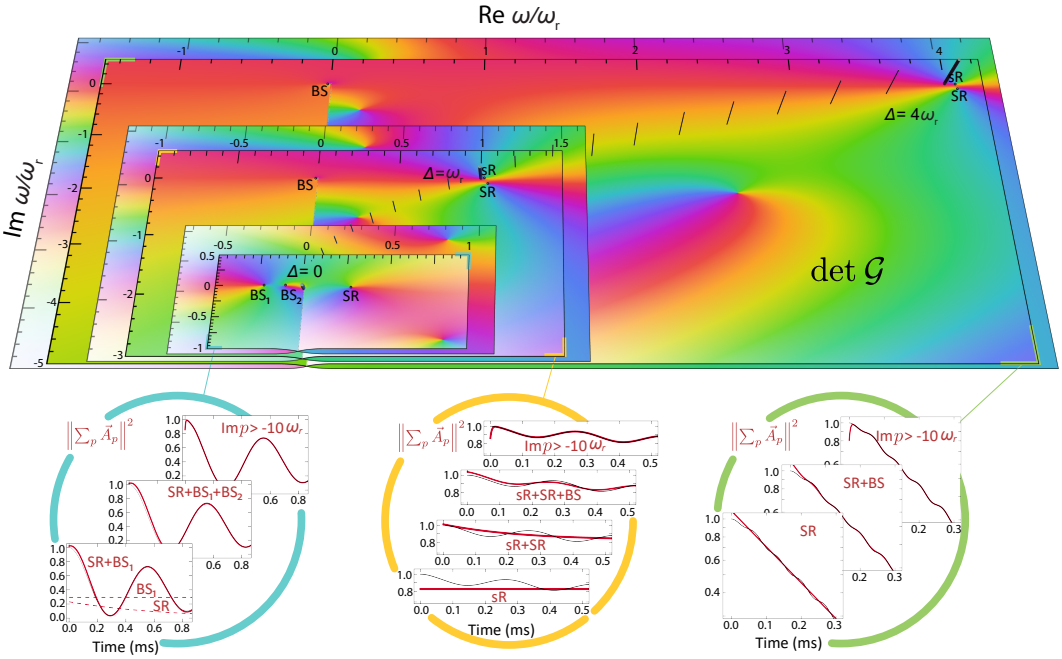

Figure 4.7: **Spectral contributions to the simulated dynamics of 3 emitters.** The domain colorings of $\det \mathcal{G}$ (with a brightness of 1, a hue proportional to the argument of $\det \mathcal{G}$, and a saturation inversely dependent on its absolute value) are represented on Riemann surfaces, along with their analytic extensions, for $s_z = 8$ and $(\Delta, \Omega)/\omega_r = (0, 0.6)$, (1,0.42) and (4,1) from left to right (the vertical bars represent the dispersion $k(\Delta)$, to which the origin of the imaginary axis for each Δ is aligned). The zeroes and branch cut of this function define the decay dynamics of the emitters, which are presented in the bottom panels. The black lines represent the simulated dynamics, while the red lines account for the various spectral contributions; with the main ones coming from superradiant (SR), subradiant (sR) and bound states (BS) [Figure credit: A. Lanuza].

diant, and a superradiant state with amplitudes that are given by

$$\boldsymbol{A_p} = \frac{e^{-i\omega_p t}}{\sqrt{3}(\det \mathcal{G})'(\omega_p)} \begin{pmatrix} \mathcal{G}_{2,2}(\omega_p) \\ \mathcal{G}_{2,2}(\omega_p) - \mathcal{G}_{2,1}(\omega_p) \\ \mathcal{G}_{2,2}(\omega_p) \end{pmatrix}. \tag{4.6}$$

These poles are tabulated together with their corresponding frequencies in Table 4.1, and their contributions to the decay dynamics are represented in Fig. 4.7. Notice that at $\Delta = 4\omega_r$ the dynamics is dominated by the superradiant state but at $\Delta = \omega_r$ besides the subradiant state, the superradiant state

has a non-negligible contribution. We note that the subradiant state has an extremely small imaginary part, so technically it is a quasi-bound state in the continuum, but its decay is too small for us to resolve experimentally and thus we treat it as a BIC in the main text. The fact that our quantum emitters have a finite size prevents this state from being perfectly bound and from having the ideal amplitude $\boldsymbol{A} \propto (1, 2, 1)^\intercal$, which otherwise allows for perfectly destructive interference between the three point-like emitters ($\sum_j A_j e^{ik_\mathrm{r} dj} = 0$). The matter-wave component B_k of the BIC follows from the A_j as

$$B_k = \frac{\Omega \sum_j \gamma_{k,j} A_j}{2(\omega_{\mathrm{sR}} - \omega_k)}. \tag{4.7}$$

We use this to compute the matter-wave momentum and position distributions $n_b(k) = |B_k|^2$ and $n_b(z) = |B_z|^2$ of the BIC in the lineout plots of Fig. 4.3c (dashed lines), where $B_z \propto \sum_k e^{ikz} B_k$.

A heuristic fit of the observed population dynamics at $\Delta = \omega_\mathrm{r}$ in Fig. 4.3a (ii) with an equation motivated by the analysis, $|\alpha_t e^{-i\omega t} + (1-\alpha_0)|^2$, where $\alpha_t = \alpha_\infty + (\alpha_0 - \alpha_\infty) e^{-3\Gamma_1 t/2}$, returns initial and asymptotic population averages, $|\alpha_0|^2 = 0.93(1)$ and $|\alpha_\infty|^2 = 0.84(2)$. These results qualitatively agree with the initial joint contribution from the super- and subradiant states (BIC), $||\boldsymbol{A}_{\mathrm{sR},0} + \boldsymbol{A}_{\mathrm{SR},0}||^2 = 1.01(2)$, and the asymptotic contribution from the subradiant state only, $||\boldsymbol{A}_{\mathrm{sR},0}||^2 = 0.83(1)$ (cf. Table. 4.1). The beat frequency from the fit, $\omega = 0.95(2) \times \omega_\mathrm{r}$, is also comparable to the frequencies of the two states, approximately at ω_r.

Finally, at $\Delta = 0$, there are two bound states below the edge. This feature does not appear with one or two symmetric emitters, and would ideally lead to persistent oscillations of very low frequency. These oscillations correspond to a periodic redistribution of population between the central emitter and its neighbors, in some analogy to vibrations in a molecule that are of low frequency compared to electronic excitations.

4.7.6 Auxiliary measurements

Collective emission versus coherence. The collective enhancement and the number of emitters in our model depend on the coherence length of the initial array population and the coherence length of the emitted matter waves ($|b\rangle$), which can be limited in deep transverse tubes. In the experiment, we

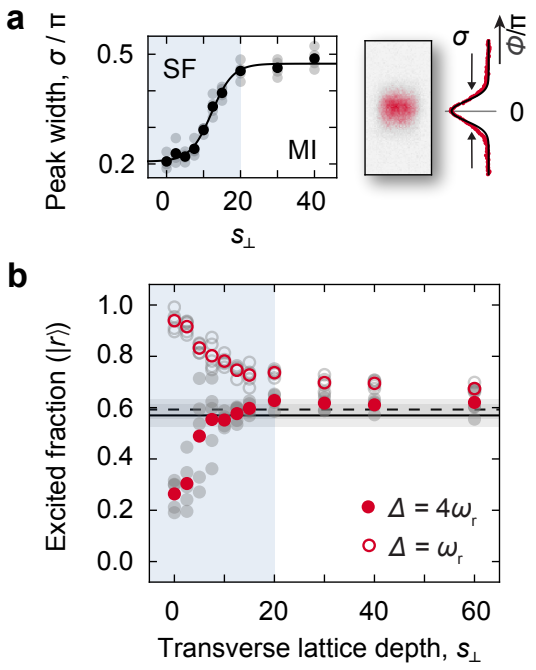

Figure 4.8: **Collective emission versus coherence. a,** Coherence of the initial array population characterized by the width σ of the phase distribution at various transverse lattice depths $s_\perp$ as seen in ToF images. **b,** Excited fraction at a fixed decay time 300 μs as a function of $s_\perp$ for two distinct excitation energies $\hbar\Delta = 4\hbar\omega_\mathrm{r}, \hbar\omega_\mathrm{r}$ with coupling strength $\Omega/\omega_\mathrm{r} = 1.00(7), 0.48(3)$. The z-lattice depth is fixed at $s_z = 15$ throughout.

can vary the lattice depths independently. We investigate the effect of the coherence length on the decay by varying the transverse lattice confinement $s_\perp$ (while leaving s_z the same). For two distinct values $\Delta = 4\omega_\mathrm{r}, \omega_\mathrm{r}$ as in the main text, with the vacuum coupling adjusted to yield the same Markovian single-emitter decay rate ($\Gamma_1 = 2\pi \times 0.31$ kHz), we measure the excited population after a fixed decay time (300 μs) as a function of $s_\perp$, as shown in Fig. 4.8b. In the deep MI regime $s_\perp \gtrsim 20$, we find that the data are consistent with the simulated populations for an isolated emitter, up to small deviations caused by reabsorption also seen in Fig. 4.4a. As we cross over from the MI to the SF regime, we gradually recover the collective enhancement and suppression. The transition from single- to multi-emitter dynamics coincides with the change of the peak width in the phase distribution of the initial array population, which reflects the coherence of the system [174] (Fig. 4.8a).

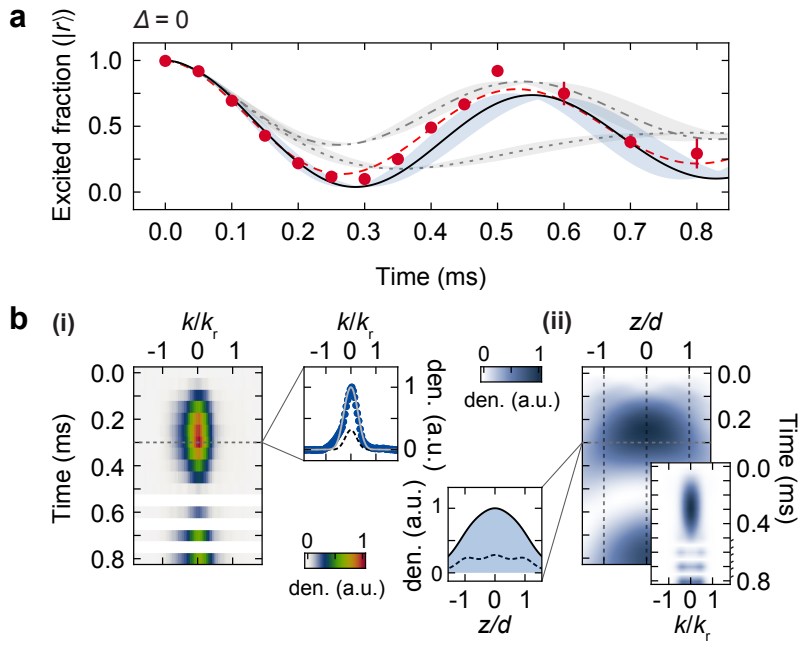

Figure 4.9: **Collective dynamics at the continuum edge in the SF regime.** **a**, Excited fraction as a function of time for $(s_z, s_\perp) = (8, 8)$, $\phi = 0$ with strong coupling $\Omega = 0.60(4)\omega_r$ at $\Delta = 0$ (red points). The solid line simulates a 3-emitter array with a coherently distributed excitation, as opposed to scenarios in which the excitation is located in an isolated emitter (dotted line) or in the central one of 3 emitters (dashed-dotted). Shaded areas represent the uncertainty in Ω. The red dashed line is a fit to the beating of a dissipative and a bound state with the decay rate fixed by our analytic model. **b**, (i) Momentum distribution of the emitted matter waves versus time. The lineout plot shows the data at 0.3 ms (blue points) along with our simulation and bound-state contributions from our analytic model (gray solid and black dashed lines). (ii) Simulated position and momentum distributions of the matter waves versus time, with a lineout plot at 0.3 ms. The dashed vertical lines are the positions of the emitters. All data are averages of at least 3 measurements; the error bars show the standard error of the mean.

Collective dynamics at the continuum edge. As mentioned in the main text, the diverging mode density near $k = 0$, i.e. $\rho(E) \propto 1/v_g \to \infty$, can also cause strong non-Markovian behavior [18, 19]. We examine this regime by tuning our emitters to $\Delta = 0$ and measure the population of the excited state prepared in a TDS with $\phi = 0$ (Fig. 4.9a). An oscillation with a near-maximum visibility is observed, much stronger than that expected both for

an isolated emitter (which shows fractional decay with damped, weak oscillations) and for an exited emitter surrounded by empty neighbors (cf. [19–21]). Instead, the behavior resembles that of a TDS with $\phi = 0$ (Fig. 4.9a solid line) strongly coupled to the $k = 0$ mode. This is confirmed in the momentum distribution of matter waves (Fig. 4.9b (i)), which is concentrated near $k = 0$, in agreement with our finite-array simulation. In position space, this corresponds to the radiation trapped inside the array including contributions from bound states, with very little escaping to the outside (Fig. 4.9b (ii)).

Motivated by our analytic theory, we fit the data to the beating between a dissipative and a bound state $|\alpha_0 e^{-i\omega t-\Gamma_{\rm SR}t/2} + (1-\alpha_0)|^2$, where $\Gamma_{\rm SR} = 2{\rm Im}(\omega_{\rm SR}) \approx 2\pi \times 0.24$ kHz (Table 4.1), yielding a frequency $\omega = 2\pi \times 1.86(2)$ kHz and a bound-state population $|1-\alpha_0|^2 = 0.43(2)$ in a qualitative agreement with the frequency difference $\omega_{\rm SR} - \omega_{\rm BS_1} = 2\pi \times 1.84(11)$ kHz between the dominant states and the joint contribution of bound states $||\boldsymbol{A}_{{\rm BS}_1,0} + \boldsymbol{A}_{{\rm BS}_2,0}||^2 = 0.30(1)$. We note that the measured frequency is very close to $\Omega\gamma_{0,0}\sqrt{L/d} = 2\pi \times 1.80$ kHz, which is consistent with the fact that, in the limit of large coherence length, the dynamics reduces to the Rabi oscillation between two polariton eigenstates due to the translational symmetry [19, 172].

Radiative decay of thermal excitations. Here we present additional decay data for an emitter array without coherence but outside the MI regime. Such a system is prepared by periodically modulating the lattices in order to slightly heat up the array population ($|r\rangle$ atoms starting from SF) before applying the coupling pulse (see Fig. 4.10a). For both $\Delta = 4\omega_{\rm r}$ and $\omega_{\rm r}$, the decay of the excited fraction resembles that of isolated emitters in contrast to the behavior of a superfluid, and stalls after a certain time ~ 0.2 ms. To understand this behavior, we consider a statistical mixture of TDSs distributed over the range $\phi \in (-\pi, \pi]$ (in the first lattice band). Since only those TDSs near $\phi \equiv \pm k(\Delta)d \pmod{2\pi}$ can effectively decay and emit matter waves, the decay dynamics stops once only the subradiant states are left. Consequently, looking at the phase distribution of the array population over time, we find that the populations at the emitted phase are depleted, i.e. there are dips at $\phi = 0(\pm\pi)$ for $\Delta = 4\omega_{\rm r}(\omega_{\rm r})$ in Fig. 4.10b. We note that these intuitive results are in fact the exact opposites of those seen in Fig. 4.4c in the Mott regime, where the gains rather than losses appear at the same values of ϕ, emphasizing the quantum many-body nature of coherence formation in the MI regime.

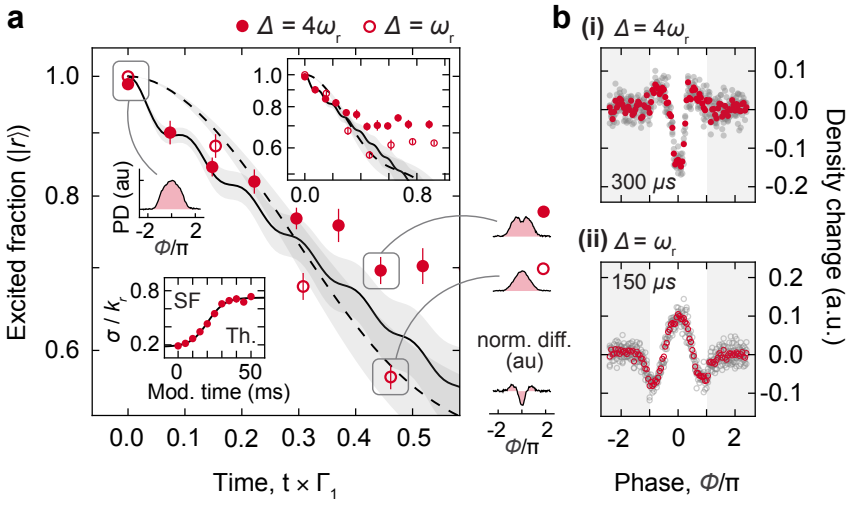

Figure 4.10: **Radiative decay of thermal excitations. a,** Excited fraction for $\Delta = 4\omega_r$ and ω_r (red points and circles), with coupling strength set to $\Omega/\omega_r = 1.00(7)$ and $0.60(4)$. A thermal gas of $|r\rangle$ atoms in the SF regime, $(s_z, s_\perp) = (8, 8)$, is prepared by heating via periodic modulation of the lattice depths s_z and $s_\perp$ with an average amplitude $\approx 30\%$ and a frequency 500 Hz for a duration of 40 ms. The solid and dashed lines are simulations of single-emitter decay for the corresponding parameters. We plot time in terms of $\Gamma_1 = 2\pi \times 0.24$ kHz (0.49 kHz) for $\Delta = 4\omega_r$ (ω_r), phase distributions of the array population ($|r\rangle$ atoms) are shown at $t = 0$ and 300 μs (150 μs). The top-right inset shows the same data including longer times. Also shown is the heating of the array population versus the lattice modulation time characterized by the momentum peak width [56]; the solid line is a sigmoidal fit. **b,** (i) Change in the normalized PD of the emitter array ($|r\rangle$) after 300 μs for $\Delta = 4\omega_r$. (ii) Same but after 150 μs for $\Delta = \omega_r$. All data are averages of at least 3 measurements with the error bars from the standard error of the mean (gray points and circles are raw data).

Chapter 5

Theoretical Basics on Interacting Bose Gases

In this chapter, we discuss some properties of ultracold Bose gases, including superfluidity, long-range coherence, and phase transition in an optical lattice, which are closely related to many-body dynamics of matter-wave emitters discussed the next chapter.

5.1 Weakly interacting bose gas

The concept of superfluidity emerges only when the interactions are included. A many-particle system can have a very complicated wavefunction, and it is preferred to work in the second-quantization picture that takes care of the symmetrization requirement [175]. The Hamiltonian in terms of the field operators in position space, in the limit of dilute gas in 3D where the interaction is characterized by the pairwise, s-wave scattering is [176]

$$\begin{aligned}\hat{H} = &\int d^3\boldsymbol{r}\hat{\psi}^\dagger(\boldsymbol{r})\left[\frac{\hat{\boldsymbol{p}}^2}{2m} + V(\boldsymbol{r})\right]\hat{\psi}(\boldsymbol{r}) \\ &+ \frac{1}{2}\int\int d^3\boldsymbol{r}d^3\boldsymbol{r}'\hat{\psi}^\dagger(\boldsymbol{r})\hat{\psi}^\dagger(\boldsymbol{r}')U(\boldsymbol{r},\boldsymbol{r}')\hat{\psi}(\boldsymbol{r}')\hat{\psi}(\boldsymbol{r}),\end{aligned} \tag{5.1}$$

where $\hat{\boldsymbol{p}} = (\hbar/i)\nabla$, and $V(\boldsymbol{r})$ is some external potential. The field operators obey the bosonic commutation relations $[\hat{\psi}(\boldsymbol{r}), \hat{\psi}^\dagger(\boldsymbol{r})] = \delta^3(\boldsymbol{r} - \boldsymbol{r}')$. The s-wave collisions provide the interaction potential $U(\boldsymbol{r}) = g\delta^3(\boldsymbol{r} - \boldsymbol{r}')$ with the coefficient $g = 4\pi\hbar^2 a_s/m$, which depends on the scattering length a_s (at low energies, scattering processes with higher angular momenta are suppressed

[113]). The value of a_s for ^{87}Rb is $a_s \approx 100a_0$, where a_0 is the Bohr radius (the exact value depends on the hyperfine Zeeman sublevels and magnetic field [177–179]). In the following, we assume that the atoms are in a box of size L and $V(\boldsymbol{r}) = 0$ inside.

5.1.1 Quasiparticle excitations and superfluidity

For superfluidity, it is important to understand the character of the elementary excitations in the system. In a BEC, these excitations will still be the bosons in the excited states, but their dispersion is modified due to the interactions with the condensate. The usual treatment is working in the momentum basis, $\psi(\boldsymbol{r}) = L^{-3/2}\sum_{\boldsymbol{k}} \hat{a}_{\boldsymbol{k}} e^{i\boldsymbol{k}\cdot\boldsymbol{r}}$. The Hamiltonian then becomes

$$\hat{H} = \sum_{\boldsymbol{k}} \frac{\hbar^2 k^2}{2m} \hat{a}^\dagger_{\boldsymbol{k}} \hat{a}_{\boldsymbol{k}} + \frac{g}{2L^3} \sum_{\boldsymbol{q},\boldsymbol{k},\boldsymbol{k}'} \hat{a}^\dagger_{\boldsymbol{k}-\boldsymbol{q}} \hat{a}^\dagger_{\boldsymbol{k}'+\boldsymbol{q}} \hat{a}_{\boldsymbol{k}'} \hat{a}_{\boldsymbol{k}}, \tag{5.2}$$

where we have relabeled the indices. In the ground state $|\mathrm{G}\rangle$ of a weakly interacting bose gas, we expect that the momentum-zero state is macroscopically populated such that $\hat{a}_{\boldsymbol{k}=0}|\mathrm{G}\rangle \approx \sqrt{N_0}|\mathrm{G}\rangle$, e.g. subtracting a particle from the condensate fraction doesn't change the state much. A state with this property is also called a coherent state.[1] We then make a replacement $\hat{a}_{\boldsymbol{k}=0} \to \sqrt{N_0}, \hat{a}^\dagger_{\boldsymbol{k}=0} \to \sqrt{N_0}$ in $\hat{H}$, and keep the terms up to the second order in $\hat{a}_{\boldsymbol{k}\neq 0}$. For example, in the interaction part, the leading term is given by setting three momenta to be zero, $\boldsymbol{k} - \boldsymbol{q} = \boldsymbol{k}' + \boldsymbol{q} = \boldsymbol{k}' = 0$, leading to $\hat{a}^\dagger_0 \hat{a}^\dagger_0 \hat{a}_0 \hat{a}_0 = N_0^2$. The next-order terms are given by setting two momenta to be zero, e.g. $\boldsymbol{k} - \boldsymbol{q} = \boldsymbol{k}' + \boldsymbol{q} = 0$, $\boldsymbol{k} - \boldsymbol{q} = \boldsymbol{k}' = 0$, ... (total six terms). The interaction part becomes

$$\hat{H}_{\mathrm{int}} \approx \frac{g}{2L^3}\left[N^2 + 2N\sum_{\boldsymbol{k}\neq 0} \hat{a}^\dagger_{\boldsymbol{k}} \hat{a}_{\boldsymbol{k}} + N\sum_{\boldsymbol{k}\neq 0} (\hat{a}^\dagger_{\boldsymbol{k}} \hat{a}^\dagger_{-\boldsymbol{k}} + \hat{a}_{\boldsymbol{k}} \hat{a}_{-\boldsymbol{k}})\right], \tag{5.3}$$

where in the second line we used $\hat{N} \approx N_0 + \sum_{\boldsymbol{k}\neq 0} \hat{a}^\dagger_{\boldsymbol{k}} \hat{a}_{-\boldsymbol{k}}$ and $\hat{N} \approx N$. The excitation Hamiltonian is then

$$\hat{H}_{\mathrm{ex}} = \frac{gn^2}{2} L^3 + \sum_{\boldsymbol{k}\neq 0} (\epsilon^0_{\boldsymbol{k}} + ng) \hat{a}^\dagger_{\boldsymbol{k}} \hat{a}_{\boldsymbol{k}} + \frac{gn}{2} \sum_{\boldsymbol{k}\neq 0} (\hat{a}^\dagger_{\boldsymbol{k}} \hat{a}^\dagger_{-\boldsymbol{k}} + \hat{a}_{\boldsymbol{k}} \hat{a}_{-\boldsymbol{k}}), \tag{5.4}$$

[1] Defined as $|\alpha\rangle = e^{\alpha \hat{a}^\dagger - \alpha^* \hat{a}}|0\rangle$ such that $\hat{a}|\alpha\rangle = \alpha|\alpha\rangle$

where $\epsilon^0_{\boldsymbol{k}} = \hbar^2 k^2/2m$ and $n = N/L^3$. Roughly speaking, the energy of excitations is modified by the interactions with the condensate population (N_0), and also excitations pop up from or disappear into the condensate.

The Hamiltonian $\hat{H}_{\rm ex}$ can be diagonalized through the Bogoliubov transformations [113, 180] $\hat{a}_{\boldsymbol{k}} = u_{\boldsymbol{k}}\hat{b}_{\boldsymbol{k}} - v_{\boldsymbol{k}}\hat{b}^\dagger_{-\boldsymbol{k}}$ with $u_{\boldsymbol{k}}$, $v_{\boldsymbol{k}}$ being real values. The canonical commutation relations $[b_{\boldsymbol{k}}, b^\dagger_{\boldsymbol{k}'}] = \delta_{\boldsymbol{k},\boldsymbol{k}'}$ require $u^2_{\boldsymbol{k}} - v^2_{\boldsymbol{k}} = 1$, and the cofficients can also be parametrized as $u_{\boldsymbol{k}} = \cosh\theta_{\boldsymbol{k}}$, $v_{\boldsymbol{k}} = \sinh\theta_{\boldsymbol{k}}$. This yields the diagonalized Hamiltonian

$$\hat{H}_{\rm eff} = \sum_{\boldsymbol{k}\neq 0} \epsilon_{\boldsymbol{k}} \hat{b}^\dagger_{\boldsymbol{k}} \hat{b}_{\boldsymbol{k}}, \tag{5.5}$$

with the dispersion

$$\epsilon_{\boldsymbol{k}} = \sqrt{(\epsilon^0_{\boldsymbol{k}})^2 - (ng)^2} = \sqrt{\frac{\hbar^2 k^2}{2m}\left(\frac{\hbar^2 k^2}{2m} + 2ng\right)}. \tag{5.6}$$

At large k, we recover the free dispersion $\epsilon_{\boldsymbol{k}} \to \epsilon^0_{\boldsymbol{k}}$, but at small k,

$$\epsilon_{\boldsymbol{k}} \to c_s(\hbar k), \quad c_s = \sqrt{\frac{ng}{m}}, \tag{5.7}$$

where c_s is the sound velocity.

Bose gases exhibit superfluidity due to this excitation spectrum, which can be seen by the Landau criterion [181]

$$v_c = \min\left[\frac{\epsilon_p}{p}\right], \tag{5.8}$$

which is called the Landau critical velocity, where $p = \hbar k$ is a momentum. If the velocities are higher than this, an excitation can be created at an angle $\cos\theta = \epsilon_p/pv$. However, at lower velocities, the motion of the gas will not be affected, and the gas will behave as a superfluid. Applying the criterion to a non-interacting Bose gas, we find that an ideal BEC is not a superfluid, as $\epsilon_p/p = p/2m$ can be as small as zero. However, for an interacting Bose gas, the minimum value of ϵ_p/p is the sound velocity c_s, leading to a non-zero critical velocity.

5.1.2 Mean-field approximation

In real experiments, atoms are usually confined in a linear or harmonic trap, and the condensate will be shaped by the potential term $V(\boldsymbol{r})$ in Eq. (5.1). This problem can be dealt with the mean-field approximation. We start by the Hartree-Fock wavefunction with all N atoms occupying a single-particle state $\phi(\boldsymbol{r})$, $\Psi(\boldsymbol{r}_1, ..., \boldsymbol{r}_N) = \prod_{i=1}^{N} \phi(\boldsymbol{r}_i)$, which is justified by the macroscopic occupation of the single-particle ground state in a Bose gas. The depletion of the condensate due to interactions is of order $(na^3)^{1/2}$ [113], and for a typical atom number $N = 10^5$ of ^{87}Rb in a box of 10 μm, this is about 0.4 %. The wavefuction follows the Hamiltonian (a representation of Eq. (5.1) for the position-space wavefunction $\Psi(\boldsymbol{r}_1, ..., \boldsymbol{r}_N)$)

$$H = \sum_i \left[\frac{\boldsymbol{p}_i^2}{2m} + V(\boldsymbol{r}_i) \right] + g \sum_{i<j} \delta(\boldsymbol{r}_i - \boldsymbol{r}_j). \tag{5.9}$$

The expectation value of energy is given by

$$\langle \Psi | E | \Psi \rangle = \int d^3\boldsymbol{r} \left[-\frac{\hbar^2}{2m} \psi^*(\boldsymbol{r}) \nabla^2 \psi(\boldsymbol{r}) + V(\boldsymbol{r}) |\psi(\boldsymbol{r})|^2 + \frac{(N-1)}{2N} g |\psi(\boldsymbol{r})|^4 \right], \tag{5.10}$$

where we defined the condensate wavefunction (order parameter [182]; see Appendix C for a summary of theoretical justification) $\psi(\boldsymbol{r}) = \sqrt{N}\phi(\boldsymbol{r})$, which is normalized to $\int d^3\boldsymbol{r} |\psi(\boldsymbol{r})|^2 = N$. The interaction contribution is proportional to $N(N-1)/2$, reflecting the number of pairwise interactions for N particles. The constraint for the atom number N is included by a Lagrange multiplier as $E - \mu N$, which is the grand canonical energy. Minimizing it with respect to the variation $\psi^* \to \psi^* + \delta\psi^*$ yields

$$\left[-\frac{\hbar^2}{2m} \nabla^2 + V(\boldsymbol{r}) + g |\psi(\boldsymbol{r})|^2 \right] \psi(\boldsymbol{r}) = \mu \psi(\boldsymbol{r}), \tag{5.11}$$

which is called the time-independent Gross-Pitaevskii equation (GPE) [176, 182, 183]. The time-dependent version can be obtained from the Heisenberg equation of motion for the field operator $i\hbar\partial_t \hat{\psi}(\boldsymbol{r}, t) = [\hat{\psi}(\boldsymbol{r}, t), \hat{H}]$ or from the stationary point of the action functional [176], and is given by

$$i\hbar\partial_t \psi(\boldsymbol{r}, t) = \left[-\frac{\hbar^2}{2m} \nabla^2 + V(\boldsymbol{r}) + g |\psi(\boldsymbol{r}, t)|^2 \right] \psi(\boldsymbol{r}, t). \tag{5.12}$$

The time-dependence of ψ can be understood by considering the time-evolution of the order parameter $\psi_0(t) \approx \langle G|e^{i\hat{H}t/\hbar}\hat{\psi}_0(0)e^{-i\hat{H}t/\hbar}|G\rangle \approx e^{-i(E(N)-E(N-1))t/\hbar}\psi_0(0)$ and $E(N) - E(N-1) \approx \partial E/\partial N = \mu$ [182].

For a slowly varying spatial distribution, one may ignore the kinetic term in the Thomas-Fermi limit [113, 182], to obtain

$$n(\boldsymbol{r}) = |\psi(\boldsymbol{r})|^2 = (\mu - V(\boldsymbol{r}))/g. \tag{5.13}$$

This can be interpreted as the energy cost of adding a particle, which is the sum of the potential $V(\boldsymbol{r})$ and the mean-field energy $gn(\boldsymbol{r})$, being uniform across the cloud. For a harmonic trap $V(\boldsymbol{r}) = (1/2)m(\omega_x^2x^2 + \omega_y^2y^2 + \omega_z^2z^2)$, setting $n(\boldsymbol{r}) = 0$ fixes the radius of a condensate (Thomas-Fermi radius)

$$R_{\mathrm{TF},i} = \sqrt{2\mu/m\omega_i^2}, \tag{5.14}$$

and the constraint $\int d^3\boldsymbol{r}n(\boldsymbol{r}) = N$ relates the atom number and the chemical potential as

$$N = \frac{8\pi}{15}\left(\frac{2\mu}{m\bar{\omega}^2}\right)^{3/2}\frac{\mu}{g}, \qquad \mu = \frac{15^{2/5}}{2}\left(\frac{Na_s}{\bar{a}}\right)^{2/5}\hbar\bar{\omega}, \tag{5.15}$$

where $\bar{\omega} = (\omega_x\omega_y\omega_z)^{1/3}$ and $\bar{a} = \sqrt{\hbar/m\bar{\omega}}$. For an isotropic trap of $\bar{\omega} = 2\pi \times 100$ Hz and an atom number $N = 10^5$, we get $R_{\mathrm{TF}} \approx 6.4$ μm (which is much larger than the harmonic oscillator length $\bar{a} \approx 1.1$ μm for a single-particle wavefunction). The radius scales very slowly with the atom number as $R_{\mathrm{TF}} \propto N^{1/5}$.

5.1.3 Bose gas in one dimension

In one dimension, a Bose gas cannot exhibit the symmetry breaking and Bose-Einstein condensation due to strong quantum fluctuations [184], but for sufficiently weak interactions, it can still behave almost like a BEC [185]. A quasi-1D system can be experimentally implemented by a tightly confining tube potential, in which the transverse degrees of freedom are frozen in the harmonic ground state. For the mean-field approximation, the single-particle ground-state wavefunction may be factored as $\phi(\boldsymbol{r}_i) = \phi(z_i)\phi_0(x_i)\phi_0(y_i)$, where $\phi_0(x) = (\pi a_{\mathrm{ho}}^2)^{-1/4}e^{-x^2/2a_{\mathrm{ho}}^2}$ (assuming an isotropic tube). The Hartree-Fock wavefunction becomes $\Psi(\boldsymbol{r}_1, ..., \boldsymbol{r}_N) = [\prod_i \phi(z_i)][\prod_j \phi_0(x_j)\phi_0(y_j)]$, and we integrate the Hamiltonian Eq. (5.9) over the transverse wavefunction. The

interaction part becomes

$$
\begin{aligned}
H_{\rm int} &= \int \left[\prod_{j'} dx_{j'} dy_{j'} \phi_0^*(x_{j'}) \phi_0^*(y_{j'}) \phi_0(x_{j'}) \phi_0(y_{j'}) \right] \sum_{i<j} g\delta^3(\boldsymbol{r}_i - \boldsymbol{r}_j) \\
&= \sum_{i<j} g\delta(z_i - z_j) \int \prod_{j' \neq i,j} dx_{j'} dy_{j'} |\phi_0(x_{j'})|^2 |\phi_0(y_{j'})|^2 \\
&\quad \times \int dx_i dy_i dx_j dy_j |\phi_0(x_i)|^2 |\phi_0(y_i)|^2 |\phi_0(x_j)|^2 |\phi_0(y_j)|^2 \delta(x_i - x_j) \delta(y_i - y_j) \\
&= \sum_{i<j} g_{\rm 1D} \delta(z_i - z_j), \qquad (5.16)
\end{aligned}
$$

where the 1D coupling strength is $g_{\rm 1D} = g/(2\pi a_{\rm ho}^2)$ (up to correction $(1 + \zeta(1/2) a_s/a_{\rm ho})^{-1}$ from an exact calculation [186]). Then the effective 1D Hamiltonian is

$$
H_{\rm 1D} = \sum_i \left[\frac{p_{z,i^2}}{2m} + V(z_i) \right] + g_{\rm 1D} \sum_{i<j} \delta(z_i - z_j), \qquad (5.17)
$$

from which the 1D version of the GPE (Eq. (5.12)) also follows with $g \to g_{\rm 1D}$.[2]

For a 1D harmonic trap $V(z) = (1/2) m\omega_z^2$, the Thomas-Fermi approximation again yields $R_{\rm TF} = \sqrt{2\mu/m\omega_z^2}$ for the radius of cloud. The 1D density $\int dz n(z) = N$ relates N and μ as [76]

$$
N = \frac{(2\mu)^{3/2}}{3 g_{\rm 1D} (m\omega_z^2)^{1/2}}, \quad 2\mu = (9 g_{\rm 1D}^2 m\omega_z^2 N^2)^{1/3}. \qquad (5.18)
$$

In this case, the radius scales as $R_{\rm TF} \propto N^{1/3}$.

5.2 Strongly interacting Bose gas

We have seen that a weakly interacting Bose gas at low temperatures behaves as a superfluid with a large condensate fraction and a long-range phase coherence (cf. Appendix C). When the interactions become strong, a transition to a new phase of matter may occur, and one simple model that captures such a quantum phase transition is the Bose-Hubbard model (BHM), first applied to liquid helium (^{4}He) in porous media [187]. Soon after the realization of the Bose-Einstein condensates [3, 4], it was suggested that ultracold atoms in

[2] The dimensions of $g_{\rm 1D}$ is now energy $\cdot$ length instead of energy $\cdot$ (length)^3 for g.

an optical lattice could be used to realize the BHM [188]. The experimental realization was achieved in the first decade of this century in 3D [5] and 2D [189], and also in 1D [74, 190]. In this section, we discuss the properties of this model, which is important for our experiments in optical lattices.

5.2.1 Band theory in an optical lattice

We first consider a single particle in an optical lattice, described by the Hamiltonian

$$H = \frac{\hat{p}^2}{2m} + V(z) \tag{5.19}$$

where $V(z) = V_0 \sin^2(kz)$ and $k = 2\pi/\lambda_z$ is the wavevector of the laser beam with a wavelength λ_z.

The lattice has a periodicity of $d = \lambda_z/2$, and the Hamilitonian with such a potential commutes with the generator $\hat{T}_d = e^{-id\hat{p}_z/\hbar}$ of the translation by d since $\hat{T}_d V(z) = V(z-d) = V(z)$. Therefore, an eigenstate of $\hat{T}_d$ will be remain as an eigenstate with the same eigenvalue after the time evolution $U(t) = e^{-i\hat{H}t/\hbar}$. To infer the eigenvalues, it is convenient to assume a box of length $L = Md$, and the periodic boundary condition (Born–von Karman boundary condition) of wavefunctions, $\psi(z+L) = \psi(z)$. This implies $(\hat{T}_d)^M \psi(z) = \psi(z)$, which requires the eigenvalues to be the Mth root of unity, $e^{i2\pi m/M}$ with integer m. We can introduce a set of crystal wavevectors $q = (2m/M)(\pi/d)$, such that $e^{i2\pi m/M} = e^{iqd}$. For even M, the index m is typically chosen to run from $-M/2+1$ to $M/2$, and for odd M, from $-(M-1)/2$ to $(M-1)/2$. In the limit $L \to \infty$, q becomes continuous and is defined in the first Brillouin zone, $q \in (-k_\mathsf{r}, k_\mathsf{r}]$, where $k_\mathsf{r} = \pi/d$ denotes the recoil wavevector (momentum).[3]

Bloch's theorem states that the eigenstates are the Bloch states, $\psi_q(z) = e^{iqz} u_q(z)$ with $u_q(z) = u_q(z+d)$ being a periodic function, satisfying $H\psi_q(z) = E_q \psi_q(z)$. To find the energy, it is convenient to expand the periodic part in a Fourier series, $u_q(z) = \sum_{l=-\infty}^{\infty} \tilde{u}_{q,l} e^{i(2\pi/d)lz}$. The eigenvalue equation $[(\hat{p} + \hbar q)^2/2m + V_0 \sin^2(kz)]u_q = E_q u_q$ leads to the following relation:

$$\left(\frac{q}{k_\mathsf{r}} + l\right)^2 \tilde{u}_{q,l} + \frac{V_0}{4E_\mathsf{r}} \left(2\tilde{u}_{q,l} - \tilde{u}_{q,l-1} - \tilde{u}_{q,l+1}\right) = \frac{E_q}{E_\mathsf{r}} \tilde{u}_{q,l}, \tag{5.20}$$

where we defined the recoil energy $E_\mathsf{r} = \hbar^2 k_\mathsf{r}^2/2m$ (which also defines the recoil frequency $\omega_\mathsf{r} = E_\mathsf{r}/\hbar$). In our experiments, we express the lattice depth as $s = V_0/E_\mathsf{r}$. The relation is a matrix equation for $\tilde{u}_{q,l}$, and can be numerically

[3] $\hbar k_\mathsf{r} = 2\pi\hbar/\lambda_z$ corresponds to the momentum of a lattice photon.

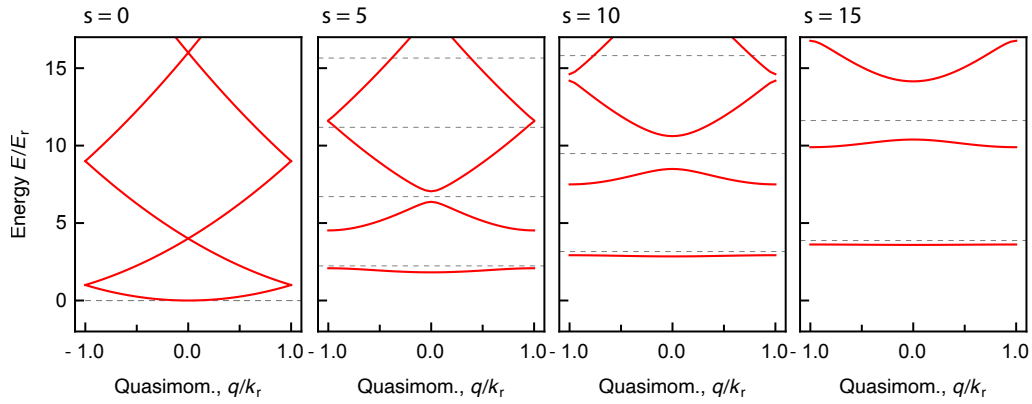

Figure 5.1: Band structures in an optical lattice of depth $s = V_0/E_\mathrm{r}$. The dashed lines are the energy levels from the harmonic approximation of each potential well.

diagonalized to obtain a set of energies and eigenstates, where the number of energies (bands) are determined by the dimensions $2l_{\max}+1$ of the matrix with $l_{\max}$ being some cutoff. The energy bands are denoted by an additional index n, e.g. $\psi_{n,q}(z)$ and $E_{n,q}$ where $n = 0, 1, 2, ...$ Fig. 5.2 shows the band structure for various V_0. The eigenvalue equation is now written as $H\psi_{n,q}(z) = E_{n,q}\psi_{n,q}(z)$.

In a deep lattice, each potential well can be approximated as an isolated harmonic potential, e.g. $V_0 \sin^2 kz \approx V_0 k^2 z^2 \equiv (1/2)m\omega_{\mathrm{ho}}^2 z^2$ with the harmonic oscillator (H.O.) frequency $\omega_{\mathrm{ho}} = 2\omega_\mathrm{r}\sqrt{s}$. The energy of each band converges to that of isolated H.O.s in the deep-lattice limit (Fig. 5.2).

Just like a plane wave, a Bloch wave has an infinite spatial extent in free space. For normalization, one can normalize it over a Wigner-Seitz (WS) cell. In our one-dimensional lattice, the lattice points (vectors) are located at $z_j = dj$ (called a Bravais lattice), and the WS cell is the region $\in (-d/2, d/2]$ (and translations by multiples of d). The normalization then requires $\int_{-d/2}^{d/2} dz \psi_{n,q}^{\mathrm{WC}}(z) = 1$. Alternatively, one can normalize over a box of size $L = Md$, such that the wavefunction is $\psi_{n,q}(z) = M^{-1/2}\psi_{n,q}^{\mathrm{WC}}(z)$

For many-body systems of interacting particles, it is useful to introduce a spatially localized basis called the Wannier functions [191]. They are defined as[4]

$$w_n(z - z_j) \equiv \frac{1}{\sqrt{M}} \sum_q e^{-iqz_j} \psi_{n,q}(z). \tag{5.21}$$

This provides another way to express a Bloch function as a sum of the Wannier

[4]There is some freedom in the definition, as the overall phase $e^{i\phi_q}$ of Bloch waves can be freely chosen [192]. Here we assume that the Wannier functions are real.

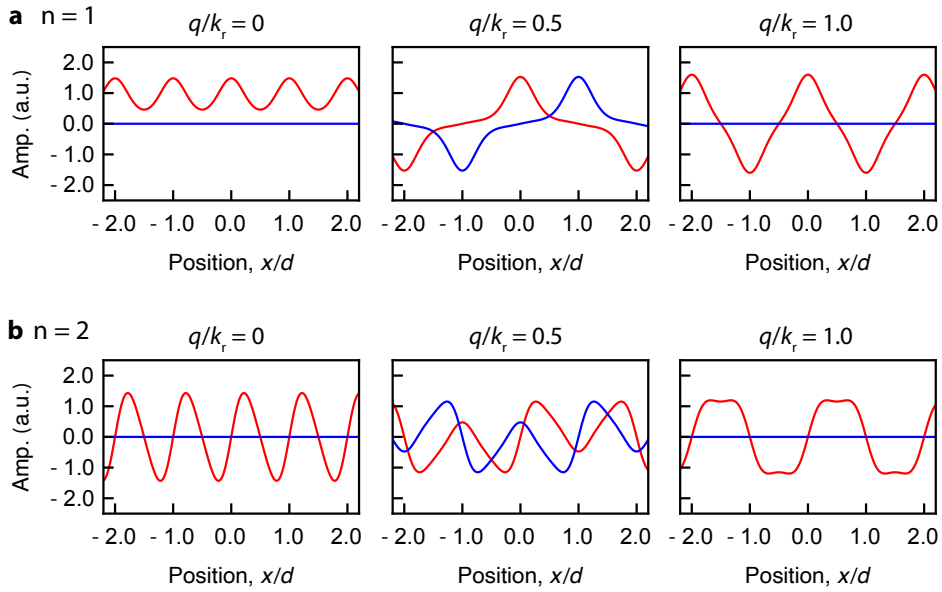

Figure 5.2: Bloch waves $\psi_{n,q}(z)$ in a lattice of depth $V_0 = 5E_\mathrm{r}$ **a,** for the first band and **b,** for the second band. The red and blue lines represent the real and imaginary parts.

functions,

$$\psi_{n,q}(z) = \frac{1}{\sqrt{M}} \sum_j e^{iqz_j} w_n(z - z_j), \tag{5.22}$$

and q basically defines the relative phase between the Wannier states of neighboring wells. Given the orthonormality of the Bloch states, one can show that the Wannier states are also orthonormal.

$$\begin{aligned} \int_L dz w_n(z - z_j) w^*_{n'}(z - z_{j'}) &= \frac{1}{N} \sum_{q,q'} e^{-iqz_j} e^{-iq'z_{j'}} \int_L dz \psi_{n,q}(z) \psi^*_{n',q'}(z) \\ &= \frac{1}{N} \sum_{q,q'} e^{-i(qz_j - q'z_{j'})} \delta_{n,n'} \delta_{q,q'} = \delta_{n,n'} \delta_{j,j'}. \end{aligned} \tag{5.23}$$

Again, in the deep-lattice limit, each well can be considered as an isolated H.O. The Wannier function then converges to the H.O. wavefunction, $\psi_n^{\mathrm{HO}}(z) = (2^n n!)^{-1/2} (\pi a_{\mathrm{ho}}^2)^{-1/4} e^{-z^2/2a_{\mathrm{ho}}^2} H_n(z/a_{\mathrm{ho}})$ where H_n is the Hermite function (the index here runs from $n = 0, 1, ...$) and $a_{\mathrm{ho}} = \sqrt{\hbar/m\omega_{\mathrm{ho}}}$. As shown in Fig. 5.3, even at a moderate depth $V_0 = 5E_\mathrm{r}$, the Wannier functions are well approximated by those of the corresponding harmonic potential.

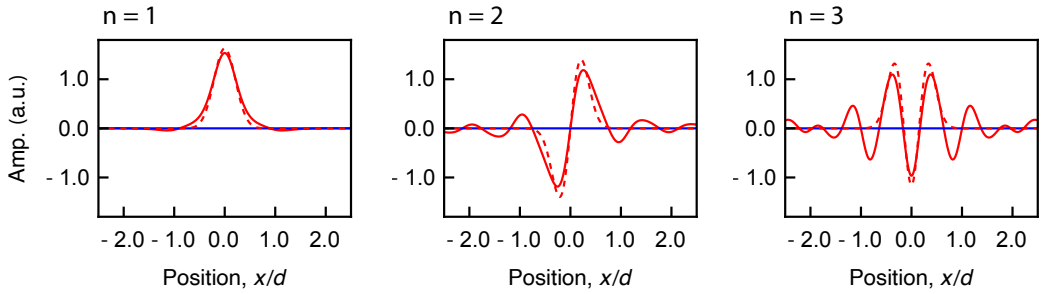

Figure 5.3: Wannier functions for band indices $n = 1, 2, 3$ for a lattice depth $V_0 = 5E_\mathrm{r}$. The dashed lines are the harmonic oscillator wavefunctions, ψ^{HO}_{n-1}. The blue lines represent the imaginary parts, which are all zero.

5.2.2 Tight-binding approximation

In condensed matter physics, the tight-binding model is used when the atoms in a solid are well isolated from each other, so that the electron orbitals of a free atom are still a good basis [192]. When the wavefunction is localized, one may include only the nearest-neighbor effect in the calculation, leading to a sinusoidal band structure. To see this in the Wannier basis, we expand $E_{n,q} = \langle \psi_{n,q} | \, H \, | \psi_{n,q} \rangle$ as

$$E_{n,q} = \int dz \psi^*_{n,q}(z) H \psi_{n,q}(z) = \frac{1}{M} \sum_{j,j'} e^{iq(z_{j'} - z_j)} J_{n,j,j'} \tag{5.24}$$

where

$$J_{n,j,j'} = \int dz w^*_n(z - z_j) H(z) w_n(z - z_{j'}) \tag{5.25}$$

is called the tunneling or hopping rate. Due to the translational symmetry, the summand only depends on the index difference, $J_{n,j,j'} = J_{n,0,j'-j}$ and $z_{j'} - z_j \equiv z_{j'-j}$. Therefore,

$$E_{n,q} = \sum_j e^{iqz_j} J_{n,0,j}. \tag{5.26}$$

Including only the 'atomic' part $\bar{\varepsilon}_0 = J_{n,0,0}$ and the nearest-neighbor contributions $J_{n,0,\pm 1}$, we obtain the tight-binding energy band

$$E^{\mathrm{TB}}_{n,q} = \bar{\varepsilon}_{n,0} + 2J_{n,0,1} \cos qd, \tag{5.27}$$

where we used $J_{n,0,1} = J^*_{n,1,0} = J_{n,1,0} = J_{n,0,-1}$. In this limit, the width of the band $|E_{n,0} - E_{n,k_\mathrm{r}}|$ is given by the quarter of the tunneling rate, $J_{n,0,1}/4$. Including more terms will result in higher harmonics, i.e. $2J_{n,0,2}\cos 2qd + ...$ Conversely, if the energy band $E_{n,q}$ is known, the values of $J_{n,i,j}$ is obtained as

$$\begin{aligned} J_{n,i,j} &= \langle w_{n,i}| H |w_{n,j}\rangle = \sum_{q,q'} \langle w_{n,i}|\psi_q\rangle \langle \psi_q| H |\psi_{q'}\rangle \langle \psi_{q'}|w_{n,j}\rangle \\ &= \sum_q e^{iq(z_i - z_j)} E_{n,q}. \end{aligned} \tag{5.28}$$

The Schrödinger equation for Eq. (5.19) can also be cast into the Mathieu equation, and the exact solutions can be obtained [76]. In the limit $s \gg 1$, the method yields $J_{0,1}/E_\mathrm{r} = 4\pi^{-1/2} s^{3/4} e^{-2\sqrt{s}}$ [193].

5.2.3 Bose-Hubbard model

In this section, we introduce the Bose-Hubbard model, which describes many interacting bosons in a lattice. In particular, we discuss how its parameters are related to that of an optical lattice used in our experiments (see also some of the previous theses [76, 122]). We first expand the field operators in Eq. 5.1 in terms of the Bloch and Wannier basis (in general dimensions),

$$\hat{\psi}(\boldsymbol{r}) = \sum_{n,\boldsymbol{q}} \psi_{n,\boldsymbol{q}}(\boldsymbol{r}) \hat{a}_{n,\boldsymbol{q}} = \sum_{n,j} w_n(\boldsymbol{r} - \boldsymbol{r}_j) \hat{a}_{n,j}, \tag{5.29}$$

where $\hat{a}_{n,\boldsymbol{q}}$ and $\hat{a}_{n,j}$ are the annihilation operators for the Bloch and Wannier states, respectively.[5] The relations may be checked by, for example, the completeness relation $|\boldsymbol{r}\rangle = \sum_{n,\boldsymbol{q}} |n,\boldsymbol{q}\rangle \langle n,\boldsymbol{q}|\boldsymbol{r}\rangle$ where $|n,\boldsymbol{q}\rangle = \hat{a}^\dagger_{n,\boldsymbol{q}} |0\rangle$. From the definition of the Wannier function in Eqs. 5.22 and 5.21, we can also relate the operators as

$$\hat{a}^\dagger_{n,\boldsymbol{q}} = \frac{1}{\sqrt{M}} \sum_j e^{i\boldsymbol{q}\cdot\boldsymbol{r}_j} \hat{a}^\dagger_{n,j}, \quad \hat{a}^\dagger_{n,j} = \frac{1}{\sqrt{M}} \sum_{\boldsymbol{q}} e^{-i\boldsymbol{q}\cdot\boldsymbol{r}_j} \hat{a}^\dagger_{n,\boldsymbol{q}}. \tag{5.30}$$

The first term of the Hamiltonian in Eq. 5.1 for the kinetic and potential energy is fully diagonal in the Bloch basis, i.e. $\hat{H}_0 = \sum_{n,q} E_{n,q} \hat{a}^\dagger_{n,q} \hat{a}_{n,q}$. Assuming that the band gaps are large, as in our typical experiments, we focus on the ground band and drop the band index n such that $\hat{H}_0 = \sum_q E_q \hat{a}^\dagger_q \hat{a}_q$. In terms of the Wannier basis, it involves all the elements of the tunneling

[5] In reverse, $\hat{a}_{n,\boldsymbol{q}} = \int d^3\boldsymbol{r} \psi^*_{n,\boldsymbol{q}}(\boldsymbol{r}) \hat{\psi}(\boldsymbol{r})$.

matrix (Eq. 5.28). An important simplification is that the nearest tunneling $J_{0,1}$ is typically dominant as the Wannier functions are localized on each site (cf. Fig. 5.3), such that we can write

$$\hat{H}_0 = \sum_{i,j} J_{i,j} \hat{a}_i^\dagger \hat{a}_j \approx -J \sum_{\langle i,j \rangle} \hat{a}_i^\dagger \hat{a}_j, \tag{5.31}$$

where $J = -J_{0,1}$ and $\langle i, j \rangle$ indicates the nearest-neighbor pairs.

We also expand the interaction term of Eq. 5.1 in the Wannier basis,

$$\begin{aligned} \hat{H}_{\text{int}} &= \frac{1}{2} \sum_{i,i',j,j'} \int\int d^3\boldsymbol{r} d^3\boldsymbol{r} \hat{a}_i^\dagger \hat{a}_{i'}^\dagger \hat{a}_{j'} \hat{a}_j w_i^*(\boldsymbol{r}) w_{i'}^*(\boldsymbol{r'}) w_{j'}(\boldsymbol{r'}) w_j(\boldsymbol{r}) g\delta(\boldsymbol{r} - \boldsymbol{r'}) \\ &= \frac{1}{2} \sum_{i,i',j,j'} U_{i,i',j,j'} \hat{a}_i^\dagger \hat{a}_{i'}^\dagger \hat{a}_j \hat{a}_{j'}, \end{aligned} \tag{5.32}$$

where

$$U_{i,i',j,j'} = g \int d^3\boldsymbol{r} w_i^*(\boldsymbol{r}) w_{i'}^*(\boldsymbol{r}) w_j(\boldsymbol{r}) w_{j'}(\boldsymbol{r}). \tag{5.33}$$

This again simplifies owing to the localized Wannier functions $w_i(\boldsymbol{r})$ as $U_{i,i',j,j'} \approx U\delta_{i,i',j,j'}$.

Combining these results, we arrive at the Bose-Hubbard Hamiltonian

$$\hat{H}_{\text{BH}} = -J \sum_{\langle i,j \rangle} \hat{a}_i^\dagger \hat{a}_j + \frac{U}{2} \sum_j \hat{n}_j(\hat{n}_j - 1) + \sum_j (\varepsilon_j - \mu)\hat{n}_j, \tag{5.34}$$

where $\hat{n}_j = \hat{a}_j^\dagger \hat{a}_j$ and ε_j is a site-dependent potential [113], such as that of a residual confinement holding the atoms in an experiment. This effectively shifts the chemical potential locally, $\mu_i = \mu - \varepsilon_i$. The Hamiltonian is invariant under a global $U(1)$ transformation $\hat{a}_i \to \hat{a}_i e^{i\phi}$, and conserves the total number of particles $\hat{N} = \sum_i \hat{n}_i$.

We can infer the many-body eigenstates by considering the limiting cases. For $J/U \to 0$, the sites are decoupled from each other, and the number states $(\hat{a}_i^\dagger)^n |0\rangle$ of each site are the eigenstates. The occupation number n minimizing

the energy for different values of μ is given by

$$\begin{aligned} \mu/U < 0, \qquad & n = 0 \\ 0 < \mu/U < 1, \qquad & n = 1 \\ 1 < \mu/U < 2, \qquad & n = 2 \\ ..., & \end{aligned} \tag{5.35}$$

which can be also written as $n(\mu/U) = \lceil \mu/U \rceil$ for $\mu/U > 0$. Therefore, in this limit, the ground state is the Mott-insulating (MI) state,

$$|\Psi_{\mathrm{MI}}\rangle \propto \prod_{i=1}^{M} (\hat{a}_i^\dagger)^{N/M} |0\rangle \,, \tag{5.36}$$

with various occupation numbers N/M, which are required to be an integer value.

In the other limit $U/J \to 0$, the system can be described as a non-interacting Bose gas in a lattice potential. The particles will condense into the single-particle ground state, which is the $\boldsymbol{q} = 0$ Bloch wave. The many-body state becomes the superfluid (SF) state, and can be written as

$$|\Psi_{\mathrm{SF}}\rangle \propto (\hat{a}_{\boldsymbol{q}=0}^\dagger)^N |0\rangle \tag{5.37}$$

where $\hat{a}_{\boldsymbol{q}=0}^\dagger = M^{-1/2} \sum_{i=1}^{M} \hat{a}_i^\dagger$. We note that this expression for an 'ideal' superfluid does not describe superfluidity, which requires non-vanishing interactions.

One simple approach to understanding the phases of a many-body model is the mean-field approximation [113, 188, 194–197]. In the Bogoliubov theory, we already used the strategy of replacing the operators with an expectation value. We would like to understand the strongly interacting limit, and thus we keep the on-site term in the Hamiltonian (Eq. 5.34) and approximate the tunneling term as

$$\hat{a}_i^\dagger \hat{a}_j \approx (\psi + \delta a_i^\dagger)(\psi + \delta a_j) \approx \hat{a}_i^\dagger \psi + \hat{a}_j \psi - \psi^2. \tag{5.38}$$

This decouples each site from neighbors, and the Hamiltonian becomes

$$H_{\mathrm{MF}} = \sum_i \left[-zJ(\hat{a}_i^\dagger + \hat{a}_i)\psi + \frac{U}{2}\hat{n}_i(\hat{n}_i - 1) - \mu \hat{n}_i + zJ\psi^2 \right]. \tag{5.39}$$

The mean field ψ can also be thought as a variational parameter. It can be shown that the energy of the original Hamiltonian $\langle H_{\mathrm{BH}} \rangle_{\mathrm{MF}}$ with respect to the

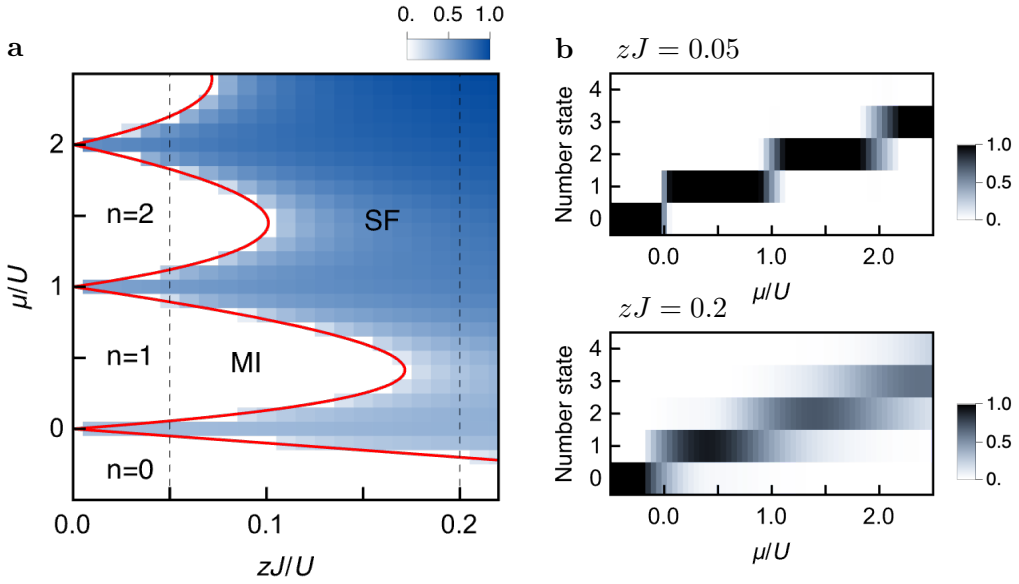

Figure 5.4: **a**, Phase diagram of the Bose-Hubbard model in the mean-field approximation, with the density showing the mean field ψ (in a.u.). The solid line is from the perturbation theory. **b**, Populations (probabilities) of the different number states $(n!)^{-1/2}(\hat{a}^\dagger)^n\,|0\rangle$ versus μ/U from the mean-field calculations for $zJ = 0.05$ and $zJ = 0.2$.

ground state of $H_{\rm MF}$ is minimized when $\psi = \langle \hat{a}_i \rangle_{\rm MF}$ [197], providing support for the mean-field treatment. The $U(1)$ symmetry is broken in $H_{\rm MF}$, implying the existence of a symmetry-broken phase with ψ being the order parameter.

The Hamiltonian $H_{\rm MF}$ can be solved numerically to a good accuracy in the number-state basis, i.e. $|\Psi\rangle = (\alpha_0 + \alpha_1\hat{a}^\dagger + \alpha_2 2^{-1/2}(\hat{a}^\dagger)^2 + ...)\,|0\rangle$ with some cutoff of the highest number state (dropping the index i as the sites are decoupled). The mean field ψ is determined by minimizing the ground-state energy, and the phase boundary can be inferred as points in the parameter space where ψ changes from zero to non-vanishing values, as shown in Fig. 5.4a. In terms of the state populations, in the MI regime $zJ/U \sim 0.05$, the many-body state is in a single number state (number squeezed), but in the SF regime $zJ/U \sim 0.2$, the state is in a superposition of various number states, exhibiting fluctuating particle numbers per site (Fig. 5.4b).

An analytic expression for the phase boundary can be obtained from the second-order perturbation theory [113, 196]. We consider $\hat{V} = -zJ(\hat{a}^\dagger + \hat{a})\psi$ as a small perturbation to $\hat{H}_0 = U\hat{n}(\hat{n}-1)/2 - \mu\hat{n} + zJ\psi^2$, and start from a number state with $n = n(\mu/U)$ (Eq. 5.35) as a ground state. We obtain up to

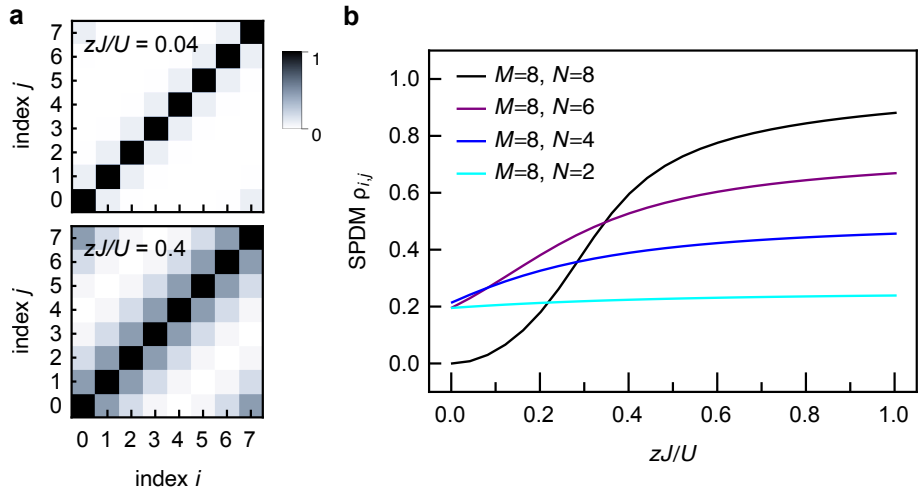

Figure 5.5: Single-particle density matrix (SPDM) of the Bose-Hubbard model obtained numerically. **a,** SPDM $\rho_{i,j}$ of the BHM ground state for $zJ/U = 0.04$ (Top) and 0.4 (Bottom). Calculated with $M = 8$ sites and $N = 8$ atoms. **b,** SPDM element $\rho_{i=1,j=3}$ versus zJ/U calculated with $M = 8$ sites and various atom number N.

the second order

$$
\begin{aligned}
E_n^{(0)} &= \langle n| \hat{H}_0 |n\rangle = \frac{U}{2} n(n-1) - \mu n + zJ\psi^2 \\
E_n^{(1)} &= \langle n| \hat{V} |n\rangle = 0 \\
E_n^{(2)} &= \sum_{n' \neq n} \frac{|\langle n'| V |n\rangle|^2}{E_n^{(0)} - E_{n'}^{(0)}} = (zJ)^2 \psi^2 \left[\frac{n}{U(n-1) - \mu} + \frac{n+1}{\mu - Un} \right]
\end{aligned}
\tag{5.40}
$$

If the multiplication factor of ψ^2 is positive, then the energy is minimized with $\psi = 0$. If its negative, ψ will start to grow (the energy will still be bounded below by the higher-order $\mathcal{O}(\psi^4)$ corrections). The factor becomes zero when

$$
zJ/U = \frac{(n - \mu/U)(-n + 1 + \mu/U)}{1 + \mu/U},
\tag{5.41}
$$

which provides the phase boundary in the parameter space μ/U vs. zJ/U, together with the discrete values of n as a function of μ/U (Fig. 5.4).

For a small system, the BHM Hamiltonian may be solved numerically by directly diagonalizing it [76, 198]. The Hamiltonian matrix can be represented, for example, in a number-state basis with some fixed number M of sites and number N of atoms. The dimension of this matrix for a one-dimensional

system will be $(M+N-1)!/N!(M-1)!$ (to infer this, one may consider $M-1$ dividers partitioning atoms). Once the ground state is obtained, we can compute a discrete version of the single-particle density matrix (SPDM; Eq. C.13), $\rho_{i,j} = \langle \hat{a}_i^\dagger \hat{a}_j \rangle$. This is related to the momentum distribution of the atoms [174],

$$n(k) \propto \sum_{j,j'=1}^{M} e^{id(j-j')k} \rho_{j,j'}, \tag{5.42}$$

and therefore relevant to the observable quantities in our experiment. The decay of the off-diagonal coherence $\rho_{i,j+r}$ as a function of j is closely related to the many-body phase. In the SF and MI phases, the rescaled SPDM $C_j(r) = \rho_{j,j+r}/\hat{n}_j\hat{n}_{j+r}$ is known to follow an algebraic decay $C_j(r) \propto A|r|^{-K/2}$ and an exponential decay $C_j(r) \propto Be^{-|r|/\xi}$, respectively [174]. In Fig. 5.5, we computed $\rho_{i,j}$ for $M = N = 8$ with a periodic boundary condition, which is sharply localized in the MI phase and smeared out in the SF phase, whose momentum version will behave in the opposite way [76]. The value of $C_j(r)$ can be used to detect the phase transition, and for our numerical simulation of a small lattice, $r = 2$ exhibits a smooth transition between the two phases (Fig. 5.5b). For the atom numbers N that are incommensurate with the site number M, the off-diagonal element does not vanish even near $zJ/U = 0$. Since the filling factor $n = N/M$ is not well defined, it will stay in the SF phase. In an inhomogeneous system with some site-dependent potential, the effective chemical potential will be position-dependent, leading to a wedding cake structure with alternating MI and SF regions. This has been measured spectroscopically [123, 199] and in spatially-resolved ways [200–202].

The behavior of a system near the phase transition is of high interest in condensed matter physics [203], as near these quantum critical points, many different systems can be described by the same theory and belong to the same universality class. The energy gap and the inverse of the characteristic length scale as some powers of the distance from the critical point. The SF-MI transitions can be described by a complex space-time dependent field $\psi(\boldsymbol{r}, \tau)$ analogous to the mean field ψ via the path-integral method (Eq. C.1), and can be systematically expanded in terms of $\psi(\boldsymbol{r}, \tau)$ near the critical point [197]. In particular, near the tips of the lobes, the transition is in the universality class of the relativistic scalar field theory with $M = 2$ components (real and imaginary) in $3 + 1$ spacetime dimensions, which also describes other important models, including the Ising model in d space dimensions [175, 203].

The effects of disorders, which are common in realistic systems, on these phase transitions are also interesting. It has been theoretically shown that

there is no direct SF-MI transition in the presence of disorders [204, 205], e.g. with the onsite energy ε being randomly distributed over some interval, and such a transition should be intervened by the Bose-glass phase [206, 207], an insulating phase without a gap. There are also interesting variations of the BHM, such as with long-range tunneling beyond the nearest neighbors [208], off-site interactions [209] (extended BHM), or multiple species [210]. In the hardcore boson limit, $\hat{a}_j^\dagger \hat{a}_j^\dagger |0\rangle = 0$, the operator can be mapped to a spin σ_j^+ and can be used to realize two-level emitters [68, 87], which we discuss further in the next chapter.

5.2.4 Lieb-Liniger parameter in one dimension

We briefly discuss the strongly-interacting limit of a Bose gas in one dimension. As discussed in Sec. 5.1.3, an effective 1D system can be obtained by confining the particles in a one-dimensinoal tube, leading to an effective interaction strength $g_{1\mathrm{D}}$ and a linear density $n_{1\mathrm{D}}$. The criterion for the weak and strong interactions without a lattice is provided by the ratio of the typical interaction energy over the kinetic energy, $\gamma \sim E_{\mathrm{int}}/E_{\mathrm{kin}}$. This is called the Lieb-Liniger parameter [211], $\gamma = g_{1\mathrm{D}} n_{1\mathrm{D}}/(\hbar^2 n_{1\mathrm{D}}^2/m)$. The mean-field description is applicable for $\gamma \ll 1$ [185], but for $\gamma \gg 1$, the bosonic gas becomes so-called the Tonks-Girardeau gas. In this regime, the bosons become distinct and behave like fermions [212], resulting in distinct momentum profiles observed in the experiments [213, 214]. The single-particle wavefunctions decay over the typical interparticle spacing, as the bending of the wavefunctions is favored over the overlapping with the neighbors, and form an effective lattice structure even without a real lattice [215]. In between the two regimes $\gamma \sim 1$, the bosons can still exhibit superfluidity, but the coherence length is limited by the interactions [171].

To compute the value of γ for our typical experiments, we consider 20×10^3 atoms distributed over 10^3 tubes, yielding $N = 20$ atoms per tube. A typical tube confinement $a_{\mathrm{ho},\perp} \sim 70$ nm (for $s_\perp = 40$) gives a 1D interaction strength $g_{1\mathrm{D}}/\hbar \approx 1.7 \times 10^3$ m/s. The chemical potential can be computed from the 1D GPE (Eq. 5.18), and the Thomas-Fermi radius is given by $R_{\mathrm{TF}} = \sqrt{2\mu/m\omega_z^2} \approx 5.8$ μm, which corresponds to $n_{1\mathrm{D}} \approx 3.5$ $\mu\mathrm{m}^{-1}$ and $\gamma \approx 0.67$. In real experiments, each tube has a different number of atoms, and taking this into account also yields a similar value [76].

Chapter 6

Realization of a Polaritonic Bose-Hubbard Model

This chapter contains a short review and some technical details regarding our publication *Formation of matter-wave polaritons in an optical lattice*, Nature Physics **18**, 657-661 (2022) [56]. The work was conducted by J. Kwon, the author, A. Lanuza, and D. Schneble. The author of this dissertation gratefully acknowledges the contributions from the co-authors. More details can be found in the PhD thesis of J. Kwon [138].

6.1 Introduction

Quantum emitters admit bound states featuring a localized evanescent photon [27, 28]. The possibility of realizing novel many-body spin systems with tunable long-range interactions is generating large theoretical [26, 64–69] and experimental [101, 102, 208, 216] interests in such systems, with motivation to understand non-local properties [217] and potential applications in quantum computing [70]. In the context of an array of emitters, such a bound state is a type of polariton [60–63], a light-matter hybrid quasiparticle with transport properties. While the bound states acquire mobility only via photon-mediated interactions, we can also imagine excitations hopping directly between the emitters in parallel. This lattice scenario for photons can be realized, for example, with direct capacitive coupling between transmon qubits in circuit quantum electrodynamics (QED) [218, 219], which has been used to prepare dark states for a pair of emitters [33].

A more direct example of radiatively-coupled mobile excitations is excitons, electron-hole pair excitations in a semiconductor. The excitons placed in a

microcavity can be strongly coupled to photons, forming exciton-polaritons [72, 73]. These quasiparticles are revealed in the mode splitting [71], as a result of hybridizing the quadratic dispersion of lighter photons in the planar cavity and the flat dispersion of heavier excitons in the semiconductor, and have been used to realize Bose-Einstein condensation [111, 220]. In these polaritonic platforms, as well as waveguide and circuit QED, novel quantum phases of light have been proposed [221, 222], but the challenge is to achieve strong many-body interactions [223, 224].

Extending our analogy of quantum emitters condensed matter physics, we realize a Bose-Hubbard model of polaritons in an optical lattice. The excitations (red atoms) in the lattice are coupled to the matter waves (blue atoms), each playing the roles of excitons and photons. By placing the energy $\sim \hbar\Delta$ of the excitations below the mode continuum of matter waves, the two constituents form a bound state, with the matter-wave part is localized in the form of $e^{-k_{\rm bs}z}$, where $k_{\rm bs} \sim \sqrt{2m|\Delta|/\hbar}$ (cf. Section 2.2.4). The quasiparticle can hop between the sites either via direct tunneling of excitations or matter-wave mediated tunneling, and will be called "matter-wave polaritons". While it contains no real photon, this quasiparticle captures the essence of polaritons, namely the hybridization of lighter and heavier constituents. In the following, we first discuss the framework of the polaritonic Bose-Hubbard model, and its experimental implementation. We then describe how our experiments using modulation spectroscopy and peak-width analysis reveal the polaritonic nature of this many-body system, the polariton branch energy gap and the renormalization of the transport coefficient.

6.2 Polaritonic Bose-Hubbard model

In Section 2.3.4, we have shown that the Weisskopf-Wigner Hamiltonian can be written in the quasimomentum basis $\hat{r}_q^\dagger = M^{-1/2}\sum_j e^{iqz_j}\hat{r}_j^\dagger$ for the emitter excitations and $\hat{b}_{n,q}^\dagger = \hat{b}_{k_{n,q}}$ for the bath (matter-wave) excitations, with coupling $g_{n,q} = \sqrt{M}|g_{j,k}|$ encoding the overlap between the two states. While $\hat{r}_q^\dagger$ creates a timed Dicke state, i.e. a coherent superposition of excitations in an array of emitters in the context of waveguide QED, it can be generalized to the Bloch waves in an optical lattice, with $\hat{r}_j^\dagger$ generating a Wannier state. The coupling reflects the overlap between a Bloch wave and a free wave,[1] $g_{n,q} = \langle 0|\,\hat{r}_q\hat{b}_{n,q}^\dagger\,|0\rangle = \sqrt{M}\,\langle 0|\,\hat{r}_{j=0}\hat{b}_{k_{n,q}}^\dagger\,|0\rangle$. The Bloch waves in the lattice have a band structure, which can be reflected in the energy $\Delta \to \Delta_q$. The lattice

[1] As before, we assume a finite system of M lattice sites with the periodic boundary condition. The system size is $L = Md$.

version of the Weisskopf-Wigner Hamiltonian can be written as

$$\hat{H} = \sum_q \hbar\Delta_q \hat{r}_q^\dagger \hat{r}_q + \sum_{n,q} \hbar\omega_{n,q} \hat{b}_{n,q}^\dagger \hat{b}_{n,q} + \sum_{n,q} \left(\hbar g_{n,q} \hat{r}_q^\dagger \hat{b}_{n,q} + \text{H.c.} \right). \tag{6.1}$$

It is diagonalized by defining the polariton operators (cf. Section 2.3.4),

$$\hat{c}_{\tilde{n},q}^\dagger = A_{\tilde{n},q} \hat{r}_q^\dagger + \sum_n B_{\tilde{n},n,q} \hat{b}_{n,q}^\dagger, \tag{6.2}$$

with the polariton band (branch) index $\tilde{n}$. The polaritons can be written either in the Bloch or Wannier bases,

$$\hat{c}_{\tilde{n},q}^\dagger = \frac{1}{\sqrt{M}} \sum_j e^{iqz_j} \hat{c}_{\tilde{n},j}^\dagger, \quad \hat{c}_{\tilde{n},j}^\dagger = \frac{1}{\sqrt{M}} \sum_q e^{-iqz_j} \hat{c}_{\tilde{n},q}^\dagger. \tag{6.3}$$

The polariton band structure $\tilde{\omega}_{\tilde{n},q}$ is determined from the eigenvalue equation

$$\tilde{\omega}_{\tilde{n},q} - \Delta_q = \sum_n \frac{g_{n,q}^2}{\tilde{\omega}_{\tilde{n},q} - \omega_{n,q}}, \tag{6.4}$$

where $\omega_{n,q} \equiv \omega_{k_{n,q}}$ is the matter-wave dispersion. In the polariton basis, the Hamiltonian can be written as

$$\hat{H} = \sum_{\tilde{n},q} \hbar\tilde{\omega}_{\tilde{n},q} \hat{c}_{\tilde{n},q}^\dagger \hat{c}_{\tilde{n},q} = \sum_{\tilde{n},j,j'} \tilde{J}_{\tilde{n},j,j'} \hat{c}_{\tilde{n},j}^\dagger \hat{c}_{\tilde{n},j'}, \tag{6.5}$$

where the tunneling rate is $\tilde{J}_{\tilde{n},j,j'} = M^{-1} \sum_q e^{iq(z_j - z_{j'})} \hbar\tilde{\omega}_{\tilde{n},q}$. This provides the quasiparticle picture, where the modes of lattice excitations and matter waves hybridize and form the polaritonic bands $\tilde{\omega}_{\tilde{n},q}$. The first and second polariton bands are also called the lower and upper polariton branches (LP and UP) [111].

In Fig. 6.1, we show the tunneling rates for polaritons and lattice excitations. The polaritons show a large offset of the tunneling rate compared to the bare excitations, especially in a deep lattice. The origin of this shift can be seen by combining the bare rate with the effective tunneling rate between quantum emitters obtained in the Markovian and the tight-binding limit (Eq. 2.73)

$$J_{j,j'}^{(\text{QE})} \approx -\frac{\Omega^2}{|\bar{\Delta}|} \frac{\sqrt{\pi}}{4} a_{\text{ho}} k(|\bar{\Delta}|) e^{-k(|\bar{\Delta}|)|z_j - z_{j'}|}, \tag{6.6}$$

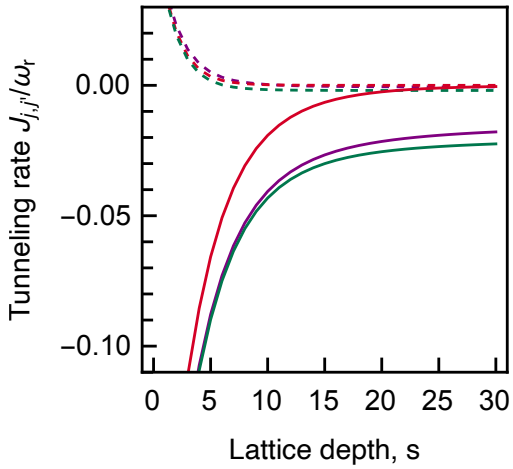

Figure 6.1: Polariton and bare tunneling rates $\tilde{J}, J$ computed for $\Omega = \omega_r$, $\Delta = -0.5\omega_r$, and for a range of lattice depth s. The purple line is the polariton tunneling rate $-\tilde{J} = \tilde{J}_{0,1}$, the red line is the bare lattice-excitation tunneling rate $-J = J_{0,1}$, and the green line is the sum of bare and the quantum-emitter tunneling rate $J_{0,1} + J_{0,1}^{(\mathrm{QE})}$. The dashed lines are for the next-nearest tunneling rates. ($\omega_r = 2\pi \times 3676$ Hz.)

with the renormalizing correction of the emitter energy Δ due to the Lamb shift $\bar{\Delta} = \Delta - \Omega^2/\omega_{\mathrm{ho}}$ [18, 20, 93]. This bound-state induced tunneling rate quantitatively captures the enhancement of the excitonic tunneling rate, indicating that the hopping is mediated by the matter waves. We note that for our typical experimental parameters, the next-nearest-neighbor tunneling is largely suppressed.

These quasiparticles will form a many-body system via interactions, e.g. quadratic terms of the form $\sim \hat{c}^\dagger \hat{c}^\dagger \hat{c}\hat{c}$. In the following, we derive the on-site interactions, focusing on the ground band $\tilde{n} = 1$ (and dropping the band index). The interactions originate from atomic scattering, and the s-wave scattering Hamiltonian for two species is given by

$$H_{\mathrm{int}} = \frac{1}{2} \sum_{\alpha,\alpha'} g_{\alpha,\alpha'} \int_{\boldsymbol{r}} \int_{\boldsymbol{r}'} \hat{\psi}_\alpha^\dagger(\boldsymbol{r}) \hat{\psi}_{\alpha'}^\dagger(\boldsymbol{r}') \delta(\boldsymbol{r} - \boldsymbol{r}') \hat{\psi}_{\alpha'}(\boldsymbol{r}') \hat{\psi}_\alpha(\boldsymbol{r}), \tag{6.7}$$

where $\alpha = r, b$ (red and blue), and the interaction strength $g_{\alpha,\alpha'} = 4\pi\hbar^2 a_{\alpha,\alpha'}/m$ depends on the scattering length $a_{\alpha,\alpha'}$ between the species. Since we are working in one dimension (tubes), we may integrate out the transverse wavefunctions $\hat{\psi}(x, y) \to \psi_\perp(x, y)$. The interaction Hamiltonian in one dimension be-

comes

$$H_{\rm int}^{(1D)} = \frac{1}{2}\sum_{\alpha,\alpha'} g_{\alpha,\alpha'}^{1D} \int dz \hat{\psi}_\alpha^\dagger(z)\hat{\psi}_{\alpha'}^\dagger(z)\hat{\psi}_{\alpha'}(z)\hat{\psi}_\alpha(z), \tag{6.8}$$

where the effective interaction strength is $g_{\alpha,\alpha'} = g_{\alpha,\alpha'}/(2\pi a_{{\rm ho},x} a_{{\rm ho},y})$, which depends on the transverse harmonic confinement ($a_{{\rm ho},x}$,$a_{{\rm ho},y}$). The operators follow $[\hat{\psi}_\alpha(z), \hat{\psi}_{\alpha'}^\dagger(z')] = \delta_{\alpha,\alpha'}\delta(z-z')$. The leading-order contribution is the on-site interactions $(\tilde{U}/2)\hat{c}_j^\dagger\hat{c}_j^\dagger\hat{c}_j\hat{c}_j$, where we define the interaction energy $\tilde{U}$ as[2]

$$\begin{aligned}\tilde{U} &\equiv \frac{1}{2}\langle 0|\,\hat{c}_j\hat{c}_j H_{\rm int}^{(1D)}\hat{c}_j^\dagger\hat{c}_j^\dagger\,|0\rangle\,|_{j=0} \\ &= \int dz\left[g_{r,r}^{1D}|\tilde{\psi}_r(z)|^4 + 2g_{r,b}^{1D}|\tilde{\psi}_r(z)|^2|\tilde{\psi}_b(z)|^2 + g_{b,b}^{1D}|\tilde{\psi}_b(z)|^4\right].\end{aligned} \tag{6.9}$$

The wavefunctions $\tilde{\psi}_r(z)$, $\tilde{\psi}_b(z)$ are the position space amplitudes of the polaritons, and we used the position space expansion of $\hat{c}_j$ as

$$\hat{c}_j = \int dz\left[\tilde{\psi}_r^*(z-z_j)\hat{\psi}_r(z) + \tilde{\psi}_b^*(z-z_j)\hat{\psi}_b(z)\right]. \tag{6.10}$$

The wavefunctions are obtained from

$$\begin{aligned}\tilde{\psi}_r(z-z_j) &= \langle 0|\,\hat{\psi}_r(z)\hat{c}_j^\dagger\,|0\rangle = \frac{1}{\sqrt{M}}\sum_q e^{-iqz_j}A_q\psi_q(z) = \frac{1}{\sqrt{M}}\sum_q A_q\psi_q(z-z_j) \\ \tilde{\psi}_b(z-z_j) &= \langle 0|\,\hat{\psi}_b(z)\hat{c}_j^\dagger\,|0\rangle = \frac{1}{\sqrt{M}}\sum_{n,q} e^{-iqz_j}B_{n,q}\psi_{k_{n,q}}(z) = \frac{1}{\sqrt{M}}\sum_{n,q} B_{n,q}\psi_{k_{n,q}}(z-z_j),\end{aligned} \tag{6.11}$$

where we used the expansions $\hat{r}_q^\dagger = \int dz\psi_q(z)\hat{\psi}_r^\dagger(z)$ and $\hat{b}_{n,q}^\dagger = \int dz\psi_{k_{n,q}}(z)\hat{\psi}_b^\dagger(z)$ in terms of the Bloch waves $\psi_q(z)$ and the free waves $\psi_{k_{n,q}}(z) = L^{-1/2}e^{ik_{n,q}z}$.

With the nearest-neighbor tunneling rate and the on-site interactions, we can construct the Bose-Hubbard model of polaritons (for the ground band

[2]The overall factor of 4 comes from the commutation relation. Alternatively, one can consider the position z as discrete, and infer the multiplicative factor from $\hat{\psi}\hat{\psi}\hat{\psi}^\dagger\hat{\psi}^\dagger\,|0\rangle = \hat{\psi}\hat{\psi}\sqrt{2}\,|2\rangle = 2\,|0\rangle$.

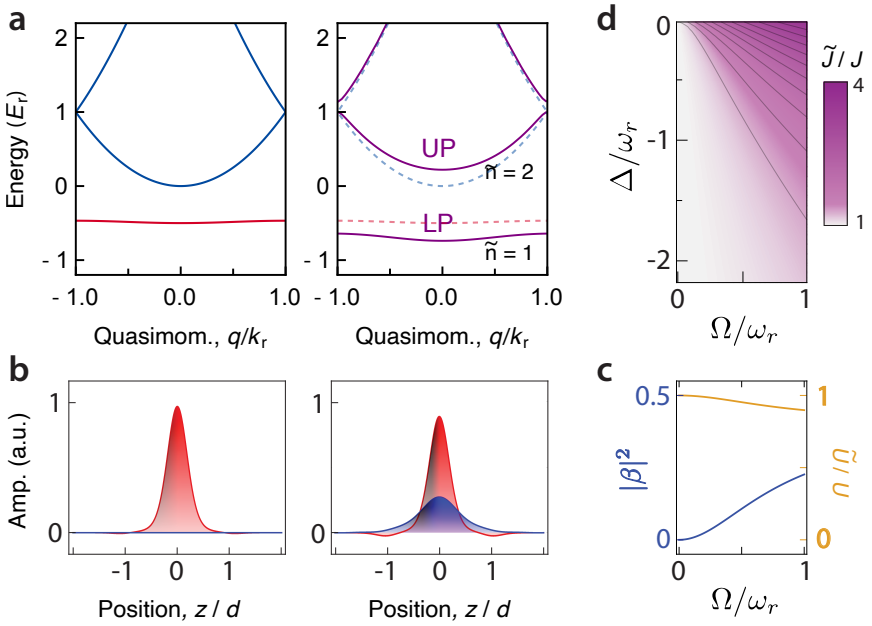

Figure 6.2: Theoretical properties of the polariton system for $s = 10$. **a,** Right, polariton band structure for $\Omega = \omega_r$, $\Delta = -0.5\omega_r$. Left, bare dispersions of the matter waves ($|b\rangle$; blue) and lattice excitations ($|r\rangle$; red). **b,** Right, position-space wavefunction of a polariton. Left, wavefunction of uncoupled lattice excitation. **c,** Fraction $|\beta|^2$ of the $|b\rangle$ state in the polariton (blue curve), and the interaction energy $\tilde{U}$ (yellow curve) as a function of Ω for $\Delta = -0.5\omega_r$. **d,** Tunneling rate of polaritons in the $\tilde{n} = 1$ band, as a function of Ω and Δ. (Figure reproduced from [56].)

$\tilde{n} = 1$) as

$$\hat{H} = -\tilde{J}\sum_j (\hat{c}^\dagger_{j+1}\hat{c}_j + \hat{c}^\dagger_j\hat{c}_{j+1}) + \frac{\tilde{U}}{2}\sum_j \hat{c}^\dagger_j\hat{c}^\dagger_j\hat{c}_j\hat{c}_j + \sum_j \tilde{\varepsilon}_j\hat{c}^\dagger_j\hat{c}_j, \tag{6.12}$$

where we included the site-dependent energy $\tilde{\varepsilon}_j$ due to the residual harmonic confinement holding the atoms. In Fig. 6.2, we show some properties of the model, including the polariton band structure and the spatial wavefunction. We expect the polaritonic properties to be mainly revealed in the renormalization of the tunneling rate, as the shift of interaction energy $\tilde{U}$ is small for the relevant parameters ($\delta U/U \sim 0.1$).

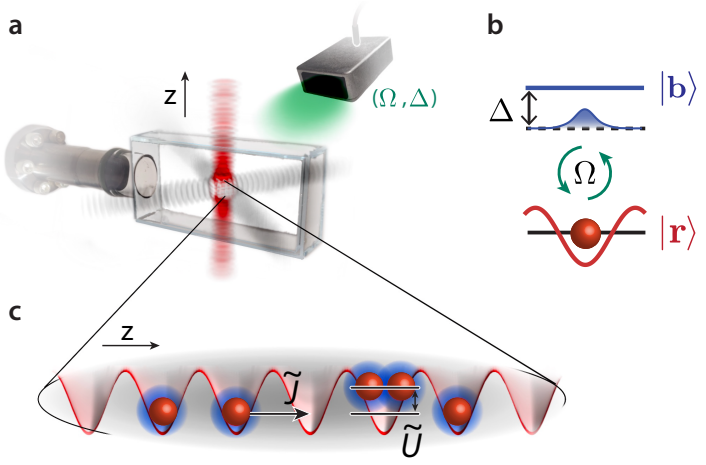

Figure 6.3: Experimental setup for matter-wave polaritons. **a,** The transverse lattices ($\lambda_\perp = 1064$ nm) generate a bundle of strongly-confining one-dimensional tubes ($s_\perp \geq 18$). The state-selective lattice (z direction; $\lambda_z = 790.0$ nm and σ^--polarized) traps the $|r\rangle$ (red) atoms, while the $|b\rangle$ atoms remain unconfined. **b,** 6.8GHz microwave couples the two species with strength Ω. The detuning $\Delta < 0$ is below the continuum of momentum states of the $|b\rangle$ atoms, generating bound states. **c,** Each tube contains a system of polaritonic quasiparticles, each as a superposition of a lattice excitation ($|r\rangle$) and a matter wave ($|b\rangle$), characterized by the tunneling and interaction coefficients, $\tilde{J}$, $\tilde{U}$. (Figure reproduced from [56].)

Experimental setup

The experimental setup is illustrated in Fig. 6.3. An optically trapped BEC of $\sim 10^4$ ^{87}Rb atoms in the hyperfine state $|r\rangle = |F = 1, m_F = -1\rangle$ $(5S_{1/2})$ is adiabiatically loaded into a bundle of $\sim 10^3$ optical-lattice tubes, which confines the atoms in isolated one-dimensional systems. The atoms are coupled to atoms in another hyperfine state $|b\rangle = |2, 0\rangle$. An additional state-selective lattice along the axial direction (z) traps only the $|r\rangle$ atoms, which are coupled to the momentum states of $|b\rangle$ atoms via microwave of strength Ω. Its negative detuning Δ places the energy of lattice excitations ($|r\rangle$) below the motional continuum of matter waves ($|b\rangle$) (Fig. 6.2a), and the polaritonic bound states are formed as discussed.

6.3 Probing transport properties

One way of understanding many-body systems is through their correlations. As discussed in Section 5.2.3, the momentum distribution $n(k)$ is related to to the single-particle density matrix $\rho_{j,j'} = \langle \hat{c}_j \hat{c}_{j'} \rangle$ via a Fourier transform, and the decay length of the correlation $C(r) = \rho_{j,j+r}$ is inversely related to the width of $n(k)$ [174]. In our experiments, we can use the inverse width of the diffraction peak in the time-of-flight (TOF) pictures as the indicator of the correlation length ξ of the system, which in turn depends on the ratio of the tunneling coefficient to interaction energy, $\tilde{J}/\tilde{U}$.

For the measurements, we use the tubes of depth $s_\perp = 18$ and the z lattice of various depths, which are ramped over $\sim$ 150 ms and $\sim$ 80 ms, respectively (reaching the maximum at the same time). From the TOF picture, we obtain the 1D atomic distributions with the transverse direction integrated, and extract the width σ of the central peak using a single Gaussian function (Fig. 6.4a inset). Our choice of the fit function reflects the assumption that the broad wings surrounding the central peak are from the thermal contributions (not from the ground-state many-body system) and that the central peak is sitting on a zero background (not on a thermal floor) (cf. [225]). The $|b\rangle$ atoms are blasted by a short pulse of cycling light during the TOF to eliminate the possibility of four-wave mixing [226].

For a typical Bose-Hubbard system in an optical lattice, the measurement of peak width vs. s_z results in two linear lines of zero and positive slope in the superfluid and Mott-insulating regimes, respectively [74, 76, 174, 206], as observed in Fig. 6.4 (red circles and lines). With the coupling turned on, we observe the reduction of σ, indicating enhanced transport (increased $\tilde{J}$). To relate this change to our model, we first obtain the function $\sigma(s_z)$ from the reference fit without coupling, relating σ and s_z. In addition, from the inverse of the function $J(s_z)$ relating the lattice depth s_z and the bare tunneling rate J, we get the effective lattice depth $\tilde{s}_z = J^{-1}(\tilde{J})$ for the coupled system. We then phenomenologically predict the new $\tilde{\sigma}$ as (assuming the change of U is negligible),

$$\tilde{\sigma} = \sigma(\tilde{s}_z), \quad \tilde{s}_z = J^{-1}(\tilde{J}). \tag{6.13}$$

We find that the predicted curve $\tilde{\sigma}$ quantitatively agrees with the observed width for a range of values of each experimental parameter, s_z, Ω, and Δ (Fig. 6.4a,b,c). In particular, near the kink at $s_z = 4$, the renormalization of the lattice depth to the effective value $\tilde{s}_z$ means the presence of the vacuum-coupling-driven phase SF-MI phase transition from the singly-occupied Mott

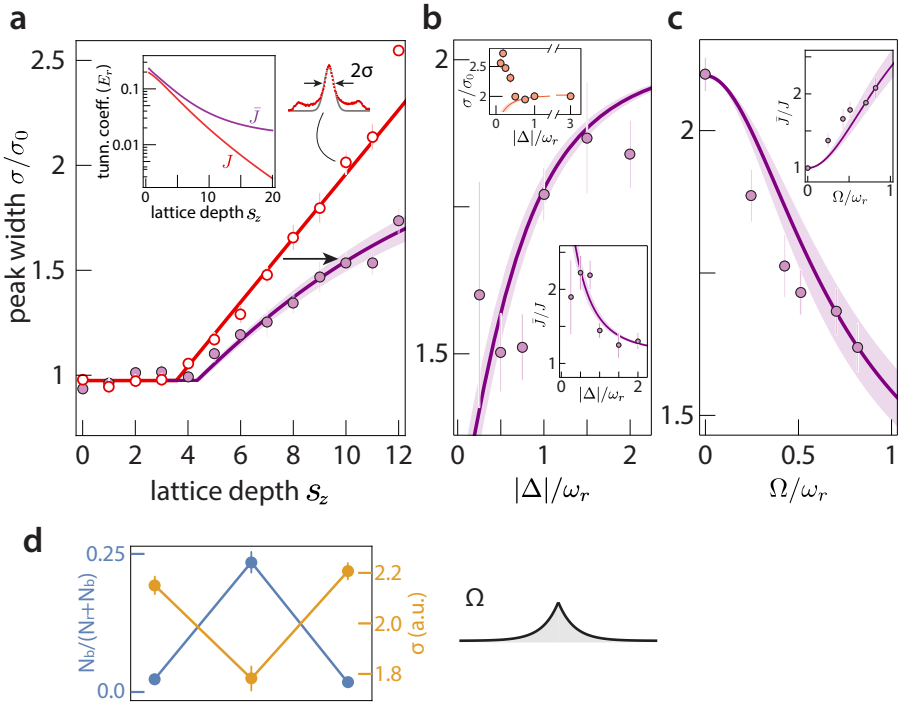

Figure 6.4: Renormalization of the tunneling rate extracted from the peak width σ of the $|r\rangle$ momentum distribution at $s_\perp = 18$. **a,** σ versus s_z for $\Delta/\omega_r = -0.50(7)$ and $\Omega/\omega_r = 0.84(2)$ (purple), compared to the reference for $\Omega = 0$ (red). The red line is the piecewise linear fit, with the slope of the first to set to be zero, establishing the operational relationship function $\sigma(s)$. The purple curve is obtained from $\sigma(\tilde{s}_z)$, with the renormalized depth $\tilde{s}_z$ from our model calculations. The shaded area accounts for the uncertainties in Δ and Ω. The inset shows the dependencies of the tunneling coefficients J (red) and $\tilde{J}$ (purple) on s_z. **b,c,** σ versus Δ or Ω at $s_z = 10$. The other paremters at $\Omega/\omega_r = 0.84(2)$ (**b**) or $\Delta/\omega_r = 1.01(1)$ (**c**). The two insets show the data points and the model curves in terms of $\tilde{J}/J$ (purple). The other inset (top of **b**) shows σ for $\Omega/\omega_r = 0.28(1)$ ($\hbar\Omega/U = 1.01(1)$). **d,** Fraction of $|b\rangle$ (blue) and $|r\rangle$ (orange) atoms after ramp up and down of the microwave (each for 2.5 ms, at $s = 10$), demonstrating reversibility. (Figure reproduced from [56].)

lobe into a superfluid (cf. Fig. 5.4), where the superfluidity is achieved via matter-wave mediated tunneling. We can also reverse the process (Fig. 6.4d), indicating that the transition coherently occurs in the ground state.

We note that for $|\Delta|$ close to zero (with $\Omega = 0.28\omega_r$ small), the peak width diverges. The energy where this happens is consistent with the on-site interaction energy, $|\Delta|/\omega_r \approx U/E_r = 0.28$. This indicates that the energy is

effectively shifted to positive due to interactions, leading to dissipation. For large $|\Delta|$ and $\Omega = 0.84\omega_{\mathrm{r}}$, the spatial extent of $|b\rangle$ component of LP is more compact, making the interaction-induced detuning shift to be also small (since $|r\rangle$ and $|b\rangle$ atoms see similar interaction shifts). Moreover, the continuum edge may be slightly moved away by the Lamb shift ($\Omega^2/\omega_{\mathrm{ho}} \sim 0.1$).

6.4 Probing the polariton energy branches

In addition to correlation properties, many-body systems can be characterized by energy gaps, and one well-known method to probe them in optical lattices is modulation spectroscopy. If a system's excitations exhibit a gapped dispersion, energy absorption from periodic perturbations of the lattice is prohibited when the modulation frequency lies within the gap. The technique is related to Bragg spectroscopy [227], with modulation creating sidebands [74, 76]. For the Bose-Hubbard model, experiments observed that a broad spectrum appears in the superfluid (SF) regime, but sharp peaks are observed at U and $2U$ in the Mott-insulating (MI) regime [5, 74]. Numerical studies attribute the first peak to the creation of a particle-hole pair, and the second peak to the hopping of a particle into a doubly-occupied site [75].

While the standard technique is to modulate the depth of the lattice in the axial direction [74, 76], this will change the ground-state energy of the confined $|r\rangle$ state, shifting the detuning Δ. In this work, we instead modulate the transverse lattice depth $s_\perp$ sinusoidally, leading to the modulation of U via that of the transverse confinement. For the measurements, we ramp up the tubes over 150 ms, and then the z lattice over 25 ms, both exponentially. We then adiabatically apply the microwave coupling, and modulate $s_\perp$ for a fixed duration and variable frequencies $\bar{\omega}$. The modulation is done by modulating the power of the 80 MHz RF input for the AOMs for the retro-reflection of the ODT1,2 beams (cf. Fig. 3.3).[3] For detection of the energy absorption, we turn off the coupling, and ramp down the z lattice to $s_z = 3$, bringing the system to a coherent regime, where the momentum diffraction peaks are visible. After thermalization, the tubes and optical trap are switched off. We

[3]During the implementation, we noticed that the outputs of our AOM drivers are frequency-dependent. We corrected the control voltage $V'(t) = f(\bar{\omega})(V_0 + \delta V \sin(\bar{\omega}t))$ with a factor

$$f(\bar{\omega}) = \frac{P(V_0 + \delta V_0) - P(V_0)}{P_{\mathrm{amp}}(V_0 + \delta V \sin(\bar{\omega}t)) - P(V_0)}, \tag{6.14}$$

where $P(V)$ is the output power without modulation, and P_{amp} is the observed amplitude for the modulated control input.

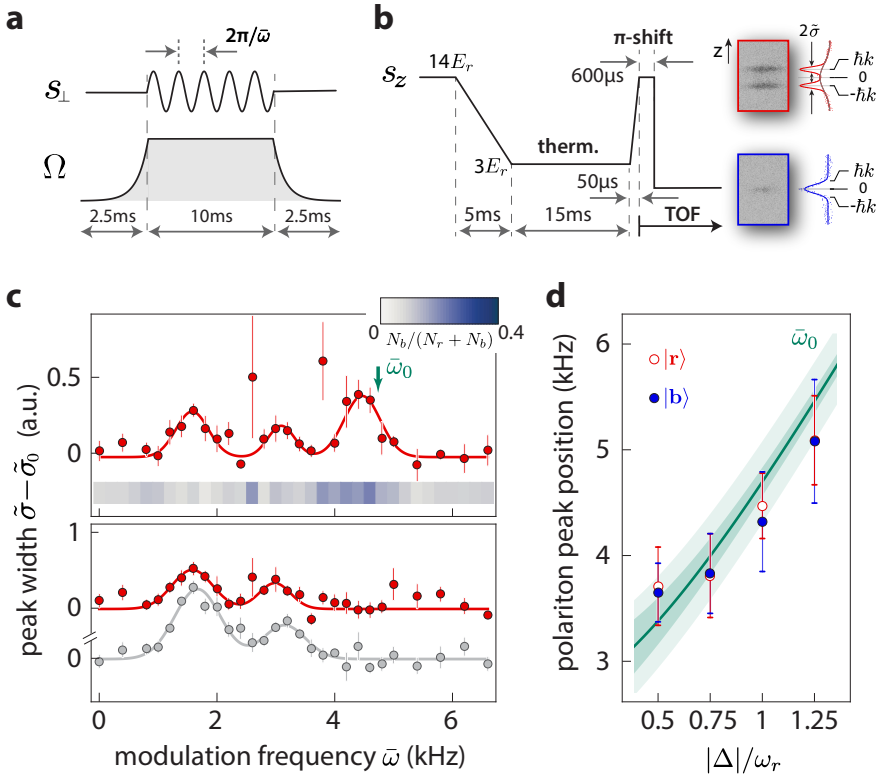

Figure 6.5: Modulation spectroscopy in the Mott regime ($s_\perp = 40, s = 14$). **a,** Modulation sequence. Ω is adiabatically ramped to prepare polaritons, and $s_\perp$ is modulated by ± 30 % at variable frequency $\bar{\omega}$. **b,** Detection sequence, including thermalization and a gravitaional π shift of the coherence peaks (separating from the thermal background). The inset panels show the momentum distributions of $|r\rangle$ and $|b\rangle$ atoms for $\Omega/\omega_r = 1.09(2)$ and $\Delta/\omega_r = -1.00(7)$. The widths $\tilde{\sigma}$ are extracted from Gaussian fits. **c,** Peak widths as a function of modulation frequency, with and without coupling (top and bottom), and additionally at $s_z = 10$ (gray). The blue stripe shows the fraction of $|b\rangle$ atoms. The error bars are the standard error of the mean (s.e.m.). **d,** Position of the third peak vs. detuning (red dots). The blue dots represent the position of the maximum $|b\rangle$ transfer. The green curve is the polariton energy gap $\bar{\omega}_0$, where the shaded area includes the width of the ground band (dark green) and the uncertainties in Δ and Ω (light green). (Figure reproduced from [56].)

temporarily jump the z lattice to $s = 15$ for 600 μs to induce the gravitational π-phase shift between the wells, to separate the peaks from a modulation-induced thermal background. We fit the resulting peaks at $\pm\hbar k_r$ on top of the thermal background with three Gaussians to extract the average width $\bar{\sigma}$ of the two diffraction peaks.

For the excitation spectra at $s_\perp = 40, s_z = 14$ (where $U = h \times 1.7kHz$),

there are two peaks at U and $2U$ already known in the MI regime. Their positions are relatively unchanged with coupling to matter waves (Fig. 6.5), indicating that the change in the on-site energy $\tilde{U}$ is small for our experimental parameters, consistent with our calculations (cf. Fig. 6.2c). However, we observe a third peak for the coupled case, whose position as a function of Δ is consistent with the energy gap between the first two polariton bands

$$\bar{\omega}_0 = \tilde{\omega}_{2,0} - M^{-1} \sum_q \tilde{\omega}_{1,q}. \tag{6.15}$$

This suggests that when the frequency of the interaction-energy ($\tilde{U}$) perturbation (caused by the periodic squeezing of tubes), exceeds the gap $\bar{\omega}_0$, the Wannier polariton states in the LP branch are converted to the quasi-free states in the UP branch, in the energy range of highest density of states. This picture is further supported by the excess $|b\rangle$ population left over near the peak position, even after the coupling being adiabatically turned off.

6.5 Concluding remarks

We have focused on the lower polariton branch (LP), and probed the excitation gap between the branches. We also demonstrated the polaritonic phase transition, driven by the vacuum coupling. The study of higher branches can be interesting, which are mostly of $|b\rangle$ atoms, corresponding to photons with renormalized transport. With a state-dependent z lattice (instead of state-selective), $|b\rangle$ atoms can be placed in a crystal structure like coupled-cavity arrays, and the analogue of photon blockade [228] can be realized. Coupling between multiple atomic species and photonic bands may enable multiexciton polaritons [229], multimode strong coupling [230], spin-orbit coupling [231], and even topological polaritons [232]. Furthermore, with higher precision on Δ [20], the interaction ranges may be extended to study novel long-range interacting quantum systems [70, 217].

Chapter 7

Conclusion and Future Directions

In this dissertation, we focused on the collective dynamics of quantum emitters simulated by our matter-wave platform in the context of waveguide QED. We demonstrated super- and subradiance of timed Dicke states in the non-Markovian regime, originating both from the propagation delay and the diverging density of states near the continuum edge. We observed the delayed onset of superradiance, and a beating of two bound states, one below the edge of the continuum (the gap) and one in the continuum. In the many-body regime, we directly probed the emergence of coherence via the quasimomentum distribution of the emitter excitations, and demonstrated its formation in the non-decaying, third state of the emitters. This experiment on collective dissipative dynamics complemented our prior work on many-body phases of matter-wave polaritons, which revealed collective coherent interactions between quantum emitters in a bandgap. There are many interesting regimes that are yet to be explored with our current setup, including strongly non-Markovian regimes (cf. Sections 2.3.5 and 4.6) or the higher polariton branches (cf. Section 6.5).

In our experiments on collective radiative phenomena, it was crucial to prepare appropriate initial states. The atoms in the optical lattice were prepared either in the superfluid or Mott-insulating phases, and when the vacuum coupling was suddenly turned on, these phases were interpreted as the timed Dicke states and the fully inverted states of quantum optics. When the vacuum coupling was ramped up adiabatically below the continuum edge, we formed polaritonic many-body phases. In the future, we can also consider an emitter array that is initially empty (in the ground state), and matter waves coming toward it. To enable this scattering scenario, our lab is currently developing

techniques to implement finite emitter arrays with clear boundaries. When a shallow lattice is used, multiple excitations are allowed to occupy the same emitter, and the scattering of multiple matter waves will be uncorrelated, simulating single-photon scattering. On the other hand, in a deep lattice, each lattice well will behave as a two-level emitter, which cannot absorb two matter waves simultaneously due to the collisional blockade. In this case, interesting photon-photon correlation effects [24, 233, 234] may be studied.

As a glimpse of future possibilities, we show some simulations in the single-photon regime, using the discrete Hamiltonian (Eq. 2.55). We use a Gaussian wavepacket to represent an incoming matter wave,

$$|\psi_0\rangle = \int dz \hat{\psi}_b^\dagger(z)\,|0\rangle\,\langle 0|\,\hat{\psi}_b(z)\,|\psi_0\rangle = \int dz (\pi\sigma_z^2)^{-1/4} e^{-(z-z_0)^2/2\sigma_z^2} e^{ik_0(z-z_0)} \hat{\psi}_b^\dagger(z)\,|0\rangle \tag{7.1}$$

in position space and

$$|\psi_0\rangle = \sum_k \hat{b}_k^\dagger\,|0\rangle\,\langle 0|\,\hat{b}_k\,|\psi_0\rangle = \sqrt{\frac{2}{L}} (\pi\sigma_z^2)^{1/4} e^{-(k-k_0)^2/2\sigma_k^2} e^{-ikz_0} \hat{b}_k^\dagger\,|0\rangle \tag{7.2}$$

in momentum space, where z_0 is the initial position and k_0 is the wavevector representing the initial momentum $\hbar k_0$. The initial width σ_z of the wavepacket is related to the momentum width $\sigma_k = 1/\sigma_z$, and we use a typical condensate size for $\sigma_z \sim 20d$. In Fig. 7.1, we show an example of a wavepacket scattering from an array containing 21 empty emitters. The Bragg condition, $k_0 = nk_\mathrm{r}$ with integer n, is used to maximize the effect. With this, we observe that the wavepacket is almost completely reflected on resonance, revealing the highly reflective character of emitters in one dimension [23, 24]. In real experiments, the resonance width can be a bit broadened by the mean-field energy of the condensate.

Using additional hyperfine levels, we can realize more interesting scenarios. A Fano resonance [235] can arise from interference of two scattering amplitudes, and we can trap additional atoms in the state $|2,2\rangle$ (or $|2,2\rangle$), which are not coupled to matter waves, to provide scattering through collisions [171]. With these atoms in the z lattice, which we may call $|g\rangle$ atoms ("green"), the s-wave interaction Hamiltonian (Eq. 6.7) can be written as

$$\hat{H}_{bg} = g_{1\mathrm{D}} \int dz \hat{\psi}_b^\dagger(z) \hat{\psi}_b(z) |\psi_g(z)|^2, \tag{7.3}$$

where $\psi_g(z)$ is the wavefunction of the $|g\rangle$ atoms, and $g_{1\mathrm{D}}$ is the 1D interaction

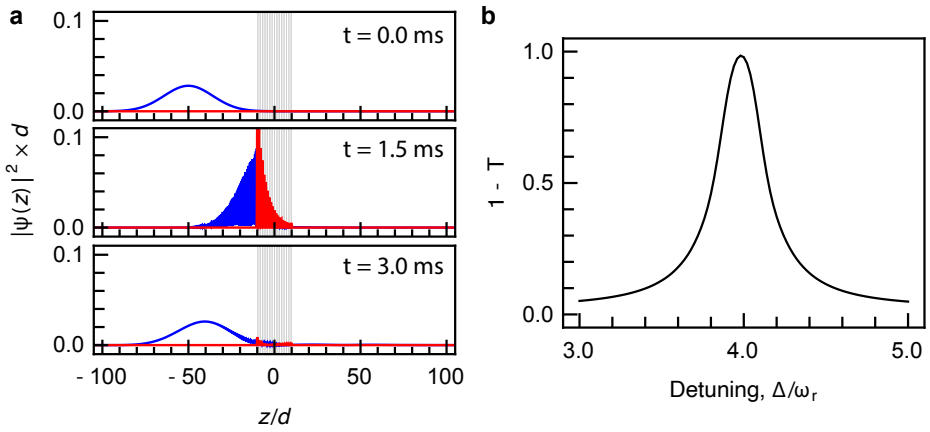

Figure 7.1: Scattering of a matter wave from an emitter array of length $M = 21$. Parameters at $\Omega = 0.5\omega_r$, $\Delta = 4.0\omega_r$, and $s = 10$. The wavepacket is launched with $k_0 = 2k_r$, $\sigma_z = 20d$, and $z_0 = -50d$. **a,** Spatial distribution of the incident matter wave (blue) and the emitter excitation (red). **b,** Reflection probability $1 - T$ as a function of detuning (emitter excitation energy) Δ. T is the integrated population over the region on the right side of the emitter array.

strength that depends on the transverse confinement (cf. Section 5.1.3). For a harmonic wavefuction $\psi_g(z) = (\pi a_{\rm ho}^2)^{-1/4} e^{-(z-z_j)^2/2a_{\rm ho}^2}$ at the jth emitter site, the potential barrier created by a $|g\rangle$ atom has a strength $g_{\rm 1D}(\pi a_{\rm ho}^2)^{-1/2}$ and width $a_{\rm ho}$, where $a_{\rm ho}$ depends on the lattice depth seen by the $|g\rangle$ atoms. With momentum-space expansion $\hat{\psi}_b(z) = \sum_k L^{-1/2} e^{ikz} \hat{b}_k$, we can write

$$\hat{H}_{bg} = \frac{g_{\rm 1D}}{L} \sum_{k,k'} e^{-(k-k')^2 a_{\rm ho}^2/4} e^{-i(k-k')z_j} \hat{b}_k^\dagger \hat{b}_{k'}, \tag{7.4}$$

which generates additional off-diagonal terms in the single-excitation Hamiltonian (Eq. 2.55). In Fig. 7.2a, we show an asymmetric resonance resulting from this additional scattering. In a deep tube confinement $s_\perp = 40$, we can make the collisional scattering comparable to the resonant scattering if we use the state $|g\rangle = |2, 2\rangle$, which experiences the z lattice twice as deep as that for $|r\rangle = |1, -1\rangle$ (cf. Fig. 3.9).

Electromagnetically induced transparency (EIT) [236] occurs in a three-level system, where coupling to the third level dresses the excited state (Autler-Townes splitting), and the destructive interference of absorption leads to a transparency window. We can simulate EIT by introducing a microwave coupling of strength Ω_c and frequency ν' to another trapped state $|g\rangle = |2, 1\rangle$

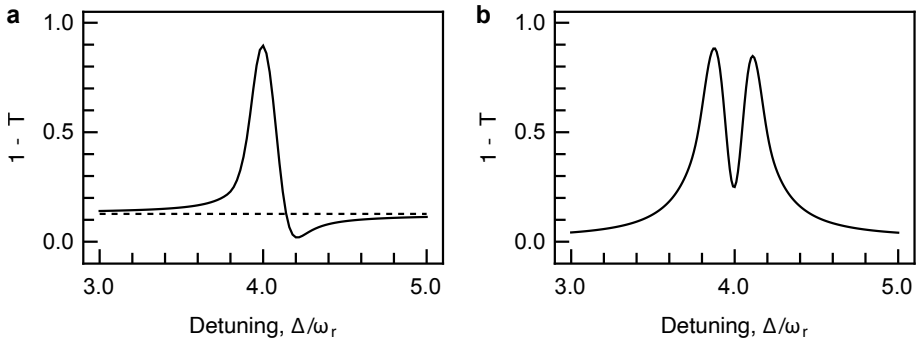

Figure 7.2: Fano resonance and electromagnetically induced transparency of a matter wave scattering from an emitter array of length $M = 21$ (thin vertical lines). The parameters are $\Omega = 0.5\omega_{\mathsf{r}}$, $\Delta = 4.0\omega_{\mathsf{r}}$, and $s = 10$, and the wavepacket is launched with $k_0 = 2k_{\mathsf{r}}$, $\sigma_z = 20d$, and $z_0 = -50d$. **a,** Collisional scattering from strongly confined $|g\rangle = |2, 2\rangle$ atoms leads to the asymmetric resonance ($g_{1\mathrm{D}}$ computed with $s_\perp = 40$). The dashed line is without vacuum coupling, $\Omega = 0$. **b,** Coupling to a third level $|g\rangle$ with strength $\Omega_c = 0.1\omega_{\mathsf{r}}$ and detuning $\delta_c = 0$ leads to a transparency window. The single-emitter decay rate for the chosen parameters is $\Gamma_1 = 2\pi \times 65$ Hz.

with energy $\omega_{0,g} > \omega_{0,r}$, which experiences the same z lattice as $|r\rangle$. This third level of the matter-wave emitter will have an energy $\Delta - \Delta_c$ with $\Delta_c = \nu' - (\omega_{0,g} - \omega_{0,r})$ in the rotating frame (e.g. via an additional transformation $U' = e^{i\nu' \sum_j \hat{g}_j^\dagger \hat{g}_j}$ in the Hamiltonian Eq. 2.7). To see how this might lead to an EIT effect, we consider a very coherent matter wave with momentum centered at $k = k_0$ that is similar to a laser beam. For a jth emitter, we can write the effective Hamiltonian as

$$\hat{H}_{j,k_0} \approx -\frac{\hbar}{2}\begin{pmatrix} -2\Delta & \Omega_c & \Omega\gamma_{j,k_0} \\ \Omega_c & -2(\Delta - \Delta_c) & 0 \\ \Omega\gamma^*_{j,k_0} & 0 & -2\omega_{k_0} \end{pmatrix} = -\frac{\hbar}{2}\begin{pmatrix} 2\Delta_{k_0} & \Omega_c & \Omega_p \\ \Omega_c & 2(\Delta_{k_0} + \Delta_c) & 0 \\ \Omega_p^* & 0 & 0 \end{pmatrix}, \tag{7.5}$$

where $\Delta_{k_0} \equiv \omega_{k_0} - \Delta$ and $\Omega_p \equiv \Omega\gamma_{j,k_0}$, and in the second equality we shifted the overall energy by $-\hbar\omega_{k_0}$ (also $\Omega \to -\Omega$ to make it a more conventional form). We can make Ω_p real by choosing $k_0 = 2nk_{\mathsf{r}}$ with integer n, and the Hamiltonian is exactly the same as that of a three-level atom interacting with a probe Ω_p and control Ω_c laser beams [236]. The decay will be induced by the coupling of the $|r\rangle$ level to the matter-wave continuum, which effectively shifts the energy by an imaginary term, $\Delta \to \Delta - i\Gamma_1/2$. In Fig. 7.2, we show an exact simulation of the full single-excitation Hamiltonian (Eq. 2.55) with

additional coupling to the $|g\rangle$ level. We can see the transparency window at the center where the two Lorentzian lineshapes overlap. With our apparatus, we may be also able to study the slowdown of the matter waves and the formation of the dark state polariton [237] by directly accessing the (quasi)momentum distributions of both the radiation and emitter components.

Besides waveguide QED, the state-selective lattice allows us to explore other interesting physics involving impurities. While the impurities moving in an ideal superfluid experience no friction below the critical velocity (cf. Section 5.1.1), their motion can still be affected in one dimension, especially in the strongly interacting regimes [215, 238, 239]. Interestingly, when the interaction strength G between an impurity and bath particles is the same as g among the bath particles, the friction is known to vanish, following the expression, $\kappa \propto T^4 \left(1 - g/G\right)^2$ [240] (see also discussion in [138]; modified when the masses of the impurity and bath particles are different [240]). The vanishing of the friction is related to the integrability and the existence of exact solutions of the bosonic particles in one dimension (Bethe ansatz), first obtained by Yang and Gaudin [241, 242]. The interaction strength can be experimentally tuned by varying the magnetic field via the Feshbach resonance (cf. Appendix A), and the resonance at $B_0 \sim 9$ G for the hyperfine ground states $|2, 0\rangle$ and $|1, 1\rangle$ of ^{87}Rb is accessible by our apparatus. The $|1, 1\rangle$ atoms in our moving state-selective lattice [76, 138] can play the role of impurities, whose frictions in the bath of $|2, 0\rangle$ atoms may be examined near the integrability point.

Lastly, we note that there are interesting theoretical proposals closely related to our waveguide-QED platform, which we have not yet explored. These include multiband effects [19], non-Markovian dynamics in higher dimensions [160, 243, 244], giant atoms in a shaking lattice [245], and topological waveguides with an optical superlattice [69, 110, 246]. Our platform has also been considered an important proof-of-principle toward more exotic possibilities, such as analogue quantum chemistry [14] or fermionic quantum optics [54]. In this regard, we anticipate that our lab will conduct many interesting experiments in the upcoming years.

Bibliography

[1] Richard P. Feynman. Simulating physics with computers. *International Journal of Theoretical Physics*, 21(6):467–488, 1982.

[2] I. M. Georgescu, S. Ashhab, and Franco Nori. Quantum simulation. *Rev. Mod. Phys.*, 86:153–185, 2014.

[3] M. H. Anderson, J. R. Ensher, M. R. Matthews, C. E. Wieman, and E. A. Cornell. Observation of Bose-Einstein Condensation in a Dilute Atomic Vapor. *Science*, 269(5221):198–201, 1995.

[4] K. B. Davis, M. O. Mewes, M. R. Andrews, N. J. van Druten, D. S. Durfee, D. M. Kurn, and W. Ketterle. Bose-Einstein Condensation in a Gas of Sodium Atoms. *Phys. Rev. Lett.*, 75:3969–3973, 1995.

[5] Markus Greiner, Olaf Mandel, Tilman Esslinger, Theodor W. Hänsch, and Immanuel Bloch. Quantum phase transition from a superfluid to a Mott insulator in a gas of ultracold atoms. *Nature*, 415(6867):39–44, 2002.

[6] Immanuel Bloch, Jean Dalibard, and Wilhelm Zwerger. Many-body physics with ultracold gases. *Rev. Mod. Phys.*, 80:885–964, 2008.

[7] M. Lewenstein, A. Sanpera, and V. Ahufinger. *Ultracold Atoms in Optical Lattices: Simulating quantum many-body systems*. OUP Oxford, 2012.

[8] Immanuel Bloch, Jean Dalibard, and Sylvain Nascimbène. Quantum simulations with ultracold quantum gases. *Nature Physics*, 8(4):267–276, 2012.

[9] Christian Gross and Immanuel Bloch. Quantum simulations with ultracold atoms in optical lattices. *Science*, 357(6355):995–1001, 2017.

[10] Florian Schäfer, Takeshi Fukuhara, Seiji Sugawa, Yosuke Takasu, and Yoshiro Takahashi. Tools for quantum simulation with ultracold atoms in optical lattices. *Nature Reviews Physics*, 2(8):411–425, 2020.

[11] Leticia Tarruell and Laurent Sanchez-Palencia. Quantum simulation of the Hubbard model with ultracold fermions in optical lattices. *Comptes Rendus Physique*, 19(6):365–393, 2018. Quantum simulation / Simulation quantique.

[12] Andrew J. Daley, Immanuel Bloch, Christian Kokail, Stuart Flannigan, Natalie Pearson, Matthias Troyer, and Peter Zoller. Practical quantum advantage in quantum simulation. , 607(7920):667–676, 2022.

[13] Erez Zohar, J Ignacio Cirac, and Benni Reznik. Quantum simulations of lattice gauge theories using ultracold atoms in optical lattices. *Reports on Progress in Physics*, 79(1):014401, 2015.

[14] Javier Argüello-Luengo, Alejandro González-Tudela, Tao Shi, Peter Zoller, and J. Ignacio Cirac. Analogue quantum chemistry simulation. *Nature*, 574(7777):215–218, 2019.

[15] Celia Viermann, Marius Sparn, Nikolas Liebster, Maurus Hans, Elinor Kath, Álvaro Parra-López, Mireia Tolosa-Simeón, Natalia Sánchez-Kuntz, Tobias Haas, Helmut Strobel, Stefan Floerchinger, and Markus K Oberthaler. Quantum field simulator for dynamics in curved spacetime. *Nature*, 611(7935):260–264, 2022.

[16] Carlos Navarrete-Benlloch, Inés de Vega, Diego Porras, and J Ignacio Cirac. Simulating quantum-optical phenomena with cold atoms in optical lattices. *New Journal of Physics*, 13(2):023024, 2011.

[17] Carlos Navarrete-Benlloch, Inés de Vega, Diego Porras, and J. Ignacio Cirac. Simulating quantum-optical phenomena with cold atoms in optical lattices. *New Journal of Physics*, 13(2):023024, 2011.

[18] Michael Stewart, Ludwig Krinner, Arturo Pazmiño, and Dominik Schneble. Analysis of non-Markovian coupling of a lattice-trapped atom to free space. *Phys. Rev. A*, 95(1):013626, 2017.

[19] Alfonso Lanuza, Joonhyuk Kwon, Youngshin Kim, and Dominik Schneble. Multiband and array effects in matter-wave-based waveguide QED. *Phys. Rev. A*, 105(2), 2022.

[20] L. Krinner, M. Stewart, A. Pazmiño, J. Kwon, and D. Schneble. Spontaneous emission of matter waves from a tunable open quantum system. *Nature*, 559:589–592, 2018.

[21] Michael Stewart, Joonhyuk Kwon, Alfonso Lanuza, and Dominik Schneble. Dynamics of matter-wave quantum emitters in a structured vacuum. *Phys. Rev. Res.*, 2(4):043307, 2020.

[22] Francesco Ciccarello, Peter Lodahl, and Dominik Schneble. Waveguide Quantum Electrodynamics. *Opt. Photon. News*, 35(1):34–41, 2024.

[23] Jung-Tsung Shen and Shanhui Fan. Coherent Single Photon Transport in a One-Dimensional Waveguide Coupled with Superconducting Quantum Bits. *Phys. Rev. Lett.*, 95:213001, 2005.

[24] Dibyendu Roy, C. M. Wilson, and Ofer Firstenberg. Colloquium: Strongly interacting photons in one-dimensional continuum. *Rev. Mod. Phys.*, 89:021001, 2017.

[25] Alexandra S. Sheremet, Mihail I. Petrov, Ivan V. Iorsh, Alexander V. Poshakinskiy, and Alexander N. Poddubny. Waveguide quantum electrodynamics: Collective radiance and photon-photon correlations. *Rev. Mod. Phys.*, 95(1):015002, 2023.

[26] D. E. Chang, J. S. Douglas, A. González-Tudela, C.-L. Hung, and H. J. Kimble. Colloquium: Quantum matter built from nanoscopic lattices of atoms and photons. *Rev. Mod. Phys.*, 90:031002, 2018.

[27] Vladimir P Bykov. Spontaneous emission from a medium with a band spectrum. *Soviet Journal of Quantum Electronics*, 4(7):861, 1975.

[28] Sajeev John and Jian Wang. Quantum electrodynamics near a photonic band gap: Photon bound states and dressed atoms. *Physical Review Letters*, 64:2418–2421, 1990.

[29] Ángel Rivas, Susana F Huelga, and Martin B Plenio. Quantum non-Markovianity: characterization, quantification and detection. *Reports on Progress in Physics*, 77(9):094001, 2014.

[30] Inés de Vega and Daniel Alonso. Dynamics of non-Markovian open quantum systems. *Rev. Mod. Phys.*, 89:015001, 2017.

[31] Arjan F. van Loo, Arkady Fedorov, Kevin Lalumière, Barry C. Sanders, Alexandre Blais, and Andreas Wallraff. Photon-Mediated Interactions Between Distant Artificial Atoms. *Science*, 342(6165):1494, 2013.

[32] Mohammad Mirhosseini, Eunjong Kim, Xueyue Zhang, Alp Sipahigil, Paul B. Dieterle, Andrew J. Keller, Ana Asenjo-Garcia, Darrick E. Chang, and Oskar Painter. Cavity quantum electrodynamics with atom-like mirrors. *Nature*, 569(7758):692–697, 2019.

[33] Maximilian Zanner, Tuure Orell, Christian M. F. Schneider, Romain Albert, Stefan Oleschko, Mathieu L. Juan, Matti Silveri, and Gerhard Kirchmair. Coherent control of a multi-qubit dark state in waveguide quantum electrodynamics. *Nature Physics*, 18(5):538–543, 2022.

[34] Bharath Kannan, Aziza Almanakly, Youngkyu Sung, Agustin Di Paolo, David A. Rower, Jochen Braumüller, Alexander Melville, Bethany M. Niedzielski, Amir Karamlou, Kyle Serniak, Antti Vepsäläinen, Mollie E. Schwartz, Jonilyn L. Yoder, Roni Winik, Joel I.-Jan Wang, Terry P. Orlando, Simon Gustavsson, Jeffrey A. Grover, and William D. Oliver. On-demand directional microwave photon emission using waveguide quantum electrodynamics. *Nature Physics*, 19(3):394–400, 2023.

[35] A. Goban, C. L. Hung, J.-D Hood, S. P. Yu, J.-A Muniz, O. Painter, and H. J. Kimble. Superradiance for Atoms Trapped along a Photonic Crystal Waveguide. *Phys. Rev. Lett.*, 115(6):063601, 2015.

[36] P. Solano, P. Barberis-Blostein, F. K. Fatemi, L. A. Orozco, and S. L. Rolston. Super-radiance reveals infinite-range dipole interactions through a nanofiber. *Nature Communications*, 8(1):1857, 2017.

[37] Xinchao Zhou, Hikaru Tamura, Tzu-Han Chang, and Chen-Lung Hung. Trapped atoms and superradiance on an integrated nanophotonic microring circuit. *arXiv e-prints*, art. arXiv:2312.14318, 2023.

[38] Neil V. Corzo, Jérémy Raskop, Aveek Chandra, Alexandra S. Sheremet, Baptiste Gouraud, and Julien Laurat. Waveguide-coupled single collective excitation of atomic arrays. *Nature*, 566(7744):359–362, 2019.

[39] R. Pennetta, M. Blaha, A. Johnson, D. Lechner, P. Schneeweiss, J. Volz, and A. Rauschenbeutel. Collective Radiative Dynamics of an Ensemble of Cold Atoms Coupled to an Optical Waveguide. *Phys Rev Lett*, 128 (7):073601, 2022.

[40] Alexey Tiranov, Vasiliki Angelopoulou, Cornelis Jacobus van Diepen, Björn Schrinski, Oliver August Dall'Alba Sandberg, Ying Wang,

Leonardo Midolo, Sven Scholz, Andreas Dirk Wieck, Arne Ludwig, Anders Søndberg Sørensen, and Peter Lodahl. Collective super- and subradiant dynamics between distant optical quantum emitters. *Science*, 379 (6630):389–393, 2023.

[41] Huaixiu Zheng and Harold U. Baranger. Persistent Quantum Beats and Long-Distance Entanglement from Waveguide-Mediated Interactions. *Phys. Rev. Lett.*, 110(11):113601, 2013.

[42] Hannes Pichler and Peter Zoller. Photonic Circuits with Time Delays and Quantum Feedback. *Phys. Rev. Lett.*, 116:093601, 2016.

[43] Fatih Dinc and Agata M. Brańczyk. Non-Markovian super-superradiance in a linear chain of up to 100 qubits. *Phys. Rev. Res.*, 1(3):032042, 2019.

[44] Kanupriya Sinha, Pierre Meystre, Elizabeth A. Goldschmidt, Fredrik K. Fatemi, S. L. Rolston, and Pablo Solano. Non-Markovian Collective Emission from Macroscopically Separated Emitters. *Phys. Rev. Lett.*, 124(4):043603, 2020.

[45] Kanupriya Sinha, Alejandro González-Tudela, Yong Lu, and Pablo Solano. Collective radiation from distant emitters. *Phys. Rev. A*, 102: 043718, 2020.

[46] Stefano Longhi. Superradiance paradox in waveguide lattices. *Opt. Lett.*, 45(12):3297–3300, 2020.

[47] Alfonso Lanuza and Dominik Schneble. Exact solution for the collective non-Markovian decay of two fully excited quantum emitters. *arXiv e-prints*, art. arXiv:2403.13871, 2024.

[48] Stuart J. Masson, Igor Ferrier-Barbut, Luis A. Orozco, Antoine Browaeys, and Ana Asenjo-Garcia. Many-Body Signatures of Collective Decay in Atomic Chains. *Phys. Rev. Lett.*, 125:263601, 2020.

[49] O. Rubies-Bigorda and S. F. Yelin. Superradiance and subradiance in inverted atomic arrays. *Phys. Rev. A*, 106(5), 2022.

[50] Stuart J. Masson and Ana Asenjo-Garcia. Universality of Dicke superradiance in arrays of quantum emitters. *Nature Communications*, 13(1): 2285, 2022.

[51] Oriol Rubies-Bigorda, Stefan Ostermann, and Susanne F. Yelin. Characterizing superradiant dynamics in atomic arrays via a cumulant expansion approach. *Phys. Rev. Res.*, 5:013091, 2023.

[52] Silvia Cardenas-Lopez, Stuart J. Masson, Zoe Zager, and Ana Asenjo-Garcia. Many-Body Superradiance and Dynamical Mirror Symmetry Breaking in Waveguide QED. *Phys. Rev. Lett.*, 131:033605, 2023.

[53] Christian Liedl, Felix Tebbenjohanns, Constanze Bach, Sebastian Pucher, Arno Rauschenbeutel, and Philipp Schneeweiss. Observation of Superradiant Bursts in a Cascaded Quantum System. *Phys. Rev. X*, 14:011020, 2024.

[54] Bennet Windt, Miguel Bello, Eugene Demler, and J. Ignacio Cirac. Fermionic matter-wave quantum optics with cold-atom impurity models. *Physical Review A*, 109(2):023306, 2024.

[55] Youngshin Kim, Alfonso Lanuza, and Dominik Schneble. Super- and subradiant dynamics of quantum emitters mediated by atomic matter waves. *arXiv e-prints*, art. arXiv:2311.09474, 2023.

[56] Joonhyuk Kwon, Youngshin Kim, Alfonso Lanuza, and Dominik Schneble. Formation of matter-wave polaritons in an optical lattice. *Nature Physics*, 18(6):657–661, 2022.

[57] Marlan O. Scully, Edward S. Fry, C. H. Raymond Ooi, and Krzysztof Wódkiewicz. Directed Spontaneous Emission from an Extended Ensemble of N Atoms: Timing Is Everything. *Phys. Rev. Lett.*, 96(1):010501, 2006.

[58] Marlan O. Scully and Anatoly A. Svidzinsky. The Super of Superradiance. *Science*, 325(5947):1510–1511, 2009.

[59] R. H. Dicke. Coherence in Spontaneous Radiation Processes. *Phys. Rev.*, 93(1):99–110, 1954.

[60] J. J. Hopfield. Theory of the Contribution of Excitons to the Complex Dielectric Constant of Crystals. *Phys. Rev.*, 112:1555–1567, 1958.

[61] S.I. Pekar. Theory of electromagnetic waves in a crystal with excitons. *Journal of Physics and Chemistry of Solids*, 5(1):11–22, 1958.

[62] D L Mills and E Burstein. Polaritons: the electromagnetic modes of media. *Reports on Progress in Physics*, 37(7):817, 1974.

[63] D. N. Basov, Ana Asenjo-Garcia, P. James Schuck, Xiaoyang Zhu, and Angel Rubio. Polariton panorama. *Nanophotonics*, 10(1):549–577, 2021.

[64] Quantum many-body models with cold atoms coupled to photonic crystals. *Nature Photonics*, 9(5):326–331, 2015. Number: 5 Publisher: Nature Publishing Group.

[65] A. González-Tudela, C. L. Hung, D. E. Chang, J. I. Cirac, and H. J. Kimble. Subwavelength vacuum lattices and atom–atom interactions in two-dimensional photonic crystals. *Nature Photonics*, 9(5):320–325, 2015.

[66] C.-L. Hung, Alejandro González-Tudela, J. Ignacio Cirac, and H. J. Kimble. Quantum spin dynamics with pairwise-tunable, long-range interactions. *Proceedings of the National Academy of Sciences*, 113(34): E4946–E4955, 2016.

[67] J Ignacio Cirac and H Jeff Kimble. Quantum optics, what next? *Nature Photonics*, 11(1):18–20, 2017.

[68] T. Shi, Y. H. Wu, A. González-Tudela, and J. I. Cirac. Effective many-body Hamiltonians of qubit-photon bound states. *New Journal of Physics*, 20(10):105005, 2018.

[69] M. Bello, G. Platero, J. I. Cirac, and A. González-Tudela. Unconventional quantum optics in topological waveguide QED. *Science Advances*, 5(7):eaaw0297, 2019.

[70] C. Tabares, A. Muñoz de las Heras, L. Tagliacozzo, D. Porras, and A. González-Tudela. Variational Quantum Simulators Based on Waveguide QED. *Phys. Rev. Lett.*, 131:073602, 2023.

[71] C. Weisbuch, M. Nishioka, A. Ishikawa, and Y. Arakawa. Observation of the coupled exciton-photon mode splitting in a semiconductor quantum microcavity. *Phys. Rev. Lett.*, 69:3314–3317, 1992.

[72] C. Schneider, K. Winkler, M. D. Fraser, M. Kamp, Y. Yamamoto, E. A. Ostrovskaya, and S. Höfling. Exciton-polariton trapping and potential landscape engineering. *Reports on Progress in Physics*, 80(1):016503, 2016.

[73] Álvaro Cuevas, Juan Camilo López Carreño, Blanca Silva, Milena De Giorgi, Daniel G. Suárez-Forero, Carlos Sánchez Muñoz, Antonio Fieramosca, Filippo Cardano, Lorenzo Marrucci, Vittorianna Tasco, Giorgio Biasiol, Elena del Valle, Lorenzo Dominici, Dario Ballarini, Giuseppe Gigli, Paolo Mataloni, Fabrice P. Laussy, Fabio Sciarrino, and Daniele Sanvitto. First observation of the quantized exciton-polariton

field and effect of interactions on a single polariton. *Science Advances*, 4(4), 2018.

[74] Thilo Stöferle, Henning Moritz, Christian Schori, Michael Köhl, and Tilman Esslinger. Transition from a Strongly Interacting 1D Superfluid to a Mott Insulator. *Phys. Rev. Lett.*, 92(13), 2004.

[75] C. Kollath, A. Iucci, T. Giamarchi, W. Hofstetter, and U. Schollwöck. Spectroscopy of Ultracold Atoms by Periodic Lattice Modulations. *Phys. Rev. Lett.*, 97(5), 2006.

[76] Bryce Gadway. *Bose Gases in Tailored Optical and Atomic Lattices*. PhD thesis, Stony Brook University, 2012.

[77] E. M. Purcell. Spontaneous Emission Probabilities at Radio Frequencies. *Physical Review*, 69:681, 1946.

[78] Serge Haroche and Jean Michel Raimond. *Exploring the Quantum: Atoms, Cavities, and Photons*. Oxford Univ. Press, 2006.

[79] Daniel Kleppner. Inhibited Spontaneous Emission. *Phys. Rev. Lett.*, 47: 233–236, 1981.

[80] Peter Lodahl, A. Floris van Driel, Ivan S. Nikolaev, Arie Irman, Karin Overgaag, Daniël Vanmaekelbergh, and Willem L. Vos. Controlling the dynamics of spontaneous emission from quantum dots by photonic crystals. *Nature*, 430(7000):654–657, 2004.

[81] A. P. Foster, D. Hallett, I. V. Iorsh, S. J. Sheldon, M. R. Godsland, B. Royall, E. Clarke, I. A. Shelykh, A. M. Fox, M. S. Skolnick, I. E. Itskevich, and L. R. Wilson. Tunable Photon Statistics Exploiting the Fano Effect in a Waveguide. *Phys. Rev. Lett.*, 122:173603, 2019.

[82] L. Scarpelli, B. Lang, F. Masia, D. M. Beggs, E. A. Muljarov, A. B. Young, R. Oulton, M. Kamp, S. Höfling, C. Schneider, and W. Langbein. 99% beta factor and directional coupling of quantum dots to fast light in photonic crystal waveguides determined by spectral imaging. *Phys. Rev. B*, 100:035311, 2019.

[83] A. Sipahigil, R. E. Evans, D. D. Sukachev, M. J. Burek, J. Borregaard, M. K. Bhaskar, C. T. Nguyen, J. L. Pacheco, H. A. Atikian, C. Meuwly, R. M. Camacho, F. Jelezko, E. Bielejec, H. Park, M. Lončar, and M. D. Lukin. An integrated diamond nanophotonics platform for quantum-optical networks. *Science*, 354(6314):847–850, 2016.

[84] Sanli Faez, Pierre Türschmann, Harald R. Haakh, Stephan Götzinger, and Vahid Sandoghdar. Coherent Interaction of Light and Single Molecules in a Dielectric Nanoguide. *Phys. Rev. Lett.*, 113:213601, 2014.

[85] Riccardo Pennetta, Daniel Lechner, Martin Blaha, Arno Rauschenbeutel, Philipp Schneeweiss, and Jürgen Volz. Observation of Coherent Coupling between Super- and Subradiant States of an Ensemble of Cold Atoms Collectively Coupled to a Single Propagating Optical Mode. *Phys. Rev. Lett.*, 128(20):203601, 2022.

[86] Peter P. Orth, Ivan Stanic, and Karyn Le Hur. Dissipative quantum Ising model in a cold-atom spin-boson mixture. *Phys. Rev. A*, 77:051601, 2008.

[87] Inés de Vega, Diego Porras, and J. Ignacio Cirac. Matter-Wave Emission in Optical Lattices: Single Particle and Collective Effects. *Phys. Rev. Lett.*, 101:260404, 2008.

[88] Tuure Orell, Maximilian Zanner, Mathieu L. Juan, Aleksei Sharafiev, Romain Albert, Stefan Oleschko, Gerhard Kirchmair, and Matti Silveri. Collective bosonic effects in an array of transmon devices. *Phys. Rev. A*, 105(6):063701, 2022.

[89] P. Meystre and M. Sargent. *Elements of Quantum Optics*. Springer, 2007.

[90] C. Gerry and P.L. Knight. *Introductory Quantum Optics*. Cambridge University Press, 2005.

[91] V. Weisskopf and E. Wigner. Berechnung der natürlichen Linienbreite auf Grund der Diracschen Lichttheorie. *Zeitschrift für Physik*, 63(1): 54–73, 1930.

[92] Paul Adrien Maurice Dirac. The quantum theory of the emission and absorption of radiation. *Proceedings of the Royal Society A*, 114:243–265, 1927. Publisher: Royal Society.

[93] Michael Stewart. *Dynamics of Matter-Wave Quantum Emitters in Engineered Reservoirs*. PhD thesis, Stony Brook University, 2020.

[94] C. Cohen-Tannoudji, J. Dupont-Roc, and G. Grynberg. *Atom—Photon Interactions*. John Wiley & Sons, Ltd, 1998.

[95] H.P. Breuer and F. Petruccione. *The Theory of Open Quantum Systems*. Oxford University Press, 2002.

[96] A. González-Tudela, V. Paulisch, D. E. Chang, H. J. Kimble, and J. I. Cirac. Deterministic Generation of Arbitrary Photonic States Assisted by Dissipation. *Phys. Rev. Lett.*, 115(16):163603, 2015.

[97] DLMF. *NIST Digital Library of Mathematical Functions*. `https://dlmf.nist.gov/`, Release 1.2.0 of 2024-03-15. F. W. J. Olver, A. B. Olde Daalhuis, D. W. Lozier, B. I. Schneider, R. F. Boisvert, C. W. Clark, B. R. Miller, B. V. Saunders, H. S. Cohl, and M. A. McClain, eds.

[98] Frederick W. King. *Hilbert Transforms*. Encyclopedia of Mathematics and its Applications. Cambridge University Press, 2009.

[99] G. Lindblad. On the Generators of Quantum Dynamical Semigroups. *Commun.Math. Phys.*, 48(2):119–130, 1976.

[100] M. Gross and S. Haroche. Superradiance: An essay on the theory of collective spontaneous emission. *Physics Reports*, 93(5):301–396, 1982.

[101] Jonathan D. Hood, Akihisa Goban, Ana Asenjo-Garcia, Mingwu Lu, Su-Peng Yu, Darrick E. Chang, and H. J. Kimble. Atom–atom interactions around the band edge of a photonic crystal waveguide. *Proceedings of the National Academy of Sciences*, 113(38):10507–10512, 2016.

[102] Yanbing Liu and Andrew A. Houck. Quantum electrodynamics near a photonic bandgap. *Nat Phys*, 13(1):48–52, 2017.

[103] Ulrich Hoeppe, Christian Wolff, Jens Küchenmeister, Jens Niegemann, Malte Drescher, Hartmut Benner, and Kurt Busch. Direct Observation of Non-Markovian Radiation Dynamics in 3D Bulk Photonic Crystals. *Phys. Rev. Lett.*, 108:043603, 2012.

[104] P. Grivet, N. Bloembergen, and United States. Office of Naval Research. *Quantum Electronics: Proceedings of the Third International Congress. Électronique Quantique; Comptes-rendus de la 3e Conférence Internationale, Paris*. Number v. 1 in Quantum Electronics: Proceedings of the Third International Congress. Électronique Quantique; Comptes-rendus de la 3e Conférence Internationale, Paris. Dunod, 1964.

[105] W. Guerin, M. T. Rouabah, and R. Kaiser. Light interacting with atomic ensembles: collective, cooperative and mesoscopic effects. *Journal of Modern Optics*, 64(9):895–907, 2017.

[106] R. G. DeVoe and R. G. Brewer. Observation of Superradiant and Subradiant Spontaneous Emission of Two Trapped Ions. *Phys. Rev. Lett.*, 76(12):2049–2052, 1996.

[107] William Guerin, Michelle O. Araújo, and Robin Kaiser. Subradiance in a Large Cloud of Cold Atoms. *Phys. Rev. Lett.*, 116(8):083601, 2016.

[108] Chia Wei Hsu, Bo Zhen, A. Douglas Stone, John D. Joannopoulos, and Marin Soljačić. Bound states in the continuum. *Nature Reviews Materials*, 1(9):1–13, 2016.

[109] Chong Chen, Chun-Jie Yang, and Jun-Hong An. Exact decoherence-free state of two distant quantum systems in a non-Markovian environment. *Phys. Rev. A*, 93(6):062122, 2016.

[110] Luca Leonforte, Angelo Carollo, and Francesco Ciccarello. Vacancy-like Dressed States in Topological Waveguide QED. *Phys. Rev. Lett.*, 126 (6):063601, 2021.

[111] Hui Deng, Hartmut Haug, and Yoshihisa Yamamoto. Exciton-polariton Bose-Einstein condensation. *Rev. Mod. Phys.*, 82:1489–1537, 2010.

[112] Nicholas E. Rehler and Joseph H. Eberly. Superradiance. *Phys. Rev. A*, 3(5):1735–1751, 1971.

[113] C. J. Pethick and H. Smith. *Bose–Einstein Condensation in Dilute Gases*. Cambridge University Press, 2 edition, 2008.

[114] Harold J. Metcalf and Peter van der Straten. *Laser Cooling and Trapping*. Springer New York, New York, NY, 1999.

[115] C.J. Foot. *Atomic Physics*. Oxford Master Series in Physics. OUP Oxford, 2004.

[116] R. Grimm, M. Weidemuller, and Y. B. Ovchinnikov. Optical dipole traps for neutral atoms. *Advances in Atomic Molecular, and Optical Physics*, 42:95–170, 2000.

[117] Stephan Albert. *Cooling, Trapping, and Transport of Atom Clouds in a New BEC Apparatus*. PhD thesis, Stony Brook University, 2007.

[118] Daniel Greif. *Evaporative Cooling and Bose-Einstein Condensation of Rb-87 in a moving coil TOP trap geometry*. PhD thesis, Stony Brook University, 2007.

[119] Rene Reimann. *Quantum Gases in State-Dependent Optical Potentials*. PhD thesis, Stony Brook University, 2009.

[120] Daniel Pertot, Daniel Greif, Stephan Albert, Bryce Gadway, and Dominik Schneble. Versatile transporter apparatus for experiments with optically trapped Bose–Einstein condensates. *Journal of Physics B: Atomic, Molecular and Optical Physics*, 42(21):215305, 2009.

[121] F.G. Kondev, M. Wang, W.J. Huang, S. Naimi, and G. Audi. The NUBASE2020 evaluation of nuclear physics properties. *Chinese Physics C*, 45(3):030001, 2021.

[122] Daniel Pertot. *Two-Component Bosons in State-Dependent Optical Lattices*. PhD thesis, Stony Brook University, 2011.

[123] Ludwig Krinner. *Exploring Spontaneous Emission Phenomena using Ultracold Atomic Matter Waves*. PhD thesis, Stony Brook University, 2018.

[124] Daniel A. Steck. Rubidium 87 D Line Data. 2023. Available online at http://steck.us/alkalidata (revision 2.3.2, 10 September 2023).

[125] E. L. Raab, M. Prentiss, Alex Cable, Steven Chu, and D. E. Pritchard. Trapping of Neutral Sodium Atoms with Radiation Pressure. *Phys. Rev. Lett.*, 59(23):2631–2634, 1987.

[126] Paul D. Lett, Richard N. Watts, Christoph I. Westbrook, William D. Phillips, Phillip L. Gould, and Harold J. Metcalf. Observation of Atoms Laser Cooled below the Doppler Limit. *Phys. Rev. Lett.*, 61:169–172, 1988.

[127] J. Dalibard and C. Cohen-Tannoudji. Laser cooling below the Doppler limit by polarization gradients: simple theoretical models. *J. Opt. Soc. Am. B*, 6(11):2023–2045, 1989.

[128] Alan L. Migdall, John V. Prodan, William D. Phillips, Thomas H. Bergeman, and Harold J. Metcalf. First Observation of Magnetically Trapped Neutral Atoms. *Phys. Rev. Lett.*, 54:2596–2599, 1985.

[129] Arturo Pazmino. *Towards Studies of the Aubry-André Model with Ultracold Atoms in Optical Lattices*. PhD thesis, Stony Brook University, 2019.

[130] Wolfgang Ketterle and N.J. Van Druten. Evaporative Cooling of Trapped Atoms. volume 37 of *Advances In Atomic, Molecular, and Optical Physics*, pages 181–236. Academic Press, 1996.

[131] P.W. Milonni and J.H. Eberly. *Laser Physics*. Wiley, 2010.

[132] Klaus Hueck, Niclas Luick, Lennart Sobirey, Jonas Siegl, Thomas Lompe, Henning Moritz, Logan W. Clark, and Cheng Chin. Calibrating high intensity absorption imaging of ultracold atoms. *Opt. Express*, 25 (8):8670–8679, 2017.

[133] I.T. Jolliffe. *Principal Component Analysis*. Springer Series in Statistics. Springer New York, 2013.

[134] Jonathon Shlens. A Tutorial on Principal Component Analysis. *arXiv e-prints*, art. arXiv:1404.1100, 2014.

[135] Xiaolin Li, Min Ke, Bo Yan, and Yuzhu Wang. Reduction of interference fringes in absorption imaging of cold atom cloud using eigenface method. *Chin. Opt. Lett.*, 5(3):128–130, 2007.

[136] Feng Xiong, Yun Long, and Colin V. Parker. Enhanced principle component method for fringe removal in cold atom images. *J. Opt. Soc. Am. B*, 37(7):2041–2044, 2020.

[137] Gourab Pal and Saptarishi Chaudhuri. Efficient denoising of cold atom images using the optimized eigenface recognition algorithm. *Appl. Opt.*, 62(33):8786–8792, 2023.

[138] Joonhyuk Kwon. *Simulating Strongly-Coupled Light-Matter Systems with Ultracold Atoms*. PhD thesis, Stony Brook University, 2022.

[139] L. Sirovich and M. Kirby. Low-dimensional procedure for the characterization of human faces. *J. Opt. Soc. Am. A*, 4(3):519–524, 1987.

[140] D. Guéry-Odelin, A. Ruschhaupt, A. Kiely, E. Torrontegui, S. Martínez-Garaot, and J. G. Muga. Shortcuts to adiabaticity: Concepts, methods, and applications. *Rev. Mod. Phys.*, 91:045001, 2019.

[141] Gabriel Cardoso. A Landau-Zener formula for the Adiabatic Gauge Potential. *arXiv e-prints*, art. arXiv:2303.12066, 2023.

[142] Muxi Liu. Shortcuts to Adiabaticity in a Hyperfine State Transfer of Optically Trapped Ultracold Atoms. Master's thesis, Stony Brook University, 2023.

[143] Clarence Zener and Ralph Howard Fowler. Non-adiabatic crossing of energy levels. *Proceedings of the Royal Society of London. Series A,*

Containing Papers of a Mathematical and Physical Character, 137(833): 696–702, 1932.

[144] Jan R. Rubbmark, Michael M. Kash, Michael G. Littman, and Daniel Kleppner. Dynamical effects at avoided level crossings: A study of the Landau-Zener effect using Rydberg atoms. *Phys. Rev. A*, 23:3107–3117, 1981.

[145] Bruce W. Shore. Coherent manipulations of atoms using laser light. *Acta Physica Slovaca*, 58(3):243–486, 2008.

[146] L. Krinner, M. Stewart, A. Pazmino, and D. Schneble. In situ magnetometry for experiments with atomic quantum gases. *Review of Scientific Instruments*, 89(1), 2018.

[147] Phillip L. Gould, George A. Ruff, and David E. Pritchard. Diffraction of atoms by light: The near-resonant Kapitza-Dirac effect. *Phys. Rev. Lett.*, 56:827–830, 1986.

[148] Yu. B. Ovchinnikov, J. H. Müller, M. R. Doery, E. J. D. Vredenbregt, K. Helmerson, S. L. Rolston, and W. D. Phillips. Diffraction of a Released Bose-Einstein Condensate by a Pulsed Standing Light Wave. *Phys. Rev. Lett.*, 83:284–287, 1999.

[149] Bryce Gadway, Daniel Pertot, René Reimann, Martin G. Cohen, and Dominik Schneble. Analysis of Kapitza-Dirac diffraction patterns beyond the Raman-Nath regime. *Opt. Express*, 17(21):19173–19180, 2009.

[150] L. Deng, E. W. Hagley, J. Denschlag, J. E. Simsarian, Mark Edwards, Charles W. Clark, K. Helmerson, S. L. Rolston, and W. D. Phillips. Temporal, Matter-Wave-Dispersion Talbot Effect. *Phys. Rev. Lett.*, 83: 5407–5411, 1999.

[151] D.J. Griffiths. *Introduction to Electrodynamics*. Cambridge University Press, 2017.

[152] Ivan H Deutsch and Poul S Jessen. Quantum-state control in optical lattices. *Phys. Rev. A*, 57(3):1972, 1998.

[153] Fam Le Kien, Philipp Schneeweiss, and Arno Rauschenbeutel. Dynamical polarizability of atoms in arbitrary light fields: general theory and application to cesium. *The European Physical Journal D*, 67(5):92, 2013.

[154] L. J. LeBlanc and J. H. Thywissen. Species-specific optical lattices. *Phys. Rev. A*, 75:053612, 2007.

[155] Aviv Keshet and Wolfgang Ketterle. A distributed, graphical user interface based, computer control system for atomic physics experiments. *Review of Scientific Instruments*, 84(1), 2013.

[156] M.G. Benedict. *Super-radiance: Multiatomic Coherent Emission*. Series in Optics and Optoelectronics. Taylor & Francis, 1996.

[157] Tobias Brandes. Coherent and collective quantum optical effects in mesoscopic systems. *Physics Reports*, 408(5):315–474, 2005.

[158] F. T. Arecchi and Eric Courtens. Cooperative Phenomena in Resonant Electromagnetic Propagation. *Phys. Rev. A*, 2(5):1730–1737, 1970.

[159] D. Porras and J. I. Cirac. Collective generation of quantum states of light by entangled atoms. *Phys. Rev. A*, 78:053816, 2008.

[160] A. González-Tudela and J. I. Cirac. Quantum Emitters in Two-Dimensional Structured Reservoirs in the Nonperturbative Regime. *Phys. Rev. Lett.*, 119:143602, 2017.

[161] A. Asenjo-Garcia, M. Moreno-Cardoner, A. Albrecht, H. J. Kimble, and D. E. Chang. Exponential Improvement in Photon Storage Fidelities Using Subradiance and "Selective Radiance" in Atomic Arrays. *Phys. Rev. X*, 7:031024, 2017.

[162] Yu-Xiang Zhang and Klaus Mølmer. Theory of Subradiant States of a One-Dimensional Two-Level Atom Chain. *Phys. Rev. Lett.*, 122(20): 203605, 2019.

[163] Janet Zhong, Nikita A. Olekhno, Yongguan Ke, Alexander V. Poshakinskiy, Chaohong Lee, Yuri S. Kivshar, and Alexander N. Poddubny. Photon-Mediated Localization in Two-Level Qubit Arrays. *Phys. Rev. Lett.*, 124(9):093604, 2020.

[164] N. Skribanowitz, I. P. Herman, J. C. MacGillivray, and M. S. Feld. Observation of Dicke Superradiance in Optically Pumped HF Gas. *Phys. Rev. Lett.*, 30(8):309–312, 1973.

[165] Michelle O. Araújo, Ivor Krešić, Robin Kaiser, and William Guerin. Superradiance in a Large and Dilute Cloud of Cold Atoms in the Linear-Optics Regime. *Phys. Rev. Lett.*, 117(7):073002, 2016.

[166] S. J Roof, K. J Kemp, M. D Havey, and I. M Sokolov. Observation of Single-Photon Superradiance and the Cooperative Lamb Shift in an Extended Sample of Cold Atoms. *Phys. Rev. Lett.*, 117(7):073003, 2016.

[167] Giovanni Ferioli, Antoine Glicenstein, Loic Henriet, Igor Ferrier-Barbut, and Antoine Browaeys. Storage and Release of Subradiant Excitations in a Dense Atomic Cloud. *Phys. Rev. X*, 11:021031, 2021.

[168] Giuseppe Calajó, Francesco Ciccarello, Darrick Chang, and Peter Rabl. Atom-field dressed states in slow-light waveguide QED. *Phys. Rev. A*, 93(3):033833, 2016.

[169] E. Sánchez-Burillo, D. Zueco, L. Martín-Moreno, and J. J. García-Ripoll. Dynamical signatures of bound states in waveguide QED. *Phys. Rev. A*, 96(2):023831, 2017.

[170] Vinicius S. Ferreira, Jash Banker, Alp Sipahigil, Matthew H. Matheny, Andrew J. Keller, Eunjong Kim, Mohammad Mirhosseini, and Oskar Painter. Collapse and Revival of an Artificial Atom Coupled to a Structured Photonic Reservoir. *Phys. Rev. X*, 11:041043, 2021.

[171] Bryce Gadway, Daniel Pertot, Jeremy Reeves, and Dominik Schneble. Probing an ultracold-atom crystal with matter waves. *Nature Physics*, 8(7):544–549, 2012.

[172] J. Reeves, L. Krinner, M. Stewart, A. Pazmiño, and D. Schneble. Nonadiabatic diffraction of matter waves. *Phys. Rev. A*, 92:023628, 2015.

[173] N. Fayard, L. Henriet, A. Asenjo-Garcia, and D. E. Chang. Many-body localization in waveguide quantum electrodynamics. *Phys. Rev. Res.*, 3 (3):033233, 2021.

[174] C. Kollath, U. Schollwöck, J. von Delft, and W. Zwerger. Spatial correlations of trapped one-dimensional bosons in an optical lattice. *Phys. Rev. A*, 69(3), 2004.

[175] Alexander Altland and Ben D. Simons. *Condensed Matter Field Theory*. Cambridge University Press, 2 edition, 2010.

[176] L. P. Pitaevskii. Vortex lines in an imperfect Bose gas. *Sov. Phys. JETP.*, 13 (2):451–454, 1961.

[177] Artur Widera, Fabrice Gerbier, Simon Fölling, Tatjana Gericke, Olaf Mandel, and Immanuel Bloch. Precision measurement of spin-dependent interaction strengths for spin-1 and spin-2 87Rb atoms. *New Journal of Physics*, 8(8):152, 2006.

[178] K. M. Mertes, J. W. Merrill, R. Carretero-González, D. J. Frantzeskakis, P. G. Kevrekidis, and D. S. Hall. Nonequilibrium Dynamics and Superfluid Ring Excitations in Binary Bose-Einstein Condensates. *Phys. Rev. Lett.*, 99:190402, 2007.

[179] M. Egorov, B. Opanchuk, P. Drummond, B. V. Hall, P. Hannaford, and A. I. Sidorov. Measurement of s-wave scattering lengths in a two-component Bose-Einstein condensate. *Phys. Rev. A*, 87:053614, 2013.

[180] N. N. Bogolyubov. On the theory of superfluidity. *J. Phys. (USSR)*, 11: 23–32, 1947.

[181] L. Landau. Theory of the Superfluidity of Helium II. *Phys. Rev.*, 60: 356–358, 1941.

[182] L.P. Pitaevskii and S. Stringari. *Bose-Einstein Condensation*. International Series of Monographs on Physics. Clarendon Press, 2003.

[183] E. P. Gross. Structure of a quantized vortex in boson systems. *Nuovo Cimento*, 20:454–477, 1961.

[184] M. A. Cazalilla, R. Citro, T. Giamarchi, E. Orignac, and M. Rigol. One dimensional bosons: From condensed matter systems to ultracold gases. *Rev. Mod. Phys.*, 83:1405–1466, 2011.

[185] V. Dunjko, V. Lorent, and M. Olshanii. Bosons in Cigar-Shaped Traps: Thomas-Fermi Regime, Tonks-Girardeau Regime, and In Between. *Phys. Rev. Lett.*, 86:5413–5416, 2001.

[186] M. Olshanii. Atomic Scattering in the Presence of an External Confinement and a Gas of Impenetrable Bosons. *Phys. Rev. Lett.*, 81:938–941, 1998.

[187] Matthew P. A. Fisher, Peter B. Weichman, G. Grinstein, and Daniel S. Fisher. Boson localization and the superfluid-insulator transition. *Phys. Rev. B*, 40:546–570, 1989.

[188] D. Jaksch, C. Bruder, J. I. Cirac, C. W. Gardiner, and P. Zoller. Cold Bosonic Atoms in Optical Lattices. *Phys. Rev. Lett.*, 81:3108–3111, 1998.

[189] I. B. Spielman, W. D. Phillips, and J. V. Porto. Mott-Insulator Transition in a Two-Dimensional Atomic Bose Gas. *Phys. Rev. Lett.*, 98: 080404, 2007.

[190] E. Haller, R. Hart, M. J. Mark, J. G. Danzl, L. Reichsollner, M. Gustavsson, M. Dalmonte, G. Pupillo, and H. C. Nagerl. Pinning quantum phase transition for a Luttinger liquid of strongly interacting bosons. *Nature*, 466(7306):597–600, 2010.

[191] Neil W. Ashcroft and N. David Mermin. *Solid State Physics*. Saunders College Publishing, 1976.

[192] Marvin L. Cohen and Steven G. Louie. *Fundamentals of Condensed Matter Physics*. Cambridge University Press, 2016.

[193] Wilhelm Zwerger. Mott–Hubbard transition of cold atoms in optical lattices. *Journal of Optics B: Quantum and Semiclassical Optics*, 5(2): S9, 2003.

[194] Werner Krauth, Michel Caffarel, and Jean-Philippe Bouchaud. Gutzwiller wave function for a model of strongly interacting bosons. *Phys. Rev. B*, 45:3137–3140, 1992.

[195] K. Sheshadri, H. R. Krishnamurthy, R. Pandit, and T. V. Ramakrishnan. Superfluid and Insulating Phases in an Interacting-Boson Model: Mean-Field Theory and the RPA. *Europhysics Letters*, 22(4):257, 1993.

[196] D. van Oosten, P. van der Straten, and H. T. C. Stoof. Quantum phases in an optical lattice. *Phys. Rev. A*, 63:053601, 2001.

[197] Subir Sachdev. *Quantum Phases of Matter*. Cambridge University Press, 2023.

[198] J M Zhang and R X Dong. Exact diagonalization: the Bose–Hubbard model as an example. *European Journal of Physics*, 31(3):591, 2010.

[199] Gretchen K. Campbell, Jongchul Mun, Micah Boyd, Patrick Medley, Aaron E. Leanhardt, Luis G. Marcassa, David E. Pritchard, and Wolfgang Ketterle. Imaging the Mott Insulator Shells by Using Atomic Clock Shifts. *Science*, 313(5787):649–652, 2006.

[200] Nathan Gemelke, Xibo Zhang, Chen-Lung Hung, and Cheng Chin. In situ observation of incompressible Mott-insulating domains in ultracold atomic gases. *Nature*, 460(7258):995–998, 2009.

[201] W. S. Bakr, A. Peng, M. E. Tai, R. Ma, J. Simon, J. I. Gillen, S. Fölling, L. Pollet, and M. Greiner. Probing the Superfluid–to–Mott Insulator Transition at the Single-Atom Level. *Science*, 329(5991):547–550, 2010.

[202] Jacob F. Sherson, Christof Weitenberg, Manuel Endres, Marc Cheneau, Immanuel Bloch, and Stefan Kuhr. Single-atom-resolved fluorescence imaging of an atomic Mott insulator. *Nature*, 467(7311):68–72, 2010.

[203] Subir Sachdev. *Quantum Phase Transitions*. Cambridge University Press, 2 edition, 2011.

[204] L. Pollet, N. V. Prokof'ev, B. V. Svistunov, and M. Troyer. Absence of a Direct Superfluid to Mott Insulator Transition in Disordered Bose Systems. *Phys. Rev. Lett.*, 103:140402, 2009.

[205] V. Gurarie, L. Pollet, N. V. Prokof'ev, B. V. Svistunov, and M. Troyer. Phase diagram of the disordered Bose-Hubbard model. *Phys. Rev. B*, 80:214519, 2009.

[206] Bryce Gadway, Daniel Pertot, Jeremy Reeves, Matthias Vogt, and Dominik Schneble. Glassy Behavior in a Binary Atomic Mixture. *Phys. Rev. Lett.*, 107:145306, 2011.

[207] Carolyn Meldgin, Ushnish Ray, Philip Russ, David Chen, David M. Ceperley, and Brian DeMarco. Probing the Bose glass–superfluid transition using quantum quenches of disorder. *Nature Physics*, 12(7):646–649, 2016.

[208] Xueyue Zhang, Eunjong Kim, Daniel K. Mark, Soonwon Choi, and Oskar Painter. A superconducting quantum simulator based on a photonic-bandgap metamaterial. *Science*, 379(6629):278–283, 2023.

[209] C. Lagoin, U. Bhattacharya, T. Grass, R. W. Chhajlany, T. Salamon, K. Baldwin, L. Pfeiffer, M. Lewenstein, M. Holzmann, and F. Dubin. Extended Bose–Hubbard model with dipolar excitons. *Nature*, 609(7927): 485–489, 2022.

[210] Yabo Li, Dominik Schneble, and Tzu-Chieh Wei. Two-particle states in one-dimensional coupled Bose-Hubbard models. *Phys. Rev. A*, 105: 053310, 2022.

[211] Elliott H. Lieb and Werner Liniger. Exact Analysis of an Interacting Bose Gas. I. The General Solution and the Ground State. *Phys. Rev.*, 130:1605–1616, 1963.

[212] M. Girardeau. Relationship between Systems of Impenetrable Bosons and Fermions in One Dimension. *Journal of Mathematical Physics*, 1 (6):516–523, 1960.

[213] T. Kinoshita, T. Wenger, and D. S. Weiss. Observation of a one-dimensional Tonks-Girardeau gas. *Science*, 305(5687):1125–1128, 2004.

[214] Belén Paredes, Artur Widera, Valentin Murg, Olaf Mandel, Simon Fölling, Ignacio Cirac, Gora V. Shlyapnikov, Theodor W. Hänsch, and Immanuel Bloch. Tonks–Girardeau gas of ultracold atoms in an optical lattice. *Nature*, 429(6989):277–281, 2004.

[215] Florian Meinert, Michael Knap, Emil Kirilov, Katharina Jag-Lauber, Mikhail B. Zvonarev, Eugene Demler, and Hanns-Christoph Nägerl. Bloch oscillations in the absence of a lattice. *Science*, 356(6341):945–948, 2017.

[216] Eunjong Kim, Xueyue Zhang, Vinicius S. Ferreira, Jash Banker, Joseph K. Iverson, Alp Sipahigil, Miguel Bello, Alejandro González-Tudela, Mohammad Mirhosseini, and Oskar Painter. Quantum Electrodynamics in a Topological Waveguide. *Phys. Rev. X*, 11:011015, 2021.

[217] Nicolò Defenu, Tobias Donner, Tommaso Macrì, Guido Pagano, Stefano Ruffo, and Andrea Trombettoni. Long-range interacting quantum systems. *Rev. Mod. Phys.*, 95:035002, 2023.

[218] Ruichao Ma, Brendan Saxberg, Clai Owens, Nelson Leung, Yao Lu, Jonathan Simon, and David I. Schuster. A dissipatively stabilized Mott insulator of photons. *Nature*, 566(7742):51–57, 2019.

[219] Iacopo Carusotto, Andrew A. Houck, Alicia J. Kollár, Pedram Roushan, David I. Schuster, and Jonathan Simon. Photonic materials in circuit quantum electrodynamics. *Nature Physics*, 16(3):268–279, 2020.

[220] Iacopo Carusotto and Cristiano Ciuti. Quantum fluids of light. *Rev. Mod. Phys.*, 85(1):299–366, 2013.

[221] Michael J. Hartmann. Quantum simulation with interacting photons. *Journal of Optics*, 18(10):104005, 2016.

[222] Changsuk Noh and Dimitris G. Angelakis. Quantum simulations and many-body physics with light. *Reports on Progress in Physics*, 80(1): 016401, 2016.

[223] Neereja M. Sundaresan, Rex Lundgren, Guanyu Zhu, Alexey V. Gorshkov, and Andrew A. Houck. Interacting Qubit-Photon Bound States with Superconducting Circuits. *Phys. Rev. X*, 9(1), 2019.

[224] Alexandre Blais, Steven M. Girvin, and William D. Oliver. Quantum information processing and quantum optics with circuit quantum electrodynamics. *Nature Physics*, 16(3):247–256, 2020.

[225] P. Pedri, L. Pitaevskii, S. Stringari, C. Fort, S. Burger, F. S. Cataliotti, P. Maddaloni, F. Minardi, and M. Inguscio. Expansion of a Coherent Array of Bose-Einstein Condensates. *Phys. Rev. Lett.*, 87:220401, 2001.

[226] Daniel Pertot, Bryce Gadway, and Dominik Schneble. Collinear Four-Wave Mixing of Two-Component Matter Waves. *Phys. Rev. Lett.*, 104: 200402, 2010.

[227] J. Stenger, S. Inouye, A. P. Chikkatur, D. M. Stamper-Kurn, D. E. Pritchard, and W. Ketterle. Bragg Spectroscopy of a Bose-Einstein Condensate. *Phys. Rev. Lett.*, 82:4569–4573, 1999.

[228] K. M. Birnbaum, A. Boca, R. Miller, A. D. Boozer, T. E. Northup, and H. J. Kimble. Photon blockade in an optical cavity with one trapped atom. *Nature*, 436(7047):87–90, 2005.

[229] C. Ouellet-Plamondon, G. Sallen, F. Jabeen, D. Y. Oberli, and B. Deveaud. Multiple polariton modes originating from the coupling of quantum wells in planar microcavity. *Phys. Rev. B*, 92(7):075313, 2015.

[230] Neereja M. Sundaresan, Yanbing Liu, Darius Sadri, László J. Szőcs, Devin L. Underwood, Moein Malekakhlagh, Hakan E. Türeci, and Andrew A. Houck. Beyond Strong Coupling in a Multimode Cavity. *Phys. Rev. X*, 5(2):021035, 2015.

[231] Dmitry D. Solnyshkov, Guillaume Malpuech, Philippe St-Jean, Sylvain Ravets, Jacqueline Bloch, and Alberto Amo. Microcavity polaritons for topological photonics [Invited]. *Optical Materials Express*, 11(4):1119–1142, 2021.

[232] Torsten Karzig, Charles-Edouard Bardyn, Netanel H. Lindner, and Gil Refael. Topological Polaritons. *Phys. Rev. X*, 5:031001, 2015.

[233] Shanhui Fan, Şükrü Ekin Kocabaş, and Jung-Tsung Shen. Input-output formalism for few-photon transport in one-dimensional nanophotonic waveguides coupled to a qubit. *Phys. Rev. A*, 82:063821, 2010.

[234] Eden Rephaeli and Shanhui Fan. Stimulated Emission from a Single Excited Atom in a Waveguide. *Phys. Rev. Lett.*, 108:143602, 2012.

[235] U. Fano. Effects of Configuration Interaction on Intensities and Phase Shifts. *Phys. Rev.*, 124:1866–1878, 1961.

[236] Michael Fleischhauer, Atac Imamoglu, and Jonathan P. Marangos. Electromagnetically induced transparency: Optics in coherent media. *Rev. Mod. Phys.*, 77:633–673, 2005.

[237] M. Fleischhauer and M. D. Lukin. Dark-State Polaritons in Electromagnetically Induced Transparency. *Phys. Rev. Lett.*, 84:5094–5097, 2000.

[238] Andrew G. Sykes, Matthew J. Davis, and David C. Roberts. Drag Force on an Impurity below the Superfluid Critical Velocity in a Quasi-One-Dimensional Bose-Einstein Condensate. *Phys. Rev. Lett.*, 103:085302, 2009.

[239] Aleksandra Petković and Zoran Ristivojevic. Dissipative Dynamics of a Heavy Impurity in a Bose Gas in the Strong Coupling Regime. *Phys. Rev. Lett.*, 131:186001, 2023.

[240] D. M. Gangardt and A. Kamenev. Bloch Oscillations in a One-Dimensional Spinor Gas. *Phys. Rev. Lett.*, 102:070402, 2009.

[241] C. N. Yang. Some Exact Results for the Many-Body Problem in one Dimension with Repulsive Delta-Function Interaction. *Phys. Rev. Lett.*, 19:1312–1315, 1967.

[242] M. Gaudin. Un systeme a une dimension de fermions en interaction. *Physics Letters A*, 24(1):55–56, 1967.

[243] A. González-Tudela and J. I. Cirac. Markovian and non-Markovian dynamics of quantum emitters coupled to two-dimensional structured reservoirs. *Phys. Rev. A*, 96(4):043811, 2017.

[244] A. Gonzalez-Tudela and J. I. Cirac. Non-Markovian Quantum Optics with Three-Dimensional State-Dependent Optical Lattices. *Quantum*, 2, 2018.

[245] A. González-Tudela, C. Sánchez Muñoz, and J. I. Cirac. Engineering and Harnessing Giant Atoms in High-Dimensional Baths: A Proposal for Implementation with Cold Atoms. *Phys. Rev. Lett.*, 122:203603, 2019.

[246] C. Vega, M. Bello, D. Porras, and A. González-Tudela. Qubit-photon bound states in topological waveguides with long-range hoppings. *Phys. Rev. A*, 104:053522, 2021.

[247] Cheng Chin, Rudolf Grimm, Paul Julienne, and Eite Tiesinga. Feshbach resonances in ultracold gases. *Rev. Mod. Phys.*, 82:1225–1286, 2010.

[248] T. Bergeman, M. G. Moore, and M. Olshanii. Atom-Atom Scattering under Cylindrical Harmonic Confinement: Numerical and Analytic Studies of the Confinement Induced Resonance. *Phys. Rev. Lett.*, 91: 163201, 2003.

[249] A. M. Kaufman, R. P. Anderson, Thomas M. Hanna, E. Tiesinga, P. S. Julienne, and D. S. Hall. Radio-frequency dressing of multiple Feshbach resonances. *Phys. Rev. A*, 80:050701, 2009.

[250] Yoichiro Nambu. Quasi-Particles and Gauge Invariance in the Theory of Superconductivity. *Phys. Rev.*, 117:648–663, 1960.

[251] J. Goldstone. Field theories with Superconductor solutions. *Il Nuovo Cimento (1955-1965)*, 19(1):154–164, 1961.

[252] H.T.C. Stoof, D.B.M. Dickerscheid, and K. Gubbels. *Ultracold Quantum Fields*. Theoretical and Mathematical Physics. Springer Netherlands, 2008.

[253] R.P. Feynman, A.R. Hibbs, and D.F. Styer. *Quantum Mechanics and Path Integrals*. Dover Books on Physics. Dover Publications, 2010.

[254] Mark Srednicki. *Quantum Field Theory*. Cambridge University Press, 2007.

[255] Oliver Penrose and Lars Onsager. Bose-Einstein Condensation and Liquid Helium. *Phys. Rev.*, 104:576–584, 1956.

[256] L. D. Landau and E. M. Lifshitz. *Statistical Physics*. Pergamon Press, 2 edition, 1958.

[257] C. N. Yang. Concept of Off-Diagonal Long-Range Order and the Quantum Phases of Liquid He and of Superconductors. *Rev. Mod. Phys.*, 34: 694–704, 1962.

Appendix A

Feshbach resonance in a state-dependent lattice

The low-energy scattering of atoms is quantified by the scattering length, a. This is affected by the Feshbach resonance, which occurs due to the bound states of closed channels that are resonant with the open channel [113, 247]. Its dependence on the magnetic field is expressed as

$$a = a_{\mathrm{bg}} \left(1 - \frac{\Delta B}{B - B_0}\right), \tag{A.1}$$

where a_{nr} is the off-resonant value. The resonance is typically accompanied by losses, as the bound states enhance coupling to inelastic outgoing channels, converting the internal energy to kinetic energy [247]. The effect of loss can be captured as an imaginary shift of the resonance,

$$\begin{aligned} a + ib &= a_{\mathrm{bg}} \left(1 - \frac{\Delta B}{B - B_0 + i\gamma_B/2}\right) \\ &= a_{\mathrm{bg}} \left(1 - \frac{\Delta B (B - B_0)}{(B - B_0)^2 + \gamma_B^2/4} + i \frac{\Delta B \gamma_B/2}{(B - B_0)^2 + \gamma_B^2/4}\right). \end{aligned} \tag{A.2}$$

The change of the atom number after some fixed time will be $dN \propto bNdt$, leading to the atom number as a function of B as

$$N \sim N_0 \left(1 - \frac{A^2}{(B - B_0)^2 + \gamma_B^2/4}\right), \tag{A.3}$$

with some constant A. In Fig. A.1, we present a measurement of the losses near the Feshbach resonance between the hyperfine ground state $5S_{1/2}\,|F = 1, m_F = 1\rangle$

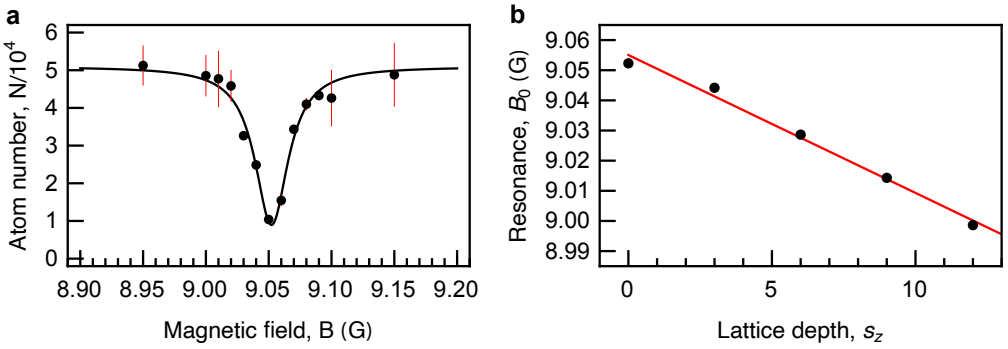

Figure A.1: Feshbach resonance in a state-selective lattice of variable depth s_z and tubes of depth at $s_\perp = 20$. **a,** Total atom number ($|1,1\rangle$ and $|2,0\rangle$) versus magnetic field B after the 10 ms holding time at $s_z = 0$. The fitting to Eq. A.3 yields $B_0 = 9.052(2)$ G, $\gamma_B = 0.032(0.005)$ G, and $A = 0.015(2)$ G. Each point represents two experimental runs. **b,** Resonance position vs. s_z.

and $|2,0\rangle$ of ^{87}Rb atoms, prepared in roughly equal proportions. For the measurement, the state-selective lattice was ramped up to s_z in 2 ms, and the magnetic field was jumped from 8.95 G to the final B in 500 μs. The atoms were held for 10 ms before the time-of-flight step to measure the total atom number. The resonant value B_0 changes in the state-selective lattice, as the relative energies of the open and closed channels change. We also note that the resonance is shifted by the presence of tubes (that are state-independent), which may be related to the confinement-induced resonance [248]. Without the lattice and tubes, we obtain $B = 9.046(2)$ G,[1] in line with the literature [249] and our previous measurement [123].

[1]Measured on 2022.02.04.

Appendix B

Some details on autonomous operation

In Section 3.6, we discussed a bot program developed with UiPath for autonomous operation, and here we show some related codes. The bot takes instructions in a JSON format. Below is an example of JSON files (the newlines are ignored),

```
{
    "seqName":"",
    "ciceroIteration":2,
    "ciceroFirstRun":false,
    "parNames":[
        "ODT1evap",
        "Blst"
    ],
    "parVals":[
        3.75538331592177,
        3.48
    ]
}
```

In this example, seqName is the name of Cicero sequence to be used (empty if the sequence is already open), ciceroIteration is the next iteration number to be run, ciceroFirstRun indicates if this is the start of a set of iterations, parNames is the list of variable names to be updated, and parVals is the list of corresponding values. The variables ODT1evap and Blst control the final depth of the ODT1 beam (for evaporative cooling) and the field coil current, respectively (the variable ODT2 is automatically related to ODT1 in the Cicero

sequence).

In Fig. B.1, we show the top-level Flowchart of our UiPath bot. The programming is done visually, with various functions and modules (like an if statement) being represented as boxes (one can also invoke hand-written codes in VB or C#). Except for the initialization step, it stays in a loop, where it waits for a JSON instruction, updates the Cicero variables, waits for another instruction, and so on.

One of the core tasks of the bot is updating the Cicero variables. In Fig. B.2, we show a snippet of the bot code for updating the variables via the Variable Preview window while an iteration is running. The UI elements of the Cicero program have a tree-like structure, which can be searched through the Find Children function of UiPath. This allows for accessing the input boxes corresponding to different variables that we wish to update.

In the below, we also show the main loop of the Mathematica notebook used in the autonomous operation, which analyzes pictures, keeps various records, displays status messages, and generates instructions for the next iterations. A user can modify this code if necessary, for example, to apply a new algorithm for updating variables or to add a new behavior for the bot.

```
(*
; Main loop
; - Generate a new instruction for UiPath (a0.json)
; - Wait and read the new picture file (a0.spe)
; - Repeat.
*)
mainLoop[] := Module[{newInstruction, newPicFile, atomNumber,
    shows, linesV, atomNumsV,
    timeBeforeWait, bTimeOut,
    bCiceroFirstRun, newInstructionNum
    },

   bCiceroFirstRun = True; (*
   To notify UiPath to start 'Continue List' *)
   newInstructionNum = newPicNum;
   While[True,

    (*
    ; Generate the instruction file (a0.json)
    *)
```

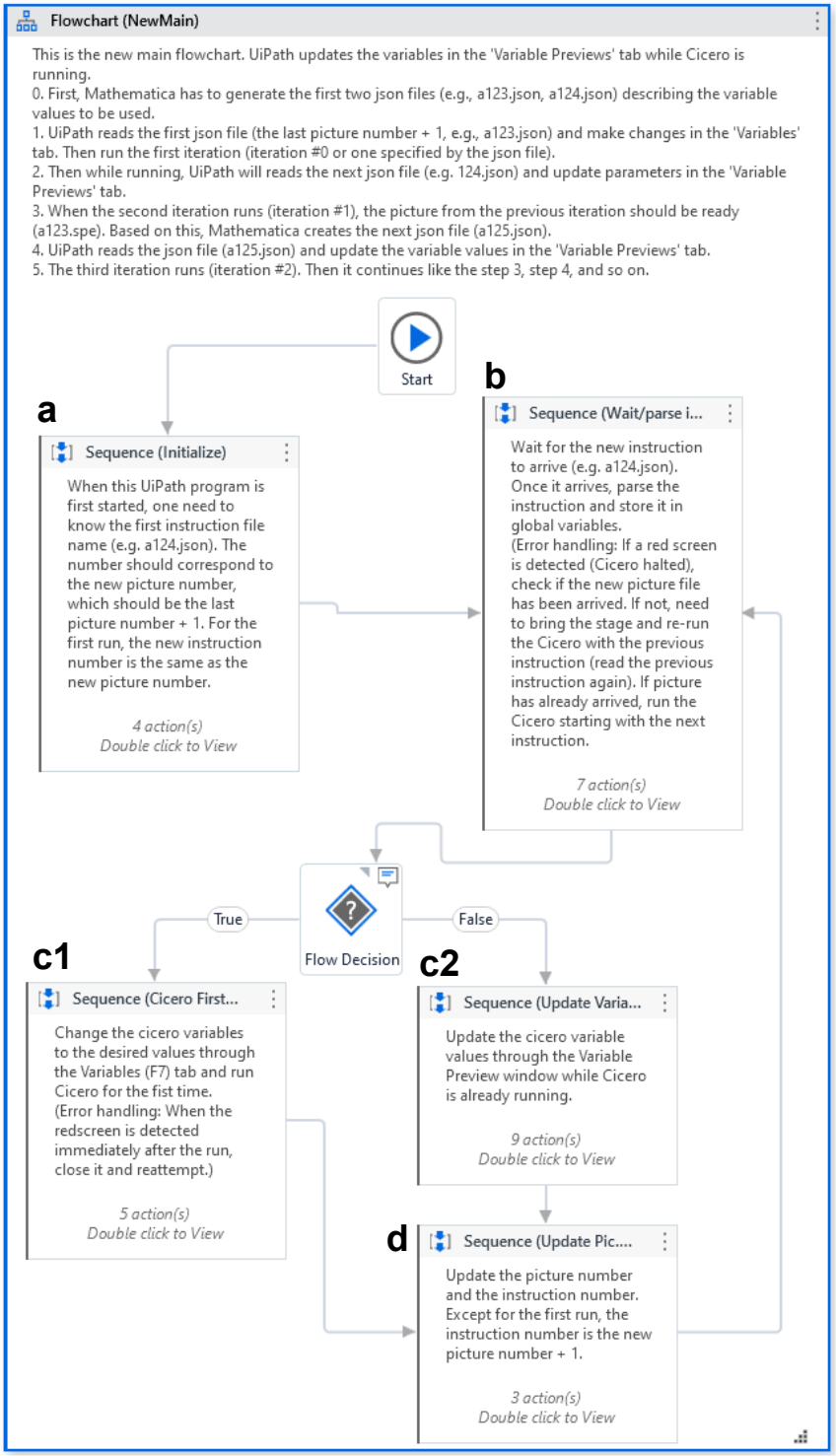

Figure B.1: **The Flowchart of our UiPath bot.** It consists of several Sequences (different from Cicero sequences), each for **a,** initializing the instruction number to read, **b,** waiting and parsing the JSON instructions, updating the variables **c1,** through the Variables tab of Cicero (if this is the first cycle) or **c2,** through the Variable Preview window of Cicero (if this is one of the subsequent cycles), **d,** updating the instruction number.

```
newInstruction = {"seqName" -> seqName,
  "ciceroIteration" -> ciceroIteration,
  "ciceroFirstRun" -> bCiceroFirstRun,
  "parNames" -> ciceroParNames, "parVals" -> ciceroParVals};
Export["a" <> ToString[newInstructionNum] <> ".json",
 newInstruction];
addLog[
 "Generated a new instruction (" <> "a" <>
  ToString[newInstructionNum] <> ".json" <> ")."];
newInstructionNum = newInstructionNum + 1;

(* If this is the first run, generate another json instruction. *)
If[bCiceroFirstRun == True,
 addLog[
  "Skipping the picture analysis to generate the second instruction"];
 bCiceroFirstRun = False;
 ciceroIteration = ciceroIteration + 1;
 Continue[];
 ];

(*
; Wait for the new picture to arrive
*)
newPicFile = "a" <> ToString[newPicNum] <> ".spe";
timeBeforeWait = AbsoluteTime[];
bTimeOut = False;
While[True,
 If[FileExistsQ[FileNameJoin[{globalDataDir, newPicFile}]],
  addLog["A new picture file " <> newPicFile <> " was found."];
  Break[];
  ];

 If[Mod[pauseMathematica[0.5], 5] == 0,
  addLog[
    "Waiting for the next picture (" <> newPicFile <>
     ") to arrive."];
  ];

 (* If the picture don't arrive for 45s, send an email alert. *)
 If[bTimeOut == False && (AbsoluteTime[] - timeBeforeWait) > 50,
```

```
  bTimeOut = True;
  sendEmail["BEC picture waiting time out (" <> newPicFile <> ")",
    "."];
  addLog["Time out: an email alert has been sent."];
  ];
 ];

(*
; Analyze picture and update parameters
*)

{shows, linesV, atomNumsV} = processPicture[newPicFile, 0.5];
addCurrentPlots[
 Join[shows, {ListPlot[linesV[[1, 1]],
    PlotRange -> All]}, {newPicFile, runCounter}]];

atomNumber = atomNumsV[[1, 1]];
AppendTo[statusAtomNums, atomNumber];

(* If the atom number is outside the upper or lower limit,
try to bring it back. *)
ciceroParVals[[
  1]] += ((atomNumUL + atomNumLL)/2 - atomNumber)/3000*0.001;

(* The next picture number, and cicero iteration number *)
newPicNum = newPicNum + 1;
ciceroIteration = ciceroIteration + 1;

addLog["Finished the run #" <> ToString[runCounter] <> "."];

(*
; Check finish condition
*)
runCounter += 1;
If[runCounter >= runCounterLast,
 addLog[
  "The last instruction has been sent " <> "(a" <>
   ToString[runCounter] <> ".json). " <>
   "Terminating the program."];
 sendEmail[
```

```
    "The last instruction has been sent " <> "(a" <>
     ToString[runCounter] <> ".json). " <>
     "Terminating the program."];
   Break[];,
   addLog[
     "Continuing to the next run #" <> ToString[runCounter] <>
      "."];
   ];
  ];
 ];
```

Additionally, exceptional situations can be detected and handled by either the UiPath bot or the Mathemtica notebook. For example, when UiPath finds that the transporter position is not correct, it triggers the controller (via Cicero) to bring the transporter back to the initial position. The bot can also monitor if Cicero reported any red screen error without completing an iteration, and can restart the iteration if necessary. When the Mathematica notebook notices an empty picture without atoms (potentially due to some missed trigger), it can also instruct the bot to repeat the iteration. If multiple empty pictures are obtained in a row (e.g. due to an unlocked laser), the notebook may notify a human operator (via an email or a beeping sound) for intervention.

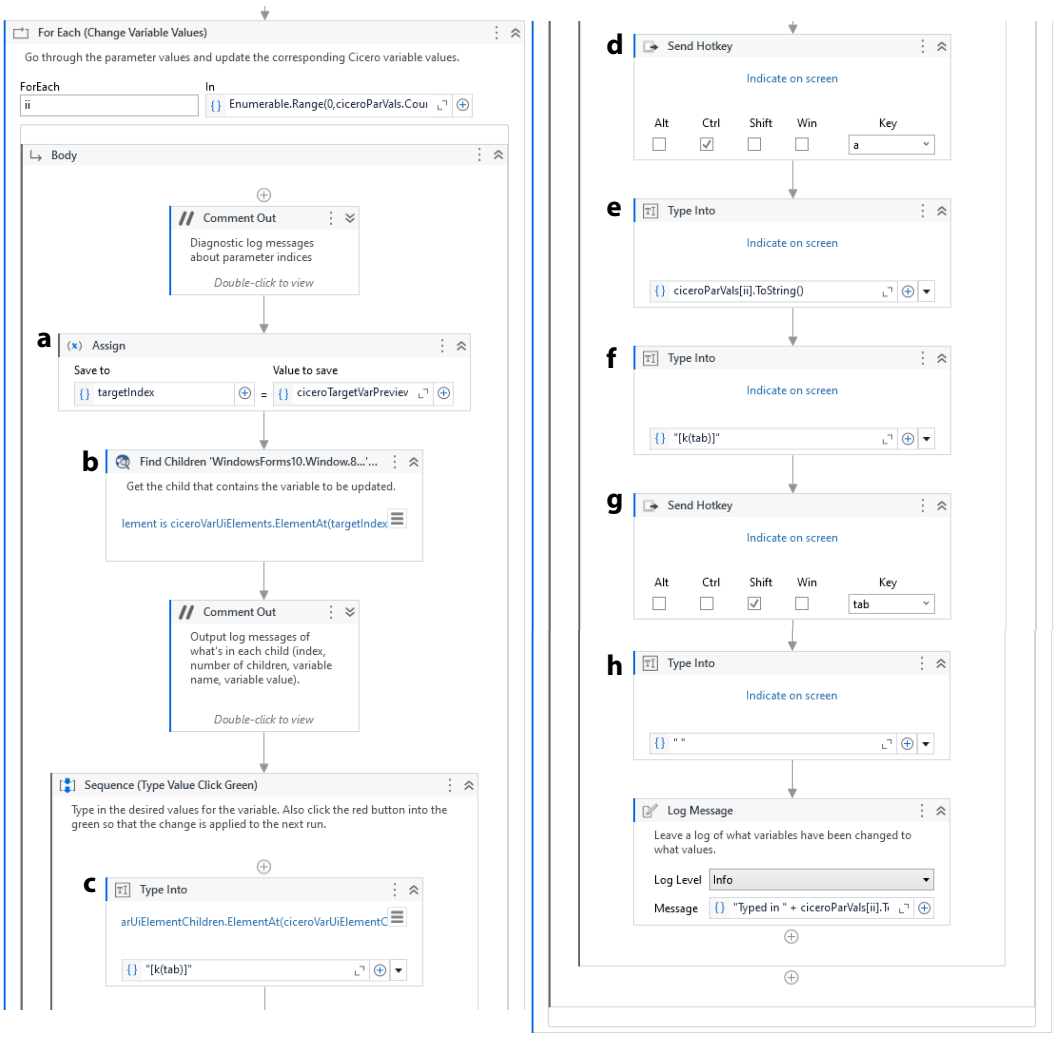

Figure B.2: A snippet of the bot code for updating Cicero variables. The For loop repeats for the number of variables to be updated. **a,** Get the index of the UiElement corresponding to one of the variables that need to be changed. (The indices are found in another part of the code not shown here.) **b,** Select the UiElement. **c,d,e** Press 'Tab' (to move the cursor to the input box), 'Ctrl + a' (to select the text representing the old value), and type in the new value for the variable. **f,g,h,** These steps are required to check the red button into green (this button appears when the variable value is being changed in the Variable Preview window), such that the change is applied for the next iteration.

Appendix C

Further discussion on coherence of interacting Bose gases

The massless Bogoliubov excitations we discussed in Section 5.1.1 are also called the Nambu-Goldstone bosons in the context of field theory [250, 251], and are linked to the spontanoues breakdown of continuous symmetry and long-range order. These are important concepts in Bose-Einstein condensation [176], and we review some aspects of these concepts for the purpose of justifying the assumption that our BECs are described by a macroscopically populated wavefunction.

As mentioned, the Hamiltonian can be written in terms of the field operators $\hat{\psi}(\boldsymbol{r})$, and coherent states can be used to approximate the operators as classical fields, e.g. $\hat{\psi}(\boldsymbol{r})\,|\psi\rangle = \psi(\boldsymbol{r})\,|\psi\rangle$. Furthermore, the time coordinate can play the role of the temperature $t/\hbar = -i\beta$ such that $e^{-iHt/\hbar} = e^{-\beta H}$. The quantum partition function $Z = \mathrm{Tr}\, e^{-\beta\hat{H}} = \sum_{\psi} \langle\psi|\, e^{-\beta\hat{H}}\, |\psi\rangle$ can be divided into infinitesimal time intervals, and inserting the identity operators leads to the path-integral formula as[1]

$$\begin{aligned} Z &= \mathrm{Tr}\, e^{-\beta H[\hat{\psi}]} = \mathrm{Tr} \prod_i e^{-\Delta\tau_i H[\hat{\psi}]} \\ &= \mathrm{Tr} \prod_i \sum_{\psi_i} e^{-\Delta\tau_i H[\psi]}\, |\psi_i\rangle \langle\psi_i| = \int \mathcal{D}\psi(\boldsymbol{r},\tau) e^{-S[\psi]}. \end{aligned} \tag{C.1}$$

In the grand canonical ensemble, the free energy should be $\hat{H} - \mu\hat{N}$ where $\hat{N} = \int d^3\boldsymbol{r}\hat{\psi}^\dagger(\boldsymbol{r})\hat{\psi}(\boldsymbol{r})$. For our interacting Bose gas in Eq. (5.1), the action

[1] Schematically; see for example [175, 197, 252, 253] for details.

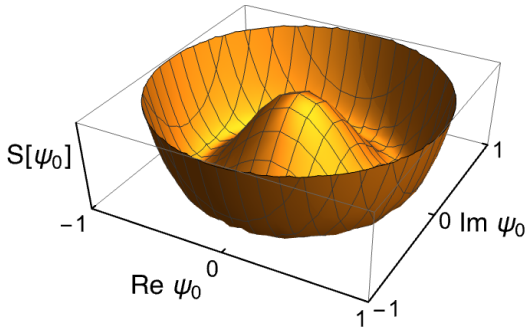

Figure C.1: Superfluid potential with spontaneously broken symmetry (with $\mu = g/2L^3$).

$S(\psi)$ is given by

$$S[\psi] = \int_0^\beta d\tau \int d^3\boldsymbol{r} \left[\psi^*\partial_\tau\psi - \frac{\hbar^2}{2m}\psi^*\nabla^2\psi - \mu\psi^*\psi + \frac{g}{2}(\psi^*\psi)^2\right], \qquad \text{(C.2)}$$

where $\psi = \psi(\boldsymbol{r},\tau)$ and $\psi^*\partial_\tau\psi$ is called the Berry phase term representing the overlap between two coherent states at different times [197]. We postulate that the $\boldsymbol{p} = 0$ state is highly populated in momentum space, $\hat{\psi}(\boldsymbol{r}) = L^{-3/2}\sum_{\boldsymbol{k}} \hat{a}_{\boldsymbol{k}} e^{i\boldsymbol{k}\cdot\boldsymbol{r}} \approx \sqrt{n_0} + L^{-3/2}\sum_{\boldsymbol{k}\neq 0} e^{i\boldsymbol{k}\cdot\boldsymbol{r}}$ where $\sqrt{n_0} \equiv \sqrt{N_0/L^3}$. If we focus on the condensed fraction, denoted by $\psi_0 \approx \sqrt{N_0}$, which is assumed homogeneous, we obtain the action functional

$$S[\psi_0] = -\beta\mu|\psi_0|^2 + \beta\frac{g}{2L^3}|\psi_0|^4, \qquad \text{(C.3)}$$

which looks like a Mexican hat in the complex plane [175]. The path integral is solved at a saddlepoint, $\delta S/\delta\psi_0 = 0$, leading to $\psi_0^*(-\mu + gL^{-3}\psi_0^*\psi_0) = 0$. Below the transition temperature $T < T_c$ ($\mu > 0$, which is now allowed due to interactions [175]), there is a non-trivial solution $\psi_0 = |\psi_0|e^{i\theta} = (\mu L^3/g)^{1/2}e^{i\theta}$, which has a continuous degeneracy parameterized by θ. To obtain the ground-state solution, one has to expand around a saddlepoint with a specific value of θ. This breaks the global $U(1)$ symmetry $\psi \to e^{i\theta}\psi$ of the action Eq. (C.2), and according to Goldstone's theorem [250, 251], there should be a massless boson associated with θ [254].

An expansion can be done as $\psi(\boldsymbol{r},\tau) = \sqrt{n_0 + n_1(\boldsymbol{r},\tau)}e^{i\theta_0 + i\theta_1(\boldsymbol{r},\tau)}$, where n_1 and θ_1 are the small fluctuations and $n_0 = \mu/g$. Choosing $\theta_0 = 0$ and taking

the leading order, we get

$$\psi(\boldsymbol{r},\tau) \approx \sqrt{n_0}\left(1+\frac{n_1(\boldsymbol{r},\tau)}{2n_0}\right)e^{i\theta_1(\boldsymbol{r},\tau)}. \tag{C.4}$$

Each term in the action (C.2) contributes the following fluctuations up to second order (except the terms that can be integrated out, e.g. $\dot{\theta}$, $n_1\dot{n}_1$, $n_1'\theta_1' + n_1\theta_1''$, etc)

$$n_0\phi^*\dot{\phi} = (n_0+n_1/2)(\dot{n}_1/2 + in_0\dot{\theta}_1 + in_1\dot{\theta}_1/2) = n_0(in_1\dot{\theta}_1) + ... \tag{C.5}$$

$$\begin{aligned} n_0\phi^*\nabla^2\phi &= (n_0+n_1/2)(n_1''/2 + in_0\theta_1'' + in_1'\theta_1' + in_1\theta_1''/2 - n_0(\theta_1')^2 - n_1(\theta_1')^2/2) \\ &= -n_0^2(\theta_1')^2 + n_1n_1''/4 + ... \end{aligned} \tag{C.6}$$

The last two terms in the action contribute

$$-\mu(n_0+n_1) + (g/2)(n_0+n_1)^2 = (g/2)n_1^2 + \text{const.} \tag{C.7}$$

where we used $n_0 = \mu/g$. With integration by parts, we obtain the action of the fluctuations

$$\begin{aligned} S_1[n_1,\theta_1] = \int_0^\beta d\tau \int d^3\boldsymbol{r}\left[in_1\partial_\tau\theta_1 + \frac{\hbar^2 n_0}{2m}(\nabla\theta_1)^2 + \frac{\hbar^2}{8mn_0}(\nabla n_1)^2 + \frac{g}{2}n_1^2\right] \\ + \text{higher orders.} \end{aligned} \tag{C.8}$$

The term quadratic in n_1 means that the density fluctuation is *massive* (coefficient proportional to the mass squared [254]), and it costs energy to vary n_1. There is no such term for θ_1, and the meaning of it becomes more clear by transforming it to momentum space, e.g. $n_1(\boldsymbol{r}) = L^{-3/2}\sum_k n_{1,\boldsymbol{k}}e^{i\boldsymbol{k}\cdot\boldsymbol{r}}, \theta_1(\boldsymbol{r}) = ...$, which yields[2]

$$S_1[n_{1,\boldsymbol{k}},\theta_{1,\boldsymbol{k}}] = \int_0^\beta d\tau \sum_{\boldsymbol{k}} in_{1,\boldsymbol{k}}\partial_\tau\theta_{1,\boldsymbol{k}}^* + \frac{1}{2}\left(g+\frac{\hbar^2k^2}{4mn_0}\right)|n_{1,\boldsymbol{k}}|^2 + \frac{n_0\hbar^2k^2}{2m}|\theta_{1,\boldsymbol{k}}|^2. \tag{C.9}$$

This is an action of harmonic oscillators, one for each $\boldsymbol{k}$ [197], of the form $P\dot{Q} + (1/2M)P^2 + (1/2)M\omega^2Q^2$ where the "coordinate" Q is $\theta_{1,\boldsymbol{k}}$ and the "momentum" P is $\hbar n_{1,\boldsymbol{k}}$, and implies that the density fluctuation is conjugate to the phase fluctuation. We can then infer the frequency of harmonic

[2] $n_{1,\boldsymbol{k}} = n_{1,-\boldsymbol{k}}^*$ since $n_1(\boldsymbol{r})$ is real. $n_{1,\boldsymbol{k}}, \theta_{1,\boldsymbol{k}}$ have unit of $L^{-3/2}$ and $L^{3/2}$, respectively.

oscillators

$$\omega_{\boldsymbol{k}}^2 = \frac{2}{\hbar^2}\left(g + \frac{\hbar^2 k^2}{4mn_0}\right)\frac{n_0\hbar^2k^2}{2m} = \left(2n_0 g + \frac{\hbar^2k^2}{2m}\right)\frac{k^2}{2m}, \tag{C.10}$$

which is that of Bogoliubov excitations in Eq. (5.6). The density fluctuation can be integrated out via Gaussian functional integral [197],[3] resulting in the action $S_{\text{eff}} = \int_0^\beta \sum_{\boldsymbol{k}} (1/2)(g + \hbar^2k^2/4mn_0)^{-1}|\dot{\theta}_{\boldsymbol{k}}|^2 + (n_0\hbar^2k^2/2m)|\theta_{\boldsymbol{k}}|^2$ of harmonic oscillators, and we see that the massless sound modes originate from the phase fluctuations of the condensate.

To understand the physical consequence of these fluctuations, we can look at the current of the field [175]. By plugging Eq. (C.4) into the standard expression for the current, we obtain at leading order

$$\boldsymbol{j}(\boldsymbol{r},\tau) = \frac{i}{2m}\left[(\nabla\psi^*)\psi + \psi^*\nabla\psi\right] = \frac{n_0}{2m}\nabla\theta_1. \tag{C.11}$$

We can also obtain the equations of motion for n_1 and θ_1 from the saddlepoints $\delta S_1/\delta n_1 = 0$ and $\delta S_1/\delta\theta_1 = 0$ of Eq. (C.8) (after using integration by part and $n = n_0 + n_1 = \mu/g + n_1$), we find

$$i\partial_\tau\theta_1 = -gn + \mu, \quad -i\partial_\tau n = \frac{n_0}{2m}\nabla^2\theta_1 = \nabla\cdot\boldsymbol{j}. \tag{C.12}$$

The second equation is a continuity equation. We can set $\partial_\tau\theta_1 = 0$, which in turn fixes $n_1 = 0$ and $\nabla\cdot\boldsymbol{j} = 0$. Therefore, the equations of motion admit a steady state supercurrent without divergence, which would not be possible if θ_1 were massive [175].

The appearance of the classical field ψ_0 of a condensate, also called the order parameter [182], is related to the off-diagonal long-range order (ODLRO), defined as

$$\rho(\boldsymbol{r},\boldsymbol{r}') = \langle\hat{\psi}^\dagger(\boldsymbol{r})\hat{\psi}(\boldsymbol{r}')\rangle, \tag{C.13}$$

which is also called a (single-particle) density matrix [113, 197]. The non-vanishing of this in the limit $|\boldsymbol{r}-\boldsymbol{r}'| \to \infty$ provides a criterion for Bose-Einstein condensation generalized to interacting particles, where the free-particle basis might not always be convenient (also called Penrose-Onsager criterion [255]; discussed as well by Landau and Lifshitz [256] and by Yang [257]).

The density matrix is related to the momentum distribution by the Fourier

[3] Similarly to $\int_{-\infty}^{\infty} dx e^{-Ax^2-Bx} = (\pi/A)e^{B^2/4A}$.

transform $\hat{\psi}(\boldsymbol{r}) = V^{-1/2}\sum_{\boldsymbol{k}} \hat{a}_{\boldsymbol{k}} e^{i\boldsymbol{k}\cdot\boldsymbol{r}}$,

$$\rho(\boldsymbol{r},\boldsymbol{r}') = \frac{1}{V}\sum_{\boldsymbol{k}} n_{\boldsymbol{k}} e^{-i\boldsymbol{k}(\boldsymbol{r}-\boldsymbol{r}')}, \tag{C.14}$$

where $n_{\boldsymbol{k}} = \langle \hat{a}^\dagger_{\boldsymbol{k}} \hat{a}_{\boldsymbol{k}} \rangle$ and we used $\langle \hat{a}^\dagger_{\boldsymbol{k}} \hat{a}_{\boldsymbol{k}'} \rangle = \delta_{\boldsymbol{k},\boldsymbol{k}'} n_{\boldsymbol{k}}$.[4] For a Bose gas with a macroscopic population in $\boldsymbol{k} = 0$, we can write $n_{\boldsymbol{k}} = N_0 \delta_{\boldsymbol{k},0} + f(\boldsymbol{k})(1 - \delta_{\boldsymbol{k},0})$ (it can be shown $f(\boldsymbol{k}) = \sinh^2(\theta_{\boldsymbol{k}})$ for zero excitations, $T = 0$ [197]). We may take the continuum limit $V \to \infty$ with $n_0 = N_0/V$ fixed, leading to[5]

$$\begin{aligned}\rho(\boldsymbol{r},\boldsymbol{r}') &= \int \frac{d^3\boldsymbol{k}}{(2\pi)^3} \left[n_0 (2\pi)^3 \delta(\boldsymbol{k}) + f(\boldsymbol{k}) \right] e^{-i\boldsymbol{k}(\boldsymbol{r}-\boldsymbol{r}')} \\ &= n_0 + \int \frac{d^3\boldsymbol{k}}{(2\pi)^3} f(\boldsymbol{k}) e^{-i\boldsymbol{k}(\boldsymbol{r}-\boldsymbol{r}')}. \end{aligned} \tag{C.15}$$

In the limit $|\boldsymbol{r} - \boldsymbol{r}'| \to \infty$, the integral of the second term vanishes due to the rapidly oscillating exponential. Therefore,

$$\lim_{|\boldsymbol{r}-\boldsymbol{r}'|\to\infty} \rho(\boldsymbol{r},\boldsymbol{r}') = n_0, \tag{C.16}$$

which is the key property of a Bose gas below the critical temperature [113]. This also implies a long-range phase coherence, $\langle \psi^\dagger(\boldsymbol{r})\psi(\boldsymbol{r})\rangle \approx \langle \psi^\dagger(\boldsymbol{r})\rangle\langle\psi(\boldsymbol{r})\rangle = (\sqrt{n_0}e^{-i\theta})(\sqrt{n_0}e^{i\theta})$, i.e. the phase is spatially uniform (This is also discussed in terms of the energy cost to twist the phase across the system known as the helicity modulus [197]).

[4] Using the translational invariance, $\langle \hat{\psi}^\dagger \hat{\psi} \rangle$, one can show

$$\begin{aligned}\langle \hat{a}^\dagger_{\boldsymbol{k}} \hat{a}_{\boldsymbol{k}'} \rangle &= V^{-1} \int_{\boldsymbol{r}} \int_{\boldsymbol{r}'} \langle \hat{\psi}^\dagger(\boldsymbol{r}-\boldsymbol{r}')\hat{\psi}(0)\rangle e^{i(\boldsymbol{k}\cdot\boldsymbol{r} - \boldsymbol{k}'\cdot\boldsymbol{r}')} = V^{-1} \int_{\boldsymbol{r}} \int_{\boldsymbol{r}''} \langle \hat{\psi}^\dagger(\boldsymbol{r}'')\hat{\psi}(0)\rangle e^{i(\boldsymbol{k}\cdot\boldsymbol{r} - \boldsymbol{k}'\cdot\boldsymbol{r} + \boldsymbol{k}'\cdot\boldsymbol{r}'')} \\ &= V^{-1} \int_{\boldsymbol{r}} e^{i(\boldsymbol{k}-\boldsymbol{k}')\cdot\boldsymbol{r}} \int_{\boldsymbol{r}''} \langle \hat{\psi}^\dagger(\boldsymbol{r}'')\hat{\psi}(0)\rangle e^{i\boldsymbol{k}'\cdot\boldsymbol{r}''} = \delta_{\boldsymbol{k},\boldsymbol{k}'} \int_{\boldsymbol{r}''} \langle \hat{\psi}^\dagger(\boldsymbol{r}'')\hat{\psi}(0)\rangle e^{i\boldsymbol{k}'\cdot\boldsymbol{r}''}\end{aligned}$$

[5] In the continuum limit, $\sum_k \to (L/2\pi)\int dk$. The Kronecker delta should transform as $\delta_{k,0} \to (2\pi/L)\delta(k)$ to satisfy the normalization $\sum_k \delta_{k,0} = 1 = (L/2\pi)\int dk \delta(k)$.